UNIVERSITY OF LIVERPOOL

Stiff stilbene as a mechanochemical force probe for fundamental studies and small molecule manipulation

By Robert T. O'Neill

Thesis submitted in accordance with the requirements of the University of Liverpool for the degree of Doctor of Philosophy.

Declaration

Except for sections in which I indicate the work was completed by a collaborator the thesis is the result of my own work. The material contained in this thesis has not been presented, nor is currently being presented, either wholly or in part for any other degree of qualification.

Robert T. O'Neill

The research was carried out in the Department of Chemistry at the University of Liverpool.

Preface

Mechanochemistry is a field within chemistry akin to photo– or electrochemistry that attempts to understand and exploit chemical phenomena that occur as a direct result of mechanical motion. The term mechanochemistry is applied to describe the rearrangement of chemical bonds driven by the dissipation of molecular strain caused by mechanochemical motion. [3,4] Apparently disparate phenomena fall into this definition such as the synthetic transformations that occur when a steel ball impacts solid chemicals,[6] the scission of polymers during strong hydrodynamic flows,[5] the failure of an overstretched elastic band[2] and the behaviour of some motor proteins.[7]

In recent decades as the field matured three distinct areas emerged, each with their preferred techniques and goals which I will term; biomechanochemistry, small molecule mechanochemistry and synthetic polymer mechanochemistry. The broad goals of biomechanochemistry are to understand how organisms harness force to achieve tasks with intricate molecular machinery yet minimize the damaging effects excessive mechanical force can cause to cells, ultimately yielding new medical interventions that target mechanochemical processes.[8-10] Small molecule mechanochemistry is concerned with how chemical reactions can be induced in small molecules by subjecting them to sudden impact from a milling ball or grinding.[11-15] Finally, polymer mechanochemistry aims to exploit our knowledge of mechanochemical reactivity to design new materials with novel responses to force, which requires identifying new reactions that are sensitive to force.[16-18] Polymer mechanochemistry is practically explored by both directly stretching a polymer containing the potential reactive moiety, which in its current form can only establish force–accelerated reactivity, and using small macrocycles designed as models of polymer mechanochemistry which allow force to be applied to a small reacting fragment. The latter method allows mechanosensitive reactions that are accelerated, inhibited or unaffected by force to be studied.[19-23]

In the introduction to this thesis (chapter 1), which has been adapted in large part from reviews in Nature Reviews Chemistry[5], Synlett[24] and a book chapter[25] that I co–authored during my PhD, I aim to provide a rigorous conceptual framework surrounding mechanochemical concepts key to understanding the projects presented. As stiff stilbene plays a key role in three of the projects its properties and previous uses in chemistry are also discussed in the introduction.

Four projects are presented after the introduction. Chapter two establishes novel fundamental insight into a previous inscrutable aspect of polymer physics, the conformation

of polymer chains during chain scission in rapid solvent flows. This chapter was adapted from a paper currently under review with Nature Chemistry for which I am the first author, and was presented by me at the STEM for Britain science competition held in the UK Houses of Parliament and at the 2021 Pacifichem conference. In it, we present a new experimental approach that allowed testing of existing models of polymer chain conformation leading to chain scission and demonstrated their inability to reproduce the exacting data. Breaking from the convention of the field that assumes changes in chain conformation occur much faster than mechanochemical reactions, we then present our model that allows the unfolding of the polymer chain and mechanochemical reactions to occur on a similar time scale and therefore compete. This model is the only one that reproduces all data within experimental error.

Chapter three describes my use of quantum chemical calculations to rationalize the experimental work conducted by our collaborators at Duke University, namely the reduction in activation energy of stiff stilbene *E*→*Z* isomerisation upon complexation of a metal centre to 2,2'-bis(diphenylphosphino)biphenyl incorporated into a macrocycle with stilbene. The work is the first to describe a model of a tractable example of synthetic allosteric kinetic control. This section was adapted from a draft paper in preparation for its upcoming submission to JACS.

Chapter four describes my attempts to use force to influence the pK_b of *N,N*–dimethyl–2,2'–diamine–[1,1'–biphenyl] (DABP) by controlling its ability to form an intramolecular H–bond. In the first project of chapter four, I attempted to apply tensile force to a DABP analogue ($DABP_a$) by embedding it in a polymer network to produce a material whose pK_b depends on the force it experiences. In the second project, I attempt to apply both compressive and tensile forces to $DABP_a$ by incorporating it into a macrocycle containing stiff stilbene to produce a photo–responsive base with superior properties to those reported previously. Despite producing target materials in both projects the interruption of the pandemic (during which key specimens deteriorated) and problems in measurements have prevented achieving these goals.

An additional publication in JACS[26] in which I played a minor part is not discussed here.

Table of content

Contents

Abbreviations and conventions

DABP (diamine biphenyl) – *N,N,N',N'*–tetra methyl–2,2'–diamine–[1,1'–biphenyl]

$DABP_a$ – analogues of DABP incorporated into a polymer or macrocycle.

SS– Stiff Stilbene

$CDCl_3$ – Deuterated chloroform

EtOAc – Ethyl Acetate

PS – Polystyrene

THF – Tetrahydrofuran

DFT– Density–Functional Theory

DP – Degree of Polymerisation

HPLC – High–Performance Liquid Chromatography

Prep GPC – Preparative Gel Permeation Chromatography

MMD – Molar Mass Distribution

SEC – Size Exclusion Chromatography

SMFS – Single Molecule Force Spectroscopy

NMR– Nuclear Magnetic Resonance

HSQC – Heteronuclear Single Quantum Coherence

RDP – Reaction distribution probability.

sRDP – Reaction distribution probability during $t_{stretch}$

$t_{stretch}$ – The time the chain is overstretched.

$\Delta t_{stretch}$ – The time the chain experiences forces $\geq$ 2.5 nN

k_s – Rate of chain segment growth

k_d – Rate of chain segment drift.

Compounds labels are assigned according to their chapter number and the order they appear e.g. cy-X where y is the chapter number and X starts from 1 in each chapter. To avoid potential confusion chapters 2 and 3 retain the naming system used in the paper as originally drafted, any compounds added for adaption to this thesis are labelled as described above. Molecules that have a colloquial name used as standard in the literature e.g. stilbene, stiff stilbene etc. do not receive a label.

1. Introduction to Mechanochemistry

Polymer mechanochemistry

Polymer mechanochemistry studies how stretching a polymer chain changes the kinetic and/or thermodynamic stabilities of its constituent monomers, and how to exploit such changes to improve existing and create new materials, devices and processes and to advance our fundamental understanding of chemical reactivity. Mechanochemical phenomena are ubiquitous wherever polymers are used. Simply stretching an elastic band can break some of its C–C and C–S bonds in microseconds. These bond scissions are mechanochemical because they do not occur unless the band is stretched or "mechanically loaded". Just like an elastic band, undisturbed polymer chains making the band, or the covalent bonds making these chains do not spontaneously break at room temperature.

A primary objective of contemporary mechanochemistry is to develop a quantitative conceptual framework within which to describe and predict the complex sequence of physical processes that translate the macroscopic (or mechanical) motion, such as that responsible for stretching an elastic band, into the up–to 10^{14}–fold acceleration of chemical reactions of its constituent monomers, such as homolysis of a covalent bond. A coherent framework (a logically organised collection of equations and concepts that form a hierarchy capable of explaining the simplest interactions of individual chains up to the most complex polymeric solids) that captures all the distinct forms of mechanochemical reactions does not currently exist, however the effects of force (and indeed the concept of the 'force formalism') have been best developed in the context of polymer mechanochemistry. This is most likely because polymers' shape – chains made of many repeating small molecules – means that unlike the small molecules themselves they have a single prominent axis that is easily strained.[2,5]

The force formalism

Qualitatively, the known manifestations of polymer mechanochemistry are rationalized as the effect of molecular strain on chemical reactivity, by analogy with many known small strained molecules that are more reactive than their strain–free analogues. This qualitative approach has been spectacularly productive during the first decade of contemporary polymer mechanochemistry, enabling the identification of over 50 unimolecular reactions which are accelerated in stretched polymer chains. The decreasing pace of the discovery of new such reactions suggests a limit of this qualitative view in guiding even empirical mechanochemistry research and illustrates the need for quantitative models to fulfil the potential of polymer mechanochemistry to yield new polymeric materials and new insights into chemical reactivity.

Molecular strain being a purely qualitative concept, its effect on reaction kinetics has long been discussed in terms of strain energy, defined as the enthalpy (or free energy) of formation of the strained molecule relative to its (often hypothetical) strain free analogue. The acceleration of a reaction due to the relief of molecular strain is estimated from the fraction of this 'ground–state' strain energy released in the transition state. This approach is useful because the fraction is approximately constant for reactions of the same type since they share similar changes in molecular geometry moving along the reaction coordinate.

The extensive (i.e., size–dependent) nature of energy makes this approach entirely unsuitable for describing mechanochemical kinetics. The strain energy of a stretched macromolecule increases rapidly with its size, whereas the kinetic stability of a reactive site in such a chain is independent of the chain size. For example, when two stretched macromolecules of different lengths but identical monomer composition fracture at an identical rate, the fraction of the 'ground–state' strain energy released in the transition state is larger for the shorter chain than the longer chain chains, and the difference increases very rapidly with the difference in length. In other words, the strain energy of a stretched chain does not allow the kinetic stabilities of its constituent monomers to be predicted.

As a result, the modern approach to mechanochemical kinetics replaces strain energy with its gradient (or restoring force), which offers several advantages but also poses numerous technical and conceptual difficulties. First, force is an intensive (size–independent) property and in theory, can be used to describe quantitatively dynamics across the range of the length scales underlying mechanochemistry. For example, the stress tensor quantifying the macroscopic load acting on a material could be expressed in terms of restoring forces of its constituent polymer chains or chain segments separated by cross–links. Each single–chain force can then be related to the force experienced by each of the (strained) monomers comprising the stretched chain. If a general relationship between the force of a strained reactive site and its reactivity exists and is known, it becomes possible, at least in theory, to express the kinetic and thermodynamic stability of an average monomer in a strained bulk material in terms of a quantifier of the macroscopic load (e.g., stress tensor).

Second, the directional (vectoral) nature of force allows force–based kinetic models to accommodate the expectation that stretching a molecule along different axes should affect its kinetic stability differently and that for each axis, stretching should have a different effect from compression.

Although an empirical relationship between force and a reaction rate was stated long ago, and since then reformulated in the language of at least one theory of chemical kinetics, such

models don't relate the properties of force (an energy gradient) to the molecular changes it induces. Treating the key variable of mechanochemical kinetics as an abstract quantity precludes systematic improvements of these models or analysis of their limitations and hence of their accuracy, predictive capacities and limits of applicability. Empirical models continue to be widely used, and yield numbers that may offer a means of systematizing measurements from single–molecule force experiments. Yet, they do not appear to have enhanced our ability to design new mechanochemical reactions or rationalize the existing phenomena beyond what a qualitative, molecular–strain view offers.

A non–empirical approach to force–based formulation of mechanochemical kinetics originates in a specific physical model of a reacting polymer chain, which takes advantage of the localised nature of covalent reactions in polymer mechanochemistry, i.e., they involve rearrangement of a few bonds within a polymer segment of <1 nm. The molecular geometry of the reactive site, however, is determined by interactions among billions of atoms comprising the rest of the polymer chain and its surroundings that stretch the chain. Acceleration of some reactions in stretched macromolecular chains may result from partial structural relaxation of distorted bond torsion, angles and possibly distances (collectively known as molecular coordinates) away from the reactive site. This suggests that the intractably many "degrees of freedom" accounting for mechanochemical reactivity fall into two distinct categories: a minority that must be treated explicitly and quantum–mechanically because their electronic structure changes during the reaction and the majority that can be treated collectively because they are either unaffected by the reaction or are affected in a very particular and limited way amenable to a simple description.

Since the number of atoms involved in most chemical reactions is much fewer than the total making up a polymer, we can greatly simplify our task by considering separately the small reacting fragment and the rest of the polymer (which is unchanged chemically but potentially undergoes relaxation of bond angles and lengths). The atoms that undergo electronic changes during the chemical reactions require quantum chemical interpretation. The rest of the molecule that is bridged to this reacting section can be usefully approximated as a compressed harmonic spring (Figure 1). Unlike a stretched molecule on its own, this hybrid construct can exist in "stationary states" (nuclear configurations in internal mechanical equilibrium), which means that its reaction rate can be estimated from the energy difference of two such states using the transition state theory. Just like in a free reacting molecule, this energy difference arises from the changes in chemical bonding, molecular geometry and electronic structure of the molecular segment that constitutes the reaction. Unlike a free molecule, it has a contribution from the compressed spring, because the spring changes its

length (and hence its strain energy) to remain in mechanical equilibrium with the new molecular geometry. For a very soft spring, this contribution is simply a product of the restoring force of the spring and the difference in its extension between the rate–limiting transition and reactant states.

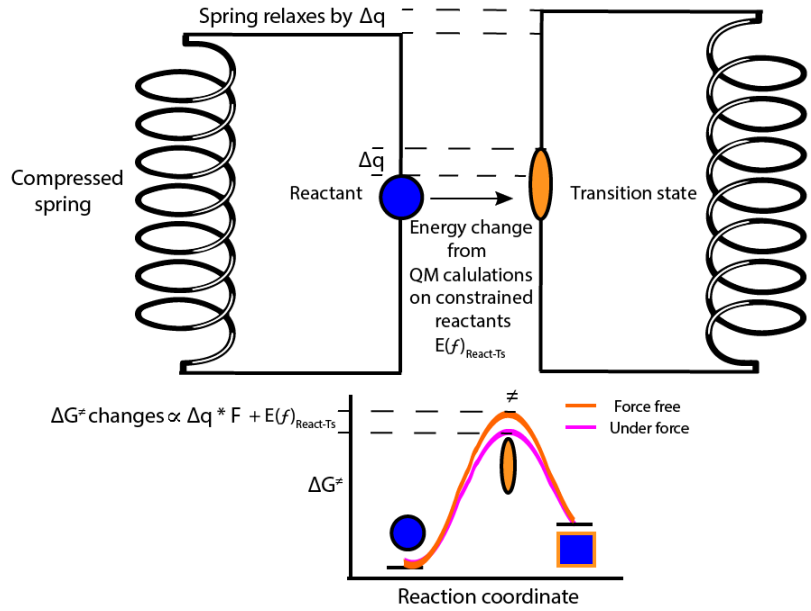

Figure 1 – **Mechanochemical reactions can be simplified by treating separately the reacting fragment and the rest of the molecule**. *Cartoon representation of a reactant stretched by a compressed harmonic spring, the energy of the spring is coupled to the reactant geometry. In this example when the reactant forms a transition state the spring relaxes because the transition state is larger than the reactant by Δq. Quantum chemical calculations on the stationary states of this spring/molecule system accurately predict changes in $\Delta G^{\neq}$ with force.*

Although the practical implementation of this model poses a number of questions (e.g., what's the minimum length of the chain segment below which the model no longer represents the reacting chain?), it defines the physical basis of both the force and how it affects the activation energy. It shows that force is always associated with a specific internal coordinate of a chain (e.g., internuclear distance) and is the gradient of strain energy of the whole system (stretched macromolecule and its surroundings) with respect to changes in this coordinate. Force reflects the contribution of changes in the strain energy of non–reactive degrees of freedom to the activation barrier. Importantly, the model shows that the same reactive site stretched to the same restoring force manifests the same reactivity regardless of the physical mechanism responsible for generating this force. Some of these mechanisms, elaborated below, include constraining the chain end–to–end distance as in single–molecule force experiments, the cumulative effect of interactions of multiple backbone atoms with a surrounding solvent in an elongational flow and properly designed macrocycles.

The model above explains the sharp contrast between the utility of force in mechanochemical kinetics and its limited ability to quantify kinetically significant molecular strain in many non–polymeric strained molecules. The very large aspect ratio of macromolecules creates a molecular axis along which dimensional changes affect the molecular strain energy of a stretched macromolecule particularly strongly. As a result, variations in strain energy due to even complex changes in molecular geometry associated with a localized reaction are approximated with useful accuracy from the energy gradient along this single axis (i.e., restoring force). In contrast, the vast majority of organic strained molecules lack such a privileged molecular axis. The model thus provides a quantitative reference point to estimate how accurately a restoring force of a strained molecule captures its kinetically significant strain.

In conventional chemical kinetics, only the energy of the transition state relative to that of the reactant is needed to estimate the reaction rate. In mechanochemical kinetics, estimating the rate of a stretched reactant requires two additional quantities: the restoring force of a molecular coordinate of the reactant (e.g., an internuclear distance), f, and the change in this coordinate between the reactant and the transition state, Δq. The product of these two quantities determines if the reaction is accelerated, inhibited or unaffected by stretching. Computations indicate that in an overstretched oligomer multiple internal coordinates, defined by different pairs of backbone atoms, manifest comparable $f\Delta q$ values even when their individual components (f and Δq) are different. This partial invariance of $f\Delta q$ to the specific choice of the reference coordinate enables force/extension curves of micron–long polymer chains to be extrapolated from the mechanochemical behaviour of nm–long oligomers.

Experimental techniques in polymer mechanochemistry

Verifying, refining and improving models of polymer mechanochemistry requires experimental tools to measure the rates and products of diverse reactions as a function of the force experienced by the reactive site. Such tools do not yet exist. The existing techniques either allow modest control over the force stretching a single polymer chain, or spectroscopic characterization of the products of mechanochemical reactions but not both. Only reactions accelerated in stretched chains are detectable and quantitation of reaction kinetics requires several assumptions of unknown validity.

For example, single molecule force spectroscopy (SMFS) is the most conceptually simple technique used in mechanochemistry, it allows a single macromolecule to be stretched and its length to be measured as a function of the applied force, analogous to stretching one end of a string that is tethered at the other end. Because only the applied force and chain

extension are measured, a change in the shape of the force/extension curve is the only indication of a reaction occurring in a stretched chain. Consequently, only reactions that either fracture the chain or increase its contour length by many times the magnitude of thermal fluctuations are detectable. Conversely, sonication of polymer solutions provides a means of transiently stretching multiple chains at a time, at the expense of eliminating any means of quantifying, much less controlling, the stretching force, stretching rate, and duration of stretching. While spectroscopic analysis of sonicated solutions allows determination of the reaction products and estimate of the rate at which they appear, these rates do not reflect the microscopic reaction probabilities (as they normally do in chemical kinetics). Instead, they represent a complex convolution of multiple microscopic probabilities, including that for a chain to become trapped in the elongational flow and for a stretched chain to react before the flow disappears. As a result, molecular interpretations of sonication experiments have been largely impossible to date (see chapter 2 for an attempt as resolving this). Reactions in melts and bulk solids under load are even less tractable. Consequently, these techniques yield a view of polymer mechanochemistry that is not simply qualitative, but exclusive of any but a very particular mechanochemical response.

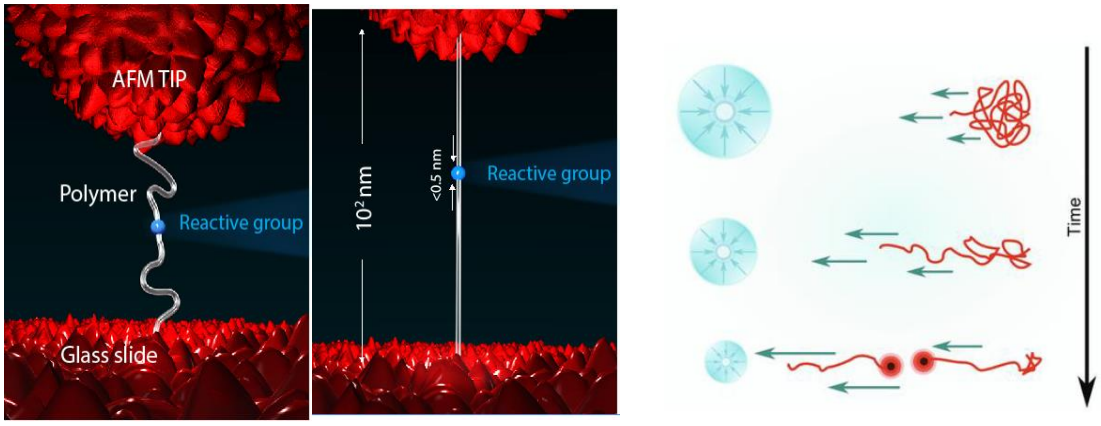

Figure 2 – **Sonication and SMFS are the two most common techniques in polymer mechanochemistry.** *Cartoon representations of a) a SMFS experiment. The reactant group (blue) embedded in the polymer backbone experienced force when the tip AFM tip is moved away from the glass slide anchoring the polymer and B) the stretching of a polymer chain in a sonicated solution when a bubble (left) collapses, dragging nearby macromolecules towards it at a rate that falls off sharply with distance.*

Using small molecules as models of mechanochemistry

The existing technical limitations of single molecule force spectroscopy and ultra–sonication elevate the role of model studies for gaining fundamental insights into covalent mechanochemical reactivity. Models of mechanochemistry distort a monomer as if it were part of a stretched polymer without using macromolecules, the magnitude of the strain is controlled by molecular design rather than macroscopic motion. The primary advantage of this approach is that non–polymeric reactants are amenable to much more detailed

characterization, both experimental and computational, than is currently possible for polymers. This strategy is not limited to a particular type of mechanochemical response, making it suitable for discovering reactions that are inhibited or unaffected in a stretched macromolecule, in addition to those that are accelerated. Both systematic mechanistic studies of mechanochemical reactivity and careful benchmarking of quantum–chemical methods of mechanochemistry become possible. The primary limitation of this approach is that the magnitude of molecular strain imposed through molecular design is likely smaller than that accessible by stretching a polymer chain. For example, a molecular architecture in which one part of a molecule (force probe) strains another part (substrate) enough to affect a C–C bond homolysis at a detectable rate, as is readily achievable by stretching a polymer, may not exist or be synthetically inaccessible because the bond making up the force probe would become similarly unstable.

Early students of polymer mechanochemistry considered the ability to reproduce some of the unique reactivity of stretched chains somewhat fantastical. The view probably reflected the gap between the attributes of known strained molecules and those needed to reproduce the strain of a monomer of a stretched macromolecule in a non–polymeric molecule. First, the majority of strained organic molecules manifest compressive strain, as evidenced, for example, by the contraction of bond angles in most known strained molecules, relative to their strain–free analogues, whereas polymer mechanochemistry reflects tensile molecular strain. Second, the reliance on small rings and steric repulsion also means that no molecular fragment is strained predominantly along a single molecular axis.

Systematic model studies of polymer mechanochemistry require molecular architectures that not just reproduce the molecular strain experienced by a monomer of a stretched macromolecule but allow this strain to be generated rapidly, varied systematically and estimated accurately. First, systematic variation of the imposed strain over a reasonably large range (e.g., equivalent to ~1 nN) is essential to understand the contribution of competing reaction mechanisms, particularly mechanisms not accessible in strain–free reactants, to the unique reactivity of stretched macromolecules. Second, to enable studies of reactions strongly accelerated by tensile load the design must allow the molecules to be switched rapidly from a strain–free to a strained geometry for which the reactive site may exist on only a millisecond time scale. An additional, key advantage of such a design is that the strain–free isomer serves as a reference of strain–free reactivity, which is particularly important for a method that requires distinct, if related, compounds to vary imposed strain. These requirements contrast with the often heroic synthetic efforts required to produce many known strained molecules, which rarely have strain–free analogues. Third, to enable a

comprehensive understanding of the diversity of chemical responses to tensile load, molecular architectures that are compatible with diverse reactive moieties and chemical reactions are required.

These requirements are sufficiently exacting that only one molecular architecture has been reported so far that satisfies them, based on macrocycles of stiff stilbene, in which the monomer whose mechanochemistry is studied is incorporated into a molecular moiety ('linker') connecting the C6/C6' atoms (Figure 3). *Z*→*E* isomerization of stiff stilbene increases this C6–C6' separation, thus stretching the monomer–containing linker. Analogous to how a steel rod connected at both ends with a tether that is shorter than the rod generates a restoring force in the tether, a molecular linker short enough to prevent *E* stiff stilbene from adopting its preferred planar geometry with the maximum separation of the C6, C6' atoms, experiences a tensile load in macrocycles of the *E* isomer. Varying the length of this linker yields a series of macrocycles, across which the force exerted on the monomer in the *E* isomers can be incremented by ~50 pN up to ~750 pN.

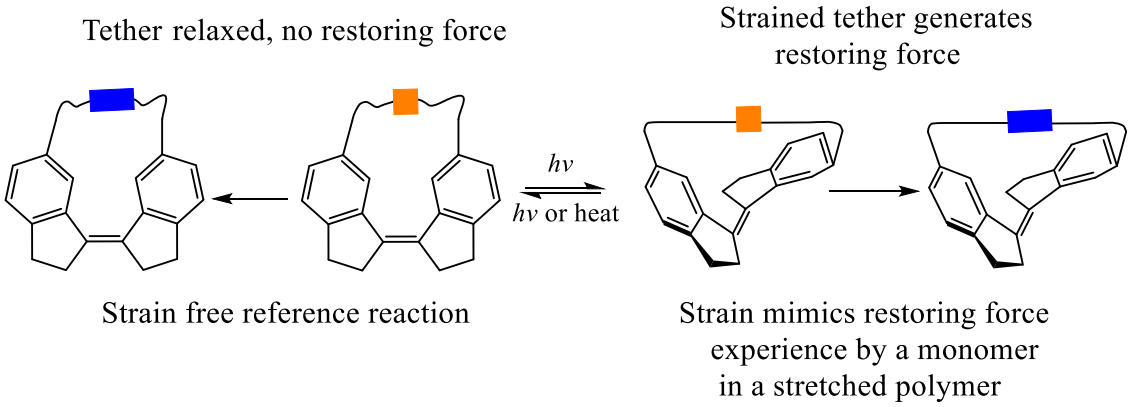

Figure 3 – ***Macrocycles containing stiff stilbene can apply a tensile force to small reactive sites.*** *Notice that the linker is depicted to be relaxed in Z stilbene but stretched in E, reflecting the shorter C6'…C6 distance in Z vs E stilbene.*

In addition to the large difference in molecular dimensions of the two isomers of stiff stilbene, its advantages for applications as a molecular force probe include the high strain–free activation free energy of thermal isomerization and its fast and efficient photoisomerisation, which allows strained molecules to be generated rapidly and in high enough concentrations for reaction monitoring. The alkyl rings of stiff stilbene prevent strain relief via rotation available to other stilbene and azo analogues, thereby maximizing the molecular strain achievable in a macrocycle. Photoisomerisation in stilbenes proceeds via two mechanisms: the simultaneous rotation of the double bond and the adjacent single bond of the 'hula–twist' mechanism means that only a single vinyl proton rotates out of the plane (Figure 4). The 'one–bond twist' mechanism requires rotation around the isomerizing C=C bond, with concomitant

out–of–plane displacement of one Ph ring, whose motion during isomerization traces the surface of a cone.[27,28] Which mechanism is favoured depends on the stilbene structure and the surrounding environment. For example, the hula–twist path is favoured by stilbenes in restricted environments[28] thanks to its low volume of activation, but is blocked by the fused five membered rings of stiff stilbene. In addition to photoisomerisation, *Z* stilbene is susceptible to photochemical ring closing to dihydrophenanthrene, whose spontaneous aerobic oxidation produces phenanthrene. This cyclization is impossible in stiff stilbene, making it better suited for applications in supramolecular chemistry[29].

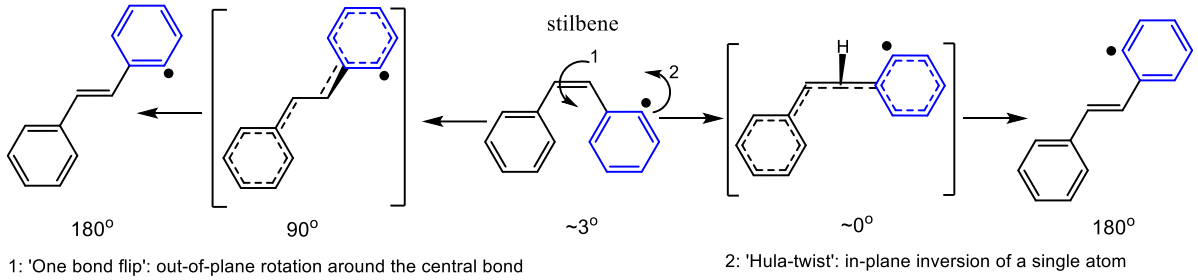

Figure 4 – ***The two mechanisms of thermal Z–E isomerisation in stilbene****. Path 2 is precluded by linking vinyl and aromatic C atoms, as in stiff stilbene, resulting in markedly different isomerisation properties.*

The relative kinetics of three reactions determines if a specific mechanochemical transformation is suitable for quantitative study by molecular force probes: the formation of the strained macrocycles containing strained but unreacted monomer (imposing force) and relaxation of this macrocycle either by the reaction of this monomer (mechanochemistry) or by isomerization of strained *E* stiff stilbene to its *Z* congener (unproductive path).[30] The simplest case is when the mechanochemical reaction is considerably slower than the *Z*→*E* photoisomerisation but considerably faster than the unproductive *E*→*Z* relaxation. Depending on the rate of the substrate reaction, the strained macrocycle containing the unreacted monomer may be isolable and fully characterisable spectroscopically. At the other extreme of relative rate constants, the unproductive relaxation by thermal *E*→*Z* isomerization is faster than the kinetics of the mechanochemical reaction, and the latter can be quantified accurately only if a steady state concentration of the strained *E* macrocycle is maintained high enough by continuous photoisomerisation of the *Z* macrocycle to allow the mechanochemical product to accumulate at a detectable rate. This strategy also requires that *E*/*Z* isomerizations not be accompanied by any side reactions.[30]

The quantum yield of *Z*→*E* photoisomerisation decreases and thermal *E*→*Z* relaxation is accelerated as the strain of the *E* macrocycle, and therefore the magnitude of the tensile force exerted by *E* stiff stilbene on the strap, increases.[31] Consequently, the kinetics of imposing a large force on the reactive site becomes increasingly unfavourable. The situation is not unique

to molecular force probes: the largest force accessible in SMF experiments is often limited by detachment of the macromolecule from the tip or the surface.

The synthesis of stiff stilbene and its macrocycles

Three strategies for efficient macrocyclization of *Z* stiff stilbenes all require McMurry coupling to form the stilbene alkene from two ketones. McMurry coupling proceeds via a low–valent titanium species generated insitu from $TiCl_4$ and Zn. The large thermodynamic driving force of the reaction is the formation of TiO_2 which has allowed many highly strained systems to be synthesised. This attribute of McMurry coupling makes it particularly valuable as it remains suitable for targets that are sterically crowded or strained.[24,32]

The methods differ in the stage that the mechanophore is cyclised with the stiff stilbene, which is captured by their names “plug–in”, “join–up” or “build–around”. Scheme 1 shows the general approach with selected examples. The first combines *Z* stiff stilbene diols with the reactive site. Its advantage is generality: once a diverse collection of *Z* stiff stilbene diols is synthesized, multiple sets of macrocycles containing different reactive sites become readily accessible. Its disadvantage is the need for careful optimization of macrocyclization conditions by sequential S_N2 displacement. This method has been applied to monomers that are not compatible with McMurry coupling, such as phosphate esters and siloxanes. In the “build–around” approach the formation of *Z* stiff stilbene also yields the macrocycle, benefiting from the known capacity of McMurry coupling to yield large strain–free macrocycles. Consequently, macrocycles of different sizes are accessible under similar conditions. The “join up” approach is only applicable to atoms that can be easily joined together once attached to a preformed stilbene structure, as such it has been used only for the preparation of disulphide macrocycles whose disulphide link forms upon reduction of two SH units (Scheme 1).[25]

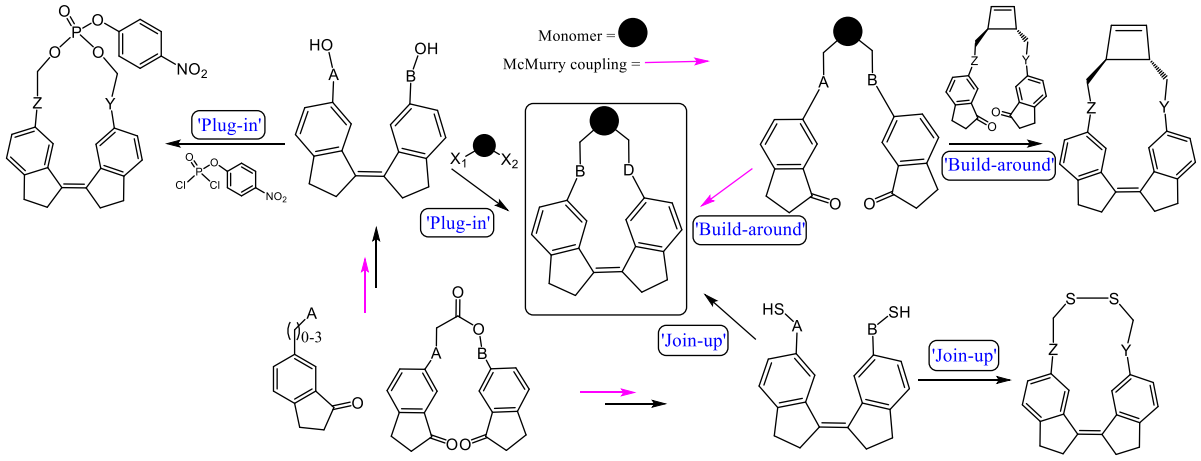

Scheme 1 – ***The three established methods for synthesising stilbene macrocycles with examples.*** *'Build-around' was used on cyclobutene containing macrocycle and 'plug-in' appropriate for synthesising a phosphate ester. Only a disulphide has been made via the 'join-up' method.*

Syntheses of strained *E* macrocycles exploits the efficient photoisomerisation of *Z* stiff stilbene under irradiation at ~400 nm. Because the absorption spectrum of *Z* stiff stilbenes is bathochromically shifted relative to the *E* isomer, photostationary states enriched with *E* macrocycles are readily accessible.[20] In all but the shortest macrocycles (in which A and B in Scheme 1 contribute only 3 bonds each to the linker length), *E* isomers were sufficiently stable to be isolated and studied independently of the *Z* analogues.[23] However, since the determination of force–dependent kinetics requires the difference in the apparent activation free energy of the two isomers, $\Delta\Delta G^{\ddagger}$, rather than the absolute values, kinetic measurements on photostationary mixtures are preferred because such competition experiments usually yield more accurate estimates of $\Delta\Delta G^{\ddagger}$ than those obtained from the difference of activation energies measurement individually.

Insights not possible from studies of polymer mechanochemistry: Experimental demonstration of force being a length–invariant measure of kinetically significant strain

The concept of force (or more precisely, restoring molecular force) is central for quantitative discussions of polymer mechanochemistry because it is a size–independent quantifier of kinetically–relevant molecular strain. In other words, knowing the restoring force of a monomer in a stretched macromolecule is thought to enable accurate predictions of the monomer's kinetic and thermodynamic stabilities regardless of the length of the chain or the physical mechanism that maintains the chain in its unfavourable stretched geometry. Yet, no fundamental law of physics requires force to underlay such a quantitative relationship between molecular strain and changes in chemical reactivity. This fact necessitates experimental demonstration that force accurately quantifies the portion of molecular strain

that affects a molecule's stability at any scale from <1 nm (monomer) to >10 μm (polymer chain) and potentially longer.

This demonstration was provided by studies of force–accelerated isomerization of *cis*–1,2–disubstituted dibromocyclopropanes (DBC) to allyl bromides using molecular force probes.[21] The rates of this isomerization were measured in a series of increasingly large stiff–stilbene macrocycles across which the restoring force of stretched DBC in the *E* isomer was calculated to increase from 0 to 400 pN. The force–dependent activation free energy, $\Delta G^{\neq}(f)$, derived from these measurements matched closely $\Delta G^{\neq}(f)$ calculated quantum chemically by applying a tensile force to the C terminus of the DBC moiety. [33]

This $\Delta G^{\neq}(f)$ was then used to predict the ensemble–average single–chain micromechanics of a polymer of DBC up to 1.5 nN, which was previously measured by SMFS.[34] This prediction relied on 2 key assumptions. First, each monomer was assumed to react independently of any other monomer in the chain (i.e., mechanochemical isomerization was non–cooperative). Second, at the range of applied forces where mechanochemical isomerization occurs at a detectable rate (>1 nN), the force experienced by each monomer of a chain approximately equals the force applied at the ends of a 1 nm–long chain, which is the only force estimated in SMFS. Both assumptions were validated by calculating $\Delta G^{\neq}(f)$ of conformational ensembles of homologous series of increasingly long oligomers of DBC and extrapolating the results to the size–independent limit using previously derived theoretical[35] and computational[36] approaches. Interestingly, these calculations also suggested that at applied force <1 nN a polymer chain is a poor transmitter of applied force, i.e., the fraction of the applied force experienced by each monomer (mechanochemical coupling coefficient[37]) is <1. This finding means that molecular interpretation of mechanochemical features of force/extension curves that occur at <1 nN (e.g., isomerization of spiropyranes[38]) is even more challenging than that of reactions occurring at higher forces because the force experienced by the reacting monomers cannot be approximated reliably from knowledge of the applied force.

The agreement between the measured and predicted force/extension curves for the polymer of DBC (Figure 5) confirms that force, when properly defined, accurately captures the effect of stretching a reactive site on the kinetic and thermodynamic stabilities of this site, regardless of what physical process causes the stretching (e.g., compressed *E* stiff stilbene in macrocycles, a compressed virtual spring in DFT calculations or the directional motion of a macroscopic object in SMFS), or the length–scale at which the force is applied (from <1 nm in direct calculations of $\Delta G^{\neq}(f)$ to 2 nm in macrocycles to 1 μm in SMFS). Because molecular restoring force can only be defined with respect to an internal coordinate of the distorted molecule, the predictive capacity of the force formalism depends on proper selection of this

coordinate. When this criterion is satisfied, force enables quantitative discussions of strain–induced chemistry over at least a 10^4 fold variation in length scales and 10^{11} – fold range of reaction half–life.

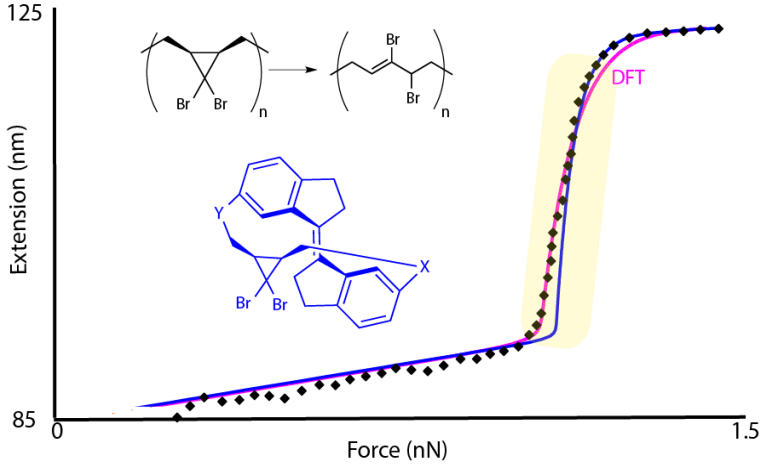

Figure 5 – ***Restoring force dictates monomer reactivity regardless of how it was generated.*** *The measured force extension curve of a dibromocyclopropane polymer (black dots), the predicted curve derived from extrapolation of the force/$\Delta G^{\neq}$ relation measured in stiff stilbene macrocycles(blue) and the predicted curved derived from $\Delta G^{\neq}(f)$ calculated by DFT (magenta). Yellow shading indicates the estimated difference between ensemble and single–chain behaviour. Adapted from [21] with permission.*

Without diminishing the validity of the preceding paragraph, the excellent agreement in Figure 5 may be somewhat fortuitous. At the time of this work, the magnitude of the variation of the applied force at which individual monomers react ("transition force"), which reflects the stochastic nature of SMFS, and its dependence on the length of the stretched segment were unknown and each measured force/extension curved was assumed to approximate the ensemble behaviour, which was predicted from measured and computed $\Delta G^{\neq}(f)$. Later studies, in which the applied force corresponding to the mechanochemical isomerization of each individual monomer was measured for a range of polymer chains,[39] demonstrated unexpectedly large variation in the "transition force" for otherwise identical monomers. Extrapolating from these later findings, the measured force/extension curves in Figure 5 may deviate by up to 150 pN (yellow shaded region) from the ensemble–average curve of the same chain.

Powder mechanochemistry

Powder mechanochemistry refers to processes designed to change the chemical compositions of powders (polymers, small organic, metal–organic/inorganic compounds and extended solids) by ball milling or grinding. It has developed over the last few decades into such an active area of chemical research that the total number of mechanochemical ball milling/grinding reactions, even when limited to small organic covalent transformations, is too large to compile exhaustively. Contemporary powder mechanochemistry is far less

amenable to conceptual systematisation than polymer mechanochemistry because of both the sheer number and variety of known powder mechanochemical reactions, which far exceeds that of polymer mechanochemistry.[40-44] Most major reaction types have been successfully conducted mechanochemically, with the notable exception of S_N1 reactions whose reliance on solvent stabilisation has apparently hindered attempts thus far.[45] The reason for the abundance of known reactions in powder mechanochemistry compared to polymer mechanochemistry, is its practical simplicity, as well as the financial and environmental incentives for conducting reactions without solvents[46]. While stretching polymers requires advanced equipment for both set–up and analysis, grinding or milling powders does not[47]. The use of liquid, ionic and polymer additives also vastly expands the number of accessible products from that available via neat grinding.[42,48,49]

However, the ease of experimental set–up does not translate into an easily tractable process. Unlike in polymer mechanochemistry in which the conceptually simple SMFS experiment is in close analogy to what is possible quantum computationally, no such computational equivalent exists for powders. Instead we are left to postulate the mechanisms by analogy and reaction outcome. Plausible suggestions include that; the ball impact either distorts reactants themselves into a more reactive strained geometry,[5] generates local hot spots,[50] or produces an insitu liquid phase containing high concentrations of each reactant unattainable in solution.[51] The extent to which each influences reaction outcomes probably varies depending on the exact set–up – especially the nature of the reactants.

The role of direct reactant distortion appears to be supported by the behaviour of polymers which tend to homolyze when milled as they do when they are stretched in SMFS. For small molecules, undergoing bimolecular reactions the role of geometric distortions is less intuitive. The rapid rate of relaxation from distorted to relaxed geometry combined with the requirement for the molecules to be in close proximity in an exacting orientation to undergo bimolecular reactions appears to limit the opportunity for any ball–induced distortion to influence the reaction to a few scenarios, for example when two reactants were already in close contact upon ball impact. The role of local hotspots appears unlikely based on the type of temperature changes associated with inorganic mechanochemical alloying (which is well accepted to proceed by local hot spots[52]) not matching that observed during small molecule ball milling reactions.[53] The role of insitu eutectic mixtures is supported by the study of 19 covalent reactions which all formed liquid phases as a prerequisite to reaction, (as monitored by insitu powder X ray diffraction), however the sample size is relatively small and some exceptions to this rule have been reported. [51]

Intuitively powder mechanochemistry is perceived as quite distinct from solution phase chemistry but asides from the few, well publicised 'impossible molecules'[40] (Figure 6) most small molecule transformation are conserved between solution and ball milling (although potentially via a distinct mechanism). However the behaviour of solid polymers under force is distinct from those in solution as evidenced by the difference in product produced when a polymer is milled vs sonicated.[54] This is attributable to solids featuring a high concentration of chains that diffuse slowly. Reactions in both scenarios are dominated by chain fracture, usually to give macroradicals. In solution, these macroradicals convert into stable chains by reactions with the solvent or small–molecule radicals derived from solvent sonolysis. In milled polymers, the macroradicals are considerably more persistent, thanks to inhibited recombination and the absence of a solvent. Conversely, the high concentration of chains favours macroradical–chain reactions that require minimal diffusion, including H–atom abstraction from adjacent chains and polymer grafting through addition to sp^2– hybridized C atoms of unsaturated polymers

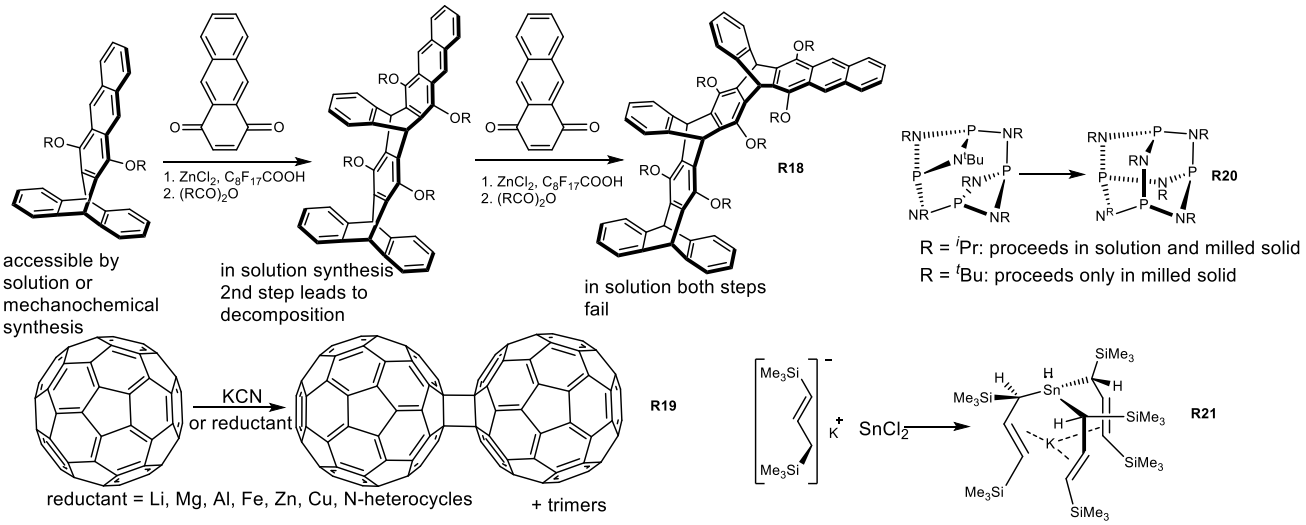

Figure 6 – ***Powder mechanochemistry enables isolation of previously inaccessible structures****. Examples of reactions that have been successfully conducted only in the solid phase using ball milling.*

2. Experimental quantitation of molecular conditions responsible for flow–induced polymer mechanochemistry.

Robert T. O'Neill, Roman Boulatov

Department of Chemistry, University of Liverpool, Liverpool, L69 7ZD.

Abstract

Fragmentation of macromolecular solutes in rapid flows is of considerable fundamental and practical significance. The sequence of molecular events preceding chain fracture is poorly understood, because such events cannot be visualized directly but must be inferred from changes in the bulk composition of the flowing solution. Here we describe how analysis of same–chain competition between fracture of a polystyrene chain and isomerization of a chromophore embedded in its backbone yields detailed characterization of the distribution of molecular conditions experienced by mechanochemically reacting chains in sonicated solutions. We find that the overstretched chain segment grows and drifts along the backbone on the same timescale as, and in competition with, the mechanochemical reactions. As a result, only 20–30% of the backbone of the average fragmenting chain is strained at any time, with both the maximum force and the maximum reaction probability located away from the chain centre. Our method is applicable to any flow fast enough to effect polymer mechanochemistry.

Background

In a stationary solution polymer chains exist as coils whose end–to–end distances are many times shorter than their contour lengths.[55] When a polymer solution flows rapidly near a surface[56,57] or is sonicated,[2,58,59] the average end–to–end distances of some chains increase. This elongation may occur by chain uncoiling or by overstretching, or both, depending on the parameters of the flow field and the residence time of the chain in it. The flow destabilizes chain conformers with short end–to–end distances, producing a partially uncoiled chain in which a contiguous segment of the backbone adopts the longest strain–free conformation.[60,61] A sufficiently fast flow can stretch this uncoiled segment beyond its strain–free length primarily by distortions of angles between backbone bonds. This overstretching is responsible for flow–induced mechanochemistry, such as chain fracture.[2,62] In many practical polymer solution flows, chain fracture is a major, usually deleterious process.[63,64]

In the laboratory, optimizing flow field parameters to suppress chain fracture enabled detailed studies of uncoiling, albeit to less than full extension, without the complications from chain overstretching.[61] Uncoiling is comparatively slow and yields large changes in chain

shape, making it amenable to direct visualization under optimal conditions or to detailed simulation, if not yet at the atomistic level. Mechanochemistry–inducing overstretching likely occurs faster, changes chain dimensions by less and requires atomistic quantum–chemical treatment that is difficult to approximate empirically. As a result, uncoiling dynamics, particularly in steady flows, is much better understood[60] than the molecular events and chain geometries responsible for flow–induced mechanochemistry.[65] At present, chain fracture or another mechanochemical reaction is the only indication that a dissolved chain has overstretched.

Macroscopic kinetics of flow–induced fracture of simple homopolymers, such as polystyrenes, PEGs, and acrylates, and its dependence on such experimental control parameters as chain length and concentration, flow rate and geometry, solution viscosity, and Reynolds number have been studied extensively in diverse flows.[63,66] These dependences, however, are difficult to interpret molecularly.[67] Experimentally, the measurable changes in the mass distribution of a polymer experiencing flow–induced chain fracture may be dominated by unwanted and uncontrollable aspects of practically achievable flow fields, such as turbulence near walls of cross–slot flow cells, shock waves in sonicated solutions or flow instabilities that limit the residence time of a chain at a stagnation point.[68-70] Conceptually, they reflect a complex convolution of the probabilities of dissolved chains to become (partially) overstretched and of these chains to fracture before the local fluid strain rate decreases below a threshold needed to maintain the required strained molecular geometry. Existing experimental designs do not allow the constituent probabilities, and the attendant molecular conditions, to be estimated. As a result, little consensus exists on even the key molecular events that precede chain fracture, including the fraction of the chain that uncoils, how fast the chain is stretched and how the molecular strain, the corresponding forces, and the mechanochemical reactivity are distributed along the backbone as the chain is stretched.

Unlike the macroscopic kinetics of chain fracture, changes in the solution composition resulting from competition between two or more mechanochemical reactions within the same overstretched backbone reflect only molecular reaction probabilities. The latter can be calculated as a function of the force on the reacting moieties by established quantum–chemical methods.[71-73] Consequently, the force, the distributions of molecular geometries of the reacting chains and the underlying molecular parameters responsible for flow–induced mechanochemistry become directly quantifiable from experiment. Implementation of this approach has been precluded by the difficulty of designing polymers that enable unambiguous differentiation between products of intra– and intermolecular competition. For example, sonicating solutions of polymers of dihalocyclopropanes[74,75] and macrocyclic cyclobutanes[76,77] both reduces the average size of the chains, signifying chain fracture, and

isomerizes individual monomers. However, in neither case could the fraction of isomerized monomers in the fractured and intact chains be quantified, making it impossible to establish how often, if ever, the two reactions occur in the same chain. The high dispersity of such "multimechanophore" polymers[78] further limits their utility for elucidating the molecular processes and conditions responsible for flow–induced mechanochemistry. As such the idea of mid-chain selectivity (i.e., chains in elongational flows react primarily or exclusively at chain centre) has not been tested systematically.

Here we describe detailed measurements and analysis of competition between fracture of a polystyrene chain and isomerization of a chromophore embedded in its backbone in a dilute sonicated solution. Our data suggests that the overstretched segment grows, drifts along the backbone and reacts all on comparable timescales and that the observed mechanochemistry reflects complex averaging of distinct microscopic reaction probabilities of chains partitioning among very different local environments. We characterized these conditions as the chain–size–dependent distributions of the lengths of the overstretched segments, their positions along the backbones, the time the chains remain overstretched, and the maximum forces they experience during this time. Contrary to a common belief, only ~20–30% of the average fragmenting chain is sufficiently strained to manifest observable mechanochemistry, with the maximum force located away from the chain centre. Because our approach exploits kinetic destabilization of any overstretched backbone regardless of the physical mechanism responsible for overstretching, it is applicable to any flows that cause mechanochemistry. Our choice of sonication for the first demonstration of our approach is motivated both by the particularly limited understanding of molecular conditions in such solutions and by the importance of sonication in contemporary experimental polymer mechanochemistry.

Results

Polymer design.

This study used 9 polystyrenes (PS) with the average strain–free contour lengths, L, from 60 to 530 nm, containing a single *Z*–stiff stilbene (*Z*–SS) moiety per chain either at its centre (**1c**–**4c**) or up to (0.30±0.03)L away from the centre (**1o**–**5o**, Figure 7a). The choice of stiff stilbene as our photochromic mechanophore derives from it meeting several exacting requirements that maximize the insight possible from this study. First its two isomers have prominent differences in their extinction coefficients with the most distinctive regions of the UvVis spectra shifted far away from that of polystyrene, making it detectable even when outnumbered by styrene monomers by 3 orders of magnitude. Second both *Z* and *E* are highly thermally stable making the ratio of *Z* and *E* isomer present in a dark sonicated solution dependent only on the force the molecules experience. Third an analogue of stilbene containing two dibromo–terminated arms positioned to exert a tensile force on the stilbene

alkene when each arm is stretched (**c2-7**) can be synthesized in high *Z* purity. The isomer selective synthesis is achieved via an intramolecular McMurry coupling of two indanones in **c2-4** with a molecular strap short enough to exclude access to the transition state that yields the *E* isomer.

We synthesized the 9 polymers by reacting dibromo–terminated *Z*–SS (**c2-7**) with either excess CO_2H–terminated low–dispersity PS to yield **1c**–**4c** or with an equimolar mixture of two polystyrenes of different sizes to yield, after size–exclusion chromatography (SEC), polymers with stiff stilbene located off centre (**1o**–**5o**). Analysis of the reaction products by SEC confirmed the expected distributions of chain masses. Deconvolution of the absorption spectrum of **1c**–**5o** into the contributions of PS, *Z*–SS and *E*–SS chromophores using independently measured reference spectra (SI, Figure 20) confirmed a single SS moiety per chain, 83–90% of which being the *Z* isomer (Table S1).

Synthesizing **1c**–**5o** by coupling pairs of macromolecules instead of by conventional polymerization from a bifunctional initiator[79,80] enabled both precise control over the location of stiff stilbene along the backbone and accurate determination of the distribution of these locations in the resulting polymers (Figure 7b and SI Figure 19). We calculated the latter distributions by assuming that **1c**–**5o** were formed by statistical combinations of pairs of the precursor chains, whose molar mass distributions (MMD) we measured independently. The good agreement between the measured and simulated MMDs (example in Figure 7c and Figure 21) validates the calculated distributions of stiff stilbene locations. In each polymer, the location of SS varies little from chain to chain: between 72 and 85% of chains in each sample contain SS within 0.05*L* of the sample–average value, where *L* is the contour length. For comparison, in a conventionally prepared polymer, the probability of finding the bifunctional initiator within any segment of 0.1*L* is <20%.[79]

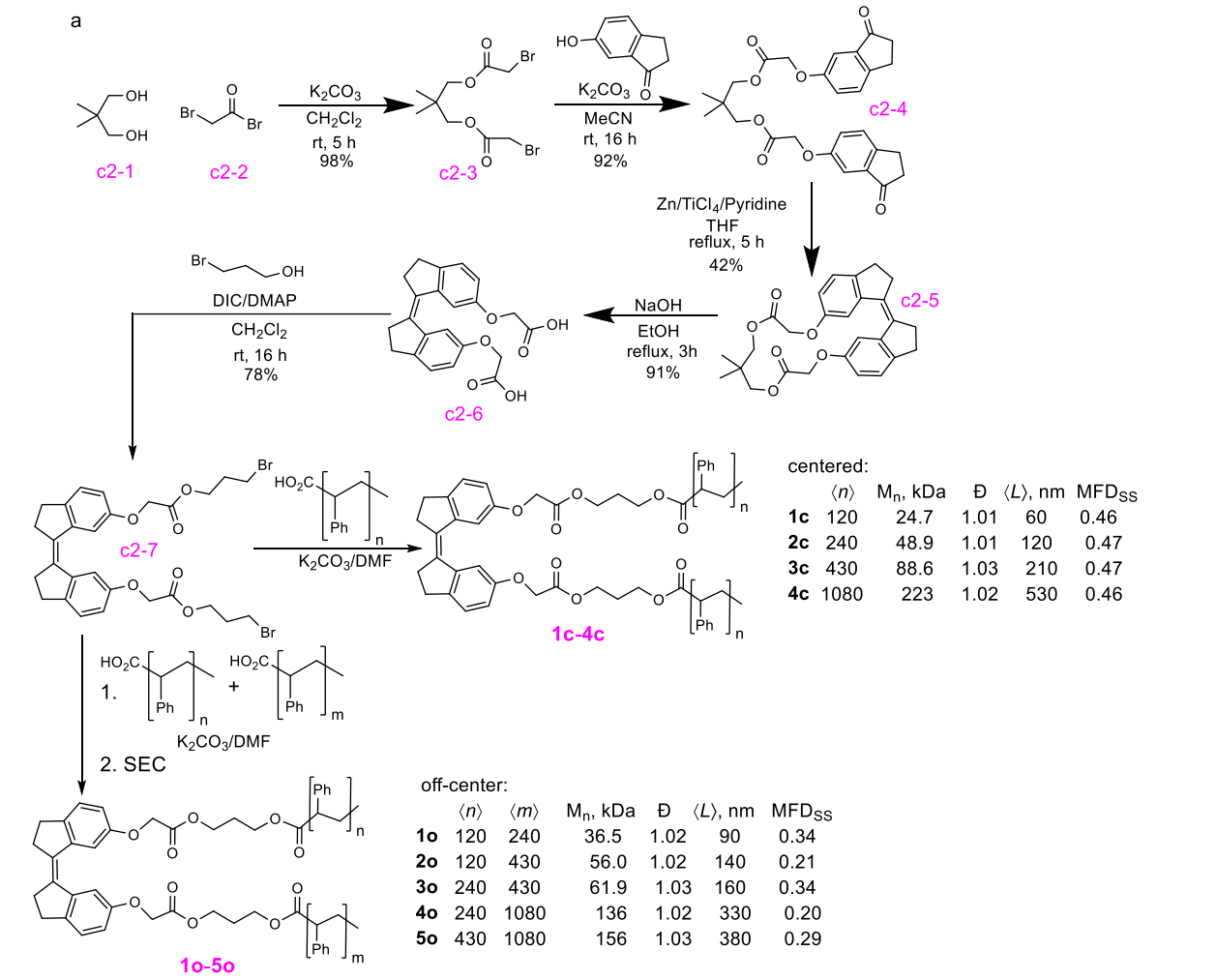

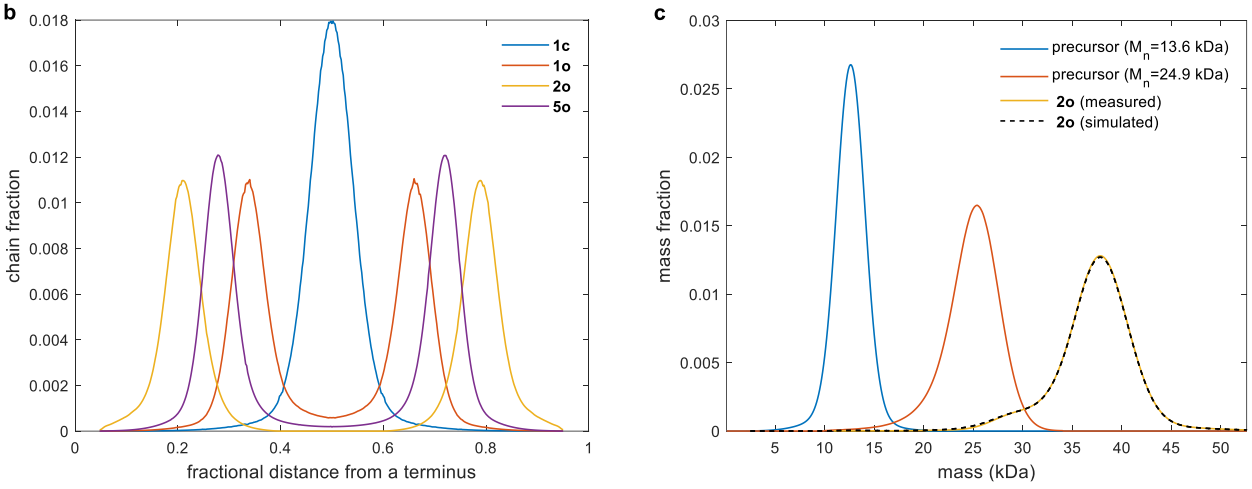

*Figure 7 — **The polymers used in the study**. (a) synthesis, chemical structures and summary of key sample–average parameters: L is the strain–free contour length; ⟨⟩ signifies number averaging and MFD_{SS} is mean fractional displacement of SS from the closest chain terminus; the deviation of MFD_{SS} of **1c–4c** from 0.5 reflects finite widths of the distributions of SS locations.* See SI Figure 18 for *further details. (b) The fraction of chains of **1c**, **1o**, **2o** and **5o** that contain stiff stilbene at the specified fractional distance from a terminus. Calculated distributions in **2c–4c**, **3o** and **4o** are very similar to those of **1c**, **1o** and **2o**, respectively and are shown in Figure 19 in SI together with the corresponding cumulative distributions. (c) measured and calculated MMDs of **2o** and the measured MMDs of the corresponding precursors. See SI Figure 19 for all other polymers. The discrete distributions in (b–c) have the bin size of 0.01L (b) and 100 Da (c).*

Sonication experiments.

We sonicated **1c**–**5o** as THF solutions of 1 mg/mL concentration under standard protocol[76] (see also the SI for experimental details), and quantified their compositions by SEC. We determined the fraction of the *Z* and *E* isomers of stiff stilbene for each mass fraction by deconvoluting its absorption spectrum at 300 – 400 nm into those of the two isomers (SI Figure 20). The total amount of SS in sonicated solutions remained constant, confirming that sonication did not destroy SS.

Sonication changed the unimodal MMD of the intact polymer (darkest blue line in Figure 8) to a bimodal distribution with the maximum of the newly formed component at ~$M_p/2$ (M_p is the mass of the most abundant chain in the intact sample; M_p = 64.4 kDa for **3o** illustrated in Figure 8a), indicative of chain fracture. Simultaneously, the high and largely mass–independent fraction of *Z*–SS, χ_Z, of the intact sample gradually decreased and became strongly mass–dependent (Figure 8 shows results for **3o**, all other polymer data shown in methods section Figure 21). The monotonic reduction of χ_Z of chains with mass >0.8M_p reveals isomerization of *Z*–SS in intact chains, i.e., without chain fracture; whereas the presence of *Z*–SS in the products of chain fracture ($\chi_Z > 0$ of chains with mass below 0.7M_p) means that some *Z*–SS survive chain fracture without isomerizing. Chains that undergo fracture–coupled *Z*–SS isomerizations are responsible for χ_Z values at (0.35–0.7)M_p being lower than χ_Z at >0.8M_p for any sonication time. A drop in χ_Z at <0.3M_p (and the shoulder at the same masses in the MMDs) result from the slow fracture of chains of (0.35–0.7)M_p, which are themselves products of fracture of intact chains.

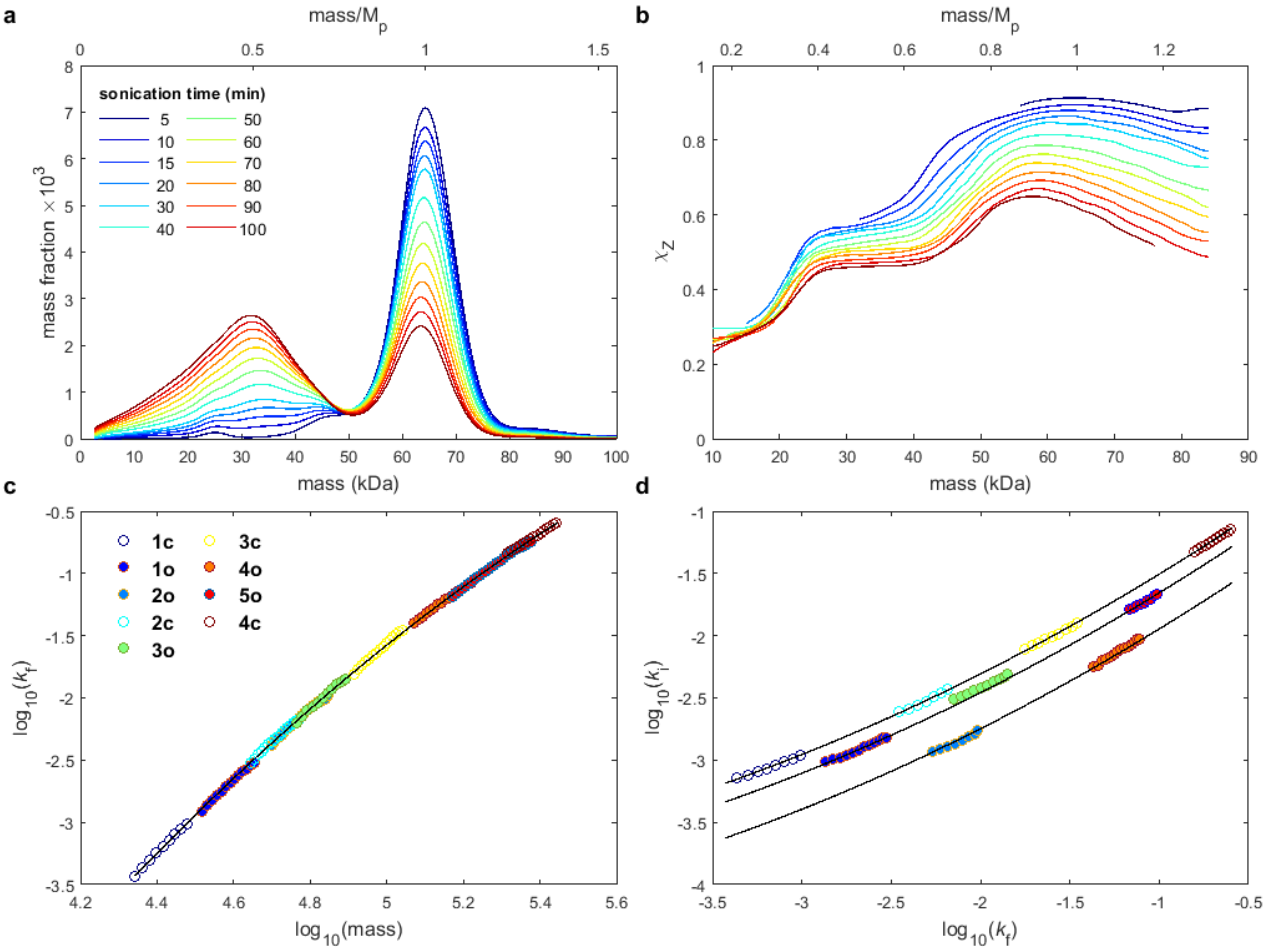

Figure 8 – ***Summary of sonication experiments****. (a) MMDs and (b) the fraction of Z–SS containing chains among all SS–containing chains of the same mass, χ_Z, as a function of the chain mass, of a sonicated solution of* ***3o****; log–log plots of (c) the measured unimolecular rate constants for fragmentation of* ***1c–5o****, k_f, as a function of the chain mass, and (d) unimolecular rate constants for isomerization of intact chains, k_i, as a function of the corresponding k_f. Only a fraction of the measured rate constants is plotted for clarity. The solid lines in (c–d) are quadratic least–squares fits of (c) log(k_f) vs. log(mass) and (d) log(k_i) vs. log(k_f) for* ***1c–4c*** *only (upper curve); lower curves in (d) are vertically shifted upper curve to best match the measured values for* ***1o****,* ***3o*** *and* ***5o*** *(middle curve), or* ***2o*** *and* ***4o*** *(lower curve). The uncertainty ranges of all rate constants are tabulated in the supplementary data file, suppdata.mat. For each sample, χ_Z values are reliably quantifiable over a shorter range of chain masses than the mass fractions so that the data in (b) covers a shorter range of chain masses than in (a) and the data in (d) covers a shorter range of k_f than in (c). See Figure 21 in SI for MMDs, χ_Z of* ***1c–5o****.*

The depletion of chains with masses >0.8M_p manifested unimolecular kinetics (example shown in SI Figure 23). The corresponding bulk rate constants, k_f, increased as a power of the chain mass (Figure 8c) with k_f of smaller chains being more sensitive to mass, m, than larger chains, e.g., $k_f \propto m^{3.2}$ for 22 kDa vs. $k_f \propto m^{2.0}$ for 280 kDa. The scaling is independent of the location of SS along the backbone and identical to chains without SS. The kinetics of $Z \rightarrow E$ isomerization in intact chains was also unimolecular and the corresponding rate constants, k_i, scale as a power of k_f (Figure 8d). The k_i/k_f ratio estimates mechanochemical selectivity,[5] i.e., the capacity to achieve desired (usually site–selective) chemistry without (usually deleterious) non–selective chain fracture. This selectivity decreases both with the chain size and the fractional displacement of SS from the chain centre. For example, 1.7 chains of **1c** of 22 kDa

isomerize without fragmentation for each fractured chain, but only 0.28 chains of **4c** (280 kDa) do. Displacing SS from the chain centre by 0.3*L* reduces this number 5–fold in a 53 kDa chain (**2o**) and 7–fold in a 160 kDa chain (**4o**). These trends cannot be explained by simple changes in the number of scissile backbone bonds per SS, suggesting a complex dependence of local conditions on chain mass. As expected, sonication of polymers containing *Z*–SS at a chain terminus yielded no detectable amount of *E*–SS either in intact or fractured chains.

Force–dependent activation free energies from DFT calculations.

To enable molecular interpretation of the experimental data, we used a previously reported and experimentally validated method[23,33,77] to calculate the free energies of activation, $\Delta G^{\neq}$, of two reactions – homolysis of the central C–C bond in $H(CH_2CHPh)_4CH_3$ (a polystyrene model) and isomerization of *Z*–(6,6–bismethoxy stiff stilbene) – as a function of stretching force applied across the terminal $_{Me}C\cdots C_{Me}$ distances (Figure 9). As previously demonstrated[54] at practically relevant forces the $RH_2C–CH(Ph)R$ bond is most dissociatively labile among the backbone bond types present in our polymers (Figure 7 and methods section Figure 22). $\Delta G^{\neq}(f)$ for C–C bond homolysis starts at 0.5 nN because the transition state does not exist at lower force, which is common for bond homolysis, and $\Delta G^{\neq}(f)$ for isomerization terminates at 5.8 nN when homolysis of the $_{Ar}C–C(sp^2)$ bond of the cyclopentane ring of SS becomes faster than C=C bond isomerization. This homolysis does not fracture the chain but would probably irreversibly bleach the SS chromophore.[30] The absence of such bleaching in our experiments suggests that few SS moieties experience force >5.8 nN long enough for this reaction to be important.

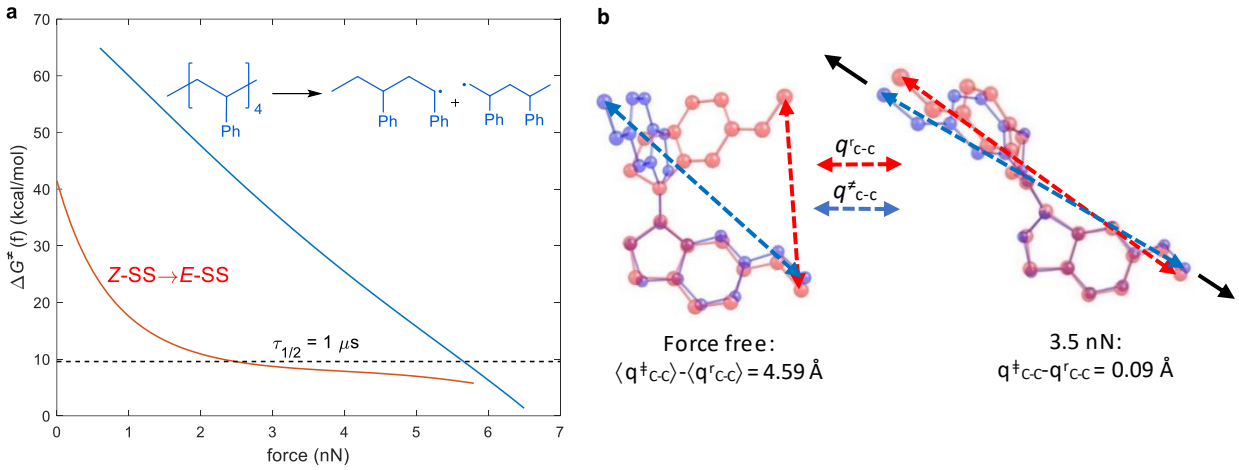

*Figure 9 – **Summary of the DFT calculations**. (a) the activation free energies of fragmentation and isomerization as a function of tensile force, $\Delta G^{\ddagger}$. The dashed line indicates $\Delta G^{\ddagger}$ corresponding to $\tau_{½}$ = 1 μs, which is the approximate timescale of cavitation bubble collapse in a liquid irradiated with 20 kHz ultrasound.[1,2] $\Delta G^{\ddagger}$ for fracture of a chain with n bonds all under the same force is reduced, relative to that of the single bond, by RTln(n). (b) overlays of the geometries of Z–(6,6–bismethoxy stiff stilbene) (red) and the isomerization TS (blue) without force and coupled to 3.5 nN: note the much larger difference of the $_{Me}C\cdots C_{Me}$ distance between the Z isomer and its TS at 0 nN compared to 3.5 nN (⟨⟩ signify Boltzmann–averaging over 3 conformers comprising each strain–free state; at 3.5 nN each state contains a single conformer). This difference is usually the primary determinant of the $\Delta G^{\ddagger}$ vs. f slope.[5] Tensile force distorts Z stiff stilbenes primarily by bending each indanone moiety, accompanied by only modest increase in the $_{Ar}C–C=C–C_{Ar}$ torsion of the isomerizing C=C bond to 39° (from 11° at 0 nN). The black arrows represent applied force vectors. All calculations were at uBMK/6–31+G(d) in vacuum.*

The origin of the nearly force–independent $\Delta G^{\ddagger}$ for *Z*–SS→*E*–SS isomerization at >2 nN is the greater compliance of the *Z* isomer compared to the TS along the pulling axis. As the force increases, the *Z* isomer distorts more than the TS, making their geometries increasingly similar (Figure 9b). This reduces how much the constrained distance elongates during the formation of the TS, thus reducing differential stabilization of the TS by tensile force. The monotonically decreasing with force difference between the isomerization and fragmentation rates favors kinetic competition between the two reactions, making *Z* stiff stilbene a particularly suitable probe of molecular environments responsible for mechanochemical chain fracture.

Molecular models of flow–induced mechanochemistry.

Below we first demonstrate that the two common molecular models of flow–induced mechanochemistry cannot be parameterized to reproduce the observed evolution of MMDs and χ_Z. We then show that relaxing the key assumption underlying all such models, that the chain geometry is static on the timescale of mechanochemical reactions, allows all measured data to be reproduced accurately. All models below assume that (a) each model parameter is independent of the presence or the location of SS and either changes with chain size monotonically or is chain–size–independent; and (b) observed mechanochemistry may reflect averaging over diverse molecular conditions, each requiring a separate combination of model parameters. We illustrate the performance of each model qualitatively, by comparing MMD

and χ_Z at a single sonication time (40 min) for a single sample (**3c**) with the respective model predictions (Figure 10a–b), and quantitatively using proxies of the dispersity of the mass distribution of the products of chain fracture and the extent of fracture–coupled isomerization of *Z*–SS, averaged over all sonication times across the full set of **1c**–**5o** samples (Figure 10c–d).

The reported molecular models.

The simplest and most common model assumes that flow–induced mechanochemistry occurs only in fully uncoiled chains,[74,81] whose backbone bonds experience force that decreases quadratically with the fractional distance from the chain centre, where the force is highest (f_{max}), to 0 at the termini. We tested two implementations of this "overstretched–chain" model: in one, the force on each monomer changes instantaneously from 0 to a time–independent value defined by the parabolic force profile with f_{max}; in the other the force on each monomer increases with time at a constant rate, υ, whose value decreases quadratically away from chain centre. In both implementations, we assumed that all forces disappear instantaneously after chain fracture (which greatly simplifies the problem and is well grounded in empirical observations of subsequent rather than simultaneous $M_p/2$ and $M_p/4$ chain production) and calculated the probabilities of each monomer to dissociate or isomerize as a function of the time the chain is overstretched ($t_{stretch}$) for chains with between 100 and 3000 monomers using $\Delta G^{\neq}(f)$ in Figure 9a. The unique distributions of molecular reaction probabilities thus produced characterize stoichiometries of mechanochemical chain fracture and isomerization (e.g., SI Eqs. 4–5) under diverse combinations of model parameters ($t_{stretch}$ and f_{max} or υ_{max}). We converted each pair of fragmentation and isomerization distributions to MMDs and χ_Z by adapting a previously reported procedure[54] (see the SI for details). We repeated these steps iteratively to find functional dependences of $t_{stretch}$, f_{max} and υ_{max} on chain size that most closely reproduced experimental MMDs and χ_Z.

Both implementations of the overstretched–chain model performed poorly, considerably underestimating the dispersity of the fragmentation products (Figure 10a,c and SI Figure 26 & Figure 27), over the whole range of $t_{stretch}$ and f_{max} or υ_{max} tested. Larger f_{max} or υ_{max}, and shorter $t_{stretch}$ improved the agreement between simulated and measured χ_Z, especially for **1c**–**4c**, thanks to the steeply decreasing with force difference between the activation barriers of isomerization and chain fracture. Consequently, aphysically short $t_{stretch}$ of ~1 ns (Figure 25) yielded χ_Z closest to the experiment.

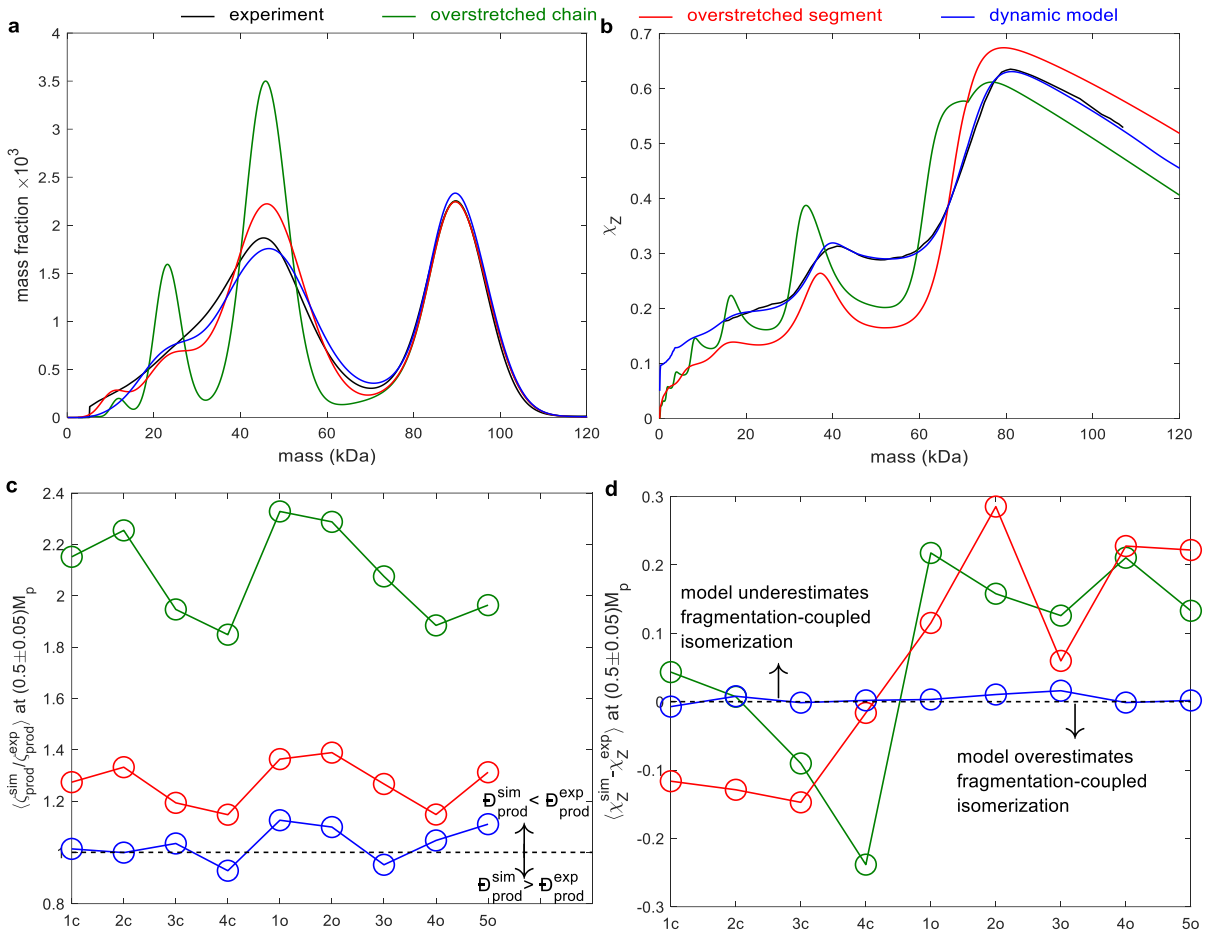

Figure 10 – **Illustrative comparisons of experiments with predictions of the molecular models.** (a–b) measured and calculated MMDs (a) and χ_z (b) of **3c** , each models predictions are for the same remaining mass fraction of the reactant chains, ζ_r. The experimental values are at 40 min of sonication. (c) the ratio of the simulated mass fraction of chains with masses of $0.45M_p$–$0.55M_p$, to the measured one, $\frac{\zeta_{prod}^{sim}}{\zeta_{prod}^{exp}}$, at the same ζ_r, averaged over all experimentally characterized values of ζ_r for **1c–5o** (M_p is the mass of the most abundant reactant chain in the original sample). Ratios >1 correspond to the simulation yielding too uniform fragmentation products (underestimating $Đ_{prod}$). (d) difference between simulated and measured χ_z of chains with masses of $0.45M_p$–$0.55M_p$ at the same ζ_r, averaged over all experimentally characterized values of ζ_r for **1c–5o**. Negative differences correspond to simulations underestimating the extent of fracture–coupled isomerization.

Several reported models allow fracture of partially uncoiled chains, with the overstretched segment fixed either at chain centre,[82,83] or at several locations distributed along the chain.[70,84] The latter allows broader mass–distributions of the fragmentation products than the former or the overstretched–chain model.[2,84] To make this overstretched–segment model as flexible as possible, we assumed that fracturing chains of each size make up an ensemble of geometries, characterized by unique combinations of the length of the overstretched segment, l_{os}; its position along the backbone; its f_{max} and the maximum time these conditions persist, $t_{stretch}$. We also assumed that the relative positions of the overstretched segment are distributed normally around the chain centre with chain–size–dependent variance σ^2 and that l_{os}, f_{max} and $t_{stretch}$ depend both on the chain size and the segment position (e.g., eqs. 14–16 in

SI). Using the procedure described above we established that differences between simulated and measured MMDs were weakly sensitive to f_{max} and $t_{stretch}$, increased with l_{os}, and varied non–monotonically with σ. Conversely, the model required incompatible sets of parameters to reproduce experimental χ_Z depending on the SS location: $t_{stretch}$>10 μs, f_{max} <5.4 nN and l_{os}<0.3 for **2o**/**4o**, but $t_{stretch}$<20 ns, f_{max} >5.8 nN and l_{os}>0.6 for **1c**–**4c** despite the overlapping chain masses of these samples. As a result, the overstretched–segment model can be parameterized to reproduce measured MMDs but not χ_Z (Figure 10a,c and SI Figure 25, Figure 26 & Figure 27), illustrating that studying chain fracture alone yields too limited data for characterizing the molecular conditions of flow–induced mechanochemistry.

The common assumption that forces of every backbone bond of a fragmenting chain are correlated (the overstretched–chain model) fails to reproduce observed MMDs because it vastly underestimates the relative mechanochemical lability of bonds away from the chain centre. Assuming that only a segment of the fragmenting chain is overstretched allows the fraction of chains fracturing by scission of a particular backbone bond to be determined by the probability of this bond falling within the overstretched segment, not by its force relative to that of the central bond. Yet, this also causes the relative isomerisation propensity of off–centre *Z*–SS to decrease too steeply with the distance to the chain centre compared to experiment. For example, measured isomerization rate constants for **2o** (average SS position at 0.2*L*) is only 5 times less than that for **2c** (centred SS), whereas the equivalent ratio in the overstretched–segment model is <0.004. Thus, neither set of models is consistent with our data.

A dynamic model that reproduces all measurements quantitatively.

All reported approaches to modeling flow–induced mechanochemistry postulate that a mechanochemical reaction (e.g., chain fracture) occurs instantaneously once a certain chain geometry (or force) is reached. As shown above this assumption is inconsistent with our experiments. We sought a simple empirical model to test if allowing the chain geometry and the chain survival probability to change at comparable rates would accurately reproduce the experimental results. Because chains often uncoil from a terminus,[60,85] we assumed that an overstretched segment also originates at a terminus, grows according to Eq. 1 (where L is the chain contour length and k_s is the rate constant of segment growth) while also drifting towards the chain centre with the rate constant k_d (Eq. 2, where d is the distance from the centre of the overstretched segment to the closest terminus). Eq. 1 is designed to approximate known uncoiling dynamics. Our model retains the quadratic dependence of f_{max} on l_{os} (Eq. 3), but with a time–dependent proportionality constant to accommodate the rapidly increasing fluid strain rates generated by imploding cavitation bubbles,[1] and derives the distribution of forces within the overstretched segment by representing each backbone bond as a harmonic spring connecting two massless spheres that act as frictional drag centres

in a 1D flow field of uniform fluid strain rate.[60]

$$\lambda_{os} = 1 - e^{-k_s t} \qquad Eq.1$$

$$d = 0.5 - 0.5e^{-(k_s + k_d)t} \qquad Eq.2$$

$$f_{max} = (\alpha + \beta t){\lambda_{os}}^2 \qquad Eq.3$$

The same parameterization approach used for the reported models yielded distributions of chain–size dependent k_s, k_d, α, β and $t_{stretch}$ parameters (Figure 30) that reproduce experimental MMDs, χ_Z and k_i/k_f ratios across the full range of chain masses and SS locations (Figure 10 blue, and SI Figure 32) to within the experimental uncertainty. This large improvement over the overstretched–segment model, which has a comparable number of adjustable parameters, has two major causes. First, an overstretched segment whose f_{max} increases while it drifts towards the chain centre strains more monomers, if some only transiently, than comprise the segment at the time of chain fracture. Because *Z*–SS isomerizes on the sub–μs timescale at lower force (>2.5 nN, Figure 9a) than the C–C bond homolyzes (>5.2 nN), this effectively decouples the distributions of the fragmentation and isomerization probabilities. Second, eqs. 1–3 produce a much more diverse set of distributions of microscopic reaction probabilities than the reported models. The more diverse the microscopic distributions that contribute to sample–average behaviour (Figure 11a–b), the closer the simulated and experimental MMDs and χ_Z become, suggesting that a complex combination of molecular conditions (strain rate, straining time, conformation preceding the strain etc) is likely responsible for the observed mechanochemistry.

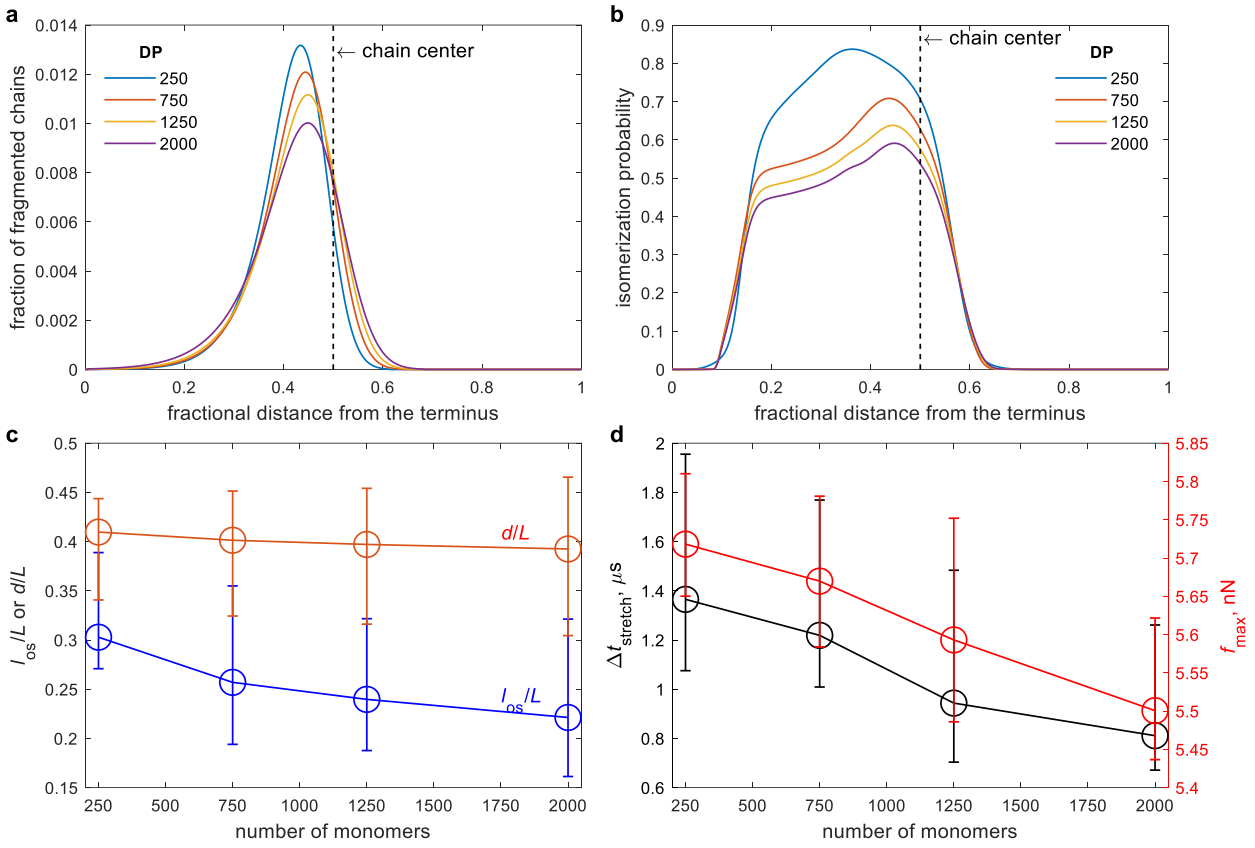

Figure 11 – ***Summary of molecular conditions underlying the observed mechanochemistry****. (a–b) the discrete sample–average distributions of probabilities of chain fragmentation (a) and fragmentation–coupled isomerization of Z–SS (b). The x axis is the fractional distance from the chain terminus where the overstretched segment originates to either (a) the backbone bond that dissociates, or (b) Z–SS whose probability to isomerize immediate prior to chain fracture is given by the corresponding y value. For example Z–SS located exactly at the centre of a chain with 250 monomers has 69% average likelihood to isomerize before the chain fractures by scission of any of its backbone bonds; in individual fragmenting chains this probability varies from ~97% to <3%. For both distributions, the bin size is 0.002. (c) the fractional length of the overstretched segment (l_{os}/L), and the fractional distance from the closest terminus to the monomer experiencing f_{max} (d/L) at $t_{stretch}$. (d) the time the chain remains loaded after its f_{max} reaches 2.5 nN, $\Delta t_{stretch}$, and the largest f_{max} achieved during this time. In (c–d) circles are average values and error bars define most probable 80% of the values.*

The key parameters in the model ($t_{stretch}$, k_s, k_d) are not physically related although they do correlate empirically for any set of parameters that reproduce our data. This is because $t_{strecth}$ is related to a physical parameter (the chain breaks or the flow field becomes too weak to trap the polymer and releases it, which is a finite time by definition since we don't consider the behavior of the polymer outside of the stretching event), whereas there are no outside requirements for k_s and k_d to be >0. During parametrization however only values of k_s and k_d >0 reproduce the data and it happens to occur in a way that appears to correlate $k_{s/d}$ to $t_{strecth}$.

Discussion

A sample–average distribution of reaction probabilities along the chain backbone (Figure 11a–b) describes the macroscopic stoichiometry of the corresponding mechanochemical reaction (e.g., Eqs. 5–6 in SI). These distributions are sums of molecular reaction probabilities

corresponding to unique combinations of conditions experienced by individual chains, weighted by the probability of each condition to occur. In **1c**–**5o**, three sample–average distributions control observed MMDs and χ_Z. First, the distribution of fragmentation probabilities (Figure 11a) defines the relative contribution of each backbone bond to fracture of a chain (partially) overstretched by the flow. The broader the distribution, the more chains fragment by dissociation of backbone bonds away from the chain centre and the greater the dispersity of the fragmented sample. Second, the distribution of probabilities of fragmentation–coupled isomerization (Figure 11b) describes the likelihood of *Z*–SS at each location along the backbone to isomerize immediately prior to chain fracture. Third, the distribution of probabilities of fragmentation–independent isomerization (SI Figure 24c) applies to *Z*–SS isomerization in partially–overstretched chains that fail to fracture before the load dissipates (e.g., ~60% of chains of **1c** meet this definition).

We find that only asymmetric distributions of reaction probabilities with maxima off chain centre (Figure 11a–b) reproduce measured mass–dependent χ_Z. The result challenges the idea of "mid–chain selectivity"[79,80,86-88] of flow–induced mechanochemistry Instead, under the standard sonication conditions studied here, the probability of an overstretched polystyrene chain to fragment by homolysis of any of the central 5% of its backbone bonds is only 13–20%, depending on chain size. Our simulations suggest that lower–barrier non–scissile reactions of "multimechanophore"[78] polymers follow the same pattern: in an average chain of hypothetical poly–(*Z*–SS), only 21–23% of SS that isomerize before chain fracture would be centrally located. This suggests at best moderate localization of flow–induced mechanochemistry along the polymer chain. Confining labile reactive moieties close to the chain centre yields apparent "mid–chain" selectivity.[89-91] For example, hypothetical polystyrene containing a single labile scissile backbone bond whose distribution follows that of SS in **1c**–**4c** (Figure 7b) and has $\Delta G^{\neq}(f)$ of an anthracene/maleimide adduct dissociation[92] would fragment by dissociation of this labile bond 68 – 98% of the time, depending on chain size; with 57–74% of the fragmentations being localized within the central 5% of the backbone.

Our analysis suggests that the asymmetric reaction probability distributions can only be produced by an overstretched segment that grows and drifts toward the chain centre on a timescale comparable with the mechanochemical reactions, with two implications. First, at any moment only 20–30% of the average chain is strained enough to manifest detectable mechanochemistry. Simultaneously and somewhat counterintuitively, the fractional length of the backbone where a non–scissile mechanochemical reaction is kinetically competitive with chain fracture can exceed ~0.6, depending on the difference between $\Delta G^{\neq}(f)$ of the scissile and non–scissile reactions. This conclusion is consistent with the high yield of productive

mechanochemical remodeling per chain fracture of certain multi–mechanophore polymers[76,93] and suggests how to control this yield systematically.

The observed MMDs and χ_Z reflect the evolution of the overstretched segment from the moment its f_{max} reaches ~2.5 nN, which is the minimum force for detectable isomerization of *Z*–SS in a sonicated solution, to the moment when the chain fractures or the flow weakens enough (Figure 35). During this period, $\Delta t_{stretch}$, which averages ~1 μs (Figure 11d), the length of the overstretched segment, l_{os}, the distance between its centre and the chain terminus, *d*, and f_{max} increase monotonically. This broadens the reaction–probability distributions and shifts their maxima towards chain centre, while lowering the fraction of the chains which isomerize without fracture relative to those that fracture from close to infinity at Δt_{strech} <0.1 μs to ~0 for Δt_{strech} >2.5 μs. As a result, simulated MMDs and χ_Z are quite sensitive to $\Delta t_{stretch}$.

The probability of the average chain to fracture by $t_{stretch}$ varies from 43% for chains with 250 monomers to 76% for 2000 monomers. For the surviving chains, $t_{stretch}$ may be limited by the complete implosion of the cavitation bubble. In a 20 kHz acoustic field a bubble would implode within <20 μs, but only the final stages of the implosion likely generate flow strain rates high enough to overstretch a detectable fraction of the dissolved chains in the vicinity of the bubble.[1,23] The decreasing survival probability with chain length is primarily due to the longer overstretched segments in longer chains, which increases the number of backbone bonds that are sufficiently destabilized kinetically to contribute to chain fracture, thus reducing the chain survival probability at constant force (Figure 36d).

The ~1.5–fold higher fraction of the chains of 2000 monomers that fracture within $t_{stretch}$ compared to those of 250 monomers contrasts with the ~260–fold difference of the measured bulk fragmentation rate constants, k_f, for the same chains (Figure 8c). This suggests that bulk kinetics reflects primarily the probability of a chain becoming overstretched rather than the probability of an overstretched chain to fracture. Why a larger fraction of longer chains in a sonicated solution are overstretched at any moment compared to shorter chains, whose concentration is higher remains to be understood. Yet, this finding also challenges another common,[94] if occasionally criticized,[58,67,74,95] belief that the bulk fragmentation kinetics reflects molecular conditions (the extent to which the chain is strecthed and for how long) due to force experienced by individual fragmenting chains. In other words, a physical process must account for the majority of the difference between bulk fragmentation rates between large and small polymers because once the polymers become mechanochemically active there is only a small dependance of fragmentation probability on chain length.

Conclusions

We demonstrated on an example of a sonicated solution that analysis of same–chain competition between mechanochemical fracture of a polymer chain and isomerization of a chromophore embedded in its backbone enables detailed characterization of the molecular conditions underlying flow–induced mechanochemistry. Under studied conditions the length of the chain segment that is strained enough to manifest mechanochemistry, its location along the chain and its force all change on the same timescale and in competition with the decreasing chain survival probability. This competition displaces the location of the highest mechanochemical reactivity away from the chain centre, makes bulk mechanochemical selectivity rather than bulk fragmentation rates the indicator of the molecular conditions experienced by individual reacting chains, and yields appreciable chain fracture at forces spaning a ~1 nN range. We suggest that by lowering the lengthscale at which the chain behaviour in the flow can be probed experimentally from ~1 μm of the optical methods to ~10 nm of our approach offers important opportunities for fundamental studies and practical exploitations of polymer rheology and mechanochemistry. For example, our method makes accessible experimental data for rigorous testing of microscopic rheological models of polymer solutions[96] and to design mechanochemical reactions to control this rheology.[97] Detailed knowledge of the molecular conditions responsible for mechanochemistry in sonicated solution would resolve continued controversies about the effects of chain topology on flow–induced mechanochemistry;[98-101] enable mechanistic studies of complex mechanochemical reactions[76,91] and cascades,[92,102] and allow sonicated solutions to be used as tractable models of mechanochemistry of polymer solids and melts.[16,103-106]

Supporting information

Below are key aspects of the SI for the upcoming paper related to the preceding chapter. Once the paper is published it is best to consult its corresponding SI as it contains more detail and more up to date explanations.

Synthesis

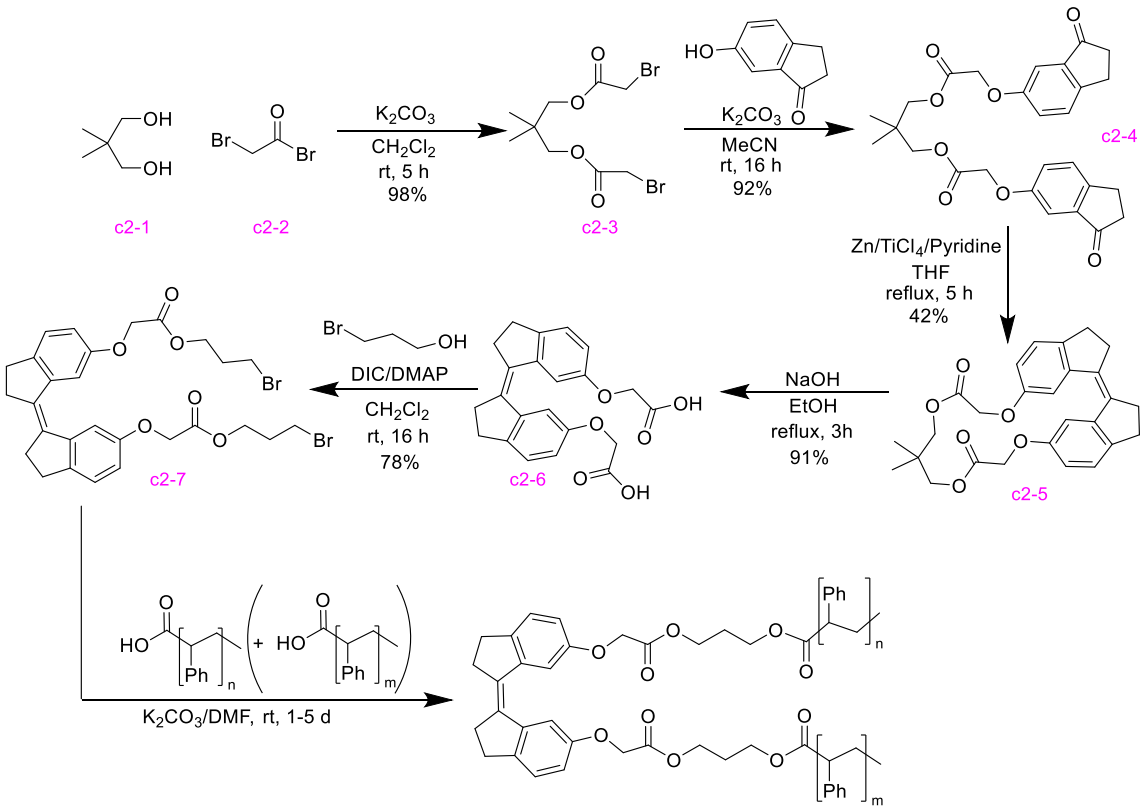

1c: ⟨n⟩=⟨m⟩=120 **1o**: ⟨n⟩=120, ⟨m⟩=240
2c: ⟨n⟩=⟨m⟩=240 **2o**: ⟨n⟩=120, ⟨m⟩=430
3c: ⟨n⟩=⟨m⟩=430 **3o**: ⟨n⟩=240, ⟨m⟩=430
4c: ⟨n⟩=⟨m⟩=1080 **4o**: ⟨n⟩=240, ⟨m⟩=1080
5o: ⟨n⟩=430, ⟨m⟩=1080

*Scheme S2–Synthesis of polymers **1c–4c** and **1o–5o**.*

2,2–dimethylpropane–1,3–diyl bis(2–bromoacetate) (c2-3)

The synthesis followed the reported procedure[107] with minor modifications. To a solution of butane–1,4–diol (0.50 g, 5.5 mmol, 1 equiv.) in 50 mL CH_2Cl_2 was added bromoacetyl bromide (1.0 mL, 2.35 g, 11.5 mmol, 2.1 equiv.) and K_2CO_3 (3.0 g, 22 mmol, 4 equiv.). The mixture was stirred at room temperature overnight before quenching with H_2O (50 mL). The organic layer was separated and washed with H_2O (2 x 25 ml), aqueous K_2CO_3 (25 mL) and brine (25 mL) before drying over $MgSO_4$. The solvent was removed under reduced pressure yielding the expected product (1.8 g, 5.5 mmol, 98%). ^{1}H NMR ($CDCl_3$, 500 MHz, 298 K) 4.01 (m, 4H), 3.85 (s, 4^{1}H NMR matches that reported previously.[107]

2,2–dimethylpropane–1,3–diyl bis(2–((3–oxo–2,3–dihydro–1H–inden–5–yl)oxy)acetate) (c2-4)

To a solution of butane–1,4–di–(2–bromoacetate) (3.10 g, 9.3 mmol, 1 equiv.) in MeCN (30 mL) was added 6–hydroxyindanone (2.77 g, 18.7 mmol, 2 equiv.) and K_2CO_3 (5.16 g, 37.3 mmol, 4 equiv.), the resulting mixture was stirred at room temperature overnight. The solution was then diluted with CH_2Cl_2 (50 mL) and washed with H_2O (25 mL) and brine (25 mL) before drying over $MgSO_4$. The solvent was removed under reduced pressure to afford the product as an off white solid (4.0 g, 8.57 mmol, 92%). ^{1}H NMR ($CDCl_3$, 500 MHz, 298 K) 7.39 (d, 2H), 7.25 (dd, 2H), 7.13 (2H, d), 4.68 (s, 4H), 3.86 (s, 4H), 3.06 (t, 4H), 2.70 (t, 4H), 0.90 (m, 6H). ^{13}C NMR ($CDCl_3$, 100 MHz, 298 K) 206.8, 168.5, 157.7, 149.0, 138.4, 127.9, 124.4, 105.9, 69.7, 65.3, 37.1, 34.8,25.3, 21.7.

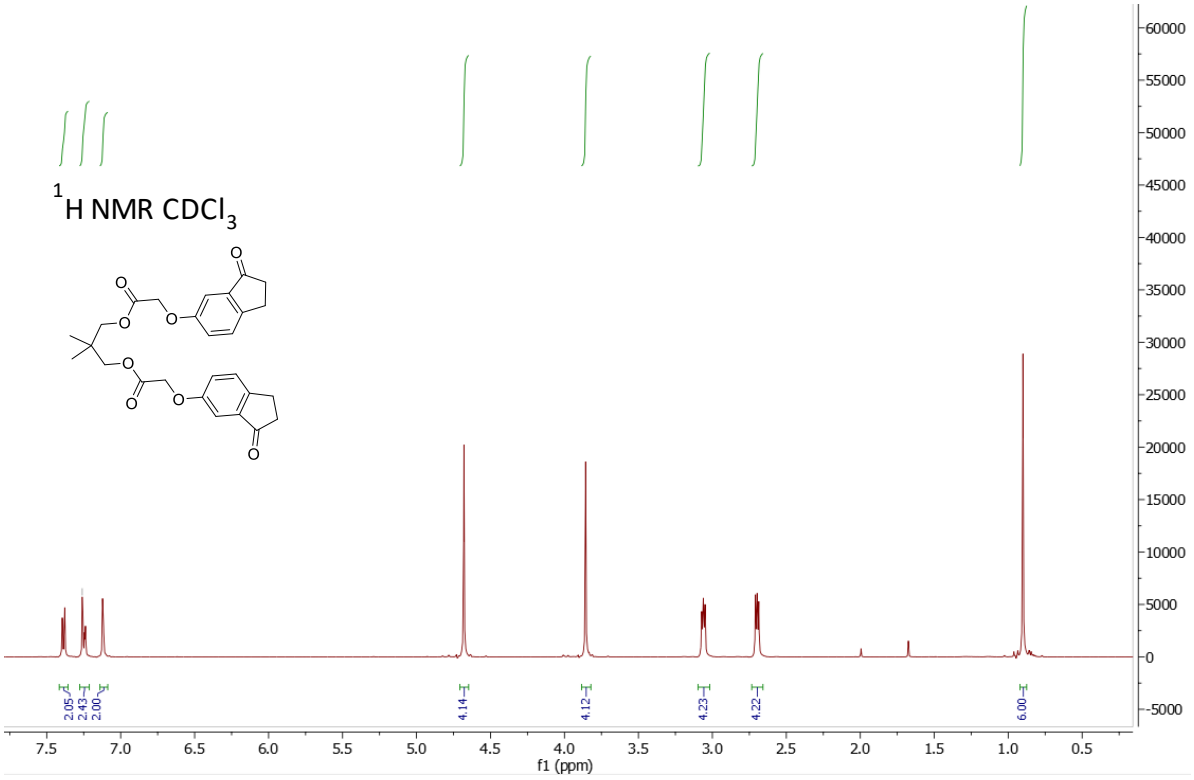

*Figure 12–**^{1}H NMR spectrum of c2-4 in $CDCl_3$.***

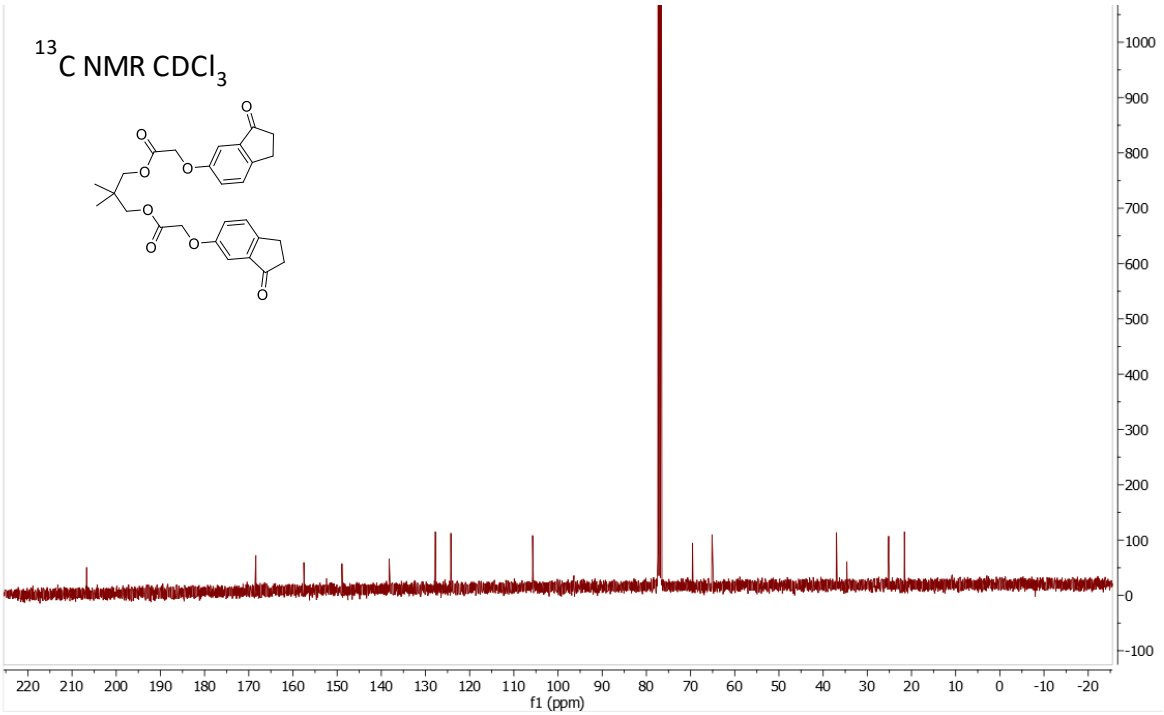

*Figure 13–**^{13}C NMR spectrum of c2-4 in $CDCl_3$.***

(*Z*)–Stiff stilbene–6,6'–2,2–dimethylpropane–1,3–diyl(oxy–ether) (c2-5)

The synthesis followed the reported procedure[107] with minor modifications. To a stirred suspension of zinc powder (3.64 g, 55 mmol, 13 equiv.) in dry THF (70 mL), $TiCl_4$ (2.87 mL, 4.88 g, 25.7 mmol, 6 equiv.) was added over 2 min at 0 °C. The resulting slurry was heated at reflux for 1.5 h, and pyridine (2.0 mL) was added. A THF solution (50 mL) of **c2-4** (2.0 g, 4.3 mmol, 1 equiv.) was added over a 5 h period by dropping funnel to the refluxing reaction mixture. The reflux was continued for 0.5 h after the addition was complete. Upon cooling to room temperature, the reaction mixture was quenched with dilute HCl (50 mL), stirred for 10 min and filtered. The THF was removed under reduced pressure and the aqueous layer was extracted with CH_2Cl_2 (3 x 15 ml). The combined organic phase was washed with H_2O (20 mL) and brine (20 mL) before drying over $MgSO_4$. The solvent was removed under reduced pressure to afford the product which was used without further purification (0.80 g, 4.3 mmol, 43%). ^{1}H NMR ($CDCl_3$, 500 MHz, 298 K) 7.67 (d, 2H), 7.18 (dd, 2H), 6.77 (d, 2H), 4.69 (s, 4H), 4.04 (t, 4H), 3.06 (t, 4H) 2.92 (t, 4H), 2.83 (m, 4H), 0.86 (s, 6H).^{1}H NMR matches that reported previously.[107]

Stiff stilbene–6,6'–diacetic acid (c2-6)

The macrocycle **c2-5** (0.30 g, 0.69 mmol, 1 equiv.) was dissolved in EtOH (10 mL) with NaOH (0.22 g, 5.5 mmol, 8 equiv.) and refluxed for 3 h. After cooling, the solvent was removed under reduced pressure and the crude product dissolved into H_2O (100 mL) and acidified to pH 3 using conc. HCl. The solution was extracted with EtOAc (5 x 15 mL), these combined organic

extracts were dried over $MgSO_4$ and the solvent was removed under reduced pressure, yielding the pure product (0.24 g, 0.63 mmol, 91%). ^{1}H NMR (DMSO–d_6 , 500 MHz, 298 K). 7.43 (d, 2H, H_{ind}), 7.23 (d, 2H, H_{ind}), 6.78 (dd, 2H, H_{ind}), 4.61 (s, 4H, H_3) ^{13}C NMR (DMSO–d_6 , 100 MHz, 298 K). 170.4, 156.3, 141.1, 140.9, 135.2, 126.0, 114.2, 109.3, 65.0, 35.0, 29.3. HRMS–ESI (m/z) $[M–H]^-$ Calculated for $C_{22}H_{19}O_6^-$: 379.1182 Found 379.1176.

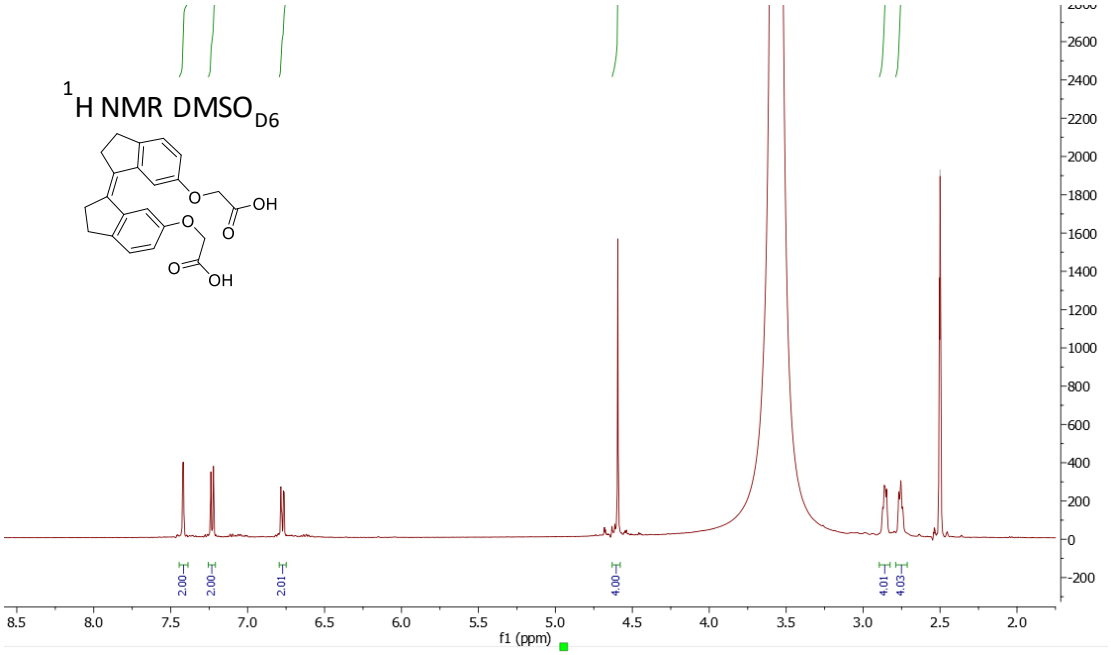

*Figure 14–**^{1}H NMR spectrum of c2-6 in DMSO–d_6.***

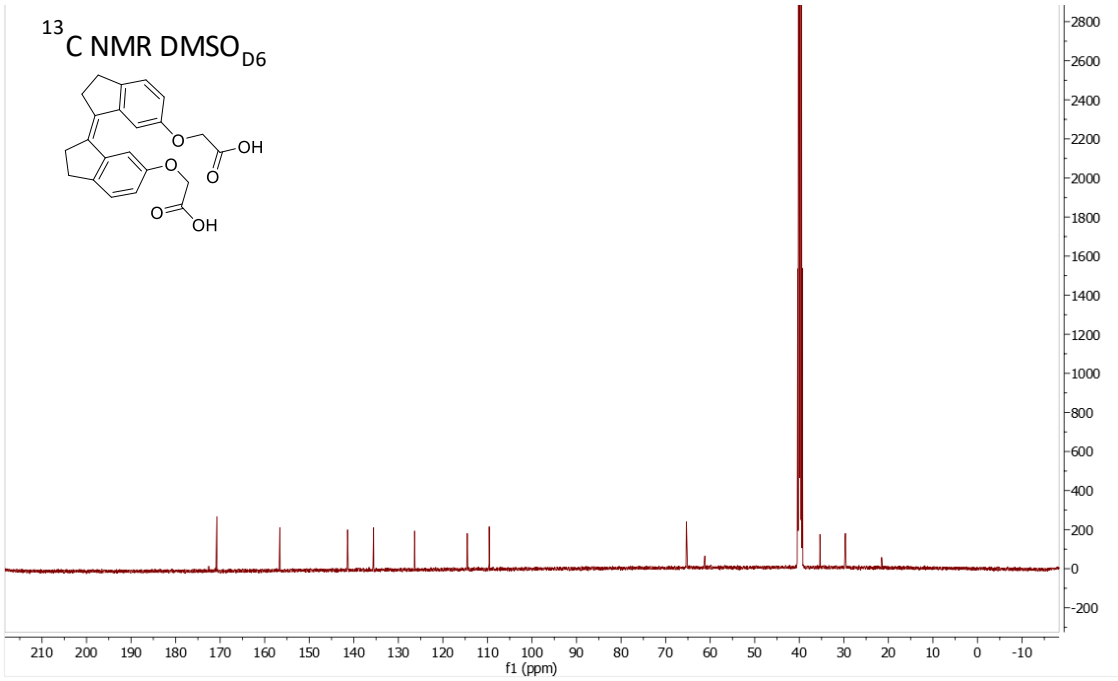

*Figure 15–**^{13}C NMR spectrum of c2-6 in DMSO–d_6.***

Stiff stilbene–6,6'–di–actyl–3–bromopropyl (c2-7)

c2-6 (150 mg, 0.39 mmol, 1 equiv.) was dissolved in CH_2Cl_2 (20 mL) with DMAP (24 mg, 0.19 mmol, 0.5 equiv.) and 3–bromopropan–1–ol (110 mg, 0.78 mmol, 2 equiv.). DIC (0.105 g, 0.83 mmol, 2.1 equiv.) was added at 0 °C before stirring overnight. The reaction was filtered through cotton wool and the solvent was removed under reduced pressure. The crude product was dissolved in EtOAc (10 mL), cooled in the freezer for 20 min and filtered again before washing with HCl (1 M, 3 x 10 mL). The organic layer was dried over $MgSO_4$ and filtered, the solvent was removed under reduced pressure to afford crude product, which was purified by automated column chromatography (4 g silica, CH_2Cl_2:EtOAc, 99:1), the first fraction contained the pure product (191 mg, 0.308 mmol, 78%). ^{1}H NMR ($CDCl_3$, 500 MHz, 298 K) 7.56 (d, 2H, H_{ind}), 7.19 (d, 2H, H_{ind}), 6.77(dd, 2H, H_{ind}), 4.62 (s, 4H, H_3), 4.29 (t, 4H, H_6), 3.33 (t, 4H, H_4) 2.92 (t, 4H, H_1), 2.80 (m, 4H, H_2), 2.13 (p, 4H, H_5). ^{13}C NMR ($CDCl_3$, 100 MHz, 298 K). 169.1 (C_{11}) 156.4 (C_6), 142.0 ($C_{3/8}$), 141.8 ($C_{3/8}$), 135.6 (C_9), 126.0 ($C_{4/5/6}$), 114.9 ($C_{4/5/6}$), 109.5 ($C_{4/5/6}$), 65.9 (C_{10}) , 63.0 (C_{14}), 35.5 ($C_{1/2}$), 31.6 (C_{13}), 30.0 ($C_{1/2}$), 29.3 (C_{12}) HRMS–ESI (m/z) $[M+Na]^+$ Calculated for $C_{28}H_{30}O_6Br_2Na^+$: 645.0286 Found 645.0284.

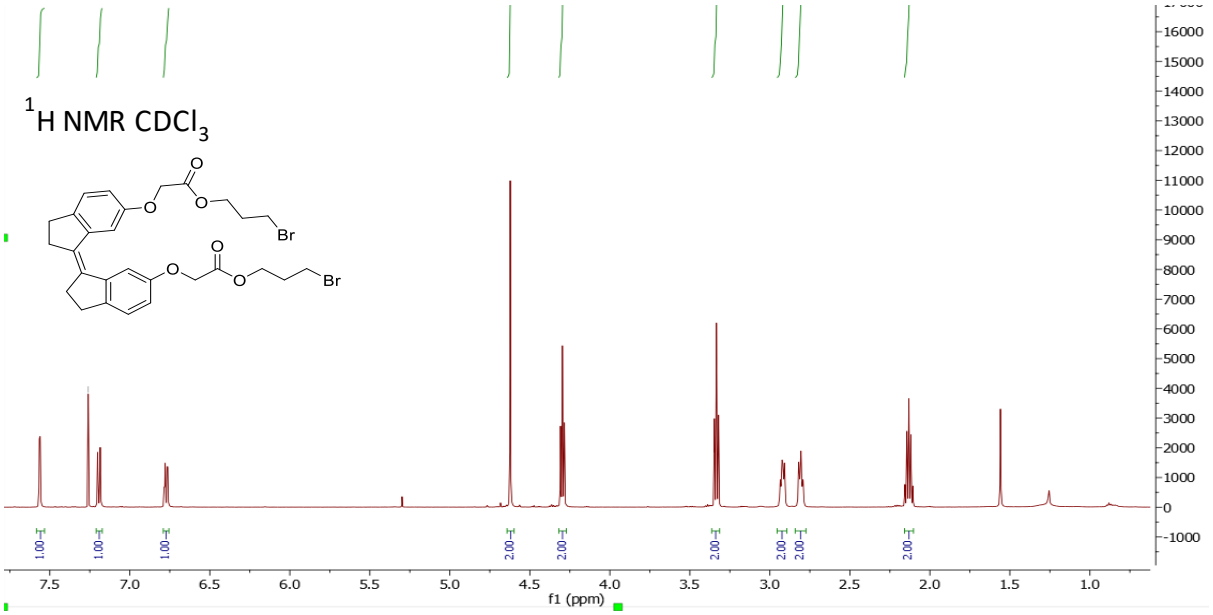

*Figure 16–**^{1}H spectrum of c2-7 in $CDCl_3$.***

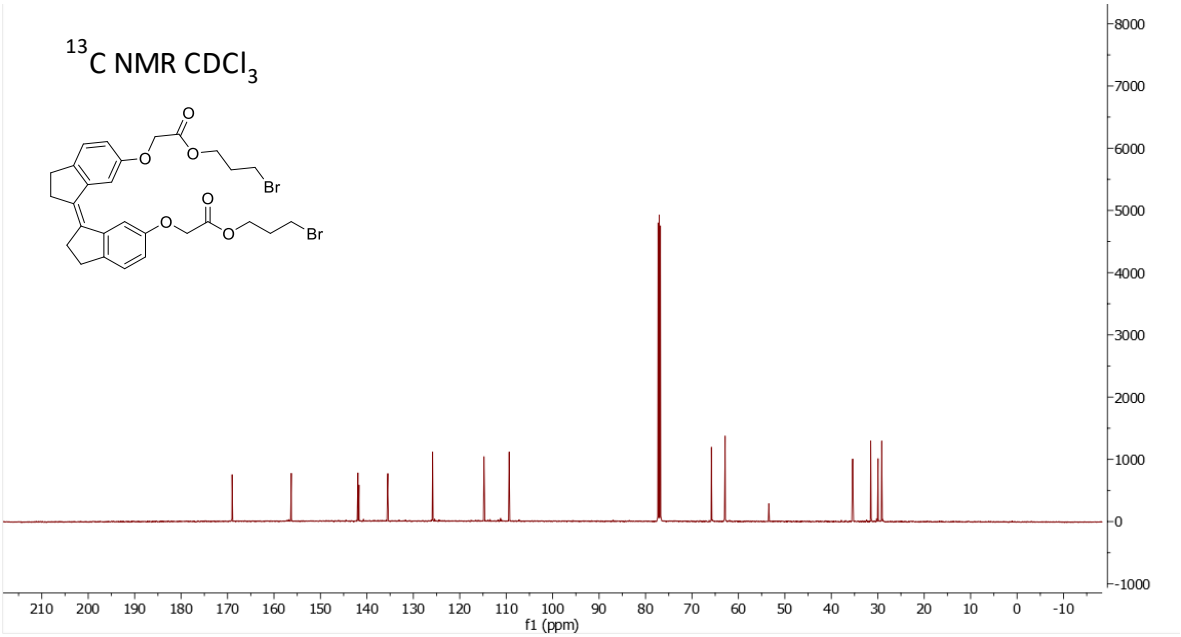

*Figure 17– **^{13}C NMR spectrum of c2-7 in $CDCl_3$.***

General procedure for synthesis and characterization of polystyrenes 1c–4c and 1o–5o:

In a glove box **c2-7** (1 equiv) was added to a solution containing K_2CO_3 (10 equiv.) and either a single nominal mass monocarboxy terminated polystyrene or two different masses (2.1 equiv. and 1 equiv. each respectively) in anhydrous DMF (1.5 – 2 mL). The solution was stirred for 1 – 5 days depending on the mass of polymer (higher mass polymers require longer to react). When SEC analysis indicated a sufficient conversion the mixture was removed from the glovebox and poured into a 1:1 mix of H_2O/EtOAc (20 mL) at ~40 °C which was separated and the aqueous phase washed with ~40 °C EtOAC (2 x 10 mL). The combined organic phase was washed with H_2O (5 x 10 mL) before drying over $MgSO_4$. The volume was reduced to ~8 mL and the solution was subjected in 1 mL batches to prep GPC. Each GPC fraction of 1 mL was analysed by SEC and fractions of similar mass distributions were combined. The combined fractions were analysed by SEC (Figure 18), the isolated yields were 5–20% for reactions using 2 precursor $PSCO_2H$ and ~40% for single $PSCO_2H$ precursor reactions. All polymers had 1 stiff stilbene moiety per chain and Z–SS fraction (χ_Z) of ~90% (Table 1).

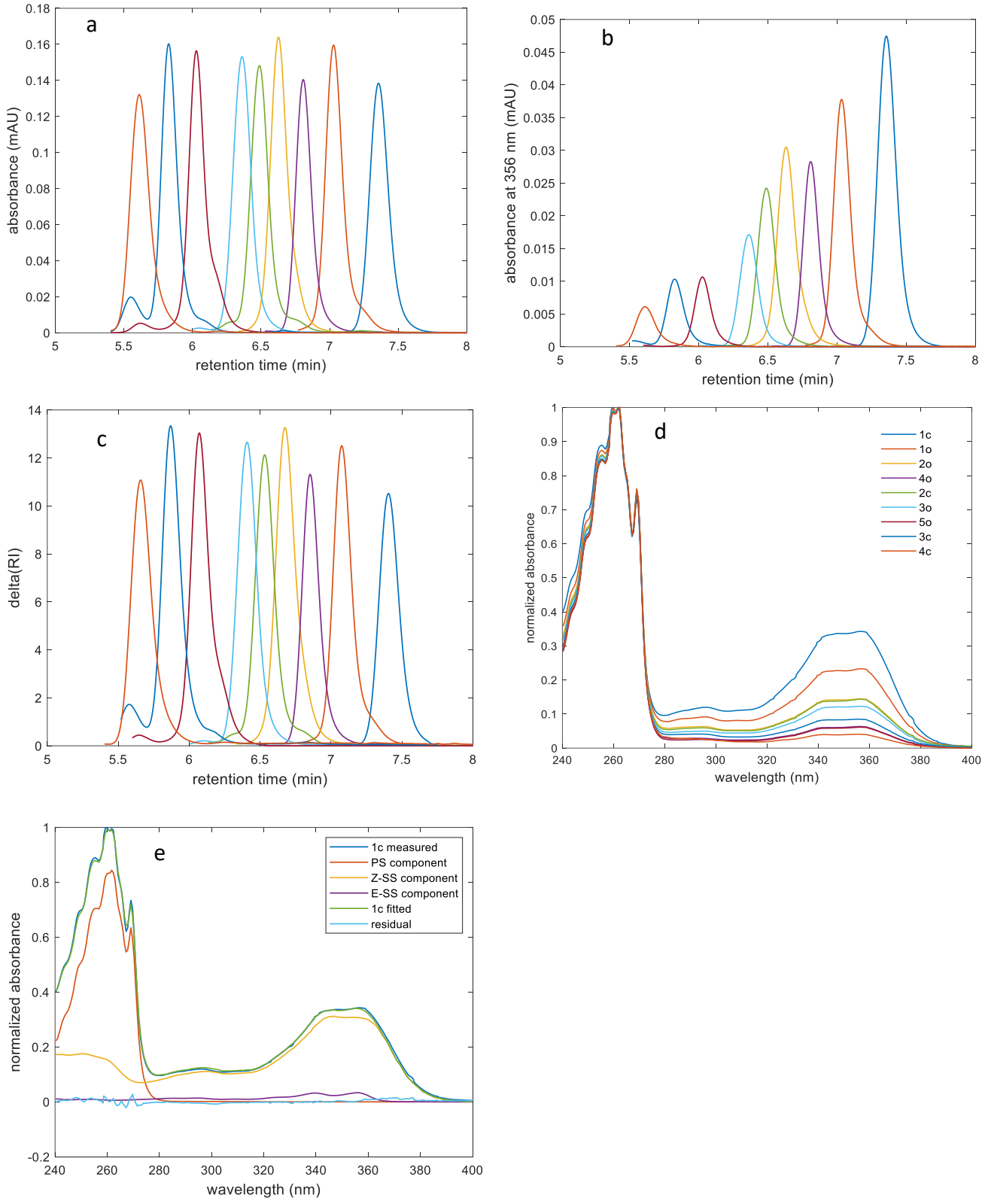

Figure 18 – ***Characterization of the polymers used in this study.*** *(a–c) Size–exclusion chromatograms of* ***4c***, ***5o***, ***4o***, ***3c***, ***3o***, ***2o***, ***2c***, ***1o***, ***1c*** *(from left to right): PDA output at 262 nm (a) and 356 nm (b), and RI output (c); (d) normalized absorption spectra of all polymers before sonication; (e) an example of deconvoluted absorption spectrum of* ***1c*** *at* M_p.

*Table 1 – Summary of the key characteristics of **1c–5o**. SS/chain is the average number of stiff stilbene moiety per polymer chain. χ_Z is the fraction of these moieties that are Z isomers.*

	1c	2c	3c	4c	1o	2o	3o	4o	5o
M_w, kDa	24.9	49.4	90.9	227	37.1	57.0	63.8	139	161
M_n, kDa	24.7	48.9	88.6	223	36.5	55.9	61.9	136	156
Đ	1.008	1.010	1.026	1.016	1.016	1.020	1.031	1.021	1.016
SS/chain	1.04±0.04	1.06±0.04	0.96±0.02	1.02±0.02	0.99±0.03	1.01±0.03	1.03±0.04	1.00±0.01	0.97±0.03
χ_Z	0.90±0.03	0.87±0.02	0.85±0.01	0.83±0.01	0.86±0.02	0.88±0.02	0.90±0.01	0.87±0.01	0.87±0.01

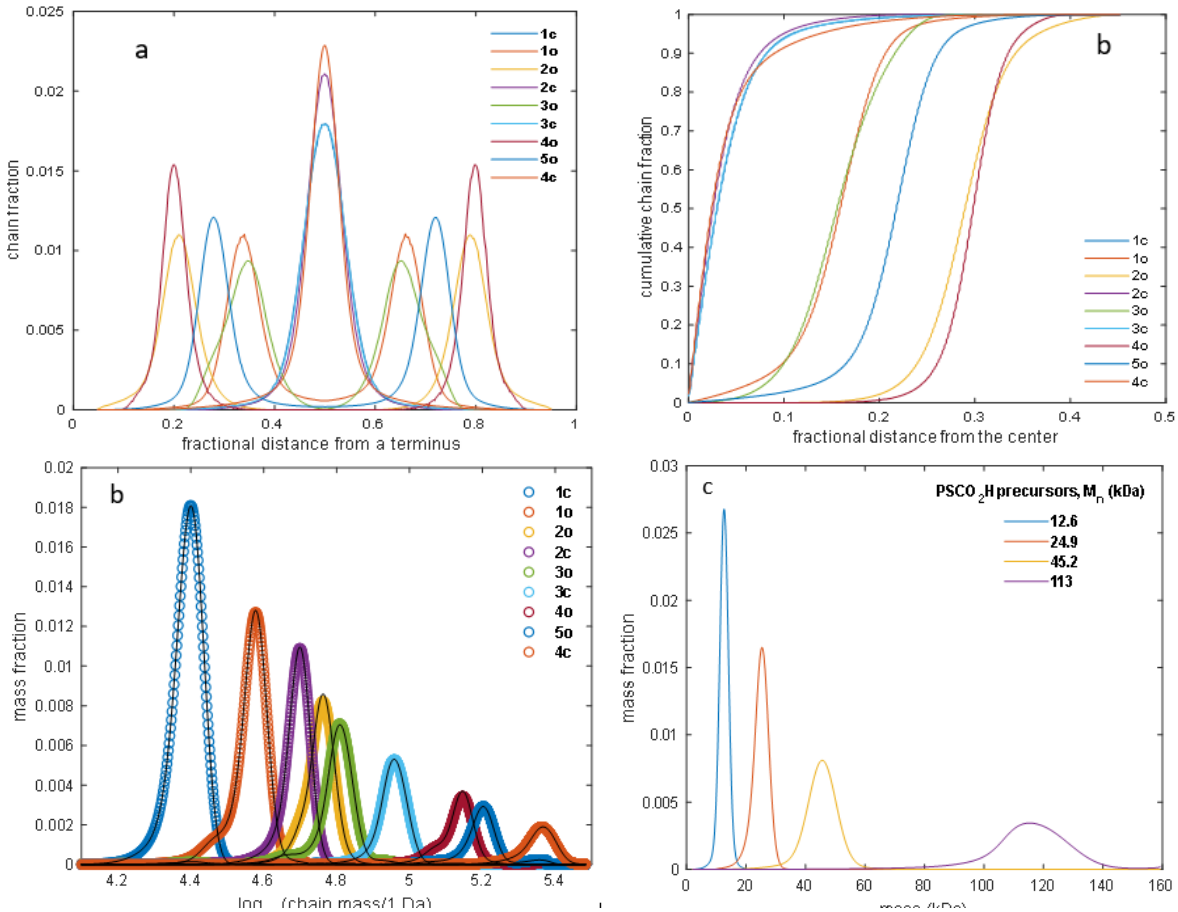

*Figure 19 – **Results of simulation of the formation of 1c-5o by pairwise coupling of precursor chains.** (a) chain fractions with SS within the 1% segment of the chain centreed at the x value. (b) cumulative distributions of SS along chain backbones. (c) Measured (dots) and calculated (black lines) MMDs of the polymers used in this study. (d) measured MMDs of precursor polystyrenes, $PSCO_2H$. Areas under each curve is 1 (MMDs of larger polymers have smaller peak intensities because they are spread over a larger number of chains). The bin sizes are 0.01 (b), 100 Da (c-d).*

Determination of the extinction coefficients

The extinction coefficients of *Z*–SS and $PSCO_2H$ at 240 – 400 nm were determined by the conventional method using samples of known concentrations in unstabilised THF. The extinction coefficients of *E*–SS, $\varepsilon_E(\lambda)$, were derived by fitting a sequence of time–lapsed

spectra of a 4.8x10^{-5} M solution of *Z* stiff stilbene in anhydrous THF irradiated with a 365 nm diode (FWHH = 7 nm) to Eq. 4, where A(λ,t) is the measured absorbance of the solution at wavelength λ and irradiation time *t*, A(λ,0) is the absorbance of the starting solution at the same wavelength; k_1, k_2 (the rate constants of photochemical *Z*→*E* and *E*→*Z* isomerization at the used photon flux) and $\varepsilon_E(\lambda)$ were the fitting parameters. The fitting was performed using the lsqnonlin function of Matlab. The absorption spectra of $PSCO_2H$ at ambient pressure and at the pressure of the PDA detector of the Acquity were indistinguishable, whereas those of Z and E SS were bathochromically shifted by 1.7 and 2.3 nm, respectively, without detectable change in the shape or the extinction coefficients.

$$\frac{A(\lambda,t)}{A(\lambda,0)} = \frac{\left(\varepsilon_E(\lambda) - \varepsilon_Z(\lambda)\right)\left(1 - e^{-(k_1+k_2)t}\right)k_1}{k_1 + k_2} + \varepsilon_Z(\lambda) \qquad (Eq.4)$$

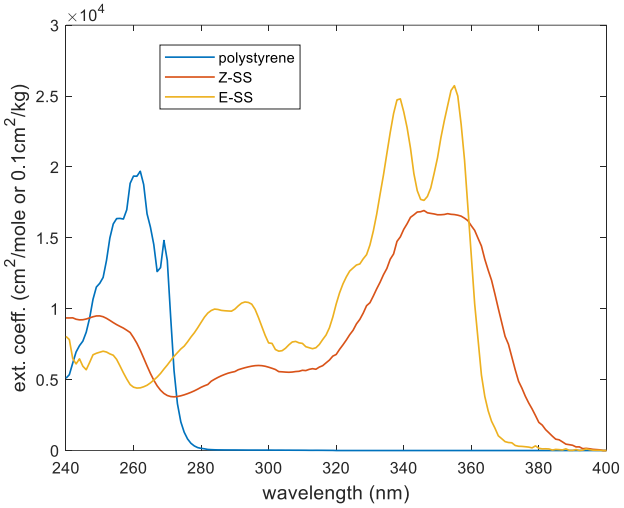

Figure 20 – ***Wavelength–dependent extinction coefficients of polystyrene (in cm²/kg) and the two isomers of stiff stilbene (in cm²/mole).*** *Measured in THF at 30 °C and ~1500 psi (the pressure of the PDA detector); the values for polystyrene are divided by 10 to fit on the same scale.*

Sonication experiments

All sonications were performed on THF solutions of polymers at 1 mg/mL concentration. The two–horn configuration of our sonicator allowed us to sonicate two samples of the same polymer simultaneously. Each cylindrical cell had 3 narrow arms and formed a gas–tight seal with a collar attached to the horn. Each cell contained 5 mL of the solution, a PTFE—coated thermocouple for temperature monitoring threaded through one side–arm, and N_2 inlet/outlet PTFE tubings threaded through another. The third side–arm was reserved for periodically sampling the sonicated solution by withdrawing 50 uL aliquots for SEC analysis. Routine measurements were performed at total absorbed acoustic power of 14.6±0.48 W, as measured separately. This power was delivered using the 20% amplitude setting in the pulse mode (1 s on/1 s off).

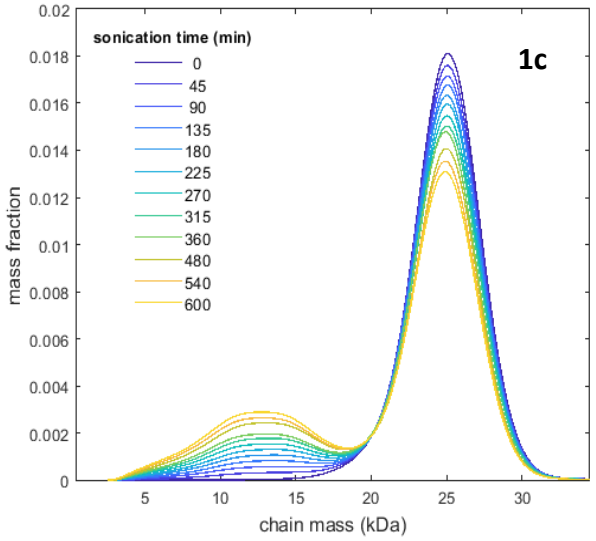
sonication time (min)
0
45
90
135
180
225
270
315
360
480
540
600
1c
mass fraction
chain mass (kDa)

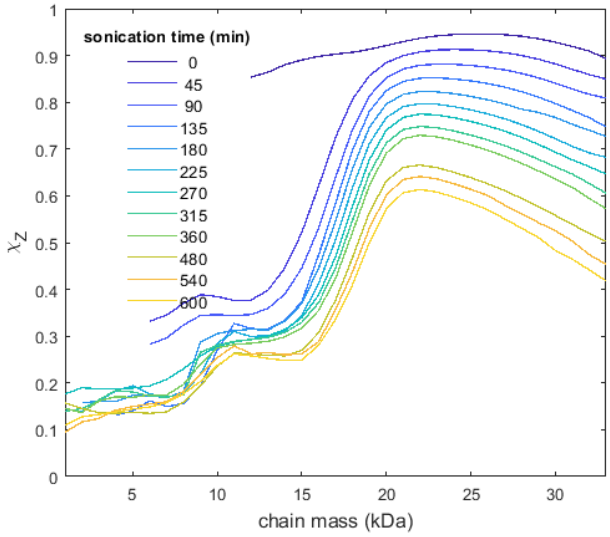
sonication time (min)
0
45
90
135
180
225
270
315
360
480
540
600
χ_Z
chain mass (kDa)

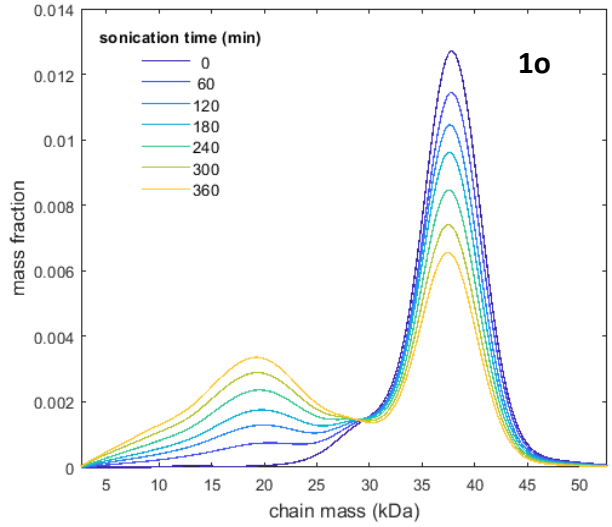
sonication time (min)
0
60
120
180
240
300
360
1o
mass fraction
chain mass (kDa)

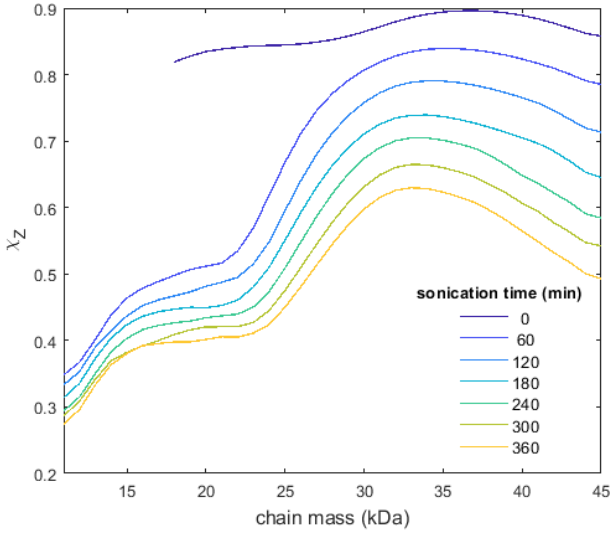
sonication time (min)
0
60
120
180
240
300
360
χ_Z
chain mass (kDa)

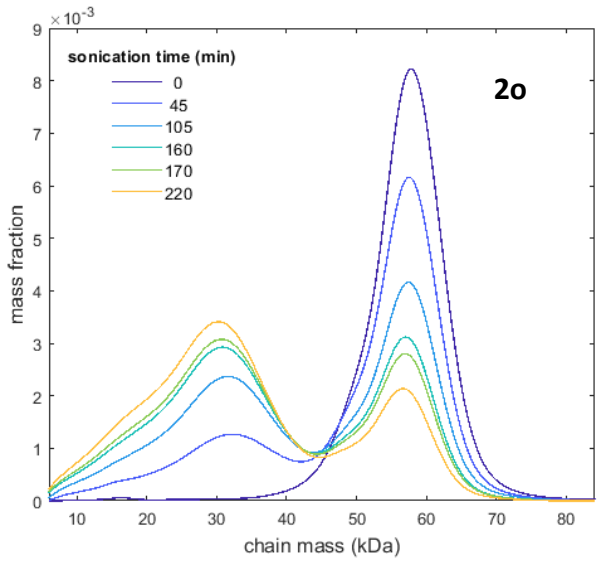
$\times 10^{-3}$
sonication time (min)
0
45
105
160
170
220
2o
mass fraction
chain mass (kDa)

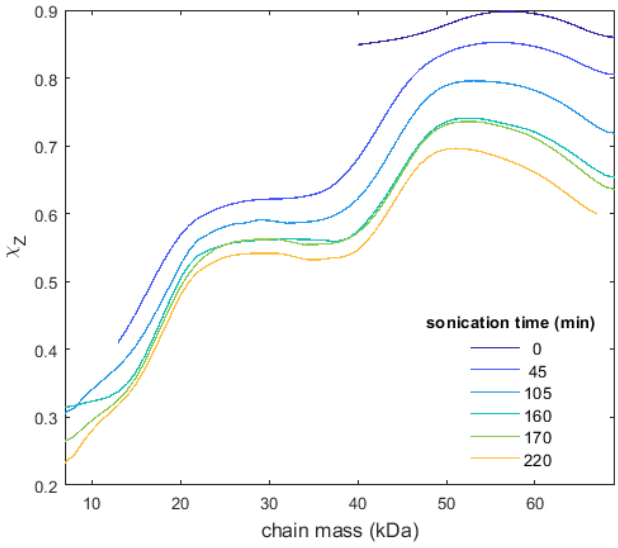
sonication time (min)
0
45
105
160
170
220
χ_Z
chain mass (kDa)

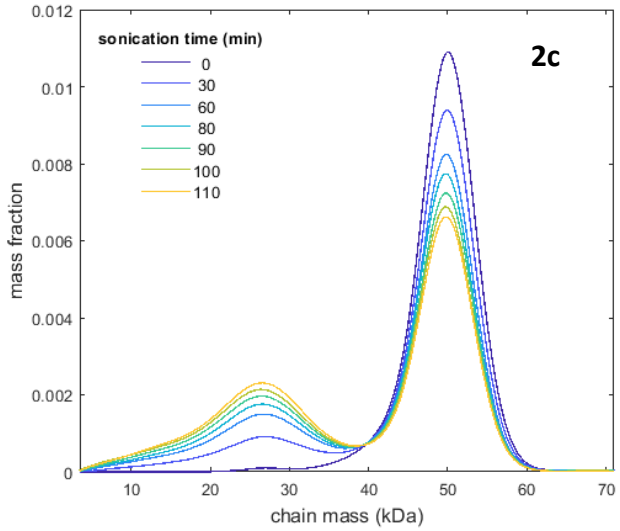
2c
sonication time (min)
0
30
60
80
90
100
110
mass fraction
chain mass (kDa)

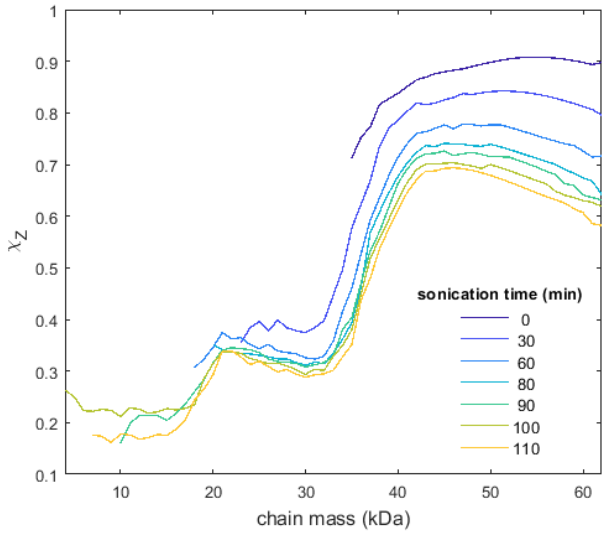
χ_Z
sonication time (min)
0
30
60
80
90
100
110
chain mass (kDa)

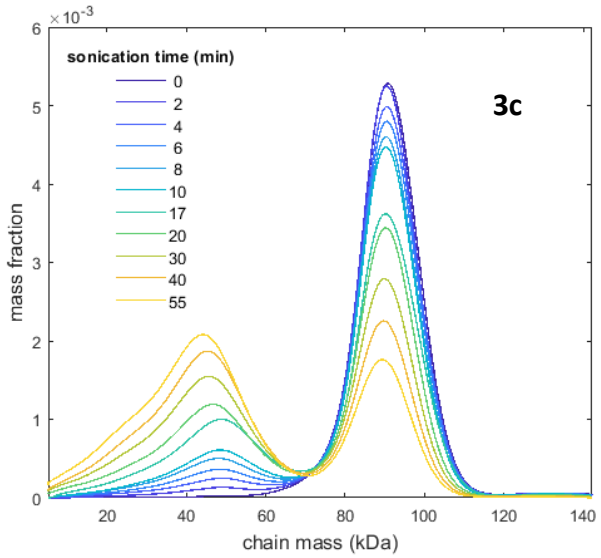
3c
sonication time (min)
0
2
4
6
8
10
17
20
30
40
55
mass fraction
chain mass (kDa)

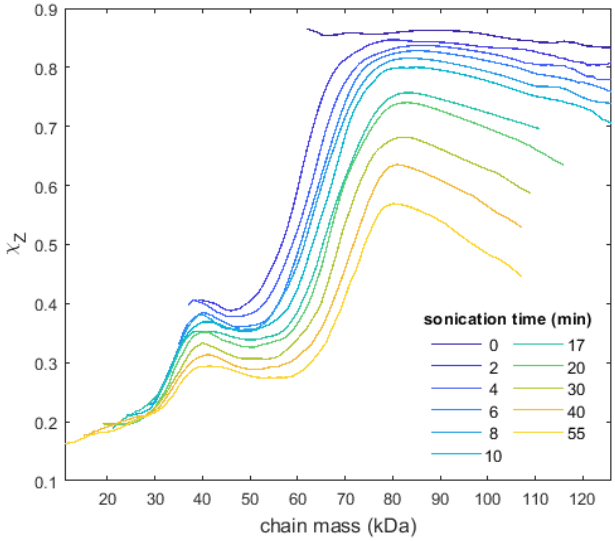
χ_Z
sonication time (min)
chain mass (kDa)

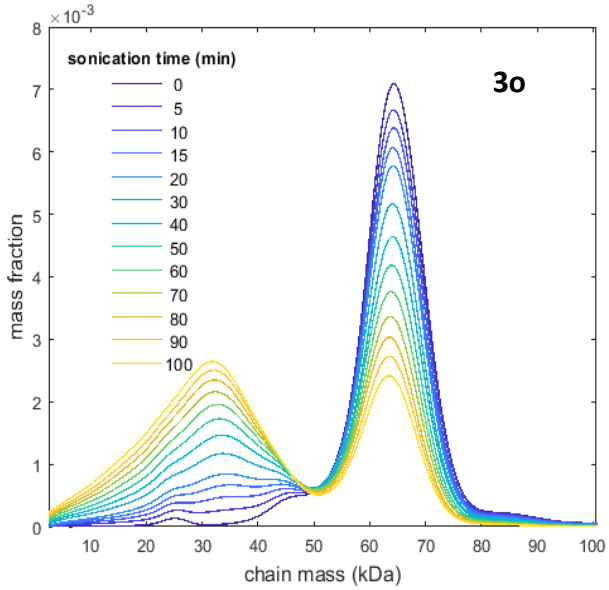
3o
sonication time (min)
0
5
10
15
20
30
40
50
60
70
80
90
100
mass fraction
chain mass (kDa)

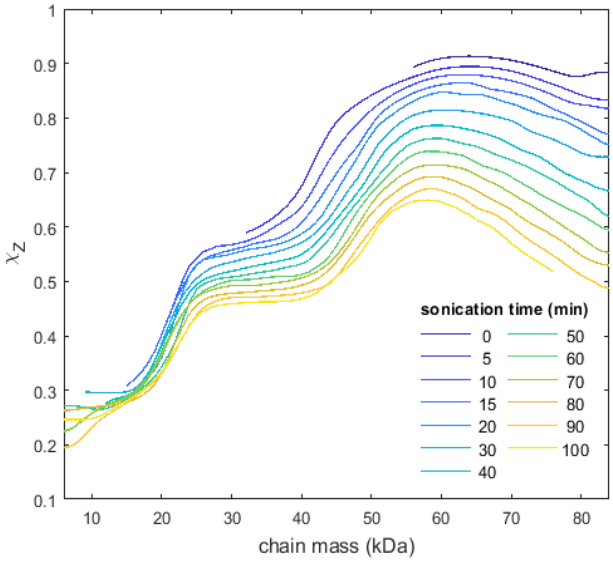
χ_Z
sonication time (min)
chain mass (kDa)

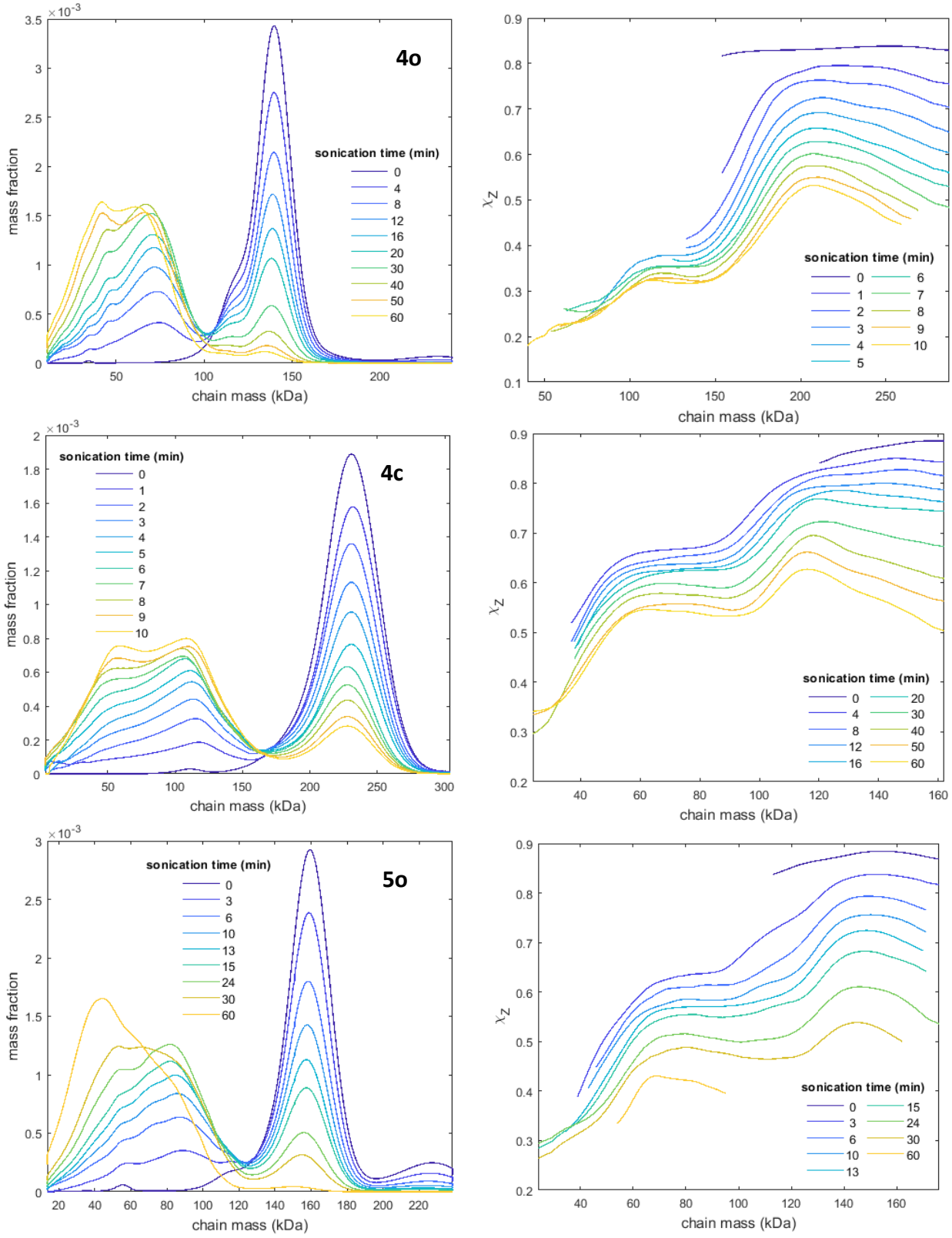

Figure 21 – ***Experimentally measured changes in MMDs and χ_z for 1c-5o at each sonication time that the solutions were analyzed.***

DFT calculations

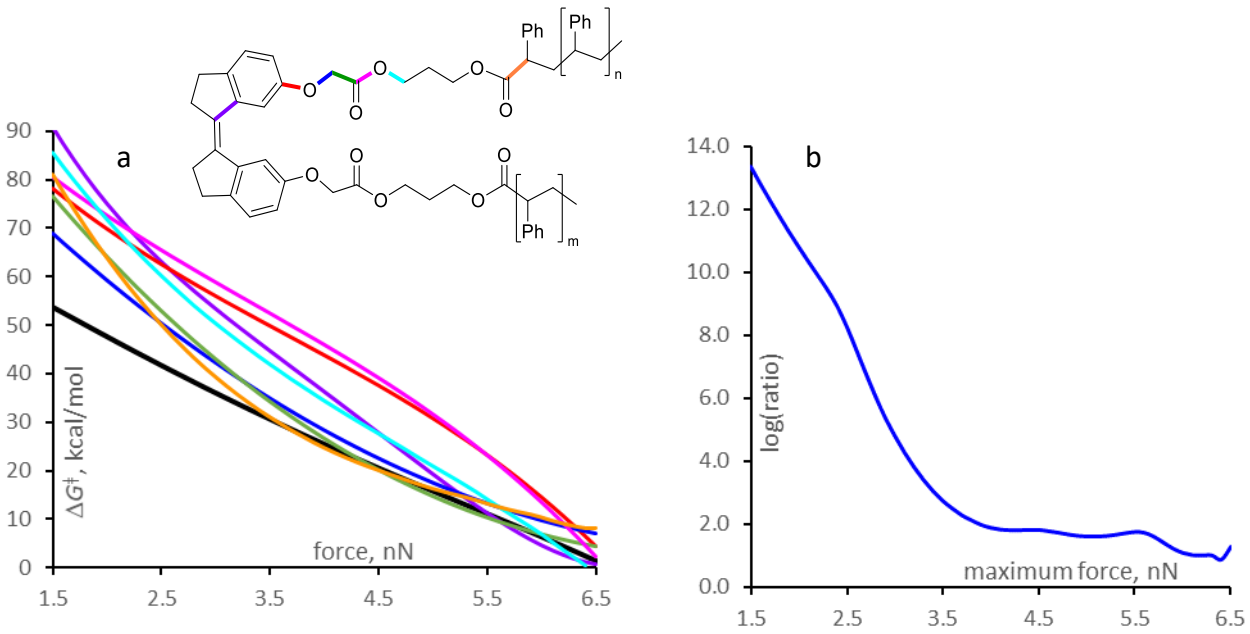

*Figure 22 – **Plausible reactions that may compete with homolysis of C-C bond in PS.** (a) Calculated force-dependent activation free energies, $\Delta G^{\neq}$ for homolysis of the highlighted bonds in polymer used in this study. $\Delta G^{\neq}$ for the primary C-C bonds of the backbone is in black. (b) Semilogarithmic plot of the ratio of the probability of mechanochemical fracture of an overstretched chain of the structure shown in the inset ($\langle n \rangle$=124, $\langle m \rangle$=125) by homolysis of the primary C-C bond to that by dissociation of any other bond. The distribution of SS in the chain was assumed to follow that in **1c** and the distribution of force along the backbone bonds was assumed to be parabolic with the maximum value corresponding to the x axis. To illustrate, the graph shows that, for example, an overstretched chain of DP = 250 with a parabolic force distribution and f_{max} = 5.5 nN is ~120 times more likely to fracture by dissociation of a C-C bond of the styrene repeat unit than by dissociation of any other backbone bond. Note that homolysis of the endocyclic bond of cyclopentane of SS (magenta) doesn't yield chain fracture but is expected to destroy the SS chromophore. The lack of experimental bleaching of SS in sonicated solutions suggests that this reaction is negligible in our polymers.*

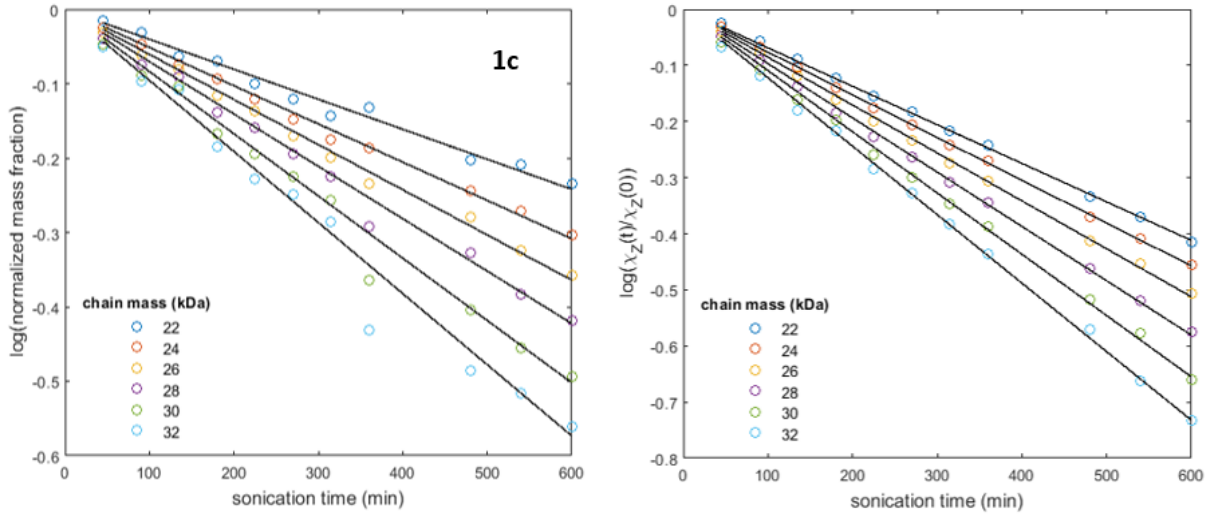

*Figure 23 - **The depletion of chains with masses >0.8M_p manifested unimolecular kinetics.** Semilogarithmic plots used to estimate rate constants for fragmentation of intact chains in **1c** (left*

*column) and isomerization of Z stiff stilbene in intact 1c chains (right column). Solid lines are linear LSFs. All other polymers (**2c-5o**) follow the same pattern.*

Microscopic modelling

The relationship between microscopic conditions and measured bulk compositions of sonicated solutions.

We used a three-step procedure to convert the model parameters of an overstretched chain to the set of time-dependent MMDs and χ_Z for direct comparison with experiment. First, for each unique set of model parameters we calculated the restoring force of each monomer of a chain of desired DP. For the time-invariant implementation of the overstretched-chain model and the overstretched-segment model these force distributions were time-independent. For the constant-loading-rate implementation of the overstretched chain model and the dynamic model, the force distributions change with stretching time, $t_{stretch}$, and were calculated for each timestep of the simulation once f_{max} reached 2.5 nN (at lower f_{max}, Z/E isomerization of stiff stilbene is too slow to be observable making the underlying force distribution experimentally inaccessible). In each case, this procedure generated an *n*x*m* matrix, where n is the number of time steps in our simulations and m is the number of monomers in the chain whose behaviour in the flow is being simulated (for stretched-segment model, m is the number of monomers in the stretched segment only).

Second, we converted the force distribution along an overstretched backbone at each timestep to the corresponding distributions of reaction probabilities (RPDs), $P_{frag}(i, m, t_n)$ and $P_{iso+frag}(i, m, t_n)$: $P_{frag}(i, m, t_n)$ is the probability that the fracture of the overstretched backbone of m monomers by time t_n occurs by dissociation of its i^{th} monomer; $P_{iso+frag}(i, m, t_n)$ is the probability that a backbone of m monomers that fractured by time t_n would have undergone $Z \rightarrow E$ isomerization prior to fracture if its i^{th} monomer contained SS (for $P_{iso+frag}(i, m, t_n)$ the location of chain fracture is irrelevant). Equivalently, $P_{frag}(i, m, t_n)$ defines the stoichiometric coefficient of the fracture reaction of a backbone with *m* monomers at time t_n (e.g., $P_{frag}(i, a+b, t_n) = \gamma_i$ in eqs. 4-5), whereas $P_{iso+frag}$ does the same for fragmentation reaction of Z-SS containing chains only (eq. 4, e.g., $P_{iso+frag}(a, a+b, t_n) = P_{iso+frag}(b, a+b, t_n) = \omega_{a,b}$). The stoichiometric coefficients of a microscopic mechanochemical reaction of an overstretched backbone depend on the reaction extent if the force experienced by individual reactive sites changes on the reaction timescale, which is true for 2 out of 4 models studied. Additionally, we calculated the ratio of the probability of a Z-SS containing chain to isomerize but not fracture, to its probability to fracture by stretching time t_n, $\rho(m, P_{SS}, t_n)$, where P_{SS} is the distribution of SS locations along the reacting chain.

$$PS_a Z_{SS} PS_b \rightarrow (1-\omega_{a,b})\left(\sum_{i=1}^{a}\gamma_i PS_{a-i} Z_{SS} PS_b + \sum_{i=1}^{b}\gamma_i PS_a Z_{SS} PS_{b-i}\right) + \omega_{a,b}\left(\sum_{i=1}^{a}\gamma_i PS_{a-i} E_{SS} PS_b + \sum_{i=1}^{b}\gamma_i PS_a E_{SS} PS_{b-i}\right) + 2\sum_{i=1}^{b}\gamma_i PS_i + \sum_{i=b+1}^{a}\gamma_i PS_i \quad (Eq.4)$$

$$PS_a E_{SS} PS_b \rightarrow \sum_{i=1}^{a}\gamma_i PS_{a-i} E_{SS} PS_b + \sum_{i=1}^{b}\gamma_i PS_a E_{SS} PS_{b-i} + 2\sum_{i=1}^{b}\gamma_i PS_i + \sum_{i=b+1}^{a}\gamma_i PS_i \quad (Eq.5)$$

$$\text{for eqs. 4-5: } \sum_{i=1}^{a+b}\gamma_i = 1 \ and \ \gamma_i = \gamma_{a+b-i}$$

$P_{frag}(i, m, t_n)$, $P_{iso+frag}(i, m, t_n)$ and $\rho(m, P_{SS}, t_n)$ are defined mathematically by eqs. S6-8, where

- $k_{frag}(i, m, t_n)$ and $k_{iso}(i, m, t_n)$ are microscopic unimolecular rate constants at time t_n for monomer i to dissociate or to isomerize (if it's SS), respectively, calculated from the force of this monomer at t_n using $\Delta G^{\ddagger}(f)$ presented in the previous section.
- $S_{iso}(i, m, t_n)$ is the probability that Z-SS at the i^{th} monomer survives up to time t_n, and $S_{frag}(i, m, t_n)$ is the probability that the overstretched segment does NOT fracture by dissociation of i^{th} monomer up to time t_n (eq. S9).
- $PSS(i)$ is the probability that at $t_n=0$, the i^{th} monomer of the chain was Z-SS.
- Δt_j is the size of the j^{th} timestep in our simulation; in general the timesteps we used decreased with t to compensate for increasing k with increasing force so that $\Delta t_j = 0.002/k_{iso}^{max}(t_j)$, where $k_{iso}^{max}(t_j)$ is the largest isomerization rate constant at time t_j; except at stretching times when the minimum of $P_{SS}(i)S_{iso}(i,m,t)$ decreased below 0.2, in which case the smallest Δt_j from either $\Delta t_j = 0.02/k_{iso}^{max}(t_j)$, or $\Delta t_j = 0.002/k_{frag}^{max}(t_j)$ was used.

$$P_{frag}(i,m,t_n) = \frac{1}{1-S_{frag}(i,m,t_n)}\sum_{j=1}^{n}\left(\underbrace{\frac{k_{frag}(i,m,t_j)}{\sum_k^m k_{frag}(k,m,t_j)}}_{\substack{relative\ probability\ of\ i\\ monomer\ being\ the\ site\ of\ chain\\ fracture\ during\ time\ step\ j}} \underbrace{\Delta t_j k_{frag}(i,m,t_j) S_{frag}(i,m,t_{j-1})}_{\substack{probability\ that\ the\ chain\ fractures\\ at\ monomer\ i\ during\ time\ step\ j}}\right) \quad (Eq.6)$$

$$P_{iso+frag}(i,m,t_n) = \frac{1}{1-\prod_{i=1}^{m}S_{frag}(i,m,t_n)}\sum_{j=1}^{n}\left(\underbrace{\left(1-S_{iso}(i,m,t_j)\right)}_{\substack{probability\ of\ monomer\\ i\ to\ isomerize\ by\ time\ t_j\\ in\ intact\ chain}} \underbrace{\Delta t_j \prod_{i=1}^{m} k_{frag}(i,m,t_j) S_{frag}(i,m,t_{j-1})}_{\substack{probability\ that\ the\ chain\ fractures\\ at\ any\ monomer\ during\ time\ step\ j}}\right) \quad (Eq.7)$$

$$\rho(m, P_{SS}, t_n) = \frac{\left(\prod_{i=1}^{m} S_{frag}(i, m, t_n)\right)\left(\sum_{i=1}^{m} P_{SS}(i)\left(1 - S_{iso}(i, m, t_n)\right)\right)}{1 - \prod_{i=1}^{m} S_{frag}(i, m, t_n)} \quad (Eq. 8)$$

$$S_x(i, m, t_n) = \prod_{j=1}^{n}\left(1 - \Delta t_j k_x\left(i, m, t_j\right)\right) \quad (Eq. 9)$$

In Eq. 8 $\prod_{i=1}^{m} S_{frag}(i, m, t_n)$ is the probability that the overstretched backbone of *m* monomers survives up to stretching time t_n; its value asymptotically approaches 0 as *t* increases. For time-invariant force distributions, the fragmentation probabilities of individual monomers, $P_{frag}(i, m, t)$, follow a similar pattern of an asymptotic increase with *t*, to the value dependent on DP, *i* and the force distribution but is always <<1 (because an overstretched chain can break by homolysis of many backbone bonds). For time-dependent force distributions, $P_{frag}(i, m,$ t) would broadly mirror changes in the force distribution and may depend on time non-monotonically, despite the total probability of chain fracture increasing to unity. Conversely, $P_{iso+frag}(i, m, t)$ can either be 0 (if PSS(*i*)=0), or increase monotonically with *t* to a maximum value of 1 corresponding to no *Z*-SS at monomer *i* surviving chain fracture. Finally, for a chain of any DP, regardless of how the force and *Z*-SS are distributed along it $\rho(m, P_{SS}, t)$ decreases with *t* from close to infinity at stretching times that are too short for chains to fragment at any appreciable extent ($\prod_{i=1}^{m} S_{frag}(i, m, t) = 1$) to 0 at long stretching times when the fragmentation probability of the chain approaches 1, even if some *Z*-SS survive fragmentation.

Third, we developed a general approach of converting reaction probability distributions (RPDs), regardless of how they were derived, to time-dependent compositions of the sonicated solutions. RPDs, exemplified by Eqs. 6-7, define product selectivities of mechanochemical reactions happening in sonicated solutions but not the rates of changes in the bulk compositions (i.e., they are stoichiometric coefficients of the bulk reactions, e.g., Eqs. 4-5) because Eqs. 6-9 only apply to overstretched chains, whereas the bulk rates measured experimentally also include probabilities of each chain to become overstretched. The latter, which necessitates macroscopic modeling of a sonicated solution, was not the goal of the current study. Consequently, to convert RPDs to time-depended bulk compositions for comparison with experiment we used experimentally measured bulk fragmentation rate as described below.

The macroscopic kinetics of SS isomerization in intact chains and of chain fracture are independent (i.e., mathematically, the measured bulk rate constant of fragmentation is unaffected by the measured bulk rate constant of isomerization in intact chains; at the microscopic level the two reactions result from the same physical process, which explains why the two sets of macroscopic rate constants are empirically correlated, Fig. 2d). Consequently, our simulations of the bulk compositions of sonicated solutions treated SS isomerization in

intact chains differently from chain fracture (with or without isomerization). The time-dependent fraction of intact chains containing *E*-SS was determined analytically using the rate constants defined by Eq. 10:

$$k_{iso}^{sim}(m, P_{SS}) = k_f^{fit}(m)\langle\rho(m, P_{SS})\rangle \quad (Eq. 10)$$

Where $k_f^{fit}(m)$ is the unimolecular bulk rate constant for depletion of a chain of DP = m obtained by fitting the experimental k_f vs. mass correlations (Fig. 2c, main text), $\langle\rangle$ signify sample-averaging over all sets of microscopic parameters that contribute to the mechanochemical reactivity of chains of the same mass and SS distribution.

Conversely, modeling the evolution of mass-dependent fractions of Z-SS, χ_Z, requires numerical propagation of a system of coupled linear differential equations for Eq. 4-5 (and the equivalent fragmentation of SS-free fragments). Because each reaction yields multiple products and each component is generated by multiple reactions, the overall kinetics cannot be expressed as close-form integrals.

The number of chains of each DP that fracture over a finite timestep Δt is determined by a set of $k_f^{fit}(DP)$ constants (represented below as an $(DP_{max}-1)$x1 vector, **K**, such that $K(j)=k_f^{fit}(j+1)$, DP_{max} is the DP of the largest chain in the intact sample). The product mixtures generated by depletion of these chains are described by Eqs. 4-5 (plus the fragmentation of SS-free chains), with each equation's contribution determined by the fraction of the corresponding reactant chain in the reactant mix consumed during Δt. Consequently, our modeling of the bulk composition of sonication solutions of polymers **1c**-**4c** and **1o**-**5o** required systematic application of Eqs. 4-5 to every component of the sonicated mixture at every timestep of the simulation. The stoichiometric coefficients in Eqs. 4-5 are defined by suitably averaged distributions of microscopic reaction probabilities along the overstretched segment/chain for each component of the reaction mixture. Whereas fragmentation and fragmentation–coupled isomerization RPDs are independent of the bulk composition of the solution, isomerisation/fragmentation selectivities, ρ, depend on the distribution of Z-SS in the intact chains, which changes with sonication time. Within the dynamic model, the sample-average selectivity $\langle\rho\rangle$ for **1c** decreases by 7% across the sonication timescale, which is too little to affect the accuracy of the simulated χ_Z; **1c** has the largest k_i/k_f ratio, so for all other samples, the error is even smaller. The Matlab code for converting an arbitrary set of mass-dependent distributions of microscopic reaction probabilities along chains into bulk compositions using this approach is provided below.

If only the evolution of the mass distribution is of interest, it can be simulated much more efficiently using Eq. 11 which describes the number of chains of each DP in a sonicated solution at time step i+1, $\mathbf{CD}_{i+1}$:

$$\mathbf{CD}_{i+1} = [\mathbf{P}(\mathbf{CD}_i(2{:}DP_{max}) \circ \mathbf{K})\Delta t; 0] - [0;\ \mathbf{CD}_i(2{:}DP_{max}) \circ (1 - \mathbf{K}\Delta t)] \quad (Eq.11)$$

Where $\mathbf{CD}_i$ is an m_{max}x1 vector of the number of chains with DP from 1 to DP_{max} (DP_{max} is the largest chain of the intact sonicated sample), P is an (m-1)x(m-1) upper triangular matrix of the normalized sample-average distributions of fragmentation probabilities along the backbone of chains with DP from 2 to DP_{max} (eq. S6); Δt is the timestep of the simulation (such that $K(DP_{max})\Delta t < 0.002$, although larger timesteps can be used to reduce the computation time at the expense of accuracy of compositions) and $\circ$ is the element-wise (Hadamard) multiplication. Note that $\sum_{i=1}^{j} \mathbf{P}(i,j) = 2$ for any j because each chain fracture produces two chains; as a result, the number of chains in the solution grows during sonication (the mass balance is preserved because smaller chains have fewer monomers, i.e., $(1{:}\ DP_{max})\mathbf{CD}_i$ = constant for any *i*)

$$\mathbf{P}(i,j) = \begin{cases} 0 \ \ if\ i > j \\ \langle P_{frag}(i,j) \rangle \ \ if\ i \leq j \end{cases} \qquad (S11) \qquad and \ \sum_{i=1}^{j} \mathbf{P}(i,j) = 2 \quad (Eq.12)$$

Expressing observed changes in the composition of a sonicated solution in terms of sample-averaged distributions of weighted-sums of microscopic reaction probabilities along the polymer backbone (sRPDs) instead of the microscopic parameters that control chain overstretching offers both conceptual and practical advantages. An example of the former is decoupling of the experimental timescales from the timescales at which individual overstretched chains react. An example of the latter is the computational efficiency which exploits the fact that for any model of chain overstretching considered here, generating an sRPD from any combination of model parameters is orders of magnitude less computationally intensive than converting an sRPD to the bulk composition at any sonication time. Thus, if the sRPDs corresponding to the measured bulk compositions are known, finding model parameters that would generate such sRPDs is fairly simple.

Whereas generating MMDs and mass-dependent χ_Z from any pair of fragmentation/isomerization sRPDs is conceptually and technically straightforward (if computationally demanding), the inverse transformation of experimental MMDs and χ_Z to the underlying sRPDs remains unknown. Consequently, the greatest challenge in parameterizing a model is to guess the underlying sRPDs, confirm that they indeed reproduce the experimental results and then identify model parameters that reproduce these RPDs as closely as the model allows.

Parameterization of the models

A parameterized model has at least a single set of model parameters that reproduces the observed changes in MMDs and χ_Z as closely as the model allows, while satisfying 3 general criteria:

1. A model parameter can either be chain-size invariant or change with chain-size monotonically; the dependence on the position along the chain backbone, if it exists, should be unimodal (i.e., to display no more than a single maximum or minimum, which need not coincide with the chain centre).
2. All chains of the same size experience the same microscopic conditions, regardless of the presence of SS or its location.
3. The observed macroscopic response likely reflects a complex combination of microscopic conditions, requiring a weighted-average of multiple sets of model parameters for chain of each size.

Overstretched-chain model: time-independent force distributions.

In the standard model every monomer of an overstretched chain is under force, which is at the maximum at the chain centre, f_{max}, and decreases to 0 at the chain termini quadratically with the fractional distances from the chain centre. The reactivity of the overstretched chain is governed by two model parameters: f_{max} and how long the chain is maintained in the overstretched state, $t_{stretch}$. Consequently, we calculated matrixes $\mathbf{P}_{frag}(DP)$ and $\mathbf{P}_{iso+frag}(DP)$ of time-dependent distributions of microscopic reaction probabilities (Eqs. 6-7 define individual elements of these matrixes) corresponding to f_{max} of 4.8, 5.2, 5.5, 5.6, 5.7, 5.8, 5.9 and 6.0 nN for chains of DP = 100, 250, 500, 750, 1250, and 2000 (a total of 48 f_{max}/DP combinations). For each such combination the longest stretching time, t_{max}, was chose to be 5 μs or the time needed to reduce the survival probability of the chain against fragmentation to 0.001, whichever time is shorter. For each DP we identified pairs of f_{max}/t parameters that produced unique combinations of the pairs of fragmentation/isomerization reaction probability distributions (RPDs). We considered any two RPDs of the same type (fragmentation or isomerization) distinct if their FWHH varied by at least 0.01DP, rounded to the closest integer (all distributions are centreed in this model). The reason is that identical RPDs yield identical simulated MMDs and χ_Z, regardless of the underlying model parameters. For each unique pair of fragmentation/isomerization RPDs we also calculated isomerization/fragmentation selectivities, $\rho(DP, P_{SS})$, for three generic P_{SS} distributions (P^{c}_{SS}, P^{o1}_{SS}, P^{o2}_{SS}), obtained by averaging SS distributions in **1c**-**4c** (P^{c}_{SS}), in **1o**/**3o** (P^{o1}_{SS}) and in **2o**/**4o** (P^{o2}_{SS}). Some identical RPD pairs yielded slightly different $\rho(DP, P_{SS})$ values: the maximum variation was 6% for the

centred SS distribution and 3.5% for off-centre distributions, which we ignored in initial parameterization.

In theory, the simplest strategy of parameterizing a model is to fit measured χ_Z of each **1c**-**4c**, **1o**-**5o** individually and then use suitable regression of the resulting [f_{max}, $t_{stretch}$] pairs with respect to chain DP to define parameters that satisfy the 3 criteria above. This approach is however unsuitable for the standard model because such [f_{max}, $t_{stretch}$] pairs are so sensitive to the location of SS in the sample (Figure 19a-b) that fitting them to a single DP-dependence yields much poorer agreement with the experiment that an iterative 4 step procedure:

1. Estimate chain-size dependence of f_{max} and $t_{stretch}$ that best fits the experimental data.
2. Convert these estimated f_{max}(DP) and $t_{stretch}$(DP) correlations to corresponding RPDs and systematically adjust these RPDs to reproduce experimental χ_Z with the minimal total residual (fragmentation RPDs were largely insensitive to f_{max} and $t_{stretch}$, making MMDs useless for model parameterization).
3. Identify the pairs of [f_{max}, $t_{stretch}$] values corresponding to the optimized RPDs and fit them to single f_{max}(DP) and $t_{stretch}$(DP) functions.
4. Calculate the final set of RPDs corresponding to these functions.

We estimated size-dependence of f_{max} and $t_{stretch}$ by first simulating measured χ_Z for **1c**-**3c**, **2o**-**4o** under the assumption that within each sample, the mechanochemical reactivity was independent of the chain size and thus captured by a single pair of fragmentation/isomerization RPDs of the DP of 250 (**1c**), 500 (**2c**, **2o**), 750 (**3c**, **3o**) and 1250 (**4o**) using the appropriate P_{SS} distributions (P^{c}_{SS} for **1c**-**3c**, P^{o1}_{SS} for **3o** and P^{o2}_{SS} for **2o**/**4o**). We simulated each χ_Z for every RPD of the corresponding DP whose ρ(DP, P^{c}_{SS}) values were below 2.2, 1, 0.7 and 0.6 for DP = 250, 500, 750 and 1250; the reason for this cutoff was that at higher ρ values, *Z*/*E* isomerization in intact chains with centrally-positioned SS was unacceptably fast. In addition, for every RPD with ρ(DP, P^{c}_{SS}) below we also calculated χ_Z using $k_{iso}^{sim}(DP, P_{SS})$ defined by Eq. 13 (instead of Eq. 10, which underestimated the rate of isomerization of intact chains for ρ(DP, P^{c}_{SS}) below the above thresholds), where ξ(DP) is a fitting parameter that gives the desired rate of isomerization of intact chains. Eq. 13 describes a scenario of the bulk macroscopic response arising from at least two subpopulations of chains of each DP, one in which a fraction of the overstretched chains fractures by the time the load dissipates, and the other in which some overstretched chain isomerise, but none fractures. The former accounts for ξ(DP) fraction of the mechanochemically reacting chains and is characterised by microscopic parameters f_{max} and $t_{stretch}$ and microscopic isomerisation/fragmentation selectivity of ρ. The latter accounts for 1-ξ(DP) fraction of the reacting chains and corresponds to any combination of f_{max} and *t* for which

$\prod_{i=1}^{DP} S_{frag}(i, DP, t) \geq 0.9999$ but $\sum_{i=1}^{m} P_{SS}(i)\left(1 - S_{iso}(i, DP, t)\right) < 0.9$. Because an infinite number of f_{max}/t combinations satisfy these conditions, the values of f_{max}/t for the isomerization-only subpopulations cannot be specified.

$$k_{iso}^{sim}(DP, P_{SS}) = k_f^{fit}(DP)\left(\rho(DP, P_{SS}) + \left(1 + \rho(DP, P_{SS})\right)\left(\frac{1}{\xi(DP)} - 1\right)\right) \quad (Eq. 13)$$

Second, we calculated the norms of the residuals between each calculated χ_Z and its corresponding measured χ_Z, scaled by the corresponding DP. From this dataset we estimated the likely monotonic dependences of f_{max}, $t_{stretch}$ and ξ on DP that best reproduce the experimental data within the standard model, while complying with the 3 criteria articulated above. Third, we converted these dependences to RPDs at DP = 100, 250, 500, 750, 1250, 2000 and 3000, which served as the initial-guess RPDs for subsequent LSFs of multiple sets of experimental χ_Z simultaneously. Note that although all RPDs are initially calculated as functions of the number of monomers from a chain terminus (the *i* variable in Eqs. 6-7), for all simulations of the experimental data that assume chain-size dependent reactivities, all RPDs are expressed in terms of fractional distances. A pair of such fractional–distance RPDs for 2 chains of different DPs can be used to estimate RPDs of a chain of any intermediate DP by interpolation.

We further optimized these monotonically DP-dependent isomerization RPDs by simultaneous non-linear LSF to a combination of experimental χ_Z using the ga function of Matlab. In these optimizations each guess RPD, and the corresponding ξ guess were scaled by a factor, which were varied systematically to minimize the total residual; the range within each fitting scaling factor was allowed to vary was conditionally bound to ensure monotonic DP-scaling of the optimizing RPDs. Fracture RPDs were assumed to be DP- independent, and chains of each DP were assigned their own isomerization RPD, obtained by linearly interpolating pairs of the optimizing isomerization RPDs (isomerization RPD for DP = 100 was used for chains with DP<100). Isomerization RPDs for DPs up to 1250 were optimized against experimental χ_Z for **1c**-**3c** + **1o**-**3o** starting with initial-guess RPDs at DP = 100, 250, 500, 750 and 1250, and using 10 fitting parameters (5 for RPDs and 5 for corresponding ξ). Next, we used these converged isomerization RPDs and the corresponding ξ values, to optimize isomerization RPDs at DP=1250-2200 by applying the same procedure to a set of experimental χ_Z for **3c** + **3o**-**4o**, with initial-guess RPDs at DP = 1250 and 2000 (and the corresponding ξ guesses) and 4 fitting parameters (two for RPDs at 1250 and 2000 and two for ξ at the same DPs). RPDs and ξ at DP between 2200 and 3000 were assumed to scale with DP with the same coefficients as those for optimized RPDs at DP 1250 and 2000. Breaking the full complement of experimental χ_Z was necessary to make LSFs computationally feasible: fitting the complete

dataset of experimental χ_Z simultaneously would have required at least 3 weeks of continuous calculations with >600 Gb of RAM, a level of computational resources that was not available to us.

We then found all [f_{max}, $t_{stretch}$] combinations corresponding to the optimized RPDs at DP of 100, 250, 500, 750, 1250, 2000 and 3000 by interpolating the set of unique RPDs calculated for the 48 f_{max}/DP combinations described in the opening paragraph of this section and selecting for each DP a single [f_{max}, $t_{stretch}$] pair that most closely followed a smooth monotonic function on DP. The final set of pairs of [f_{max}, $t_{stretch}$] (Figure 24) was obtained by moving averaging of interpolated f_{max} and $t_{stretch}$ to values at DPs from 100 to 3000 in increments of 50. The final set of RPDs (Figure 25) and the corresponding predicted MMDs and χ_Z (Figure 26) were calculated from these smoothed [f_{max}, $t_{stretch}$] pairs using the standard procedure.

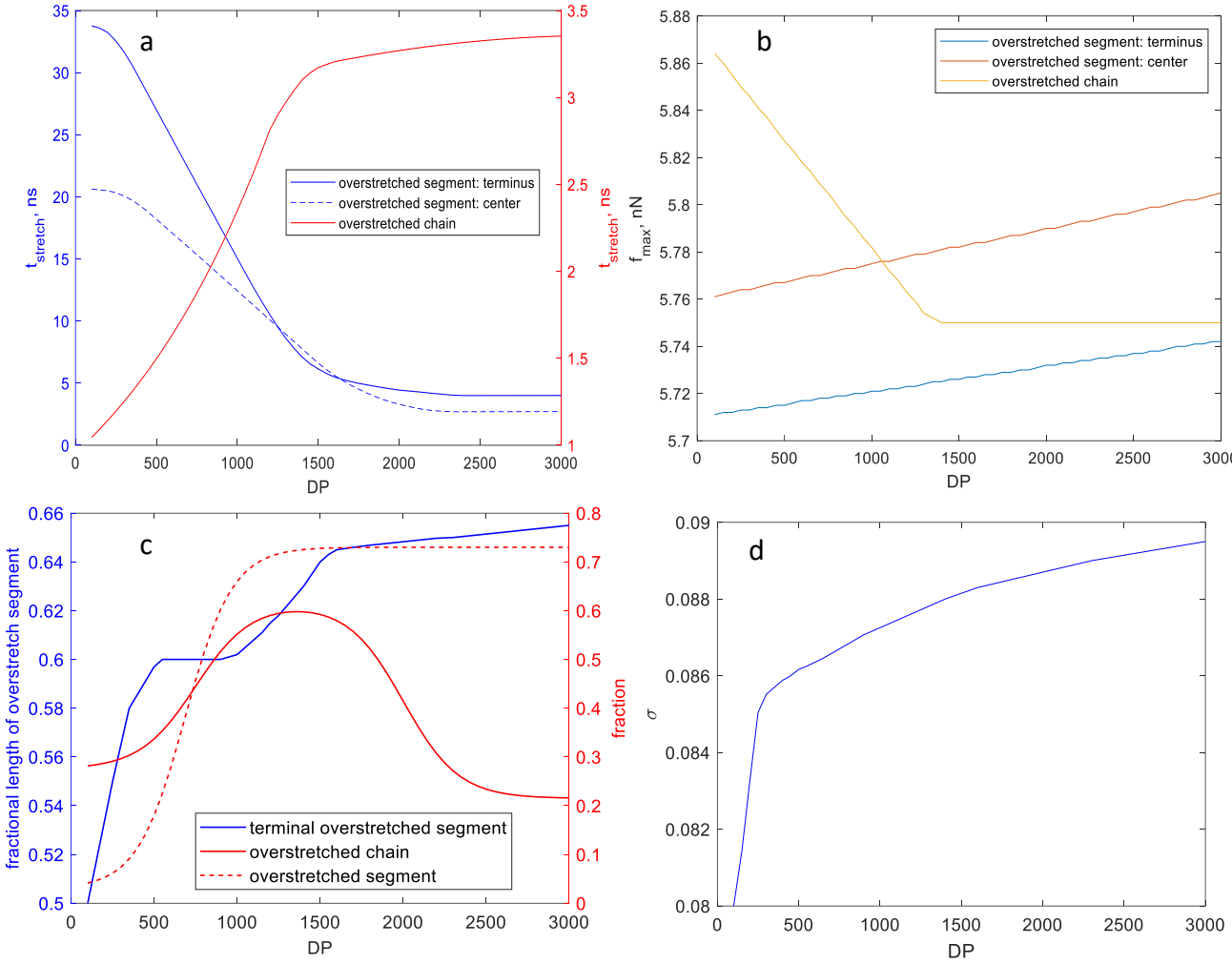

Figure 24 – DP-dependent parameters of the 2 reported models: overstretched-chain and time-independent overstretched segment: (a) $t_{stretch}$; (b) f_{max}; (c) the fractions of mechanochemically reacting chains that experience the microscopic conditions shown, ξ (Eq. 13) (red) and (overstretched segment only) fractional length of the overstretched segment at the terminus (blue; the fractional length of the

overstretched segment centreed at the chain centre was 0.5 at all DPs) and; (d) for the overstretched segment only: standard deviation of the Gaussian probability of each monomer to be at the centre of the overstretched segment, σ, Eqs. 14-16.

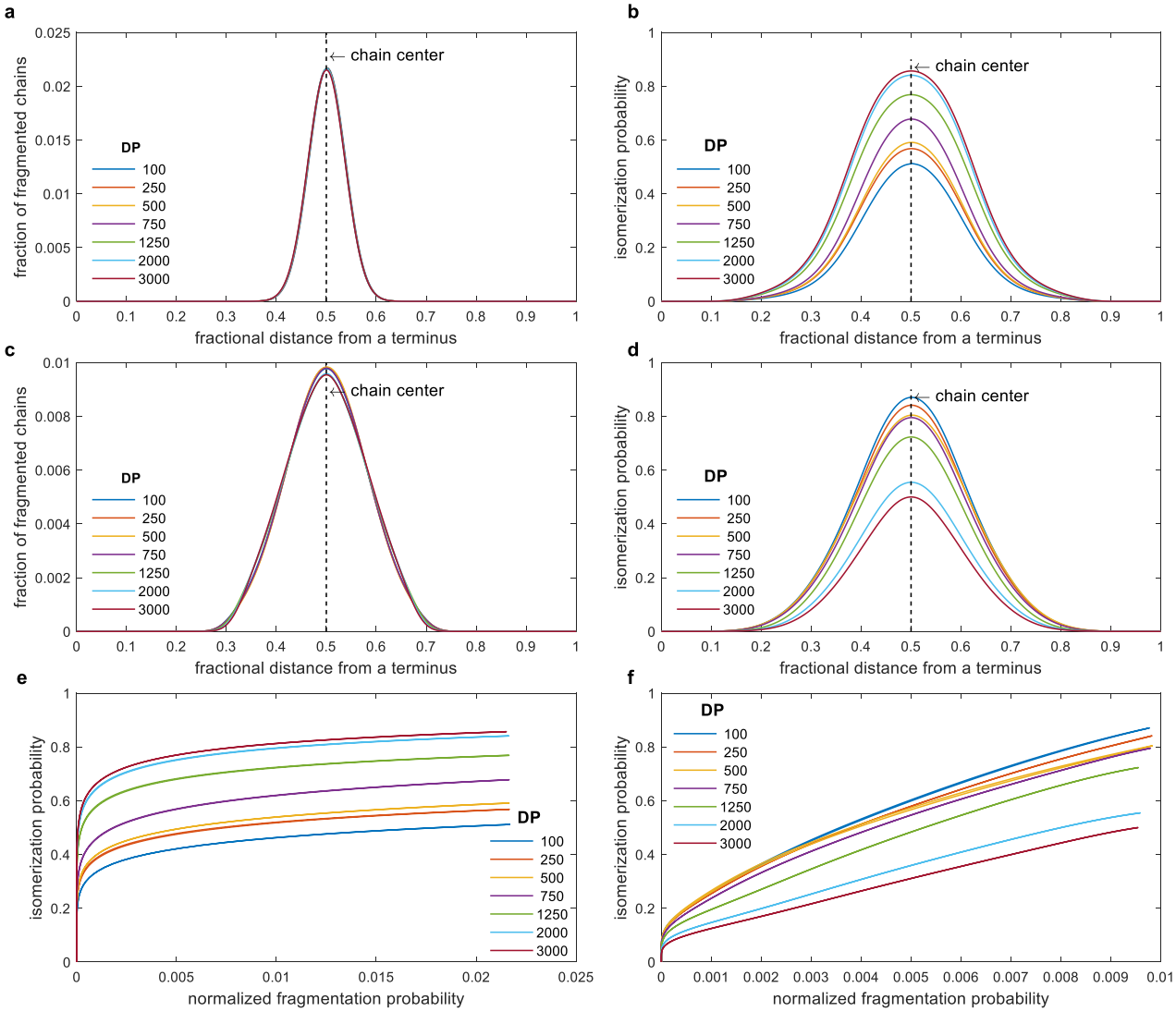

Figure 25 – *Discrete sample-average reaction probability distributions from the standard models; (a-b) overstretched chain; (c-d) overstretched segment; (a,c) normalized fragmentation probabilities; (b,d) fragmentation-coupled isomerization probabilities; (e-f) correlation between distributions of isomerization and fragmentation probabilities. For the overstretched-chain model, sample-average and single-chain (or microscopic) RPDs are identical, whereas for the overstretched-segment model, the sample-average RPDs are weighted averages of single-chain (microscopic) RPDs (eq. 14). The bin size is 0.002.*

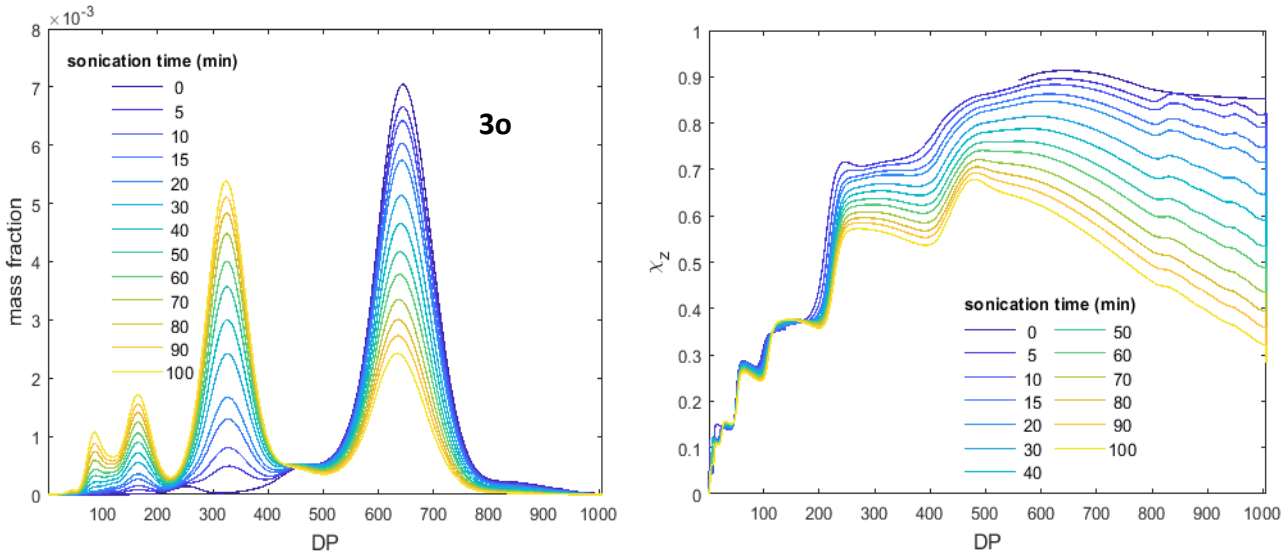

*Figure 26 – The evolution of MMDs and chain-size dependent χ_Z in sonicated solutions of **3o** predicted by the overstretched-chain model parameterized against the experimental measurements.*

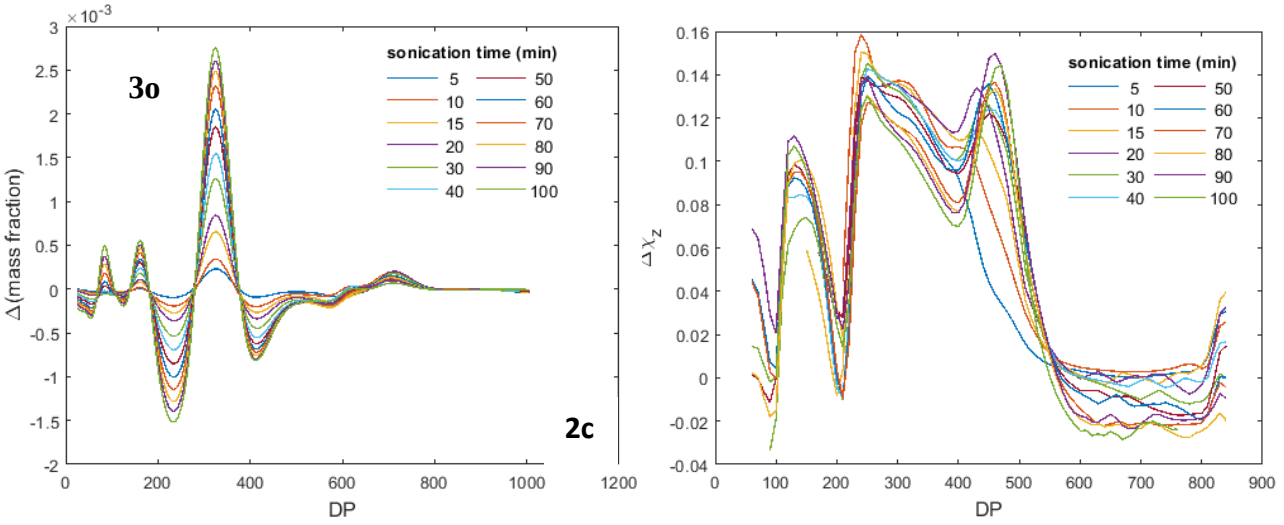

Figure 27 – The difference between observed MMDs and χ_Z and those predicted by the overstretched chain model.

Overstretched-chain model: time-independent loading rate distribution.

We calculated fragmentation and isomerization RPDs for chains with DP = 250, 500, 750, 1250, 2000, following the procedure described above for maximum loading rates, υ_{max}, of 5, 2, 1 mN/s, 0.05, 0.02, 0.01, 0.8, 0.5, 0.2, 0.1, 1, 2, 3, 3.5, 4, 4.5, 5, 5.5 and 6 N/s until either the total survival probabilities of each chain decreased to 0.001, or for 5 μs, whichever is shorter. For all values of DP and υ_{max}, the loading rate of monomers away from the centre decreased quadratically with the fractional distance between the monomer and the chain centre. We then identified unique RPDs from this set and compared them to unique RPDs calculated for the time-independent force distributions. The lack of any new RPDs in this set suggested to us that the MMDs and χ_Z calculated above represent the best achievable agreement with the experiment for fully overstretched chains.

Overstretched-segment model.

In this model, each reacting chain is characterized by at least 4 chain-size dependent parameters: f_{max}, $t_{stretch}$, DP_{os} (the number of monomers in the overstretched segment) and σ (the standard deviation of the normal distribution of probabilities of each monomer to be at the centre of the overstretched segment, $P_{centre}(i)$). We approximated $P_{centre}(i)$ by a Gaussian function because of its computational flexibility, which allowed diverse distributions, from nearly uniform (a stretched segment is equally likely to be centred at any position along the chain that is removed from the terminus by half the segment width) to nearly δ-function (the centre of the stretched segment coincides with the chain centre) to be generated and tested by varying a single parameter (σ). Within each overstretched segment, the force decreased quadratically with the fractional distance from the segment centre to 0 at segment termini.

In this and the dynamic model discussed below, RPDs describing the reactivity of a single randomly selected chain (microscopic RPDs, or μRPDs) are distinct from RPDs that underlie the observed changes in the bulk composition (sample RPDs, or sRPDs). The latter are sums of the former weighted by the probability of each μRPD to occur in the bulk sample. For example, the relative sample-average probability of a dissolved chain of m monomers to fragment by dissociation of its i^{th} monomer (as opposed to by dissociation of any other monomer), $sP_{frag}(i,m)$, is given, in the simplest case of the length of the overstretched segment, DP_{os}, being independent of the location of this segment along the chain, by Eq. 14, where $\mu P_{frag}(i\text{-}j+ DP_{os}/2, DP_{os})$ is the probability that the chain with an overstretched segment of the length DP_{os} centred at j^{th} monomer fragments at the location $i\text{-}j+ DP_{os}/2$ monomers from the edge of the overstretched segment, which is i^{th} monomer of the whole chain (see Eqs. 6-7 for the mathematical definitions of μRPD elements, $P_x(i,m)$).

$$sP_{frag}(i,m) = \frac{\sum_{j=\frac{DP_{os}}{2}}^{\frac{m}{2}} P_{frag}\left(i-j+\frac{DP_{os}}{2}, DP_{os}\right) e^{-\frac{\left(j-\frac{m}{2}\right)^2}{\sigma}}}{\sum_{j=\frac{DP_{os}}{2}}^{\frac{m}{2}} e^{-\frac{\left(j-\frac{m}{2}\right)^2}{\sigma}}} \quad (Eq.\,14)$$

To parameterize this model, we fist calculated time-dependent microscopic fragmentation and isomerization μRPDs for f_{max} of 5.2, 5.5, 5.6, 5.7, 5.8 nN for DPs between 25 and 1400 (corresponding to overstretched segments of 0.1, 0.2, 0.3, 0.4, 0.5 and 0.7 of the size of the full chain with DP = 250, 500, 750, 1250, and 2000), for a total of 150 f_{max}/DP combinations. Only μRPDs corresponding to $t_{stretch}$ in the following limits were retained: the shortest $t_{stretch}$ was when the total fragmentation survival probability of the segment reached 0.999 ($\prod_{i=1}^{DP} S_{frag}(i, DP, t_{min}) = 0.999$) and the longest was either 5 μs or satisfied the condition

$\prod_{i=1}^{DP} S_{frag}(i, DP, t_{max}) = 0.001$, whichever is shorter. For each DP, we selected all unique pairs of fragmentation/isomerization RPDs, as defined above.

We generated the initial guess of DP dependences of the model parameters by fitting observed MMDs under the assumption that each sample-specific set of observed MMDs can be reproduced with a single DP-independent fragmentation sRDP. These sRDPs were combinations of μRPDs (e.g., Eqs. 14-16) corresponding to DP_{os} of 25 – 175 for **1c**; 50 – 350 for **1o** and **2c**; 75 – 525 for **2o**, **3o** and **3c**; 125 – 875 for **4o**; 200 – 1400 for **4c** and **5o**. Because simulating MMDs alone, using Eq. 10, is 100 – 10^5 times faster than simulating corresponding χ_Z for the same sample, and for each experimental sample we had to consider <50 unique fragmentation μRPDs (which includes all tested fractional segment lengths), we could test three physical scenarios that define the relationships between microscopic and sample-average RPDs. The first scenario postulated that the microscopic parameters (f_{max}, $t_{stretch}$ and DP_{os}) were independent of the location of the overstretched segment along the chain backbone, i.e., each sRPD was made of a single μRPD (Eq. 14). In the second, the microscopic parameters (f_{max}, $t_{stretch}$ and DP_{os}) varied linearly with the distance between the centre of the overstretched segment and the chain centre; this dependence is defined by a pair of μRPDs, corresponding to the overstretched segment at the terminus (P^{term}_{frag}) and at the centre (P^{centre}_{frag}, eq. 15) and their length, DP_{os} and $DP_{os}{}^{centre}$. In the third, the sample average fragmentation probability distribution, sRPD represented two subpopulations of fragmenting chains, with relative chain fraction of ϕ and 1-ϕ, each subpopulation being characterized by its own location-independent μRPD, DP_{os} and σ (Eq. 16).

$$sP_{frag}(i,m) = \frac{1}{\sum_{j=\frac{DP_{os}}{2}}^{\frac{m}{2}} e^{-\frac{\left(j-\frac{m}{2}\right)^2}{\sigma}}} \sum_{j=\frac{DP_{os}}{2}}^{\frac{m}{2}} \left(2\frac{P_{frag}^{term}(i-DP_{os}, DP_{os}) - P_{frag}^{centre}\left(i-\frac{m}{2}+\frac{DP_{os}^{centre}}{2}, DP_{os}^{centre}\right)}{DP_{os}-m} j + \frac{m \times P_{frag}^{term}(i-DP_{os}, DP_{os}) - DP_{os} \times P_{frag}^{centre}\left(i-\frac{m}{2}+\frac{DP_{os}^{centre}}{2}, DP_{os}^{centre}\right)}{DP_{os}-m} \right) e^{-\frac{\left(j-\frac{m}{2}\right)^2}{\sigma}} \quad (Eq.\,15)$$

$$sP_{frag}(i,m) = \phi \frac{\sum_{j=\frac{DP_{os}}{2}}^{\frac{m}{2}} P_{frag}\left(i-j+\frac{DP_{os}}{2}, DP_{os}\right) e^{-\frac{\left(j-\frac{m}{2}\right)^2}{\sigma}}}{\sum_{j=\frac{DP_{os}}{2}}^{\frac{m}{2}} e^{-\frac{\left(j-\frac{m}{2}\right)^2}{\sigma}}} + (1-\phi) \frac{\sum_{j=\frac{DP'_{os}}{2}}^{\frac{m}{2}} P'_{frag}\left(i-j+\frac{DP'_{os}}{2}, DP'_{os}\right) e^{-\frac{\left(j-\frac{m}{2}\right)^2}{\sigma'}}}{\sum_{j=\frac{DP'_{os}}{2}}^{\frac{m}{2}} e^{-\frac{\left(j-\frac{m}{2}\right)^2}{\sigma'}}} \quad (Eq.16)$$

For each set of experimental MMDs we parameterized Eqs. 14-16 for all respective unique µRPDs (scenario 1), or all pairwise combinations of unique µRPDs (scenarios 2-3) by non-linear LSFs. This yielded, for each experimental sample, a set of fragmentation sRPDs together with their constituent microscopic parameters (single µRPD + σ for scenario 1; a pair of µRPDs + σ for scenario 2 and a pair of µRPDs + σ, σ' and ϕ for scenario 3), and a measure of how accurately each sRPD reproduced the corresponding experimental MMDs (norms of the residuals). For all fragmentation sRPDs with norms of residuals within 1.1 times that of the respective minima we calculated corresponding isomerization sRPDs and sample-average isomerization/fragmentation selectivities, $\langle\rho\rangle$. Because all these $\langle\rho\rangle$ were below experimental k_i/k_f ratios (i.e., all sRPDs that best reproduced experimental MMDs also considerably underestimated the measured rates of isomerization of intact chains) for each pair of fragmentation/isomerization sRPD we performed non-linear LSF against experimental χ_Z for **1c**, **1o**, **2o**, **3c** and **3o** to estimate corresponding ξ (Eq. 13), the fractional size of a subpopulation of overstretched chains that contribute to isomerization of intact chains without any contribution to chain fracture. These LSFs yielded norms of the residuals of the corresponding isomerisation sRPDs. For samples **4c**, **4o**-**5o**, the analogous residuals were calculated from simulated χ_Z using experimental k_i/k_f ratios (Fig. 2, main text) to account for the isomerization kinetics of intact chain, irrespective of the underlying isomerization RPDs and their $\langle\rho\rangle$ values. The values of ξ corresponding to these norms were obtained by Eq. 17, where $(k_i/k_f)_{exp}$ is the experimental k_i/k_f ratio for each sample (**4c**, **4o**, or **5o**) at the corresponding DP (2000 for **4c** and **5o** and 1250 for **4o**) and $\langle\rangle$ signifies sample averaging.

$$\langle\xi(DP)\rangle = \left(\frac{\left(\frac{k_i}{k_f}\right)_{exp} - \langle\rho(DP, P_{SS})\rangle}{\langle\rho(DP, P_{SS})\rangle + 1} + 1 \right)^{-1} \quad (Eq.17)$$

This procedure yielded a discretized set of correlations between norms of the residuals, sRPDs and the corresponding sample-averaged ξ. We used the same procedure described for the overstretched chain model to estimate a sequence of monotonically DP-dependent sRPDs and ξ that most accurately reproduce the whole complement of experimental χ_Z; sRPDs obtained with the 2nd scenario (microscopic conditions vary linearly with the location of the overstretched segment along the chain backbone) gave the lowest estimated total norm of residual. Consequently, all subsequent computations were limited to only these sRPDs. Again using the procedure described above, we refined these DP-dependent isomerization sRPDs and corresponding ξ by LSFs using the corresponding fragmentation sRPDs and σ(DP) estimated from the fit of MMDs.

The final set of sRPDs is shown in Figure 25, the corresponding time-lapsed MMDs and χ_Z in Figure 28 and DP-dependent model parameters (f_{max} and $t_{stretch}$ for the overstretched segment at the terminus and at the centre; fractional length of the overstretched segment, DP_{os}/DP, at the terminus and the standard deviation of the Gaussian distribution of the probabilities of each monomer to be at the centre of the overstretched segment, σ) in Figure 24d.

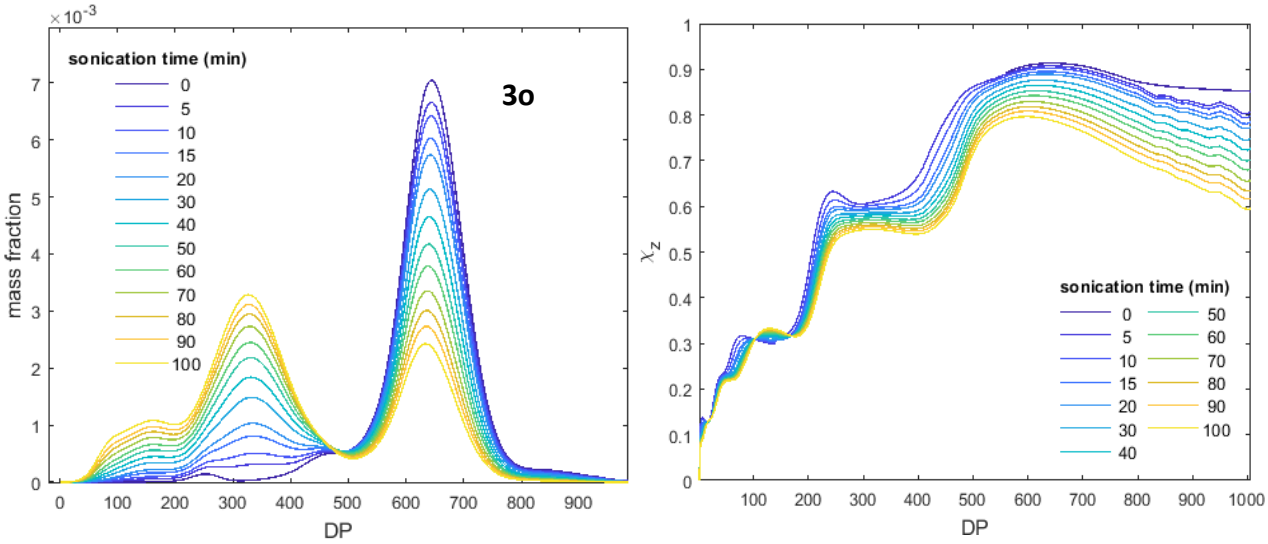

*Figure 28 – The evolution of MMDs and chain-size dependent χ_Z in sonicated solutions of **1c**-**5o** predicted by the overstretched-segment model parameterized against the experimental measurements.*

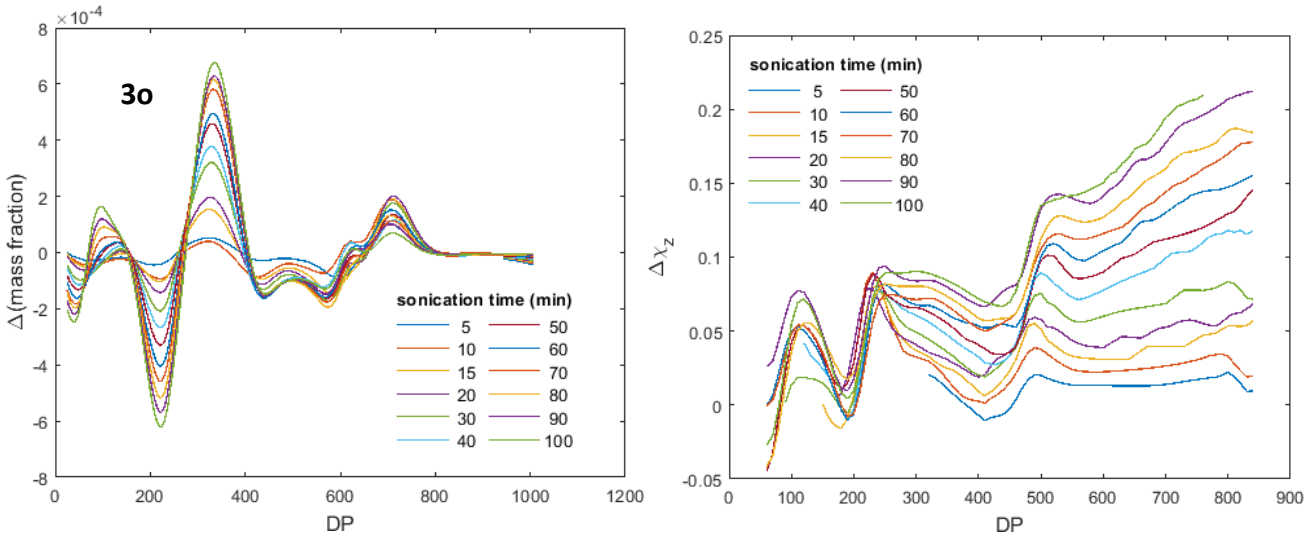

Figure 29 – The difference between observed MMDs and χ_z and those predicted by the overstretched-segment model.

Dynamic model.

In this model, each reacting chain is characterised by at least 5 chain-size dependent parameters: $t_{stretch}$, k_s, k_d, α and β. The last 4 parameters define the fractional length of the overstretched segment at stretching time *t*, λ_{os}; its fractional distance from a chain terminus to its centre and its maximum force (Eqs. 18-S0, expressing f_{max} as a function of the fractional length of the overstretched segment, instead of the absolute length as in the main text simplifies computations by minimizing variations of α and β with DP).

$$\lambda_{os} = \left(1 - e^{-k_s t}\right) \quad (Eq.18)$$

$$\delta_{os} = \frac{1 - e^{-(k_s + k_d)t}}{2} \quad (Eq.19)$$

$$f_{max} = (\alpha + \beta t)\left(1 - e^{-k_s t}\right)^2 \quad (Eq.20)$$

The flexibility of the dynamic model offers an opportunity to identify true sRPDs that underlie the observed mechanochemical selectivities. The attendant challenge is that the shapes of these RPDs are not constrained as they are in the standard models. Because of the narrow distribution of SS in individual polymer samples **1c**-**4c** and **1o**-**5o**, each sample reports on only a portion of the isomerization sRPD. Consequently, we had to adopt a more complex iterative approach to derive true sRPDs. In all these steps, sRPDs are expressed in terms of the distance from the chain terminus at which the overstretched segment originates.

First, we selected, among all isomerisation sRPDs generated during parameterization of the overstretched segment model described above the two sRPDs that most accurately reproduced experimental χ_z for **1c** and **2o** (these have the largest difference in the most

probable location of the SS), individually. We did the same for fragmentation sRPDs, which we then averaged because the fragmentation RPDs in the standard models have weak chain-size dependence. We ignored the fact that the sets of parameters of the overstretched segment model that yielded the two best isomerization sRPDs were different from the model-parameter sets than underlay the two best fragmentation sRPDs, because we were only interested in sample-average RPDs corresponding to experimental results, not the underlying microscopic conditions.

Second, we used these isomerisation sRPDs as starting guesses for a non-linear LSF of a combination of experimental χ_Z sets for **1c**-**2c** and **1o**-**3o** under the following assumptions: (a) fragmentation sRPDs were chain-size invariant; (b) the isomerisation kinetics of intact chain was determined by experimental k_i/k_f ratios (Fig. 2, main text), irrespective of the corresponding sRPDs; (c) DP specific isomerisation sRPDs were determined by linear interpolation of isomerization sRPDs at DP = 250 and DP = 750, which were the fitting parameters to minimize the residual (isomerization sRPDs at DP <250 were DP-independent). To allow desymmeterization of the initial-guess sRPDs, which was essential for improving the agreement with experimental χ_Z, each isomerization sRPD was represented by 19 isomerization probabilities at fractional distance from a terminus of 0.05 to 0.95 in 0.05 increments, which were allowed to vary independently, albeit within conditional boundaries to maintain a unimodal distribution.

The converged asymmetric isomerization sRPDs (which we call 1st-generation true isomerization sRPDs) yielded simulated χ_Z in much better agreement with the experiment than those obtained within the standard models. However, they also were incompatible with the symmetric fragmentation sRPD used in these simulations, i.e., no combination of model parameters could yield the employed fragmentation and isomerization sRPDs simultaneously.

Third, we identified fragmentation sRPDs that matched the 1st-generation true isomerization sRPDs at DP = 250 and 750. We started by generating μRPDs for all combinations of the model parameters drawn from the range: k_s = [0.05, 0.55] μs^{-1}; α =[0, 1] μN; β = [0, 1] N/s in 0.1, 0.2 and 0.1 increments, respectively. The distribution of force within each overstretched segment was determined by the ball–and–spring model with f_{max} located at the centre of the overstretched segment at each timestep. For each set of [k_s, α, β] μRPDs were calculated for k_d between 0 and 7.5 μs^{-1} and the longest stretching time, t_{max}, of either 5 μs or that satisfied the equality $\prod_{i=1}^{DP} S_{frag}(i, DP, t_{max}) = 0.001$, whichever is shorter. However, in all deconvolutions of estimated sRPDs, for each set of [k_s, α, β] parameters we only used μRPDs for combinations of k_d and $t_{stretch}$ such that f_{max} was located at the distance from the terminus of 25, 40, 55, 70, 85, 100 or 115 monomers (for chain with DP = 250), or 45, 95, 145, 195, 245,

295 or 345 monomers (for DP = 750) and the total survival probability of the chain against fragmentation, $\prod_{i=1}^{DP} S_{frag}(i, DP, t)$ of either 0.999, 0.01, or any value between 0.1 and 0.9 in 0.1 increment. This provided sufficient sampling of the full complement of μRPDs at all physically meaningful values of [k_s, α, β, k_d, $t_{stretch}$] without creating an intractably large combinations of μRPDs to test. We confirmed that linear interpolation of pairs of μRPDs corresponding to f_{max} at the selected locations yielded usefully approximations of μRPDs corresponding to f_{max} at all other fractional distances between 0.1 and 0.49. Unlike μRPDs generated by the standard models, all those in the dynamic model were unique.

We fitted the 1st generation true isomerization sRPDs for each of the two DPs (250 and 750) to weighted sums of up to 14 isomerization μRPDs corresponding to each pairwise combinations of [k_s, α, β, $t_{stretch}$] parameter sets. We then calculated the corresponding 1st generation fragmentation sRPDs as sums of fragmentation μRPDs for the pair of microscopic model parameters that most closely reproduced the 1st generation true isomerisation sRPDs, assigning each fragmentation μRPD the same weight as that of the corresponding isomerisation μRPD.

Fourth, we used this pair of the 1st generation fragmentation sRPDs to optimize the 2nd generation true fragmentation sRPDs at DP 100 – 1250 by non-linear LSF of experimental MMDs of **1c**-**3c** and **1o**-**4o** collectively (the number-averaged degrees of polymerization, DP_n, of these samples varied from 240 for **1c** to 1300 for **4o**). We used sRPDs at DP = 100, 250, 500, 750 and 1250 as fitting variables. The initial guesses of the sRPDs at DP = 100, 500 and 1250 were generated from the 1st generation true fractional fragmentation sRPDs at DP = 250 and 750 ($P^*_{frag}(\iota, 250)$ *and* $P^*_{frag}(\iota, 750)$) by eq. 21, where ι is the fractional distance from a terminus and * signifies that the distribution is in terms of fractional rather than absolute distances.

$$sP^*_{frag}(\iota, DP) = \frac{sP^*_{frag}(\iota, 750) - sP^*_{frag}(\iota, 250)}{500} DP - 0.5sP^*_{frag}(\iota, 750) + 1.5sP^*_{frag}(\iota, 250) \quad (Eq. 21)$$

As above, each fragmentation sRPD contained 19 fragmentation probabilities for a total of 95 fitting parameters against ~17500 independent observables. The range within which each fitting parameter could vary was constrained conditionally to ensure that each sRPD remained unimodal and to avoid non-monotonic scaling of any part of sRPDs on DP. sRPDs at DPs other than those of the fitting sRPDs were obtained by linearly interpolating the suitable pair of the fitting sRPDs, except that the fragmentation sRPDs at DP<100 were assumed to equal sRPD at DP = 100. All fragmentation sRPDs were renormalized to 1 at every iteration.

Fifth, we fitted the 2nd generation true fragmentation sRPDs for DP = 250 and 750 to weighted sums of up to 21 μRPDs (corresponding to all combinations of three sets of [k_s, α, β, $t_{stretch}$] parameters) for k_s = [0.05, 0.3] μs^{-1}; α =[0, 1] μN; β = [0, 0.5] N/s in 0.05, 0.1 and 0.05 increments (for DP = 750 and 1250 k_s was limited to 0.2 μs^{-1}). For DP = 1250 we used 36 μRPDs, with each [k_s, α, β] combination contributing 12 μRPDs corresponding to f_{max} located at every 50th monomer up to 600th monomer.

We repeated step 4 with model-fitted fragmentation sRPDs at DP = 250, 750 and 1250 to fit experimental MMDs of **4c**, **4o** and **5o** collectively (experimental DP_n from 1300 to 2250) using sRPDs at DP = 2000 and 3000 as the fitting parameters (the inclusion of **4o** in both sets of LSFs ensured internal consistency). The initial guesses were generated by Eq. 21 but using sRPDs at 750 and 1250, and each fitting sRPD was represented by 36 fragmentation probabilities at fractional distances of 0 to 0.7 in 0.02 increments (sRPDs at fractional distances >0.7 were set to 0). Using model-fitted sRPDs at DP = 250, 750 and 1250, instead of the equivalent sRPDs generated directly in step 4, ensured stable convergence. We deconvoluted the converged fragmentation sRPD at DP = 2000 to constituted μRDPs using the same procedure as for DP = 1250 described in the preceding paragraph.

Sixth, the final round of refinement of the true sRPDs was performed by fitting both MMDs and χ_Z simultaneously. We first refined sRPDs at DP = 100, 250, 500 and 750 by fitting MMDs and χ_Z of **1c**-**2c** and **1o**-**2o**, collectively. We then used the converged sRPDs at these DPs to fit MMDs and χ_Z of **3c** and **3o**, collectively to refine sRPDs at 1250. Finally, sRPDs at DP = 2000 and 3000 were estimated from MMDs and χ_Z of **4o**-**5o**. In all LSFs, residuals of MMDs were assigned a 50-times greater weight than residuals of χ_Z because of the different dynamic range of mass fractions (~10^{-3}) and *Z*-SS fractions (0.5). Unlike previous LSFs of the experimental data, the fitting parameters were not probabilities, but scaling factors of individual probabilities of sRPDs at the "reference" DPs (a subset of 100, 250, 500, 750, 1250, 2000 and 3000, depending on the combination of experimental samples). These scaling factors were constrained to [0.9, 1.1] for sRPDs at 250, 750, 1250; [0.85, 1.15] at 2000 and [0.8, 1.15] for 100 and 3000, and were additionally constrained at individual iterations to ensure unimodal distributions, monotonic DP-dependence of probabilities and isomerisation probabilities not exceeding 1. The reference isomerisation sRDP at DP = 100 was the model-fitted 2nd generation true isomerisation sRPD at DP = 250 multiplied by 1.12; that at DP = 500 was weighted average of model-fitted isomerization sRPDs at DP = 250 (0.65) and 750 (0.35); and at DP = 3000 was obtained by multiplying model-fitted 2nd generation true isomerisation sRPD at DP = 2000 by 0.9. In each iteration, sRDPs at intermediate DPs were obtained by

interpolation of the reference sRPDs at that iteration, except for DP < 100, which were assumed to equal sRDP at DP = 100.

The converged pairs of fragmentation and isomerisation sRDPs at DP = 250, 750, 1250 and 2000 were refitted to weighted sums of corresponding μRDPs. Pairs of sRDPs at DP = 250 and 750 were fitted to weighted sums of up to 28 μRDPs, corresponding to all combinations of 4 [k_s, α, β, $t_{stretch}$] parameter sets specified above; DP = 1250 to sums of 48 μRPDs; and for DP = 2000 to sums of 57 μRPDs. In all fits, the each pair of the fragmentation and isomerisation μRPDs corresponding to the same combination of the model parameters had the same weight. The residuals of isomerisation sRPDs were assigned 50-fold higher weight than those for fragmentation sRPDs. We didn't attempt to parameterize the model for DP = 100 because the experimental data is least sensitive to sRPDs at this DP, making the derived true sRPDs at DP = 100 least accurate of all true sRPDs derived here. Parameterization of the model for DP = 3000 is computationally unfeasible at this time.

In the final parameterization step, all μRPDs contributing >0.1% to sums that gave the 20 lowest norms of residuals for each reference DP were used together to fit the corresponding true sRPDs, reducing the resulting norms of the residuals by 1.6 – 2.2 times compared to the use of any combination of 28 – 57 μRPDs drawn from 3-4 sets of [k_s, α, β, $t_{stretch}$]. This improvement supports our hypothesis that the observed changes in the bulk composition of sonicated solutions reflect a broad range of microscopic conditions experienced by the reacting chains. The likely reason that the same approach of weighed sums of multiple μRPDs representing several distinct sets of microscopic conditions does not improve the performance of the standard models is the high degree of similarity among μRPDs corresponding to diverse parameters of the standard models.

Finally, fragmentation sRPDs at DP = 250, 750, 1250 and 2000 obtained by fitting to μRPDs and at DP = 100, 500 and 3000 obtained in step 6 were smoothed by fitting each to a sum of 2 sigmoidal functions. The equivalent isomerisation sRPDs were smoothed by moving averaging their derivatives with respect to the distance from the terminus, integrating the result and rebinning it to give probability vs. fractional distance suitable for simulating MMDs and χ_Z (Figure 28).

The relationship between the sample-average distributions of mechanochemical reactivities (Fig. 24) and the observed mass-dependent χ_Z appears to be unique and independent of a specific model. Conversely, the empirical nature of the equations underlying the model makes the fitted model parameters significant only insofar as they allow the experimental measurements to be related to the physical microscopic conditions experienced by the

mechanochemically reacting chains (Figure 31). Since mechanochemical reactivity at f_{max} <2.5 nN is too slow to detectably alter the bulk compositions of sonicated solutions, the converged distributions of the model parameters are only valid for chains experiencing f_{max} > 2.5 nN. It seems plausible that the same distributions of the microscopic parameters could be produced by other (yet unknown) microscopic models with their own distributions of model parameters.

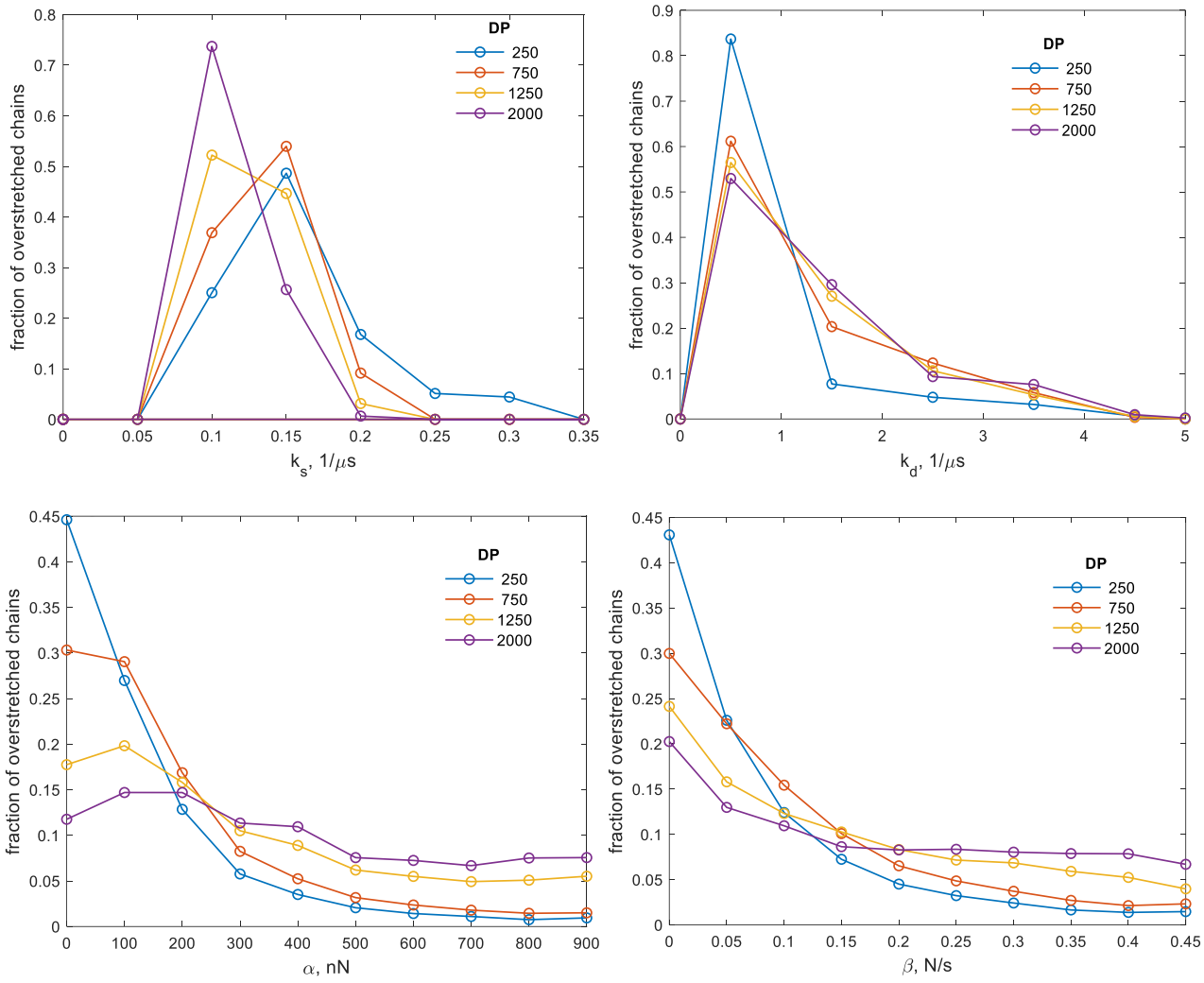

Figure 30 – ***Discrete distributions of the fitted parameters of the dynamic model****. (a) the rate constant of the growth of the ovestretched segment, k_s; (b) the rate constant of drift of the overstretched segment along the backbone, k_d; (c) the time-independent proportionality constant between maximum force, f_{max}, and the fractional length of the overstretched segment, α; (d) the time-dependent proportionality constant between the maximum force, f_{max}, and the square of the fractional length of the overstretched segment, β. These distributions have been derived for overstretched chains with f_{max} >2.5 nN: the model is unparameterizable by fitting to experimental MMDs and χ_Z at lower forces, because the underlying mechanochemical reactions are too slow to detectable affect the bulk compositions. The distributions of k_d were obtained by rebinning the fitted values into bins of 1 s^{-1} width centreed at 0.5, 1.5, 2.5, 3.5 and 4.5 s^{-1}. The distributions are strongly cross-correlated so that the probability of a mechanochemically-reactive chain to experience a specific combination of the 4*

model parameters does not equal the product of the fractions of chains experiencing the same parameter values individually.

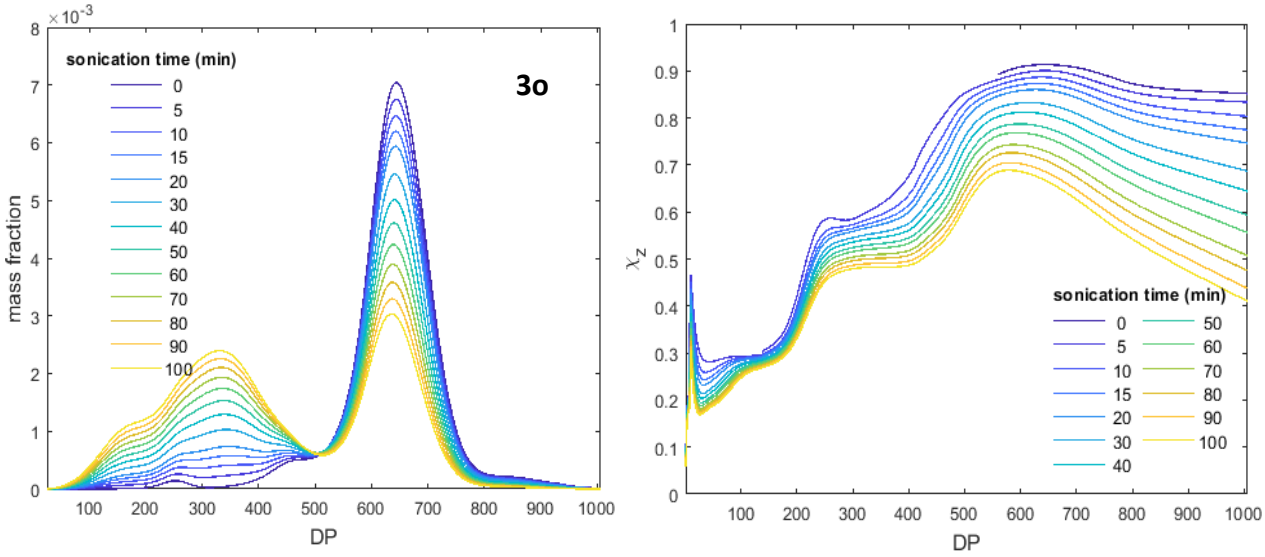

*Figure 31 – The evolution of MMDs and chain-size dependent χ_z in sonicated solutions of **1c**-**5o** predicted by the dynamic model parameterized against the experimental measurements.*

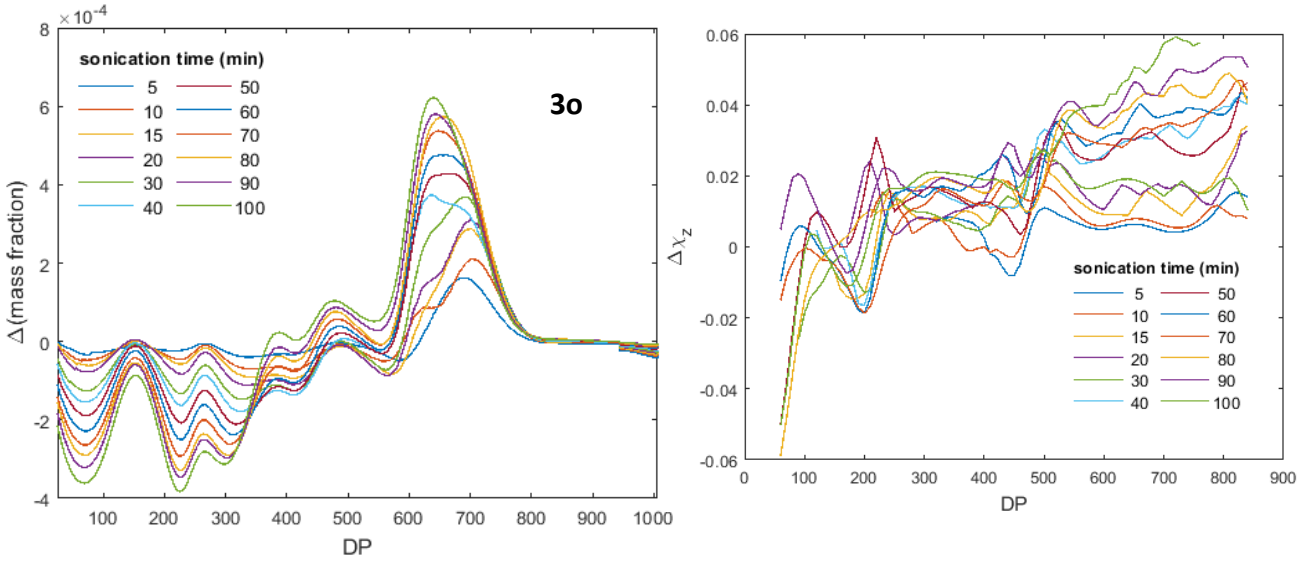

Figure 32 – The difference between observed MMDs and χ_z and those predicted by the dynamic overstretching model.

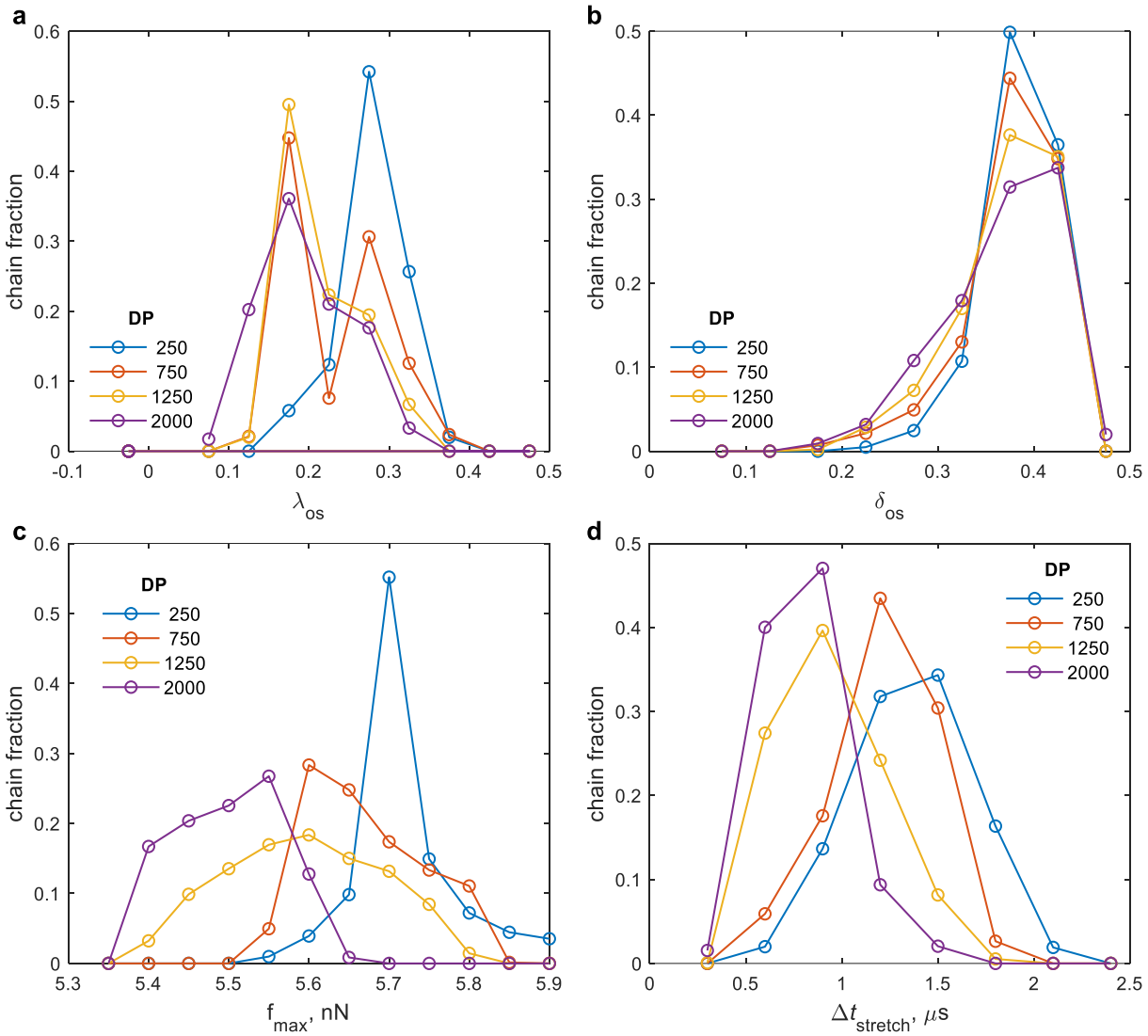

Figure 33 – The calculated discrete distributions of molecular conditions responsible for the observed mechanochemistry. (a) fractional length of the overstretched segment (λ_{os}) at $t_{stretch}$; (b) fractional distance from the centre of the overstretched segment to the chain terminus at chain fracture, δ_{os}, at $t_{stretch}$; (c) maximum force, f_{max}, at $t_{stretch}$; (d) the time the average chain remains loaded after its f_{max} reaches 2.5 nN, $\Delta t_{stretch}$. In all distributions the x value is the centre of the bin; the bin widths are 0.05 (a-b), 50 pN (c) and 0.3 μs (d). The distributions cover chains whose f_{max} exceeds 2.5 nN.

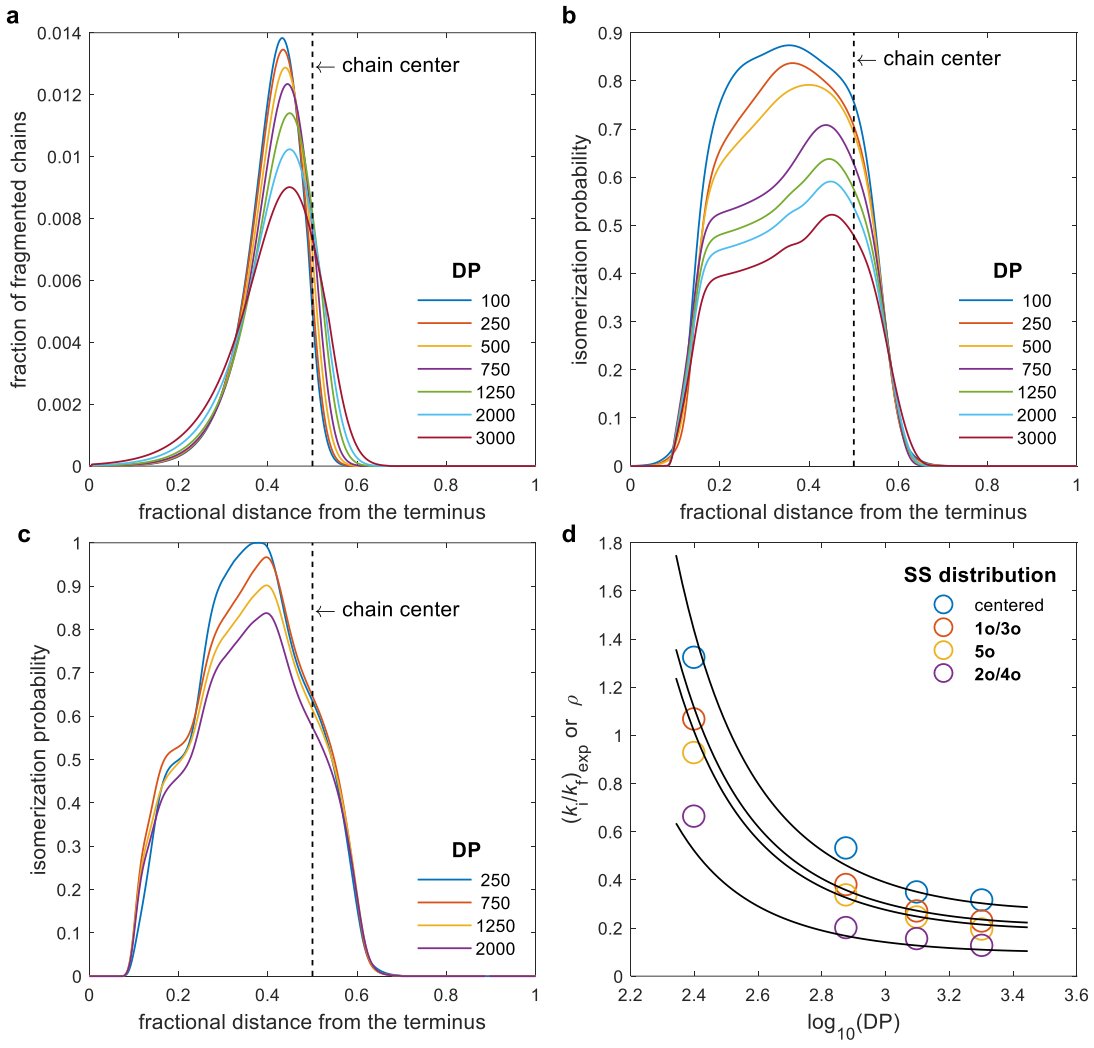

Figure 34 – Discrete sample-average distribution of reaction probabilities from the dynamic model. (a) relative fragmentation(relative); (b) fragmentation-coupled isomerisation (isomerisation in overstretched chains that fracture); sRPDs at DP = 100, 500 and 3000 were used in simulating MMDs and χ_z but were generated by interpolation instead of parameterization of the dynamic model. (c) fragmentation-independent isomerisation (isomerisation in overstretched chains that don't fracture); (d) the ratio of fraction of chains that isomerised but didn't fracture to the fraction of chains that fractured, ρ, (circles) averaged over duration of sonication. Solid lines are LSFs of experimental k_i/k_f for ***1c-4c***, ***1o/3o*** *and* ***2o/4o****. In contrast to the literature models, fragmentation-independent isomerisation probabilities and ρ are not independent descriptors of mechanochemical reactivity in the dynamic model. Instead, they derive from the microscopic fragmentation and fragmentation-coupled isomerisation probabilities according to eqs. S8-S9. Consequently, these were not optimized, nor used explicitly in simulating χ_z and are shown here for illustrative purposes. The additional empirical parameter, ξ required by the literature models (eq. S13 and S17), makes ρ independent of the fragmentation and fragmentation-coupled isomerisation probability and makes fragmentation-independent isomerisation probability undefined. All distributions have the bin size of 0.002.*

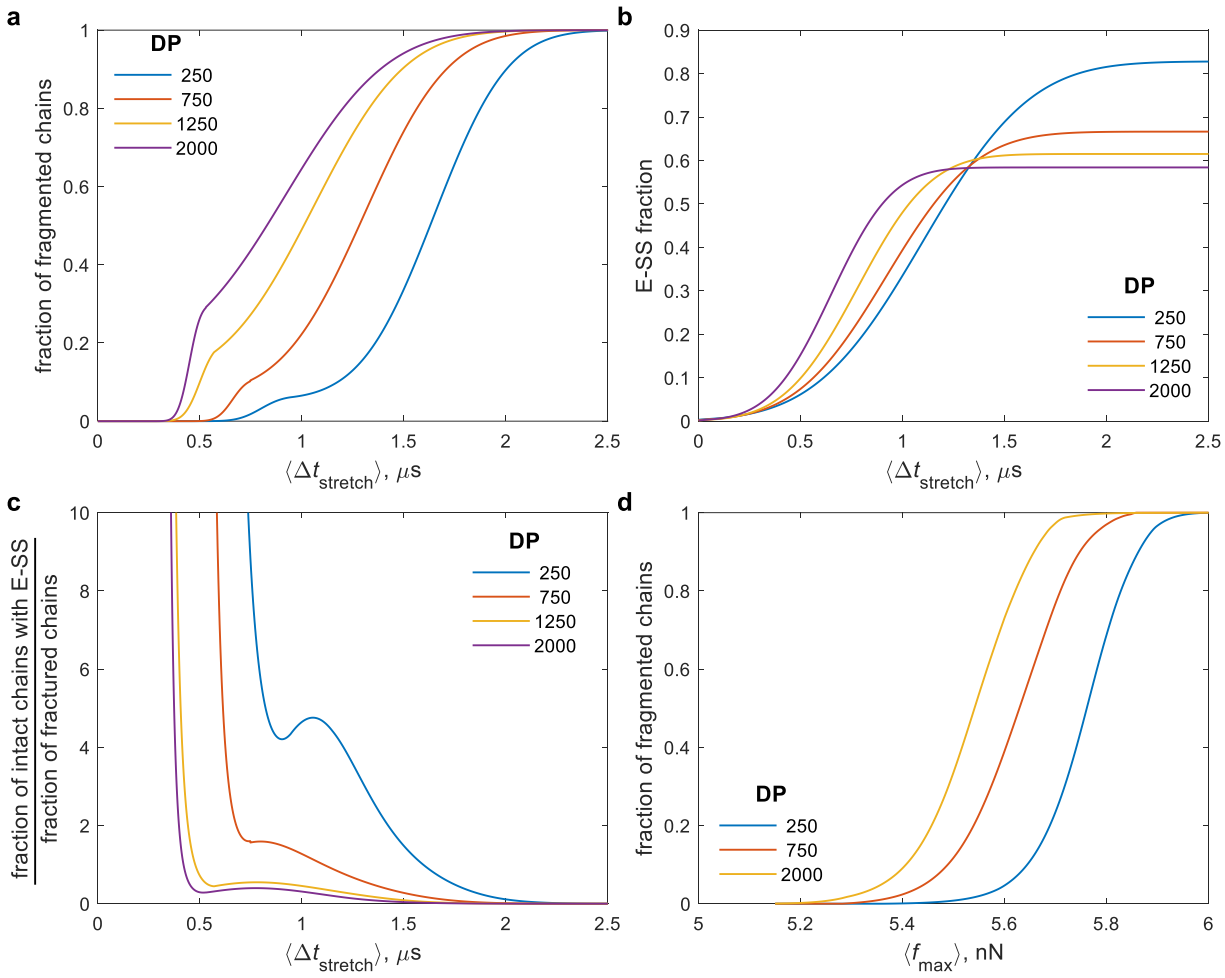

*Figure 35- The evolution of average-chain reaction probabilities in the flow as a function of time since f_{max} reached 2.5 nN, $\Delta t_{stretch}$: (a) chain fracture; (b) isomerisation of Z-SS whose distribution around the backbone follows the average distribution in **1c-4c**, P^c_{SS}; (c) the ratio of the intact chains with E-SS to the ratio of the fragmented chains for P^c_{SS}; (d) chain fragmentation probability as a function of f_{max}.*

3. The mechanochemistry of functionalised biphenyls: exploring mechanosensitive torsion angles to force *E*→*Z* alkene isomerisation and reversibly release protons.

Preface to remaining chapters

The majority of the mechanochemistry literature details the force sensitivity of irreversible covalent bond breakage and formation.[5] The most common examples of the latter are in powder mechanochemistry for which hundreds of examples of ball milling induced covalent bond formations are known.[108] The former is most associated with polymer mechanochemistry due to the established acceleration of covalent bond scission during polymer chain stretching both in solution and in solid materials under macroscopic loads.[97,109,110] Such covalent bond scission typically becomes prominent only at high forces (2–5 nN).[2]

The mechanochemistry of non–covalent interactions is also well explored with multiple reports of force–induced changes occurring in supramolecular structures, such as the breaking of weak interaction during SMFS controlled protein unfolding,[111] the conformational flips observed when chains of sugars are stretched,[112] or the formation of non–covalent bonds upon ball milling induced crystallisation.[113] With a single exception,[114] studies of small molecules undergoing highly localised reversible conformational changes are absent from the literature despite the desirability of materials that produce a highly sensitive, rapidly reversible and reusable chemical response to force. Such mechanosensitive materials could have applications in robotics as force detectors and enhance our understanding of equivalent processes in biology.

Mechanosensitive ion channels conserved across a wide range of organisms illustrate the importance and utility of force–induced conformational rearrangements.[115] Specifically, the Pizeo1 ion channel has been widely studied for the last few decades because of its importance in numerous pathologies and its fundamental role in many of the basic sensing abilities of organisms, such as detecting touch and sound. Although the exact mechanism of transducing force into signal remains to be fully enumerated, there is agreement that temporary, highly mechanosensitive conformational changes underlie its function. The force stimuli is thought to be channelled to the Piezo1 gate by either the surrounding lipid bilayer or local filaments and cytoskeletons, which change electrical potential across the membrane by opening ion channels.[116,117] The ion channel gates are rapidly shut upon the removal of force with the channel assuming its unstrained conformation (Figure 36).

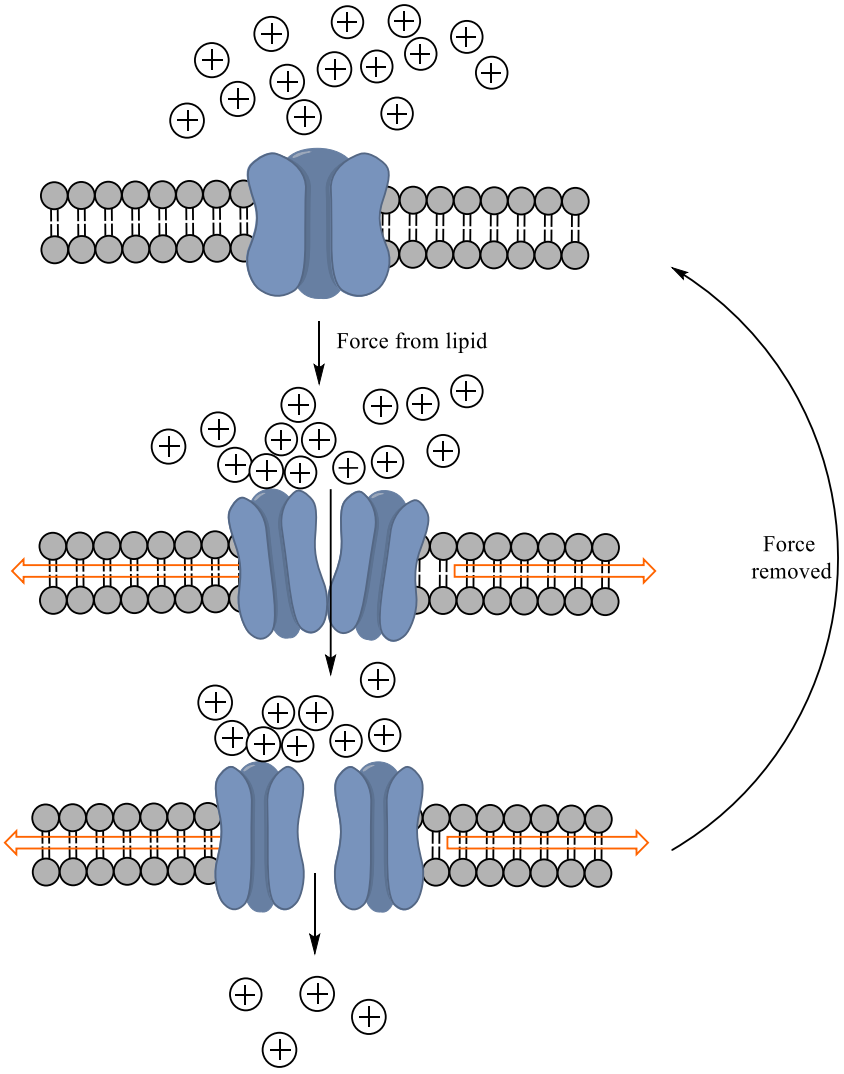

*Figure 36 – **Mechanosensitive ion channels enable force detection in living organisms.** A cartoon representation of the mechanism of force detection in living organisms. The force is shown as being transduced to the ion channel from the lipids, but other mechanisms are proposed.*[118]

Designing tractable model systems that mimic this force–sensitive reversible conformation change has the potential both to produce new materials with mechanotuneable chemical properties and allow insights into the mechanism that channel force transduction into a cellular biochemical response.

Figure 37 shows a biphenyl containing macrocycle (further explored in chapter 3), the previously reported behaviour of which demonstrates that the highly force–sensitive torsion angle of functionalised biphenyls makes them ideal candidates as simple models of how force induced conformational changes influence chemistry.

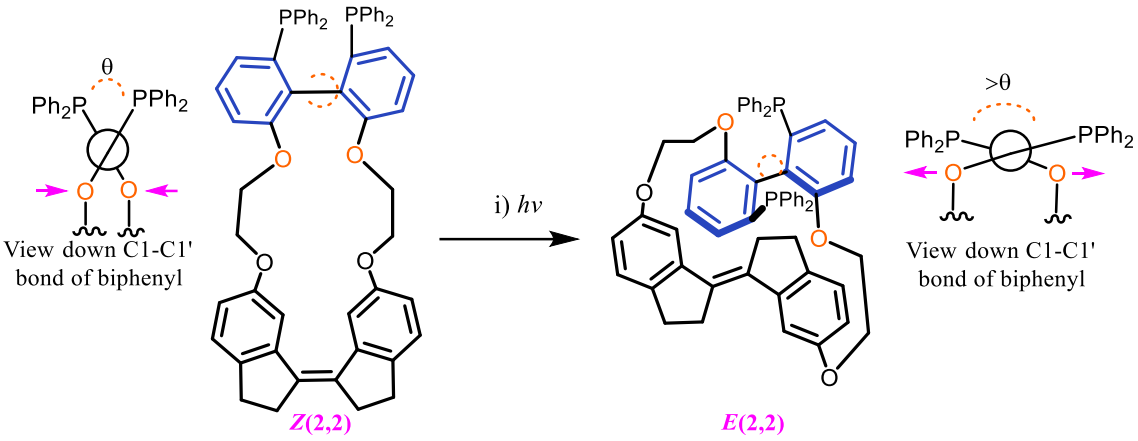

Figure 37 – **A *previously reported macrocycle that has a mechanosensitive biphenyl torsion angle.*[114]** *Multiple macrocycles of varying alkyl linker lengths were reported, only the shortest with the largest force on the biphenyl torsion is shown here. The magenta arrows indicate the direction of force applied to biphenyl by stilbene.*

The macrocycles in Figure 37 can coordinate to a metal centre via their phosphine atoms. The effect of applying force to the diphosphine biphenyls on the catalytic reactions occurring at a metal centre bound to diphosphine substituents is well understood.[114,119,120] This molecular motif allows two further mechanochemical exploitations of force modulating torsion angles. First, the binding of a guest molecule to the 2,2' substituents of a biphenyl can reduce its torsion angle (y in Figure 38a) and thereby generate a compressive force on a rigid moiety bridging the 4,4' positions (magenta line Figure 38a) . Such compressive strain can alter the reactivity of the bridging moiety (Figure 38b) shows a practically realised example presented in chapter 3).

Conversely applying a tensile force to a suitable biphenyl chelating acceptor reduces its affinity for guest molecules by destabilising small torsion angles needed for bidentate binding, shown generically in Figure 38C, Figure 38D shows key components of a diamine explored for this purpose in chapter 4. Controlling the release and uptake of small–molecule cargo with force in a reusable material opens intriguing opportunities for exploitation and would represent a departure from the existing examples of such delivery systems, which rely solely on irreversible chemistries and can be used only once.[121,122]

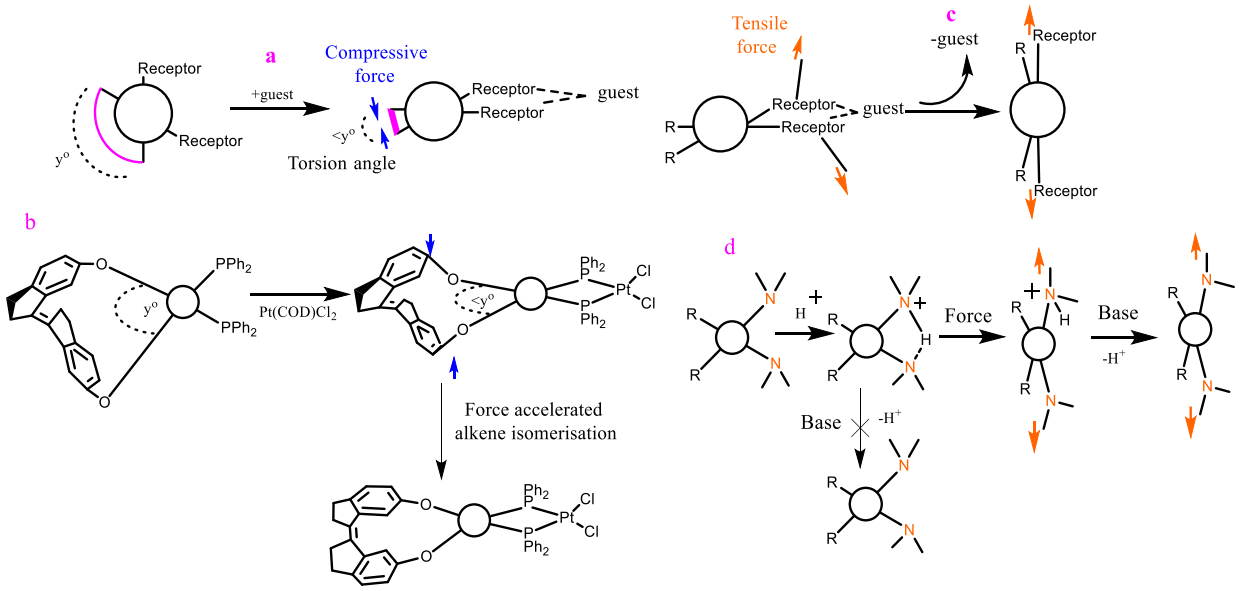

*Figure 38 – **Potential applications of mechanosensitive torsion angles in mechanochemistry** a) a Newman representation down the $_{Ar}C–C_{Ar}$ bond of a biphenyl showing how changes in the torsion angle of a biphenyl applies a compressive force to a rigid group. b) a practically realised example of a) discussed in chapter 3. c) a Newman representation down the $_{Ar}C–C_{Ar}$ bond of a biphenyl showing how the mechanosensitivity of a biphenyl torsion angle can control the affinity of two substituents for a guest. d) a diamine system that is explored as a practical realisation of c in chapters 4a and b.*

Here projects exploring these two concepts are described. Except for the work in chapter 3 for which I am responsible for computations only, I conducted all synthetic, experimental, modelling and computational work.

Chapter 3: Allosteric control of olefin isomerization kinetics and its mechanochemical model.

Yichen Yu[1‡], Robert T O'Neill[2‡], Roman Boulatov[2,*], Ross A. Widenhoefer[1,*], and Stephen L. Craig[1,*].

[1]Department of Chemistry, Duke University, Durham, North Carolina 27708, USA.
[2]Department of Chemistry, University of Liverpool, Crown Street, Liverpool L69 7ZD, UK.

[‡] equal contribution

ABSTRACT: Allosteric regulation underlies important phenomena in biochemistry and information science. Allosteric control of reaction thermodynamics is well understood as evidenced by the thousands of reported synthetic allosteric systems, largely focused on controlling small molecule binding affinity. The kinetics of allosteric control is relatively unexplored conceptually, with known examples exploiting simple on/off switching of catalysis by off-site binding – few generalisable insights are available from such systems. Here we describe a mechanochemical model of allosteric kinetics and test some of its key predictions using small macrocycles. The model adapts the mechanochemical framework developed for polymer mechanochemistry to the compressive regime which is reproduced in practice by coupling the isomerisation of an olefin (stiff stilbene) with the torsion angle of 2,2'-bis(diphenylphosphino)biphenyl. Metal binding to the diphosphine alters the force transduced to the stilbene accelerating its isomerisation kinetics up to 10^4–fold. DFT calculations and modelling indicate changes in the relative stability of reactant and transition state upon binding contribute more to $\Delta\Delta G^{\neq}$ than the relaxation of the constraining potential. The model demonstrates the importance of understanding the properties of the constraining potential, such as its stiffness and equilibrium geometry, in reactions under compressive load. The work offers a starting point for a mechanochemical framework that enables quantitative predictions of enzyme allostery in terms of structural parameters of stiff bioactive proteins.

Introduction

The central role of allosteric regulation in enabling life as we know it[123] and the fundamental questions in information transfer, conformational dynamics[124] and emergent properties that allostery presents underlie continued effort to design synthetic molecules with allosteric behaviour.[125,126] Allosteric control of reaction thermodynamics, particularly binding affinities of small ligands, has been realized in thousands of synthetic molecules, and the design principles of such receptors are well understood.[127-129]

In comparison, abiological examples of allosteric control of reaction kinetics are few.[128] The most productive approach to date has been to combine a known catalyst with a regulating moiety for on/off control, with the catalyst in the on state retaining the properties of the non-allosteric equivalent largely unchanged.[130,131] Despite clever applications of such catalysts, they are generally thought to offer only limited insights into how electronically-uncoupled changes in local geometries of remote receptor sites lower activation reaction barriers below those of non-allosteric equivalents.

Here we report a molecular scaffold that allows the acceleration of thermal isomerization of an alkene (stiff stilbene, Figure 39) to be varied systematically up to 10^4–fold in response to fast binding of a metal ion to a remote receptor site. We used these observations to demonstrate that the formalism of mechanochemical kinetics, generalized to compressive loads, constitutes a productive approach to quantitative analysis of the structural and energetic basis of allosteric control of reaction kinetics. We demonstrate that a simple model explains quantitatively the experimental measurements by representing the remote binding site as a harmonic spring that imposes variable compressive load on the substrate. By decreasing the equilibrium distance of the spring effector, binding increases the load on the *E* isomer without affecting the strain energy of the transition state. Our findings provide quantitative support for a promising if controversial, "mechanical" picture of allosteric control of enzymatic reactivity.

Results

In this work we used strained macrocycles comprising a 2,2'-Bis(diphenylphosphino)biphenyl (BiPHEP) moiety as the effector binding site that bridges and constraints C6,C6' atoms of *E*-stiff stilbene (the substrate) on the opposite side of the macrocycle (Figure 39). The macrocycles were synthesized as *Z* isomers followed by preparative photoisomerisation and separation to yield pure *E* congeners (Figure 39). The axial chirality of stiff stilbene and BiPHEP[132] means that our syntheses should yield pairs of diastereomers, but only the diastereomers of the largest macrocycle in the series, *E*(3,3), could be separated and studied individually. ^{1}H NMR spectra of *E*(2,2) and *E*(2,3) macrocycles are consistent with the presence of a single diastereomer. Previously, photoisomerisation of *Z* stiff stilbene macrocycles was reported to produce predominantly the least strained *E* macrocycles, which was rationalized by a combination of rapid epimerization of *Z* stiff stilbene and the strong dependence of the quantum yields of $Z \rightarrow E$ photoisomerisation on the strain energy of the product.

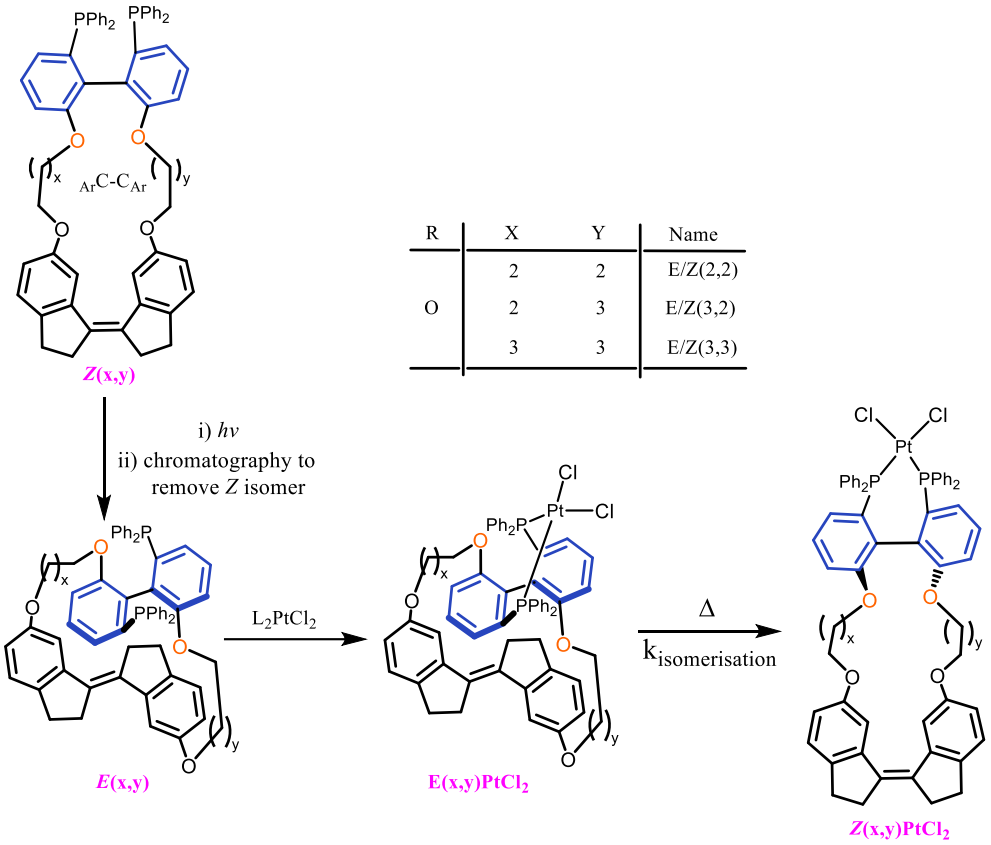

R	X	Y	Name
	2	2	E/Z(2,2)
O	2	3	E/Z(3,2)
	3	3	E/Z(3,3)

Figure 39 – Photoisomerisation of Z macrocycles yields their E analogues which spontaneously complex with $PtCl_2$ in solution. Thermal E/Z isomerization of E(m,n)]$PtCl_2$ gives their Z(m,n)]$PtCl_2$ analogues.

We measured the activation enthalpies and entropies of *E*→*Z* isomerisation in the absence of metal ions and in the presence of (NBD)$PtCl_2$, which spontaneously reacts with the macrocycles to yield *E*(m,n)$PtCl_2$ complexes (Figure 39) as evidenced by ^{1}H NMR spectroscopy. *E*→*Z* isomerisation of stiff stilbene in all complexes manifested first-order kinetics over at least 3 half-lives and we derived $\Delta H^{\neq}$ and $\Delta S^{\neq}$ from the rate constants measured at 3-4 temperatures (Table 2). The Pt complex of the smallest macrocycle, *E*(2,2)PtCl2, isomerises too fast at room temperature to allow kinetic measurements. Consequently, DMF-d_7 solutions of *E*(2,2) and (NBD)$PtCl_2$ were mixed at –50 °C, the formation of *E*(2,2)PtCl2 was confirmed spectroscopically, the solution allowed to warm to -10 – 3 °C and the isomerisation kinetics was measured at these temperatures.

Table 2 - The measured and calculated activation free energies of stiff stilbene isomerisation in E(m,n) macrocycles and their platinum complexes [E(m,n)]PtCl2

	Measured[a]		Computed [a,b]	
		$\Delta G^{\ddagger}$	$\Delta G^{\ddagger}$	
macrocycle	Metal-free[c]	Pt[d]	Metal-free	Pt
E(2,2)	27.1 ± 0.1	20.2 ± 0.1	26.1*, 23.7	18.7*, 18.0
E(2,3)	32.0 ± 2.1	26.8 ± 0.1	29.6*, 30.4	26.4*, 24.7
(S,R)/(R,S)-*E*(3,3)	32.3 ± 5.4	30.4 ± 4.2	32.9	29.0
(S,S)/(R,R)-*E*(3,3)	32.3 ± 4.7	31.5 ± 0.4	32.3	31.7

*[a] at STP; [b] in a vacuum; the two values for E(2,m), m = 2 or 3 correspond to the (S,R)/(R,S) and (S,S)/(R,R) diastereomers; * indicates the more stable diastereomer; [c] in p-xylene-d_{10}; [d] in DMF-d_7; [d].*

Metal coordination lowered the standard activation free energies of isomerization, $\Delta G^{\ddagger}_{o}$, by between 6.9± 0.1 kcal/mol in the smallest *E*(2,2) macrocycle and 0.8± 0.1 kcal/mol in the largest. The difference is enthalpic in origin, as expected for an elementary reaction with a non-polar transition state. We previously demonstrated that the isomerisation kinetics of stiff stilbene varies little with reaction solvent, thus ruling out the solvent effects as a major contributor of measured $\Delta\Delta G^{\neq}$.[23]

To understand the structural and energetic origin of the acceleration of isomerisation by metal coordination and to test the utility of a force-based approach to a broader analysis of allosterically controlled reaction kinetics we optimised conformational ensembles of *Z* and *E* isomers of both metal-free and Pt-coordinated macrocycles at (u)BMK/def2SVP//(u)B3LYP/def2SVP level of DFT in a vacuum. The calculations reproduced measured $\Delta G^{\neq}$ accurately (Table 2).

The optimized geometries reveal compressively strained *E* stiff stilbene, as evidenced by the contraction of its $_{ar}$C-C=C-C_{Ar} torsion, θ, relative to that of free stiff stilbene (~180°), in all macrocycles (Figure *40*a). In all Pt complexes this torsion was reduced further by 4-8° compared to the metal–free congeners, which can be attributed to the contraction of the BiPHEP–containing strap needed to accommodate the preferred Pt–P bond distances and P–Pt–P bond angle.[133] Conversely, the corresponding torsion angles of the conformers comprising the transition states of isomerisation deviated from the strain-free value by between -4° and 2°, depending on the conformer, suggesting low strain of either direction.

Across all conformers, the molecular geometries of the SS(OCH2)$_2$ moieties (blue + red symbols, Figure 40) resembled closely those of bis-(6,6'-dimethoxy)stiff stilbene, SS(OMe)$_2$, with a compressive force of varying magnitude applied across the $_{Me}$C…C$_{Me}$ coordinate (black line, Figure 40a). A reactive moiety coupled to an external force acting across a pair of atoms is a widely used model in polymer mechanochemistry, suggesting that the observed variation of isomerization $\Delta G^{\neq}$ across the series, and the allosteric effect of Pt binding on it, could be amenable to analysis within the formalism of mechanochemical kinetics.

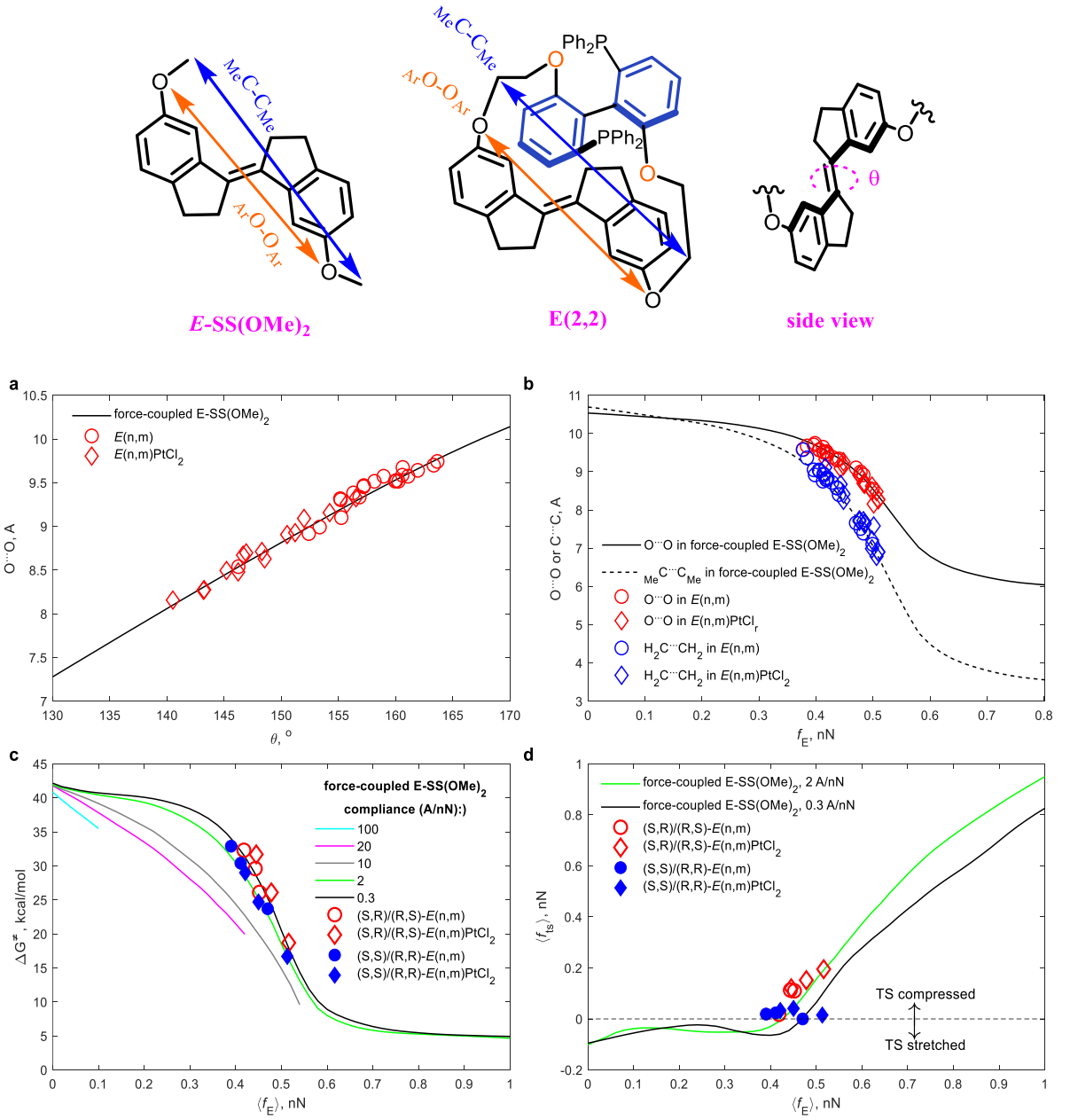

Figure 40 – Top) defines the $_{Me}$C-C$_{Me}$ $_{Ar}$O-O$_{Ar}$ and ϑ referred to in figure a-d for E-SS(OMe)$_2$ and E(2,2). (a-b) SS(OMe)$_2$ with compressive force acting on its methyl C atoms reproduces the structures of the stiff stilbene moiety in the macrocycles as illustrated by the close correlation between O…O and C…C distances in both metal free and complexed macrocycles and the values obtained from DFT calculations on E-SS. In (a) the underlying structural homology is illustrated by the correlation between the $_{Ar}$C-C=C-

C_{Ar} torsion and the O…O distance (a). (b) The corresponding force, f_E, was found. (c) The calculated $\Delta G^{\neq}$ in the two sets of diastereomers of the macrocycles follow that obtained by comparing the energy of E and the ts for $SS(OMe)_2$ coupled to a constraining potential with compliance of 2 and 0.3 Å/nN respectively. Maximum f_E imposed on $SS(OMe)_2$ by a potential decreases with increasing compliance, explaining truncated $\Delta G^{\neq}(f)$ for compliances >2 A/nN. (d) Force exerted on $SS(OMe)_2$ by a compressive potential with finite compliance decreases as the molecule progresses along the isomerisation reaction path, resulting in lower ensemble-average force in the transition state, f_{ts}, compared to that in the E isomer, f_E

The latter is a framework for quantitative analysis and predictions of the effect of molecular strain on reaction rates and selectivities when the strain results from interactions of intractably many molecular degrees of freedom. It was developed and validated for reactions of polymer chains stretched beyond their strain–free geometries by energy-dissipative environments such as elongational flow fields in rapidly flowing polymer solutions or elastomers undergoing plastic deformations.

The measured kinetics of reactions in overstretched polymer chains or non–macromolecular mimics reported to date can be analysed productively by representing the reactant and its environment as the small reactive site coupled to an infinitely compliant harmonic stretching potential.[5] Such a potential applies identical force on every conformer of the reactive site (and any transition state), independent of their molecular geometry. In this model, acceleration (or occasional inhibition)[134] of reactions in stretched reactants is primarily determined by the difference in the potential energy of the constraining potential coupled to the reactant and the rate-determining transition state, which is proportional to this force.

This picture, however, becomes non–physical in the case of a compressive potential. The rate of a chemical reaction is sensitive to applied force only if the formation of the rate–determining transition state is accompanied by changes in the separation of the two atoms across which the force acts. Only a very soft stretching potential (with a correspondingly very long equilibrium distance) would apply a finite force that remains approximately constant despite changes in the coupled distance. A similarly soft compressive potential would require an equilibrium distance shorter than zero, which is impossible.

The finite compliance of a physical constraining potential means that each conformer comprising each kinetically–significant state coupled to the same constraining potential experience different force. The stiffer this potential, the greater both the variation of the force among the conformers and the difference of the ensemble-average forces of the reactant and the (rate–determining) transition state. As a result, the activation barrier of the compressed reactant depends both on its ensemble-average force and the potential stiffness or, alternatively, the ensemble–average force of the rate-determining transition state.

To apply the formalism of mechanochemical kinetics to the macrocycles in this study, we first calculated the force on the methyl C atoms of $SS(OMe)_2$ needed to reproduce the geometry of the corresponding moiety in each thermally accessible conformer of each macrocycle (Figure 40b). Second, we calculated $\Delta G^{\neq}$ of isomerization in each conformer of $SS(OMe)_2$ coupled to a harmonic potential of fixed compliance whose equilibrium distance was reduced systematically to 0 to increase the compressive force it applies to $SS(OMe)_2$. From this data we calculated $\Delta G^{\neq}$ as a function of the ensemble-averaged compressive force experienced by the *E* isomer, f_E, for constraining potentials with harmonic compliances between 0.1 Å/nN and 100 Å/nN (Figure 40c). Compressive potentials with compliances of 2 Å/nN or 0.3 Å/nN, depending on the diastereomer, reproduced isomerization $\Delta G^{\neq}$ and the relationship between f_E and f_{ts} in each conformer of every macrocycle (Figure 40d) most accurately.

These calculations reveal that stiff stilbene in free macrocycles experience considerable compressive force and Pt coordination is equivalent to increasing this force by only between 30 and 80 pN (7-15%). The mechanochemical formalism allows the molecular basis of the exceptionally large allosteric acceleration of isomerization accompanying Pt binding to be understood by analyzing $\Delta G^{\neq}(f_E)$ correlation (Figure 40c) in terms of 4 components: the ensemble-average strain energies of the *E* isomer and the transition state of $SS(OMe)_2$ and those of the constraining potential in mechanical equilibrium with the corresponding conformers (Figure 41).

Larger compressive force on the reactant causes larger strain energy of both the reactive moiety and the constraining potential (red curves), as expected. The non-zero strain energy of the transition state at $f_E = 0$ and the reduction of its strain energy with increasing f_E below a threshold (0.42 nN in Figure *40*a) are the direct consequence of the finite compliance of the potential. At sufficiently low f_E the equilibrium length of the potential exceeds the strain–free internuclear distance of the transition state to which it couples, imposing on it tensile force whose absolute value may exceed (compressive) f_E (Figure 40d). As the equilibrium distance of the potential contracts with increasing f_E, the corresponding f_{ts} changes to compressive.

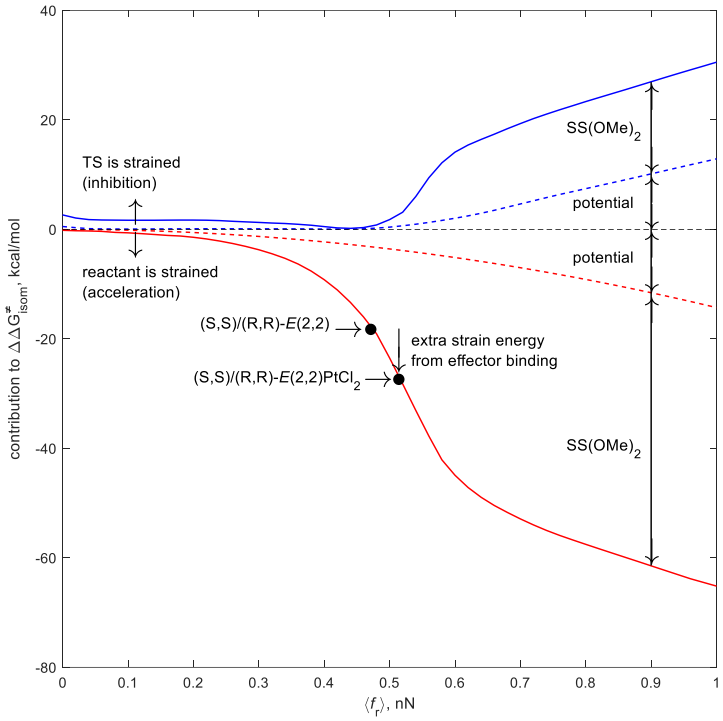

Figure 41 – Strain energy of the reactant (ERstr: blue solid line) and the transition state (TSstr: red solid line) as the function of the ensemble-average compressive force of the reactant for potential with 2 Å/nN compliance; the contributions of the constraining potential are shown by dashed lines.

This model suggests two mechanisms by which effector binding that increases f_E can accelerate a substrate reaction. In one, it reduces the strain energy of the transition state, which is already more strained than the reactant in the absence of the effector. Such effector–induced relaxation of a "pre-strained" transition state is a common approach to achieving allosteric control of reaction kinetics, but it cannot lower the activation barrier below that in the non–allosteric equivalent. This mechanism would operate in *E*-SS(OMe)$_2$ compressed to f_r < 0.2-0.3 nN, depending on the compliance of the coupled receptor. At higher force, as in the macrocycles studied here, this mechanism contributes negligibly to allosteric acceleration.

Conversely, effector binding can accelerate a reaction by increasing the strain of the reactant without a concomitant increase in the strain energy of the transition state (Figure 41). Such an increase must come at the expense of the less–favorable binding free energy of the effector, compared to an analogue in which the receptor and substrate are uncoupled. In this approach, the magnitude of the allosteric acceleration is likely limited by the acceptable reduction of the affinity of the coupled receptor for the effector, which may be constrained, for example by a practically achievable concentration of the effector. Consequently, the design of molecules capable of allosterically controlled reaction kinetics must consider efficiency of allosteric control, i.e., the ratio of the allosteric barrier lowering to the sacrificed binding free energy.

A key parameter is the minimum reduction in the enthalpy of effector binding needed to affect a given reduction in the activation energy of isomerisation of *E*-SS(OMe)$_2$ coupled to constraining potentials of varying compliances. Our data suggest that the molecular scaffold exemplified by the macrocycles and modelled here as springs of varying stiffness provides an internally consistent means of analyzing the molecular origin of this sensitivity. The efficient coupling of effector binding destabilisation to the reactant destabilisation resulting in molecular strain–induced changes in the activation barrier. All macrocycles in this study occupy a regime of allosteric acceleration of the substrate reaction relative to the rate in non–allosteric analogue because effector binding increases the strain energy of the reactant without a compensatory increase in the strain energy of the transition state.

A potential approach to quantitative analysis of the molecular mechanisms of allosterically controlled enzymatic activity is the structural transmission of molecular strain across suitably stiff portions of the biomolecular scaffolds. In theory, the realization of allosteric kinetic control in synthetic molecules offers a tractable system in which to test molecular quantitative descriptions of such conformational transition. No attempts to develop a similar interpretational framework for the more tractable examples of synthetic allosteric kinetic control have been reported.

Conclusion

The reported macrocycles represent one of the very few examples of synthetic molecules which exploit allostery to lower the activation barrier of a reaction below that in the equivalent free reactive moiety. The formalism of mechanochemical kinetics, generalised to compressive load, suggests the force dependence of reactive fragments is highly sensitive to the equilibrium length and stiffness of the constraining potential, reactant and transition state. Predictions of force sensitivity in such systems may inform enzymatic allostery and help understand the delicate interplay between effector affinity and reaction acceleration in biochemical allostery.

Chapter 4: The mechanochemistry of *N,N,N',N'*–tetra methyl–2,2'–diamine–[1,1'–biphenyl]

By controlling the protonation states of solutes, pH can profoundly affect the outcomes of solution reactions. For example, solubility,[135] susceptibility to nucleophilic attack[136] and the minimum energy conformation[137] of a molecule are often drastically altered upon protonation. A real–world consequence of the dramatic influence of pH on chemistry is the need for a control mechanism dedicated to buffering blood pH within narrow limits as part of homeostasis in living organisms. For example, the human bloodstream is maintained close to pH 7.4 by a carbonate/carbonic acid buffer system. So sensitive is human biochemistry to pH that sustained high (alkalosis) and low (acidosis) blood pH both lead to multiple organ failure.[138]

Creating materials that allow rapid and reversible changes in pH has been a long–standing pursuit of the chemical sciences. So far only light has been used as the stimulus.[139-141] Using light to control chemical changes is particularly attractive because it avoids chemical contamination of the solution and can be applied with high spatiotemporal control suitable for potential medicinal applications (since some wavelengths of light can penetrate human tissue without damage).[142]

Several prominent examples of molecules with optically accessible meta–stable states that differ in basicity are shown in Figure 42. All reported examples operate by either light triggered *cis*/*trans* isomerisation or electrocyclic ring opening. For example, a ~6–fold lower pK_b of *cis* azobenzene (**c4-1-*cis***) compared to its *trans* analogue (**c4-1-*trans***) has been attributed to the unfavourable steric crowding around the N of the ^{t}Bu–piperidine moiety, enforced by the strong preference of the ^{t}Bu substituent for the equatorial position.[139] The intramolecular H–bonding in **c4-2-*cis*H$^+$** contributes to the greater basicity of **c4-2-*cis*** compared to the *trans* moiety (**c4-2-*trans***).[143] A similar principle is responsible for a 2.2 unit increase in the second pK_a of the *cis* isomer of the bisphenol (**c4-4-cisH$^-$**), compared to the *trans* analogue (**c4-4-*trans*H$^-$).**[141] N–alkylated merocyanines (**c3-3-mer**) are considerably less basic than their spiropyrane isomers (**c3-3-spr**) by virtue of conjugation of the lone pair of the N atom. Despite the largest pK_b difference known, merocyanines usually revert rapidly to spiropyranes in the dark, reducing their potential utility. A single reported example exists of an efficiently reversible isomeric pair with greater than 2.5 pK_b difference and high stability, **c4-5-open/c4-5-closed**, for which the aromatic stabilisation of the open form isomer upon deprotonation makes it a much stronger acid than the close form.[144]

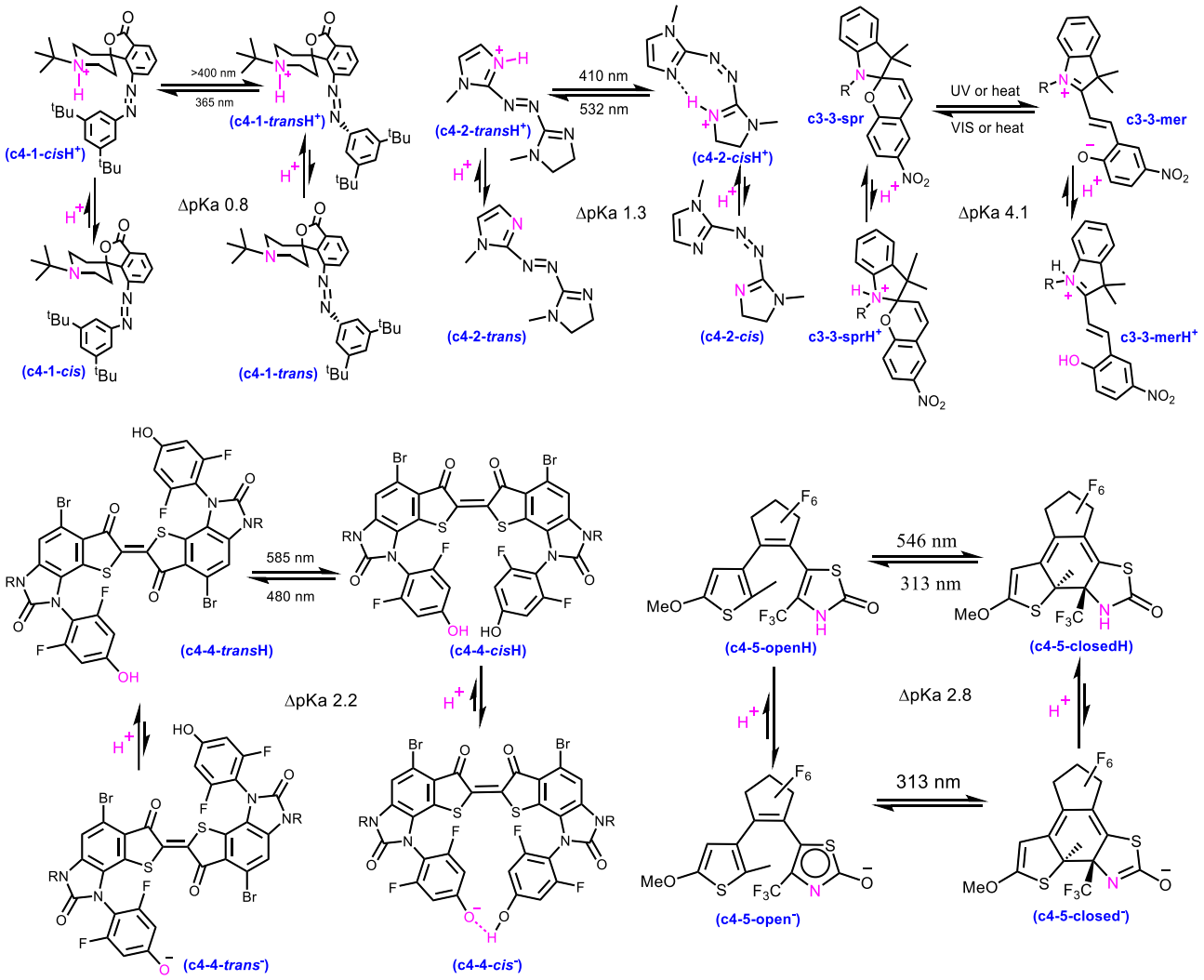

*Figure 42 – **Previously reported examples of photoresponsive pH switches.** Magenta atoms indicate the site of proton exchange.*

Equilibria are controlled by the relative energy of the two states, destabilising one relative to the other shifts the position of the equilibrium. Despite the established ability of force to change the minimum energy conformation of molecules, no attempt at controlling the position of a protonation equilibrium using force has been reported. Irreversible release of protons upon force activation has however been demonstrated in several polymers, both in solution and a bulk elastomer.[145-147] Two of the three reported examples release HCl by spontaneous elimination from the products of mechanochemical opening of the dichlorocyclopropane ring. The HCl elimination is driven either by aromatization of the dichlorodihydronaphthalene (Figure 43b)[147] or by stabilization of a carbocationic intermediate by the OMe substituent in Figure 43a.[147] In the final example, presumable mechanochemical scission of the O–N bond (orange, Figure 43c) ultimately produces the strongly acidic sulfonic acid group.[146]

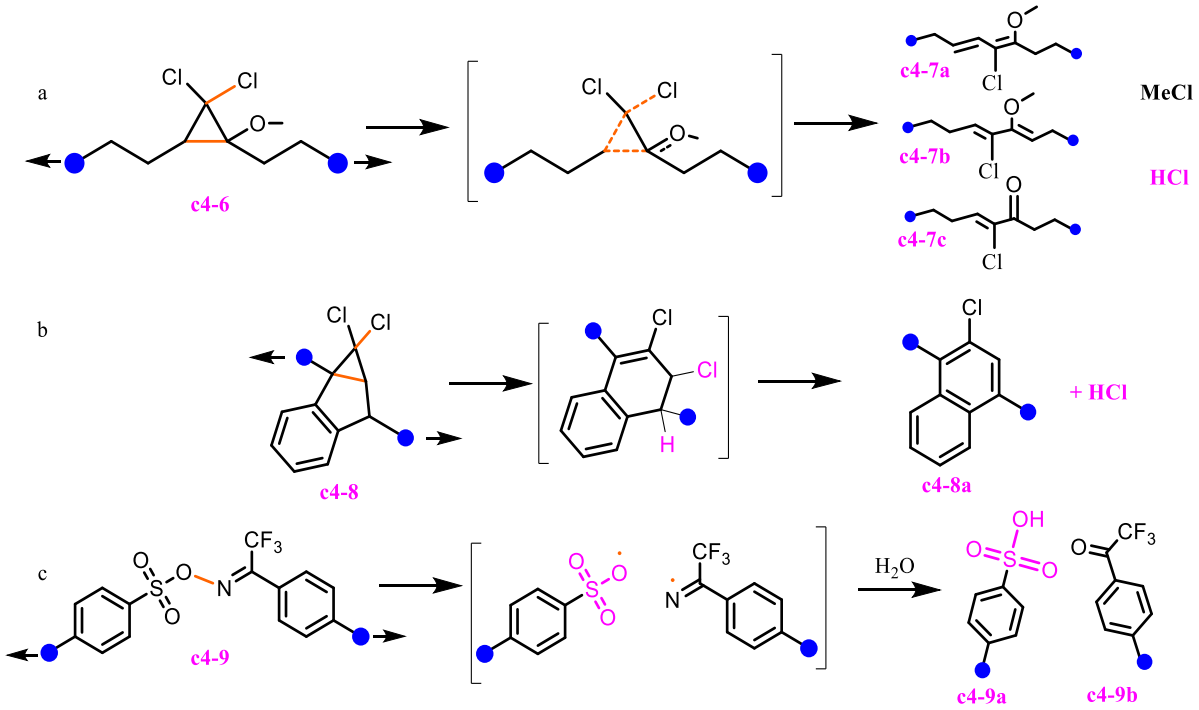

*Figure 43 – **Mechanoacids are molecules that release protons upon application of force.** Three examples have been reported in the literature. Since all involve the high energy change in covalent bonding they cannot be used more than once.*

N,N,N',N'-tetramethyl–2,2'-diamine–[1,1'–biphenyl] (DABP) is a suitable base for force–triggered H^+ release because its pK_b is sensitive to the $_{Ar}C–C_{Ar}$ torsion angle, which opens up in response to tensile force applied across $_{Me}C…C_{Me}$ distance, in turn controlling the proximity of the two nitrogens. For practical exploitation analogues of DABP modified with an arm that can transduce force to the torsion angle are required (DABP analogues, $DABP_a$) (Figure 44).

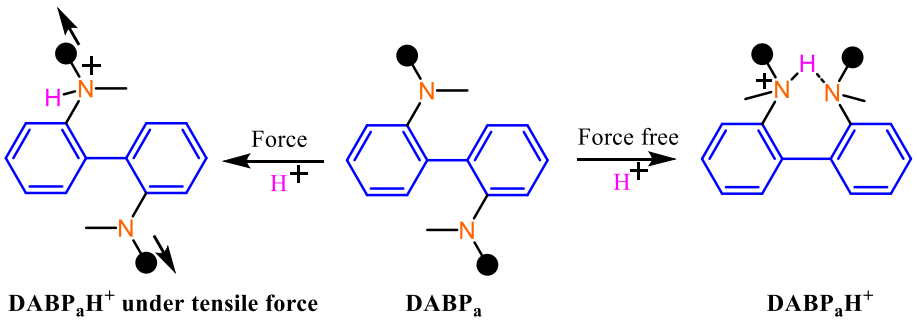

*Figure 44 – **$DABP_a$ have a force sensitive torsion angle and therefore force dependent pK_b.** Under force free conditions DABP can form an intramolecular N…H–N^+ interaction which is not possible when sufficient tensile force is applied.*

The magnitude of the effect can be estimated from the pK_b differences of protonated di and mono amine biphenyls (Figure 45 **c4-10** and **c4-11**) and 'proton sponge' analogue **c4-12**.[137] First, the pK_b of **c4-10** is 0.8 units smaller than that of **c4-11** (see the methods section for measurement details, Figure 58), suggesting the stabilisation of the protonated form by

intramolecular H–bonding less the entropic cost of the required conformation lock. Second the 10^4–fold greater H^+ affinity of **c4-12** relative to **c4-10** suggests the effect of destabilisation of the free base by Coulomb repulsion of the two lone pairs forced into close proximity by the sulfur molecular strap.[137] These trends suggest that DABP can be switched from a highly basic state, that resembles a proton sponge to a low basicity state, comparable to free dialkylaniline, simply by applying compressive or tensile force across its two N atoms.

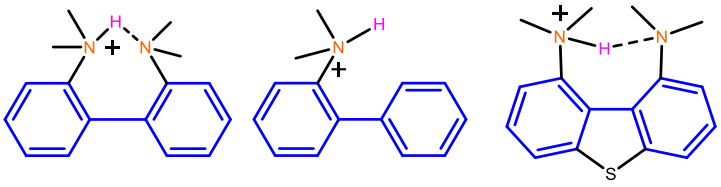

*Figure 45 – **The pK_b of DABP and its close analogues suggest DABP has a highly force sensitive pK_b.** The conjugate bases of DABP, N,N'–dimethyl–2–amino–[1,1'–biphenyl] and N,N,N',N'–tetra methyldibenzo[b,d]thiophene–1,9–diamine.*

Here I will describe two attempts to apply force to $DABP_a$: first, direct transduction of macroscopic force to the switching units via a polymer network and second, coupling the diamine to a photoisomerisable moiety (stiff stilbene) to yield macrocycles in which the biphenyl is forced into different conformations depending on the isomeric state of stiff stilbene. The goal of the former is to produce a material with a pK_b that is highly mechanosensitive allowing the uptake and release of protons to be reversibly controlled by external force. The latter project aims to improve on the existing attempts at optical control of solution pH.

A hydrogel with a mechanosensitive pK_b

The mechanosensitive $DABP_a$ was incorporated into a polymer network with the goal of producing a gel that sequesters protons from its environment in its relaxed formed and releases them when it experiences force. The mechanosensitive pK_b of the material is envisaged to occur because in the unstrained gel the polymer strands are slack enough not to impede the formation of the N...H–N^+ moiety upon protonation. In a stretched material however, contracting the polymer chains to enable hydrogen bonding would be associated with an unfavourable increase in strain energy Figure 46.

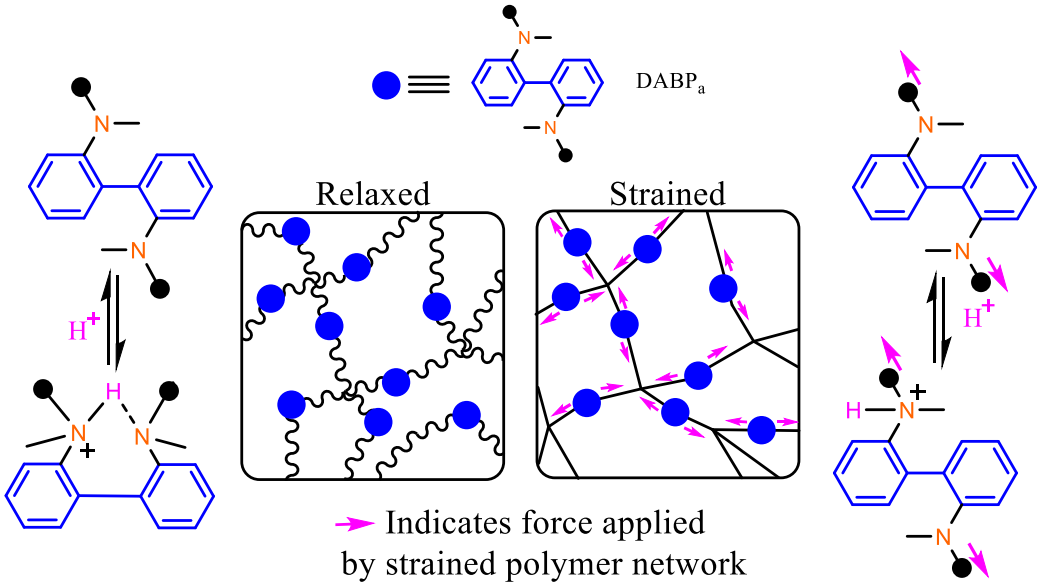

Figure 46 – ***When embedded in a polymer network gel, DABP$_a$ interaction with an acid depends on if the gel is strained or relaxed.*** *Sufficient tensile force transduced to the DABP$_a$ disfavours the geometry required to form an intramolecular N…H–N$^+$ bond strained.*

The initial goal of the project was to demonstrate that stretching the gel immersed in an aqueous solution of appropriate pH reduces this pH in correlation with the applied strain. Combined with the dependence of pK_b of the diamine on the force coupled to it from quantum–chemical calculations, the force experienced by an average polymer strand of the gel becomes accessible from the measured correlation between material strain and pH, potentially offering an alternative method of analysing force distributions in materials complementary to that of observing the changes in optically mechanosensitive molecules as a function of force.[16,148,149] Measuring the temporal evolution of the pH as a function of the straining rate of immersed samples of different aspect ratios under uniaxial and biaxial loading, would enable experimental tests of various kinetic models of internal mechanical and chemical equilibration of the gel under load.

Synthesis

I synthesized diamine–containing gel in 5 steps from commercial precursors (Scheme 3). Few syntheses involving a diamine biphenyl have been reported and I failed to reproduce the ones that could yield the target. Consequently, I designed my own synthetic sequence starting with the Steglich esterification of the diamine with commercial 1–carboxy–but–4–yn to give the di–alkyne containing di–amide **c4-15** quantitatively. The crude product was reduced with $LiAlH_4$ followed by methylation with CH_3I to yield the desired di–alkyne dimethyl amine monomer **c4-17.**

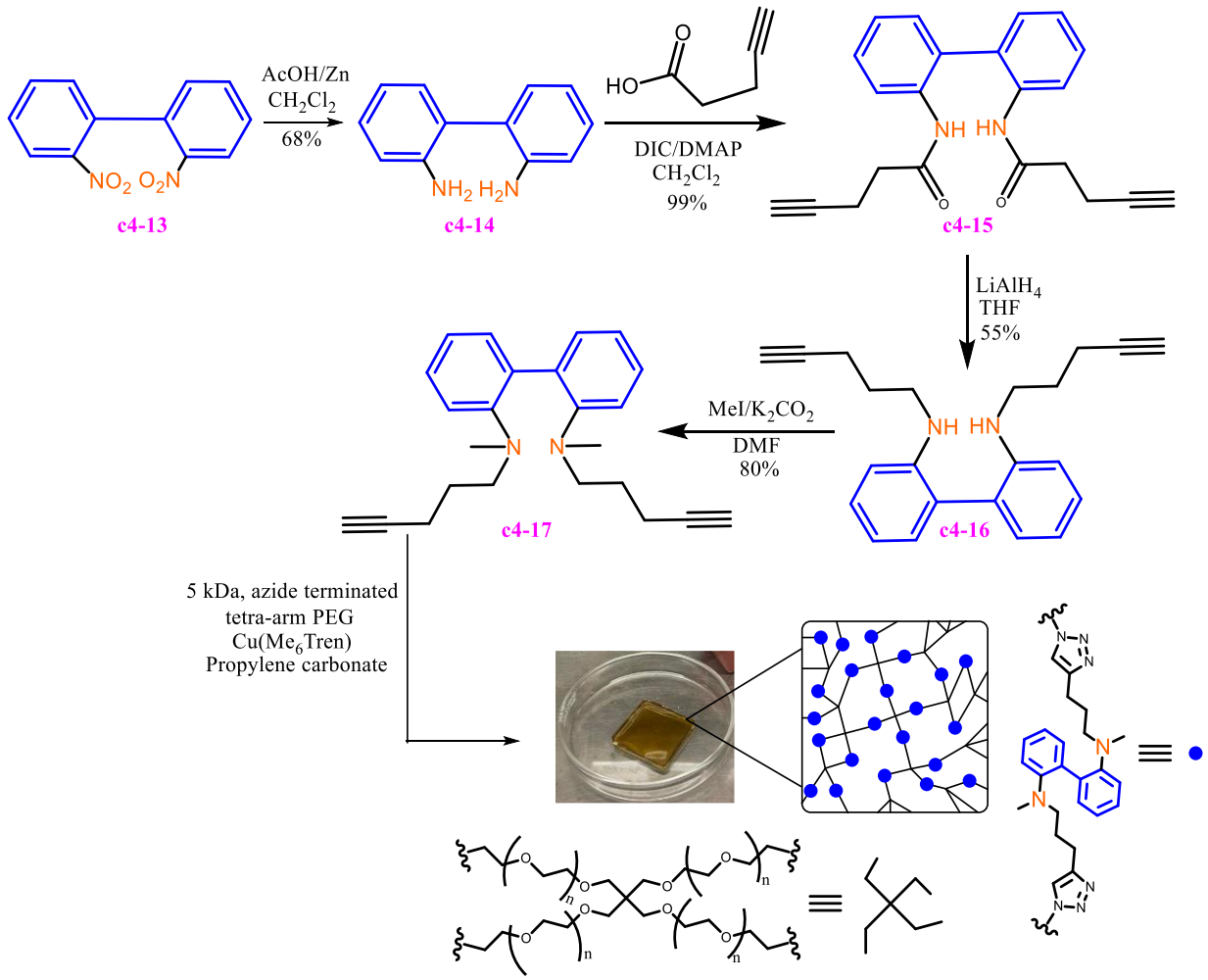

Scheme 3 – ***The synthetic route used to produce a hydrogel containing a DABP$_a$.***

The gel was prepared in a silicone mould using a literature procedure.[150] The gel was washed 5 times with distilled water, which gradually reduced the colour of the gel to colourless, indicating the successful removal of the catalyst.

Results

Unlike structurally related free diamines which deprotonate neutral red in water (see method section, Figure 58) a single piece of pristine gel added to a solution of neutral red did not change its absorption spectrum even when containing up to 10 equivalents of the diamine (Figure 47). However when the same piece of gel was cut up with a razor inside the cuvette the change in the spectrum suggested deprotonation of ~7% of the indicator. This result was reproducible and shown not to be a consequence of contamination by the razor.

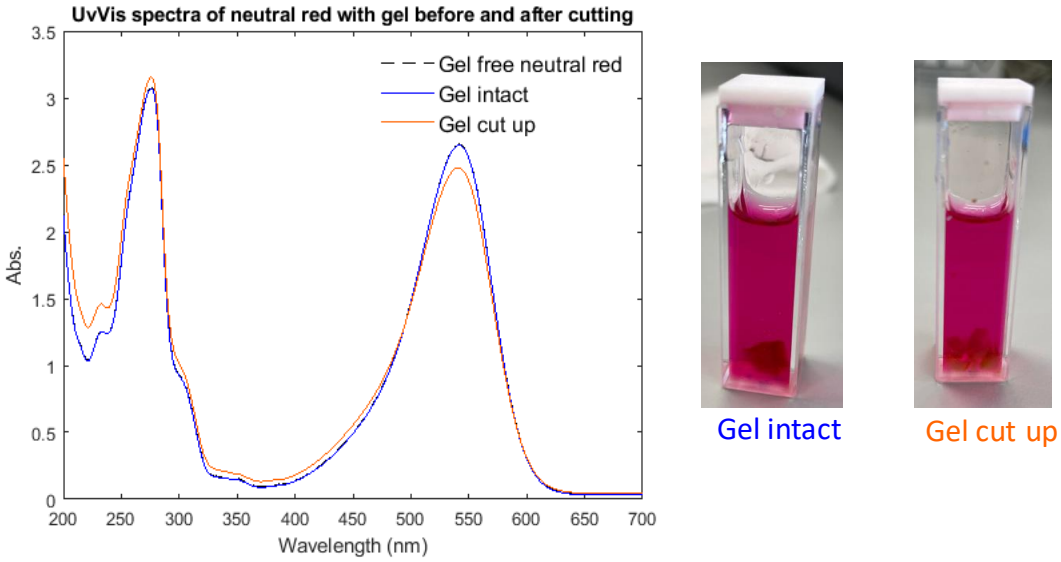

Figure 47 – ***A gel containing a DABP$_a$ interacted differently with a solution of neutral red depending on its shape.*** *The Uv-Vis spectra of neutral red before addition of gel (dashed line), with intact gel (blue line) and after cutting up the same gel with a razor (orange line).*

To explore whether an alternative solvent may be more conducive to the projects goals two pieces of hydrogel were dehydrated using a vacuum oven. One was swelled in a solution of the indicator in MeCN and the other in pure MeCN. The UvVis spectra of the neutral red solution was unchanged by the addition of the PEG swelled in MeCN and by the addition of the dehydrated polymer, even after 5 hours of allowing the latter gel to swell in the solution.

Discussion

I could find no literature to help explain the apparent lack of uptake of H^+ by a gel immersed in an aqueous solution of neutral red. I speculate that the PEG network, which has been reported to have unusual acid/base properties, is competing with H^+ for the amine groups preventing any further protonation.[151] My choice of a PEG gel was motivated by three considerations: first, availability of a 5 kDa tetra arm azide terminated macromer that can be easily cross–linked with synthetically accessible alkyne–terminated biphenyl diamine derivatives. Second, it is hydrophilic enough to allow free exchange within the aqueous indicator solution, allowing the measurements to be conducted in water which is most practically applicable. Lastly, facile mechanochemical dissociation of cyclobutane–based mechanophores embedded in PEG gels of identical topologies to those used here was demonstrated in bulk gels under tensile load (Figure 48).[152]

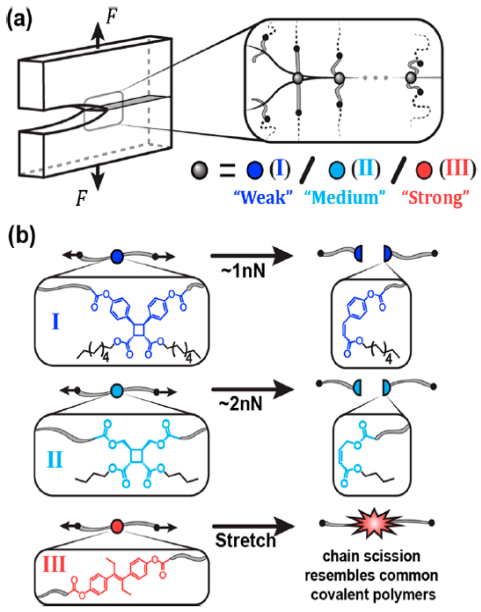

Figure 48 – ***PEG polymer networks have been used to demonstrate mechanochemistry.*** *The structure of mechanophores whose response to force was shown to differ by observing the fracture energy of PEG polymer networks.*[152] Reproduced with permission.

I plan to explore alternative polymer network architectures that the literature has established to be compatible with the acid/base chemistry of its monomers. Methyl acrylate structures have been used for such application.[147] Synthesizing an $DABP_a$ with a compatible linker to incorporate it into the network, such as **c4-21**, offers an alternative realisation of the projects goals. Scheme 4 shows a plausible route.

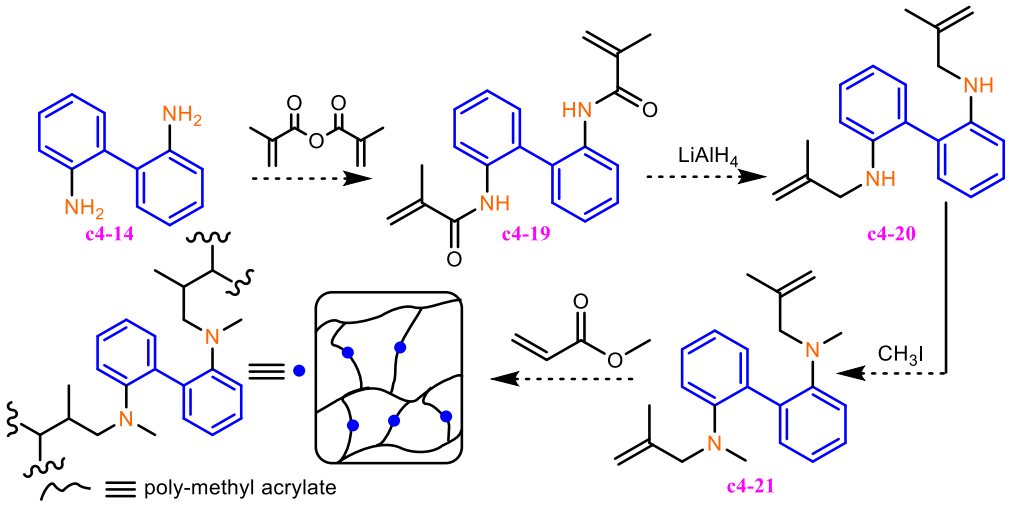

Scheme 4 – ***A proposed synthetic route to an alternative polymer network containing a $DABP_a$.***

Modelling

Any further efforts in this project will be informed by the model I developed to simulate the acid/base equilibria between force–coupled biphenyl and an acid (HA), which is independent of the specific polymer architecture around the biphenyl amine. Figure 49 shows the equilibria established when force is applied to a fraction of the biphenyl moieties in the presence of an indicator, HA, assuming no secondary protonations occur on either biphenyl species. The less basic conformer has a longer $_{Me}N...N_{Me}$ distance and hence is stabilised by tensile force.

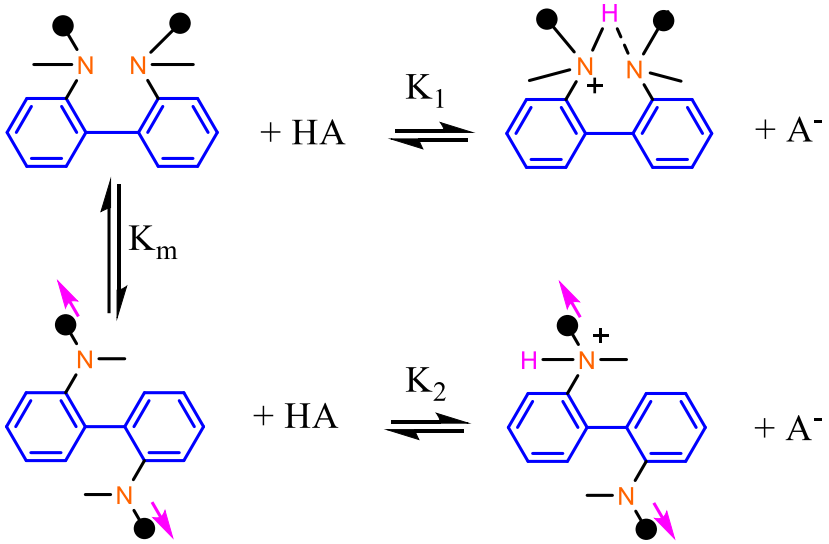

*Figure 49 – **The equilibrium established when a DABP moiety is subjected to tensile force in the presence of a suitable acid, HA.** K_m is a mechanochemical equilibrium constant.*

Equation 22 relates the concentration of spectroscopically detectable anion, $[A^-]$, to parameters that can be estimated (K_1 and K_2), controlled, T_a and T_b (the total concentration of indicator and base respectively) or systematically varied (K_m) to estimate how the protonation state of biphenyl dependence on load–dependent distribution of its conformations, K_m. The derivation of Eq. 22 is described in the methods section. Eq. 22's behaviour in the limits is sensible: for K_m=0 the absorbance has no dependence on K_2 and the equation collapses into that which is derived using the same method only considering K_1. For K_1=K_2 the equation has no dependence on K_m. For K_m=1 i.e. 50% conversion of relaxed biphenyl into constrained biphenyl then the average of the two K's appears in the equation, and for very high values of K_m the dependence of the absorbance on K_1 shrinks to negligible values.

$$\frac{[A^-]^2}{([T_a]-[A^-])(T_b-[A^-])} * \frac{K_m+1}{1+\frac{K_m K_2}{K_1}} - K_1 = 0 \quad \text{Eq. 22}$$

Simulating the system had two aims. The first aim was to enumerate the functional dependence of $[A^-]$on K_m because experimentally accessible value of K_m may be limited by the maximum load that the gel can sustain without experiencing chain fracture on the timescale of experimental measurements (or subsequent use). The second aim was to estimate the T_a/T_b ratio corresponding to the maximum–response regime (maximum $|\partial[A^-]/\partial K_m|$) to increase the chances of detecting the generation of even a small amount of low–basicity conformer. In my calculations K_1 was equated to the measured basicity of free DABP, which is equivalent to neglecting the effect of the polymer matrix, specific *N*–substituents and potentially secondary protonation on the basicity. These assumptions have good support in the literature, the former because of the small difference in pK_b of methyl vs ethyl substituted proton sponge analogues and the latter because of the 4 unit difference in the first and second pK_b of 1,4–diaminobenzene.[153]

A Matlab script was written to take estimated inputs for control parameters and systematically vary the value of K_m for different values of T_a (see methods section for script details).

Figure *50*a shows how for values of K_m in 0.25 increments from 0 to 5 the fractional change in absorbance relative to K_m=0 depends on the total concentration of T_a. The value explored were between 0.025 and 2 equivalents relative to the base. For all values of T_a 1 equivalent gave the largest difference.

Figure *50*b shows how, with T_a set to the optimised value, different values of K_m translate into changes in $[A^-]$ (and therefore absorbance). At 90% activation an absorbance change of over 25 % would be expected but more promising still is that at tiny (2%) levels of activation

a

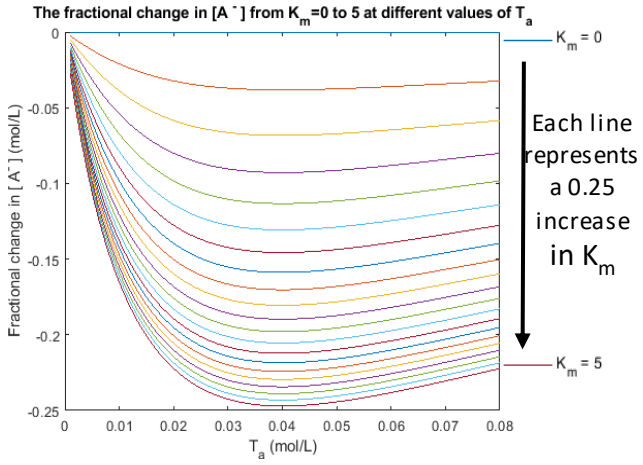

b

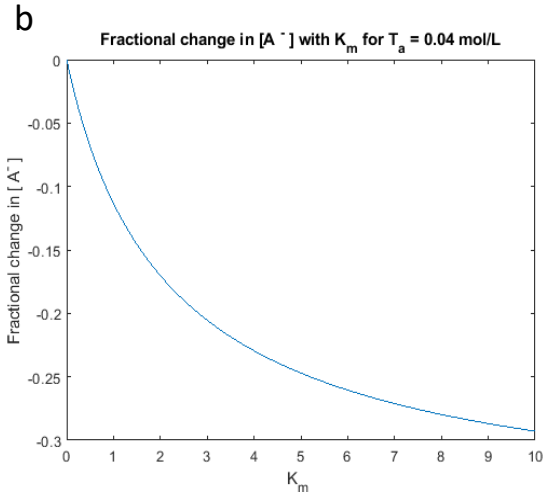

statically significant changes in UV would be expected (~1%).

Figure 50 – ***Modelling equation 22 allows simulation of a DABP$_a$ polymer network under various conditions*** *A) the relationship between T_a and the fractional change in [A^-] relative to K_m=0 for difference values of K_m at T_b=0.04 M. b) the relationship between the fractional change in [A^-] and K_m for 1:1 ratio of T_a and T_b.*

Optical control of solution pH

Stiff stilbene has been used extensively to apply tensile forces of up to 0.8 nN to small reactive moieties.[24,154] Here I describe the successful synthesis and investigation of a macrocycle containing a $DABP_a$ and stiff stilbene. These macrocycles are too short to accommodate simultaneously the preferred planar geometry of *E* stiff stilbene and the short N…N separation in biphenyl diamine required for the bridging geometry of H^+ (Figure 51B). In previously reported macrocycles with sufficiently short linkers,[114] *Z* stilbene applies a compressive force to the rest of the molecule which would enforce close N…N distance of the biphenyl, thus destabilizing the free base by increasing the Coulombic repulsion of the electron densities of the N atoms, and stabilizing the protonated form by allowing H^+ to form a bridge between the two nitrogens. *Z* to *E* isomerization of stiff stilbene eliminates these effects, thereby reducing the pK_b of the macrocycle. As illustrated by the proton sponge compounds in Figure 45 the extent of pK_b change depends on how constrained the biphenyl is in both isomers. At the extreme, the local geometry of diamine in the *Z* isomer mimics that of a proton sponge, whereas the biphenyl of the *E* isomer is locked in a conformation where neither N…N repulsion nor, N–H…N^+ binding mode is energetically accessible, leading to ΔpK_b >4.5 units between the *E* and *Z* containing macrocycles.

Computations

I relied on quantum–chemical calculations to design macrocycles with the largest accessible ΔpK_b. So far, I've assessed two molecular architectures that differ in the nature of the linkers connecting the 6 and 6' carbons of the stiff stilbene to biphenyl. In one design, the linkers are simple aliphatic ethers, and in the other it is a triazole derivative, which is both easy to synthesize and whose rigidity magnifies the structural differences between the *Z* and *E* isomers of stiff stilbene (Figure 51a). The ranking of candidate macrocycles for subsequent synthesis was based on computations of standard energies of two reactions $ZH^+ \rightarrow EH^+$ and $Z \rightarrow E$: the first informs on ΔpK_b of the two isomers and the second suggests how accessible the *E* macrocycle is by photoisomerisation of the *Z* analogue (the fraction of the *E* macrocycle in a photostationary state decreases with the excess strain energy of this isomer relative to the *Z* congener) (Figure 51).

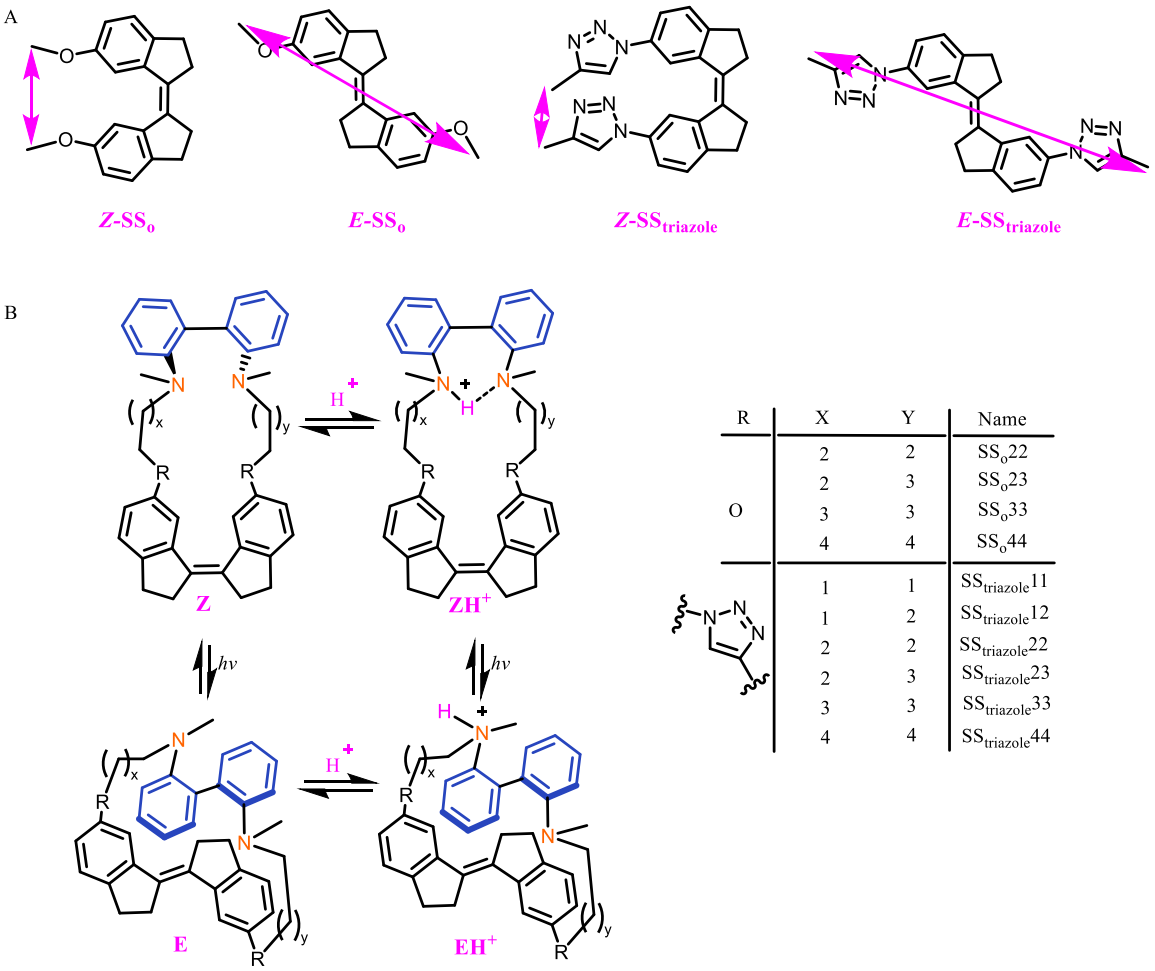

Figure 51 – ***The structures studied as potential pK$_b$ photoswitches*** *A) Compares the change in distance between the two points in which a linker connects to the rigid moiety of SS$_o$ and SS$_{triazole}$ structures. B) the equilibrium established when Z macrocycles are irradiated to form E in a solution with a source of H$^+$.*

I first generated conformers of both *E* and *Z* isomers of the 10 macrocycles and optimized minimum energy structures at BLYP 6–31+G* allowing an estimate of the energy difference of *E* and *Z* macrocycles (Figure 52b). As expected macrocycles with larger linkers have smaller *E* vs *Z* energy differences. The sudden increase in *E* energy relative to *Z* for the **SS$_O$44**, which bucks this overall trend, suggests that the structure identified here was in fact a local minimum considerably higher in energy than the global minimum. The absence of such dramatic deviations from the trend for SS$_{triazole}$ suggests that the multiple iterations of modifying and optimizing structures of both diastereoisomers conducted for these macrocycles is warranted if resource consuming. This strategy was pursued for triazole structure only because this novel stilbene lacks historical precedent to assist judgement of which structures look most sensible.

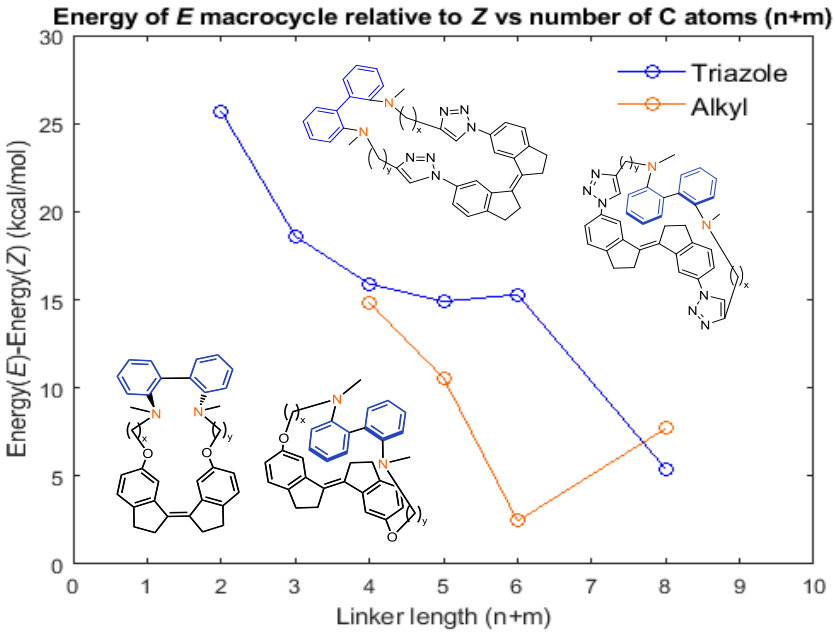

Figure 52 – ***Linker length controls strain energy in SS macrocycles.*** *The relationship between the linker length and E to Z electronic energy difference of triazole (blue line) and alkyl (orange line) macrocycles. Lower E to Z difference is favourable for the accessibility of the E macrocycle via photoisomerisation. The energy refers to electonic energy.*

Structures that had *Z*→*E* energies < 15 kcal/mol were then modified to contain a single proton (excluding **SS$_o$23** since its unsymmetrical structures makes it a more difficult synthetic target and should only be pursued in the absence of other viable candidates). For short linker species that previous experience indicated would subject the largest forces to the biphenyl, only unbridged protonated *E* structures were explored, for others both unbridged and bridged *E* structures were optimized to verify that the tensile force in the *E* isomer was sufficient to prevent H–bonding. Once obtained the optimized *Z*H$^+$ and *E*H$^+$ structures allowed me to calculate the energy associated with *E*H$^+$ → *Z*H$^+$ (a measure of the combined effects of differential Coulomb repulsion and H–bonding ability in the two isomers).

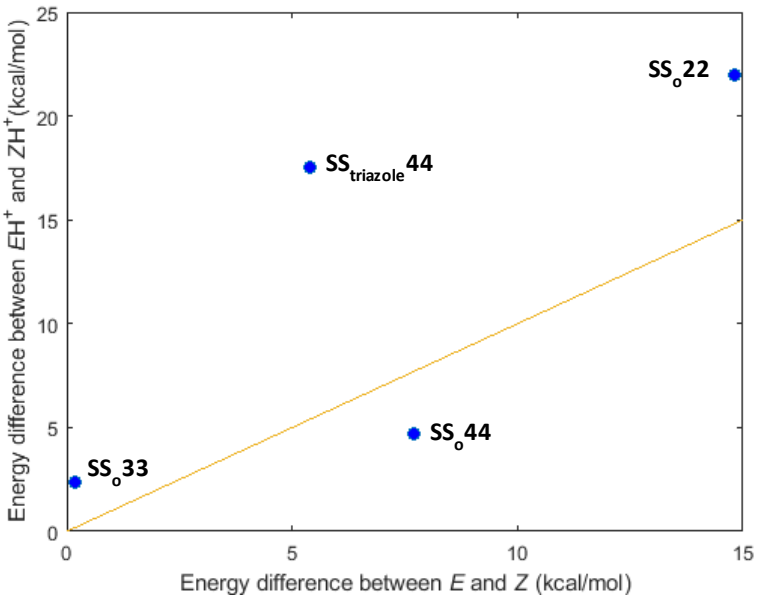

Figure 53 – ***The balance between accessibility and effectiveness as a photoswitchable base depends on both E→Z and EH⁺→ZH⁺ energy differences.*** *The relationship between the energy difference of E and Z isomers in their neutral and protonated states. The yellow line indicates no change in energy difference upon protonation.*

The best candidates photobases are ones for which the *E* isomer is much higher in energy than Z when both are protonated than when both are neutral i.e. those that fall above the yellow line in Figure 53. As such **SS$_o$22** and **SS$_{triazole}$44** are the most promising candidates. Unlike **SS$_o$33** (for which the *E*→*Z* *E*H⁺→*Z*H⁺ energy changes are similar), and **SS$_o$44** (for which the energy increase of the *E* relative to *Z* isomers is reduced upon protonation) the **SS$_o$22** and **SS$_{triazole}$44** have a *Z* isomer specific hydrogen bond (Figure 54).

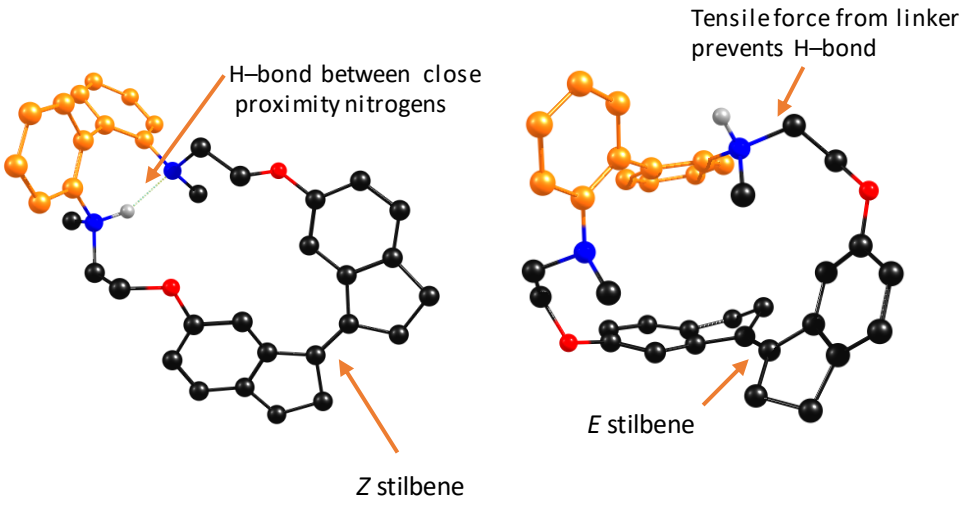

Figure 54 – ***SS$_o$22 has an isomer specific H–bond****. Optimized geometries of a) Z– and b) E–SS$_o$22H⁺. Importantly the N…H–N⁺ H–bond is specific to the Z conformer which reduces its pK_b relative to E.*

Synthesis

The synthesis of **SS$_{triazole}$44** requires novel synthetic routes to be devised so I prioritized **SS$_o$22**, which is currently the only macrocycle to be successfully synthesized so far in overall isolated 29% yield according to Scheme 5.

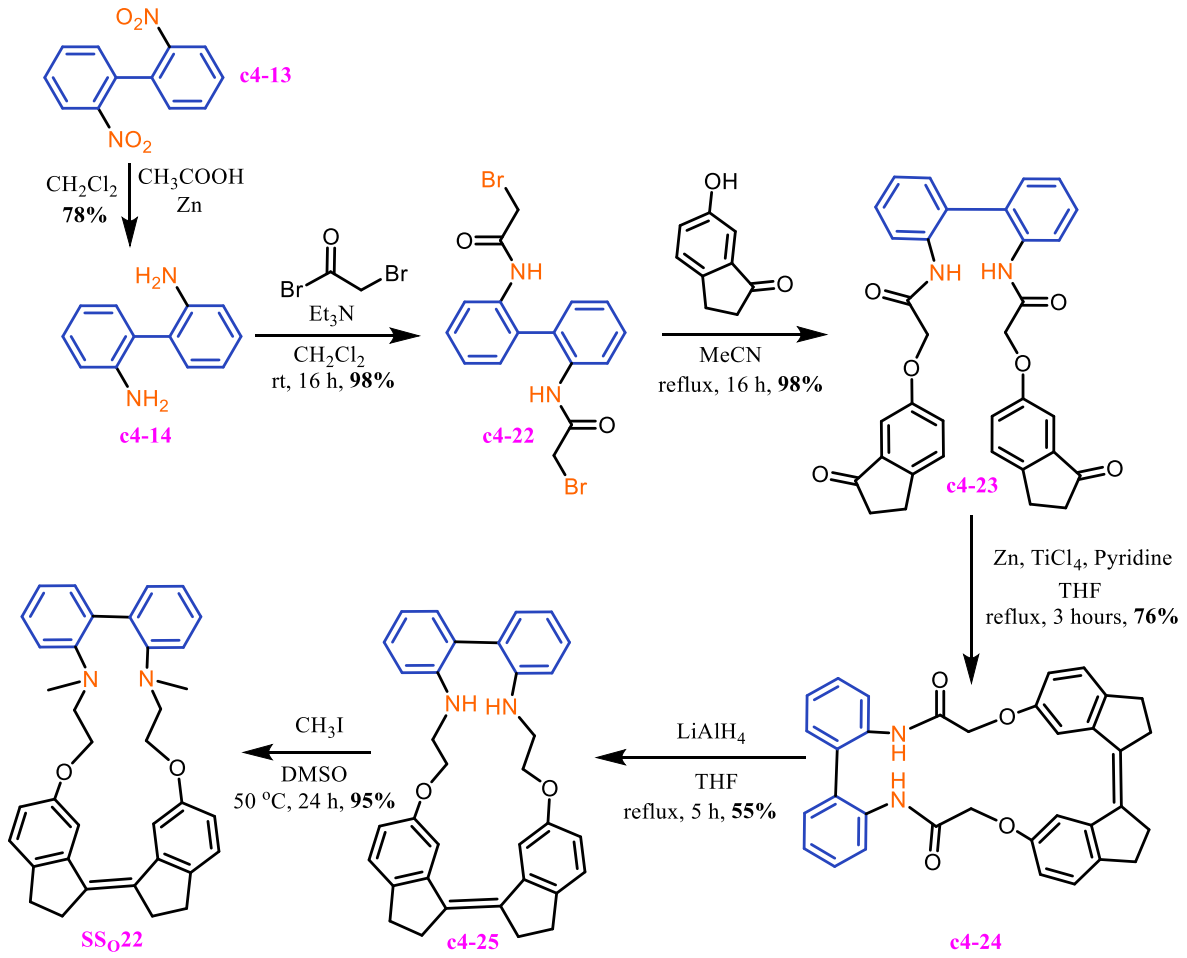

Scheme 5 – ***The synthetic route successfully used to synthesise SS$_o$22.***

The synthesis of **SS$_o$22** requires two parts, the formation of a suitable DABP$_a$ and its incorporation into a stiff stilbene macrocycle. The few reports of substituting diamine biphenyl are discussed in the methods section below and were not successful in this project, which instead required the formation of a diamide that was reduced and methylated to give the desired DABP$_a$. The stiff stilbenes was formed from a 'build around' route (Scheme 1, chapter 1), in which an intramolecular coupling of the two indanones attached to the biphenyl diamine moiety in **c4-23** yields the stiff stilbene alkene **c4-24**.

The crude ^{1}H NMR spectrum of the final product (**SS$_o$22**) is shown in Figure 55 with the diastereotopic CH_2 groups appearing as 4 unique peaks. 2D NMR experiments indicate that the additional peaks at 4.3 and 4.7 ppm that are not expected for the product may be a result

of multiple diastereoisomers present in the product, although the evidence for this is not conclusive (method section Figure 73).

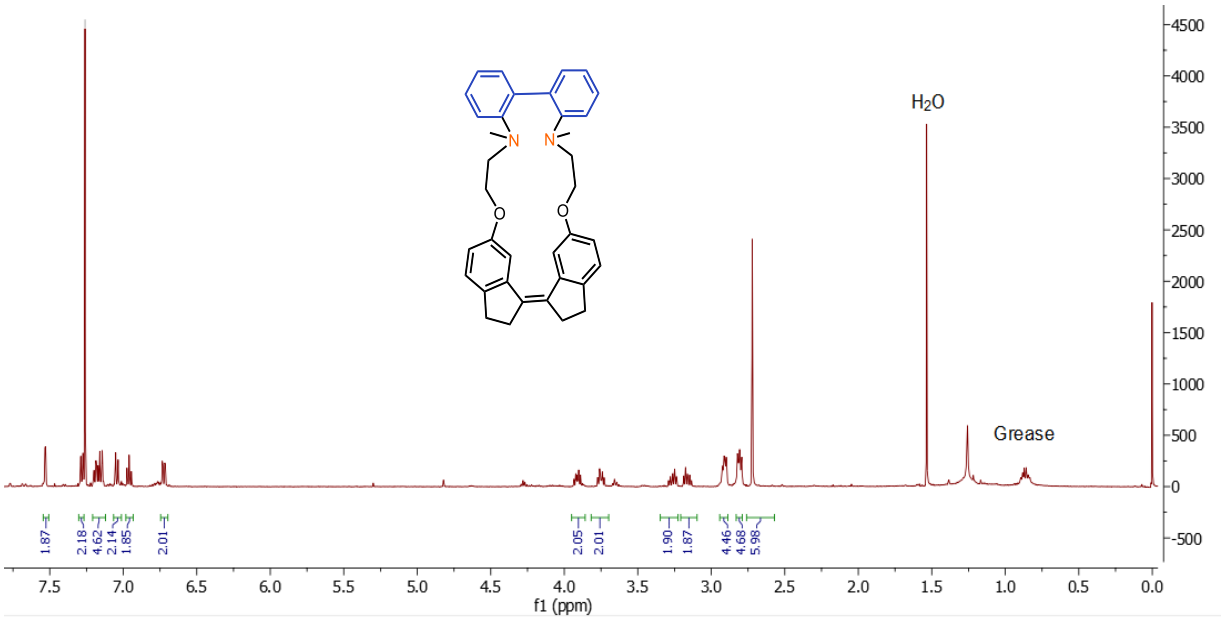

*Figure 55 – **^{1}H NMR spectra of SS$_O$22 in CDCl$_3$.***

I obtained a PSS of *Z* and *E* macrocycles by irradiation of a dilute solution of the isolated *Z* isomer at 354 nm. The small change in the UvVis spectra of the PSS compared to pure *Z* is consistent with the observations made by Kean *et al*. with a macrocycle of similar structure for which the *E* isomer was calculated to be similarly destabilised relative to the *Z* isomer and represented around 4% of the photostationary state (PSS).[114] Irradiation of a solution of the macrocyclic amide precursor lead to gradual bleaching of stiff stilbene absorbance without indication of isomerization as evidenced by time–lapsed absorption spectra.

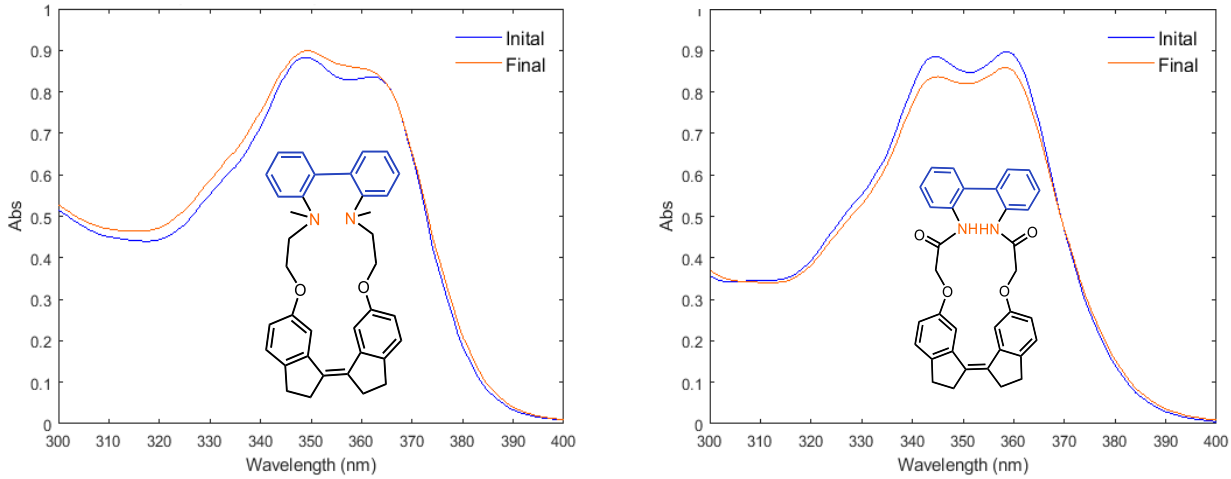

*Figure 56 – **Irradiating Z–SS$_O$22 macrocycle and its amide analogue isomerises a small amount of the Z isomer to the E.** The change in UvVIs spectra upon irradiation with 365 nm light in CH$_2$Cl of a) **SS$_O$22** and b) its precursor amide **c4-25.** The decrease in absorbance in b suggests bleaching of the macrocycle.*

The pandemic interrupted lab work in this project and the macrocycle deteriorated over the months I was unable to access the lab, preventing me from measuring its pK_b. Although since then I prioritized other projects I envision two possible future directions for this project. The first involves synthesizing the **$SS_{triazole}$44** species as a potential pH switch that achieves the large pK_b changes but has an *E* isomer that is more accessible and therefore a potentially more useful pH switch. Alternatively isolating the *E* isomer of **SS_o22** and studying the pH dependence of its isomerisation kinetics could establish a biologically compatible trigger for allosteric induced changes to its kinetics (analogous to the metal complex discussed in chapter 3).

Methods

Synthetic behaviour of DABP

In both projects described above several synthetic routes based on literature were unsuccessful. The existing literature on synthetic manipulations of diamine–[1,1'–biphenyl] directly into N–tetralkyl substituted species exists only for tetramethylation using iodomethyl or dimethyl sulphate meaning a brief summary of my experience in the area may be of value.

The two step transformation from biphenyl diamine to N,N'–dimethyl biphenyl–2,2'–diamine is well established and offers an alternative starting point to the simple diamine analogue. However, searches for reactions of this species to substitute the amine hydrogen for a new group results in just 3 types of reactions reported in the last 50 years.[155-157] Of the 3 reactions, only Mazzati. et al's report of acylating dimethyl biphenyl aniline with isobutyryl chloride (Scheme 6a **c4-27a**) (albeit requiring prep HPLC to purify) and Passera et al's nucleophilic substitution (**c4-27c**) Scheme 6b are useful precedents guiding initial synthetic attempts in this project.

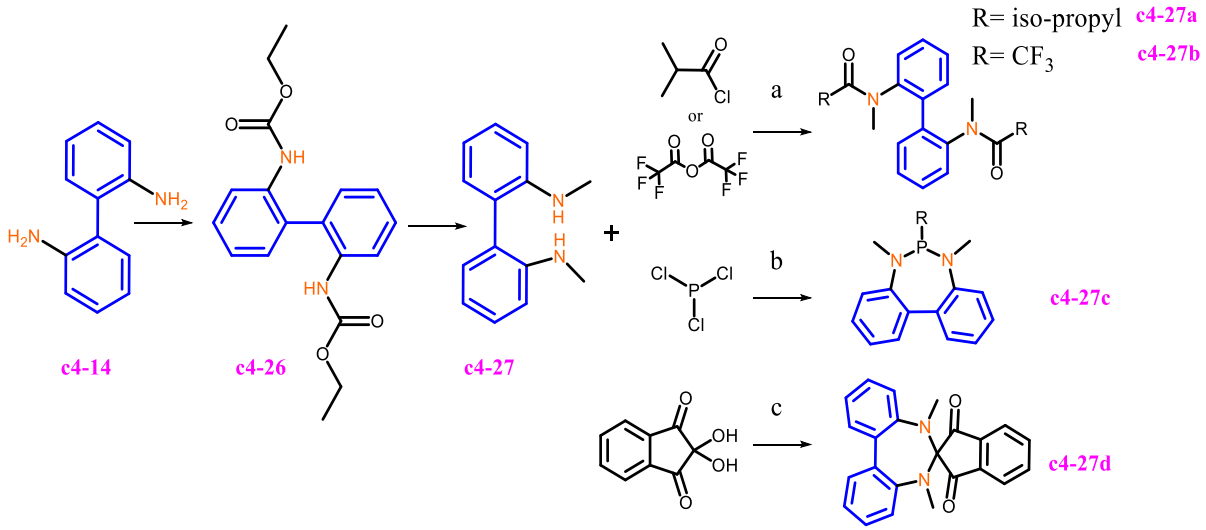

Scheme 6 – ***The reported reactivity of N,N'–dimethyl–2,2–diamine–[1,1'–biphenyl].***

These reactions informed three synthetic routes to the target macrocycle (Scheme 7) exploiting either nucleophilic substitution or acetylation reaction of the *N*–methyl biphenyl. However neither reaction turned out to be compatible with the partner reactants here. Namely, in attempts to utilize a nucleophilic substitution reaction to the macrocycle (Scheme 7 Route 1) the dimethyl diamine proved insufficiently nucleophilic to react with the dibromo stiff stilbene analogue (**c4-28**) with multiple reaction conditions including strong bases returning only starting materials. Alternatively in an attempt to avoid methylation in the final step by introducing N*Me* to the starting amine, and then building the stiff stilbene around this structure (**c4-31**, Scheme 7, Route 2) , the aniline analogue (**c4-27**) proved incompatible with

acylation – using bromo acetyl bromide results in a messy spectrum of unidentified peaks indicative of multiple aromatic containing products. Problems of reaction technique were ruled out by demonstrating the successful high yield and purity synthesis of acetyl bromide methyl aniline (**c4-29**), which could also be further reacted with the indanone in the analogous desired fashion (**c4-30**, Scheme 7, Test synthesis).

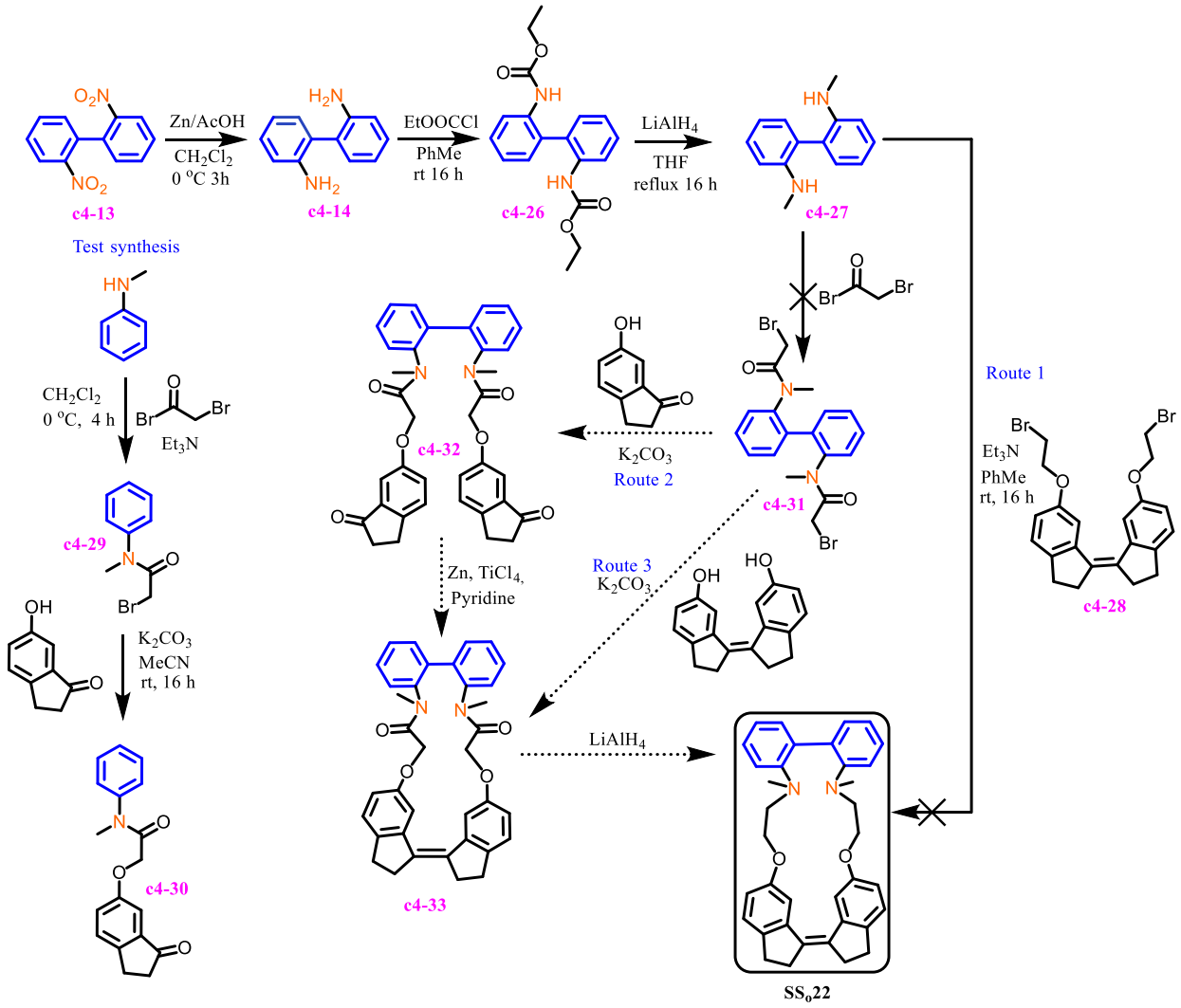

Scheme 7 – ***The reactivity of N,N'–dimethyl–2,2'–diamino–[1,1'–biphenyl] is not as would be predicted by analogy to aniline****. Two alternative routes to the macrocycle that were unsuccessful. The test synthesis was conducted to ensure the reaction technique was not the source of the lack of reactivity.*

Whilst the Steglich esterification was found to be the best route to the desired monomer for the gel synthesis, it was not always a reliable tool for substituting the diamine – its success depended on the carboxylic acid used. For example, an initial attempt to add the alkyne **c4-37** to the diamine (which was motivated by the availability of the precursors (**c4-35**) in the lab and the possibility of avoiding the purchase of the expensive pent–4–ynoic acid eventually used) led to extremely low conversion of the 5–(prop–2–yn–1–yloxy)pentanoic acid (**c4-37**) and the diamine, **c4-14**. Yet the same carboxylic acid without the alkyne gave the product

amide (**c4-39**) in good yield but produced only starting material when reacted with the prop–2–yn–1, which contrasts with the success of the same reaction on the methyl ester analogue **c4-35** which occurred in high conversion (albeit in poor yield due to messy workup requirements).

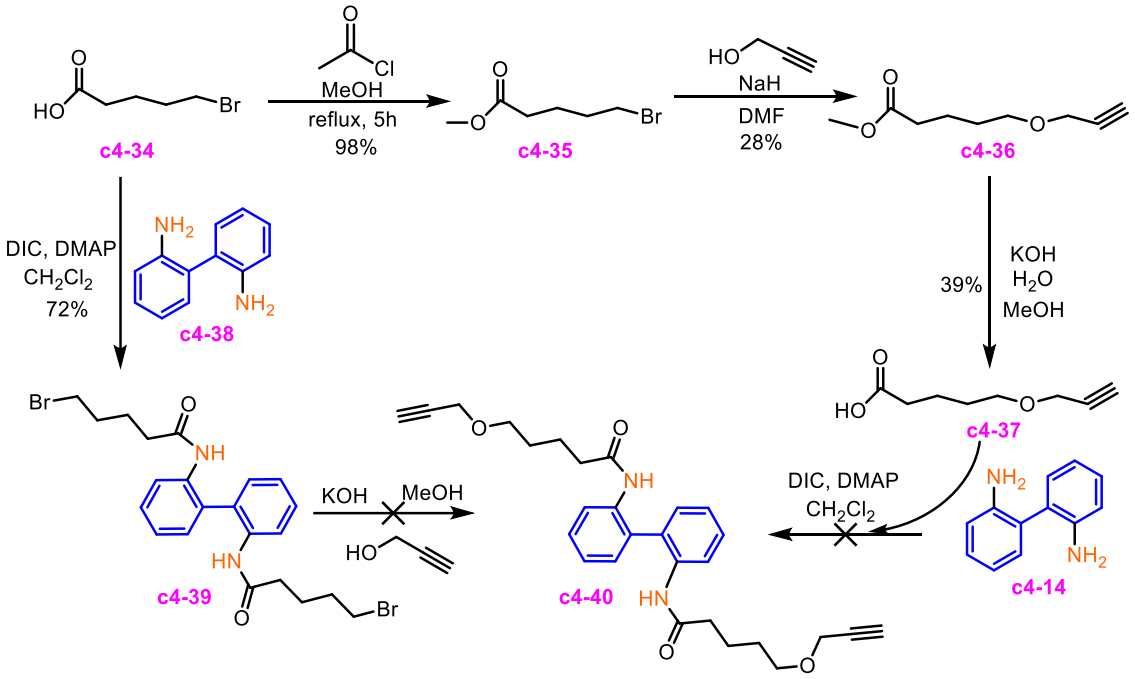

Scheme 8 – **The Steglich esterification of 2,2'–diamino–[1,1'–biphenyl] is highly sensitive to coupling partner**. Two synthetic routes to a dialkyne diamide (**c4-40**) were unsuccessful.

Finally, in both projects the reduction of the dinitro species was required as the first step, the overall yield of both routes could be improved with access to appropriate high pressure chemistry equipment since the yield suffers from the Zn catalysed acid reduction of the nitro compound (**c4-13**), which was pursued only because the reported quantitative palladium catalysed reduction[158] required a high pressure H_2 stream. Despite reports of 94% yields for Zn catalysed conversion,[159] in the ~20 times this reaction was carried out over the course of both projects the Zn mediated single electron transfer reduction in the presence of acetic acid only ever achieved 84% conversion to desired product because upon complete consumption of the starting material a mixture of the 2,2'–diamine–[1,1'–biphenyl] (**c4-14**) and benzo[c] cinnoline (**c4-41**, Figure 57) in a 1:7 ratio is present regardless of reaction time, temperature, solvent or concentration. The impurity was identified by HRMS (found: 181.0761 m/z; calculated 181.0766) and confirmed by comparison with a reported ^{1}H NMR spectrum.[160] The two components then require separation by column chromatography which reduces the converted yield into a yield typically around 55% (for <100 mg scales, analytically pure diamine can reach 68% isolated yield). Alternative work ups were attempted but the impurity could not be removed by extracting a solution of the crude material in 2 M HCl with CH_2Cl_2

with 5% (mol) remaining even after 25 extractions. The poor result suggests that the two species have comparable basicities and H_2O/CH_2Cl_2 partitioning coefficients.

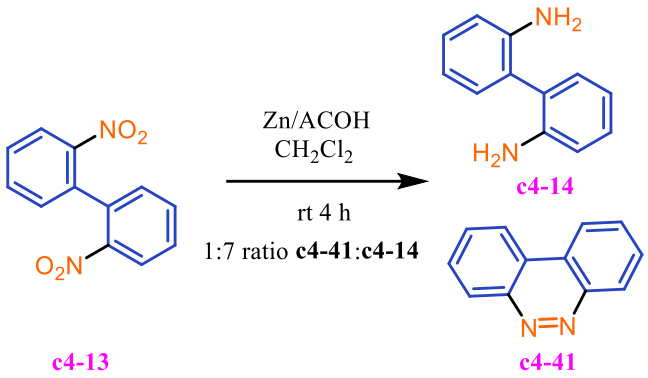

Figure 57 – ***Zn/AcOH reduction of dinitro(c4-13) is limited in yield by the persistent presence of (c4-41). c4-41*** *or benzo[c] cinnoline is a side product formed in ~14% during the reduction of 2,2'–dinitro–[1,1'–biphenyl].*

Determination of a suitable pH indicator for diamine biphenyl

To ensure there was a suitable indicator for pK_b measurements (ideally one with a pK_b in–between the values of the two states of compressed and extended $DABP_a$) and also to provide an estimate of K_1 and K_2 for the modelling of the gel with the most accurate values possible, I synthesized DABP and its single amine analogue N,N–dimethyl–[1,1'–biphenyl]–2–amine from their amine precursors and measured their UVVis spectra with various indicators of known pK_b. Neutral red proved such a suitable indicator and the pK_b of both mono and di free biphenyl amine were determined by measuring the UvVis changes of a solution of neutral red, with pK_b 6.5, when 1 equivalent of each amine was added. To enable fitting of the resulting spectra the reference data for fully protonated and fully deprotonated neutral red and each amine was required. The former was obtained by measuring known concentration of neutral red in water, followed by remeasuring the spectra after the addition of 2 equivalent NaOH, assumed to fully deprotonate the indicator. The latter were obtained by measuring UvVis of the amines before and after the addition of two equivalents of acetic acid. These reference data were then used to fit the spectra obtained when 1 equivalent of each amine was separately added to a solution of indicator using the lsqnonlin fitting function in Matlab to determine the ratio of protonated to deprotonated indicator. From this the pK_b of the amines could be obtained using eq. 24 below. Plugging in the measured values for $K_{NR–MDABP}$ and $K_{NR–H2O}$ gives a pK_b of the biphenyl diamine in agreement with the reported of 6.1 but a much lower pK_b for biphenyl monoamine (6.9) than that approximated by analogy with *N,N*–methyl aniline (8.9).

$$K_{NR–MDABP}=\frac{[BH^+][NR^-]}{[B][NR]} \quad \text{Eq.23} \qquad K_{NR–H2O}=\frac{[H_3O^+][NR^-]}{[H_2O][NR]} \quad \text{Eq. 24}$$

$$\frac{Eq.2}{Eq.3} = K_{B-H2O} = \frac{[H_3O^+][B]}{[H_2O][BH^+]} \quad \text{Eq.25}$$

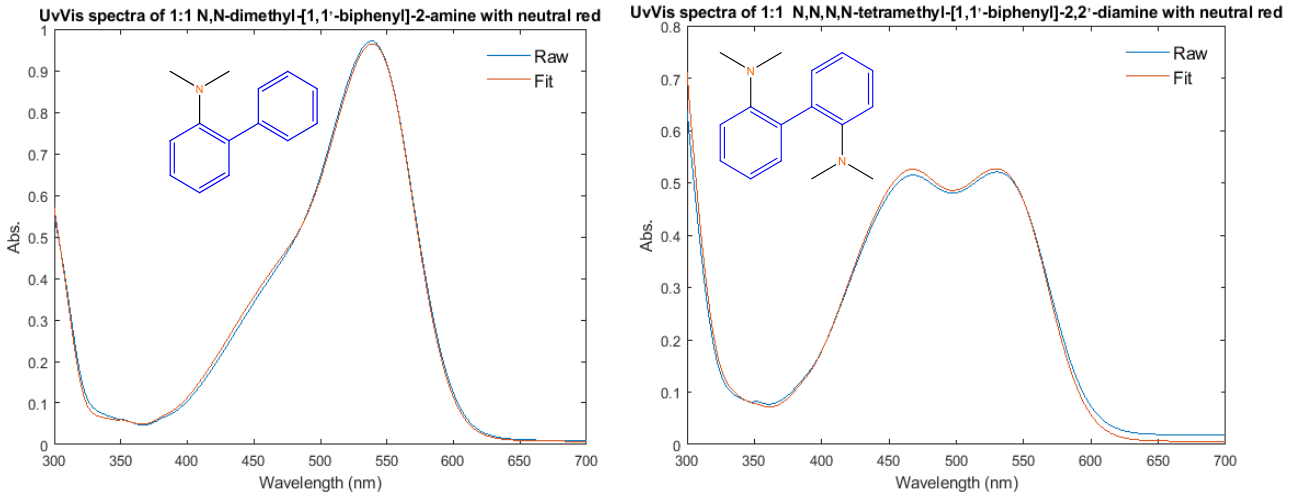

Figure 58 – ***Neutral red is deprotonated to different extents by N,N–dimethyl–[1,1'–biphenyl]–2–amine and DABP.*** *UVvis spectra of neutral red with 1 equivalent of a) N,N–dimethyl–[1,1'–biphenyl]–2–amine and b) DABP.*

Derivation of eq 1

Eq. 26 $K_1 = \frac{[B_1H^+][A^-]}{[B_1][HA]}$ Eq. 27 $K_m = \frac{[B_2]}{[B_1]}$ Eq.28 $T_a = [HA] + [A^-]$

Eq.29 $[A^-] = [B_1H^+] + [B_2H^+]$ Eq.30 $K_2 = \frac{[B_2H^+][A^-]}{[B_2][HA]}$

Eq.31 $T_b = [B_1] + [B_2] + [B_1H^+] + [B_2H^+]$ Eq.32 $Abs = [A^-].\epsilon.l$

$\frac{eq.26}{eq.30} = \frac{K_1}{K_2} = \frac{[B_1H][B_2]}{[B_2H][B_1]}$ → **eq.27**→ $[B_1H^+] = \frac{K_1}{K_mK_2}[B_2H^+]$ → **eq 29.** → $[B_1H^+] = \frac{K_1}{K_mK_2}([A^-] - [B_1H^+])$

Rearrange → $[B_1H^+] = \frac{[[A^-]}{1 + \frac{K_mK_2}{K_1}}$ (Eq. 33)

Use eq. 26, eq. 31 and eq. 27 to get $B_1 = \frac{T_b - [A^-]}{K_m + 1}$ (Eq.34) use **Eq 27** to get $B_2 = \frac{T_b - [A^-]}{\frac{1}{K_m} + 1}$ Eq 35

eq. 26 + eq. 28 give $K_1 = \frac{[B_1H^+][A^-]}{([T_a] - [A^-])[B_1]}$ (eq. 36)

use eq. 36 and eq. 35 in eq. 33

$K_1 = \frac{[A^-]}{([T_a] - [A^-])(\frac{T_b - [A^-]}{K_m + 1})} * \frac{[A^-]}{1 + \frac{K_mK_2}{K_1}}$ or $\frac{[A^-]^2}{([T_a] - [A^-])(T_b - [A^-])} * \frac{K_m + 1}{1 + \frac{K_mK_2}{K_1}} - K_1 = 0$

As well as K_1, K_2 and K_m, 3 equations related to the processes were required to derive the final expression which is related to absorbance by eq 32. Eq 28 defines the total concentration of acid T_a, eq 31 defines the equivalent for base T_b. Eq 29 describes how the total of $[A^-]$ must be equal to the sum of $[B_1H]$ and $[B_2H]$ (since B_1 and B_2 are the only species in the solution capable of deprotonating HA to form A^-). Dividing equation 26 by 30 produces an expression

involving K_2 and K_1 that contains a B_2/B_1 term equivalent to K_m in eq. 3. Replacing $[B_2H]$ using eq 29 reintroduces $[A^-]$ and rearrangement simplifies $[B_1H]$ terms. Combining eq. 26, 31 and 27 yields expressions for B_1 in terms of T_b, $[A^-]$ and K_m and rearranged equation 27 gives an expression for HA in terms of T_a and $[A^-]$. Equation 36, 35 and 33 can then be substituted into K_1 to give an expression which contains only $[A^-]$, K_1, K_2, K_m, T_b and T_a.

Synthesis of monomer c4-17

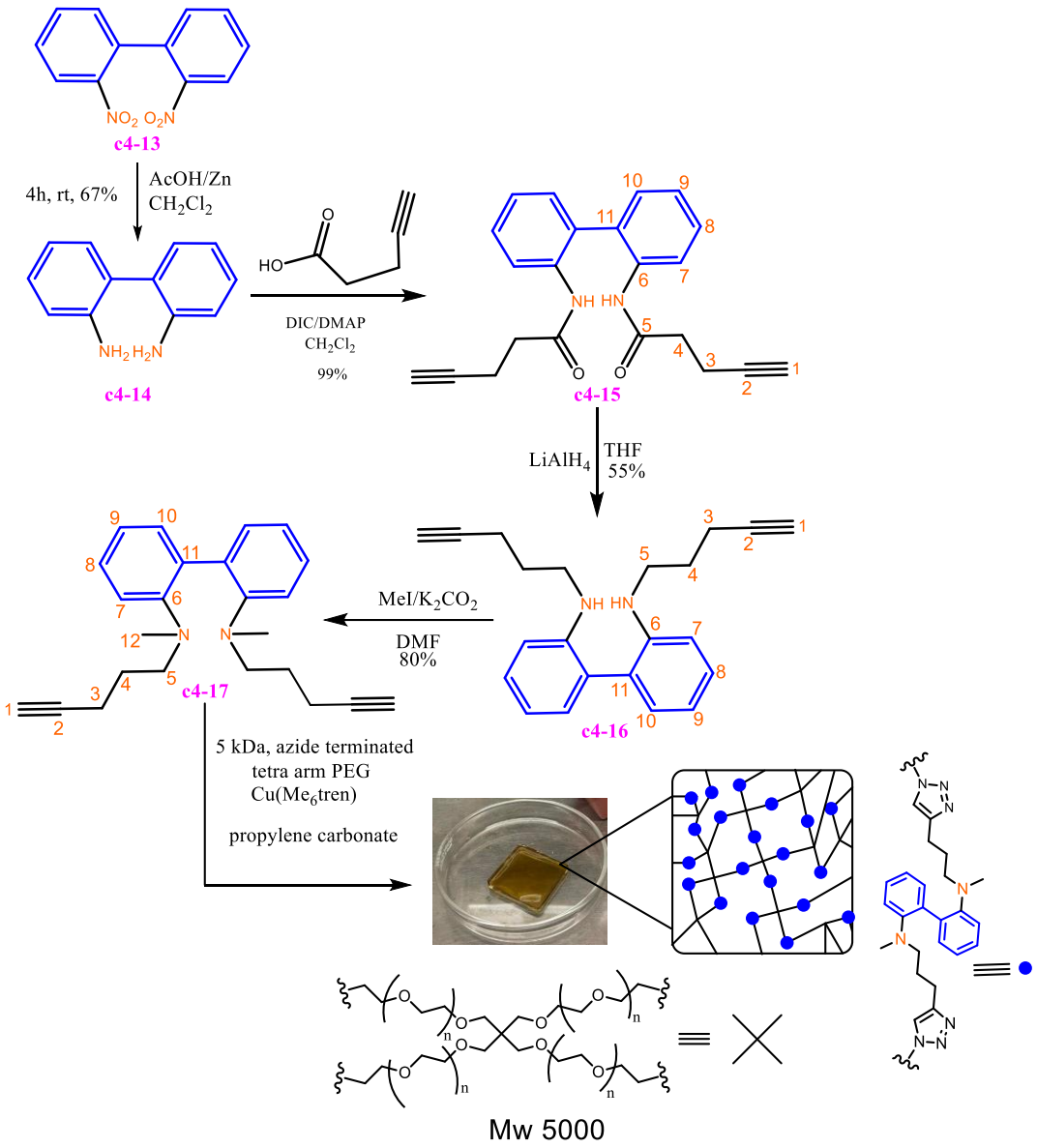

2,2'-diamino-1,1'-biphenyl (**c4-13**)

A mixture of 2,2'–dinitrobiphenyl (0.90 g, 3.7 mmol, 1 equiv.), and Zn (3.61 g, 55.3 mmol, 15 equiv.) in CH_2Cl_2 (40 mL) was cooled to 0°C, followed by slow (0.2 mL/min) dropwise addition of AcOH (4.22 mL, 73 mmol, 20 equiv.). The reaction was maintained at 0°C for 15 min after full addition of AcOH then allowed to warm to rt and stirred for 4 h. The mixture was slowly quenched with 10% NH_4OH (25 mL), filtered through cotton wool and washed through with NH_4OH and CH_2Cl_2. The filtrate was separated and the organic layer washed with NH_4OH sat. solution (10 mL), dried with Na_2SO_4, concentrated under reduced pressure and purified by flash column chromatography ($N(Et)_3$/MeOH/CH_2Cl_2, 0.1 : 0.5 : 99.4). The first fraction was collected and evaporated to give **c4-13** (0.46 g, 2.5 mmol, 68%).^{1}H NMR (500 MHz, $CDCl_3$) 7.18

(td, 2H) 7.12 (dd, 2H), 6.83 (dt, 2H), 6.79 (dd,2H). Spectroscopic data was in agreement with that reported previously.[161]

N,N'-([1,1'-biphenyl]-2,2'-diyl)bis(pent-4-ynamide) (c4-15)

c4-14 (0.25 g, 2.71 mmol, 1 equiv.) was dissolved in CH_2Cl_2 (18 mL) with DMAP (166 mg, 1.36 mmol, 0.5 equiv.) and pent–4–ynoic acid (0.56 g, 5.70 mmol, 1.99 equiv.,) and DIC (0.72 g, 5.70 mmol, 2.1 equiv.) was added at 0 °C and allowed to warm to rt before stirring overnight. The resulting solution was filtered through cotton wool and the solvent removed under reduced pressure. The solid was redissolved in EtOAc and cooled in the freezer for 30 min then filtered once more through cotton. The filtrate was washed with HCl (0.4 M, 3 x 10 mL) and dried over Na_2SO_4. The solvent was removed under reduced pressure yielding a solid containing the product and a small amount of urea side product which could be removed using column chromatography in CH_2Cl_2 but did not interfere with the subsequent step making it more efficient to proceed without further work up to this step. (0.41 g, 1.90 mmol, 80%) ^{1}H NMR (500 MHz, $CDCl_3$) 8.17 (d, 2H, **H^{10}**), 7.44 (td, 2H, **H^{8or9}**), 7.25 (td, 2H, **H^{8or9}**), 7.21 (dd,2H, **H^{7}**), 7.14 (S, 2H, **N*H***), 2.44 (m, 4H, **H^{4}**), 2.38 (m, 4H, **H^{3}**), 1.84 (t, 2H, **H^{1}**). ^{13}C NMR (100 MHz, $CDCl_3$) 170.0 (**C_5**), 135.6 (**C_6**), 130.6(**C_7**), 129.6 (**C_{8or9}**), 129.2 (**C_{11}**), 125.4 (**C_{8or9}**), 123.4 (**C_{10}**), 82.5(**C_2**) 69.7 (**C_1**), 36.1(**C_4**), 14.7 (**C_3**).

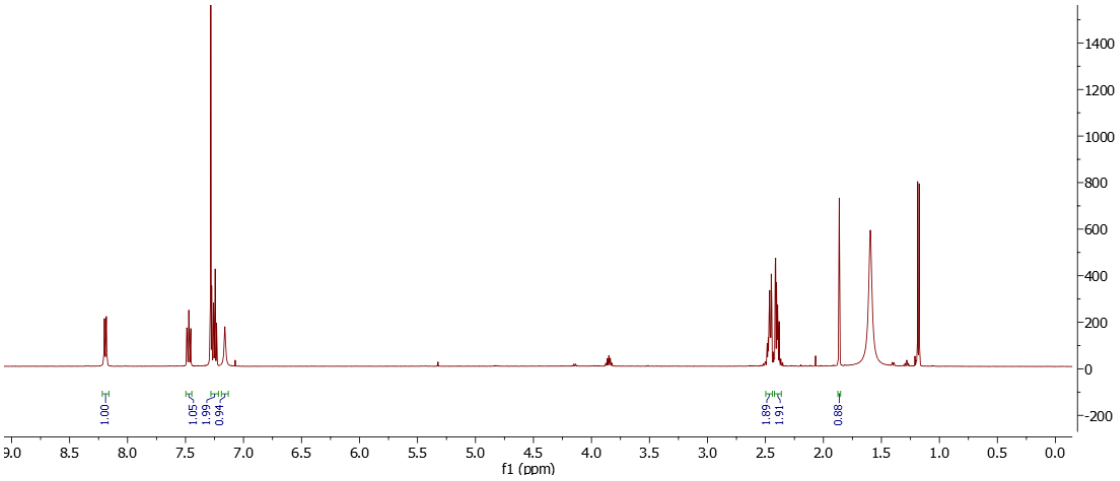

*Figure 59 – **^{1}H NMR spectra of c4-15 in $CDCl_3$.***

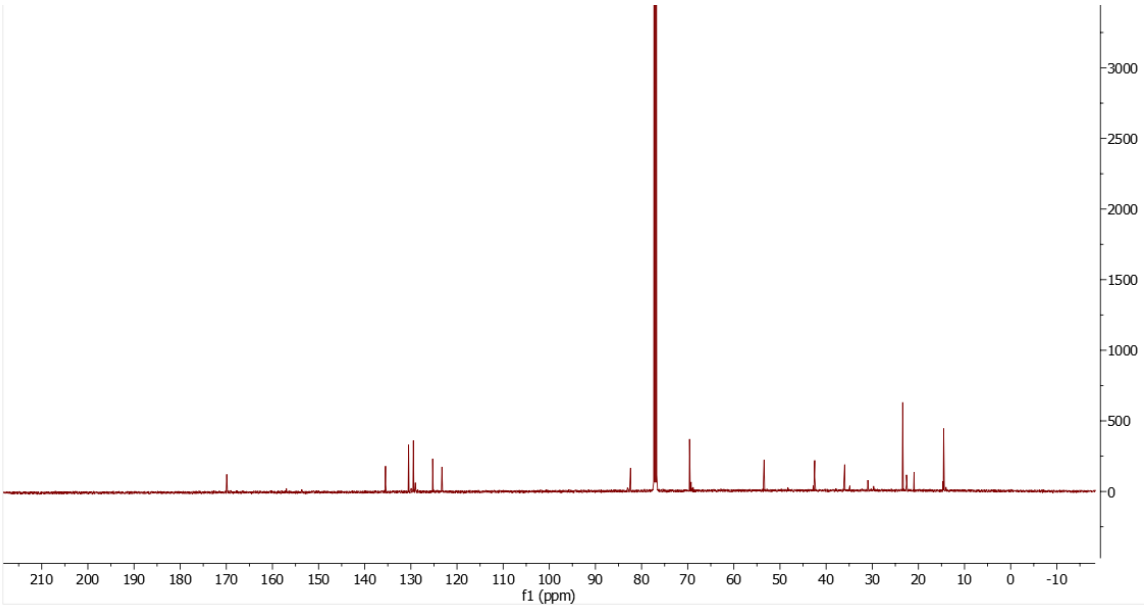

*Figure 60 – **^{13}C NMR spectra of c4-15 in $CDCl_3$.***

N,N'-di(pent-4-yn-1-yl)-[1,1'-biphenyl]-2,2'-diamine (c4-16)

To a stirred suspension of the **c4-15** (50 mg, 0.074 mmol, 1 equiv.) in dry THF (10 mL) LiAlH4 (141 mg, 3.70 mmol, 50 equiv.) was slowly added over 2 min. and stirred for 5 min then refluxed overnight (81°C), cooled to 0 C° and the excess of $LiAlH_4$ was quenched with H_2O (10 mL) . The grey precipitate was filtered off and aqueous layer washed with EtOAc (3 x 50 mL) and CH_2Cl_2 (1 x 10 mL). The filtrate and washings were combined, washed with brine (2 x 10 mL) and dried over anhydrous Na_2SO_4. The solvent was removed at reduce pressure to give **c4-16** (23 mg, 0.073, 98%). ^{1}H NMR (500 MHz, $CDCl_3$), 7.27 (td, 2H, **H^8**), 7.07 (dd, 2H, **H^7**), 6.78 (t, 2H, **H^9**), 6.76 (d, **H^{10}**), 3.24 (pent, 4H, **C^5**), 2.21 (td, 4H, **C^3**), 1.88 (t, 2H, **C^1**), 1.76 (pent, 4H, **C^4**). ^{13}C NMR (100 MHz, $CDCl_3$) , 145.7 (**C_6**), 131.3(**C_7**), 129.2 (**C_8**), 124.3 (**C_{11}**), 117.4 (**C_9**), 110.6 (**C_{10}**), 83.7 (**C_2**), 69.1(**C_1**), 43.0(**C_5**), 27.9 (**C_4**), 16.3 (**C_3**). HRESI–MS *m/z* = 317.2018 calc. for $[M+H]^+$ 317.2018 found.

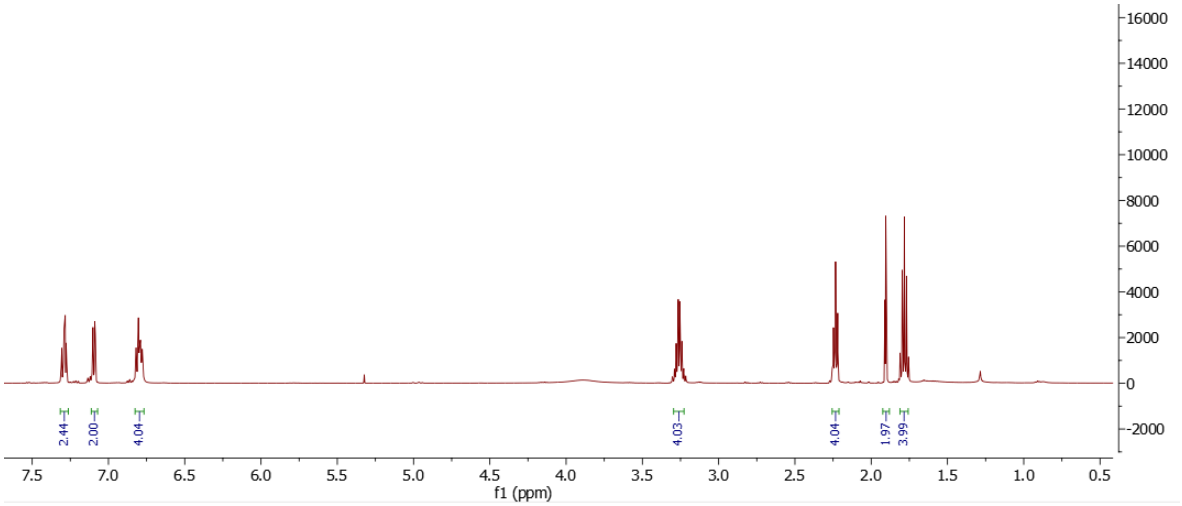

Figure 61 – **^{1}H NMR spectra of c4-16 in $CDCl_3$.**

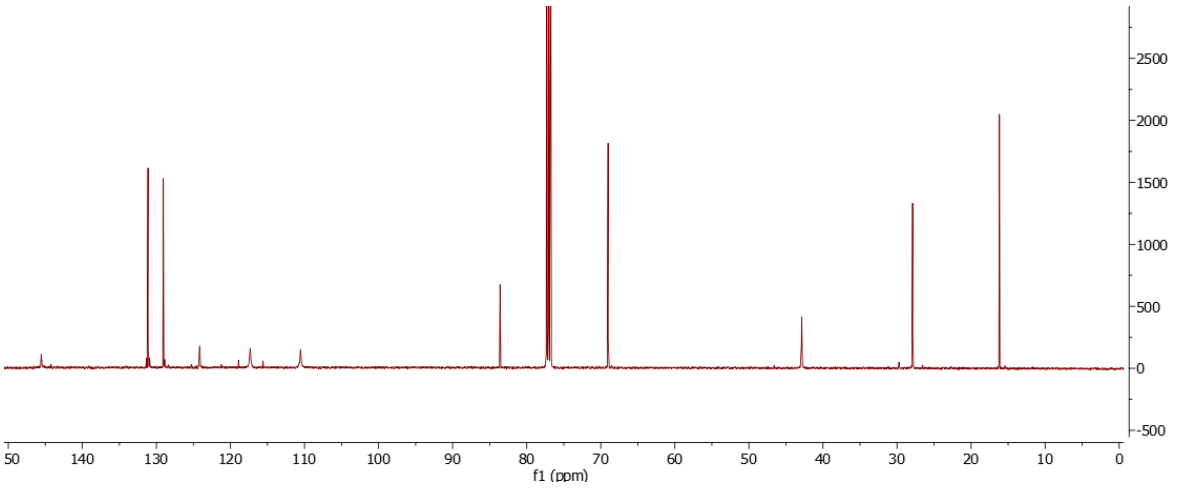

Figure 62 – ***^{13}C NMR spectra of c4-16 in $CDCl_3$.***

N,N'-dimethyl-N,N'-di(pent-4-yn-1-yl)-[1,1'-biphenyl]-2,2'-diamine (c4-17)

c4-16 (40 mg, 0.13 mmol, 1 equiv.) was dissolved in dry DMF (3 mL) with the K_2CO_3 (105 mg, 0.76 mmol, 6 equiv.) and MeI (72 mg, 0.506 mmol, 4 equiv.) added dropwise before stirring at rt overnight. The reaction was quenched with a sat. aq NH_4Cl solution (15 mL) and extracted with EtOAc (4 x 15 mL) then washed with NH_4Cl (3 x 10 mL), H_2O (6 x 10 mL) and brine (10 mL) and dried over Na_2SO_4. The EtOAc was removed under reduced pressure to give a crude solid which was purified by automated column chromatography (4 g silica, MeOH/CH_2Cl_2, 1:99) the first fraction was evaporated to give the title compound (24 mg, 0.070 mmol, 55%). ^{1}H NMR (500 MHz, $CDCl_3$) 7.27–7.23 (m, 4H, **H^{7+8}**), 7.06 (d, 2H, **H^{10}**), 6.99 (t, 2H, **H^{9}**), 2.76 (s broad, 4H, **H^{5}**), 2.57 (s, 6H, **H^{12}**), 1.94–1.80 (m, 6H, ^{13}C NMR (100 MHz, $CDCl_3$) 151.2 (**C_6**), 135.4 (**C_{11}**),

131.9 **($C_{7/8}$)**, 127.8 **($C_{7/8}$)**, 121.9 **(C_9)**, 119.6 **(C_{10})**, 84.6 **(C_2)**, 68.3 **(C_1)**, 55.1 **(C_5)**, 40.2 **(C_{12})**, 26.5**(C_4)** 15.9 **(C_3)**. HRESI–MS *m/z* = 345.2330 calc. for $[M+H]^+$ 345.2333 found.

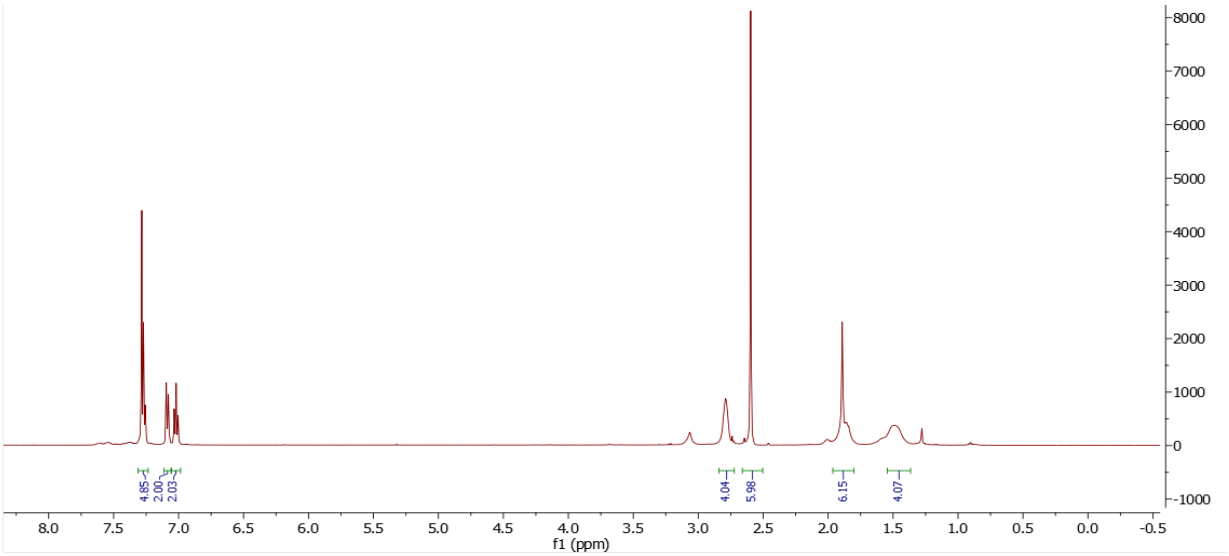

*Figure 63 – **^{1}H NMR spectra of c4-17 in $CDCl_3$.***

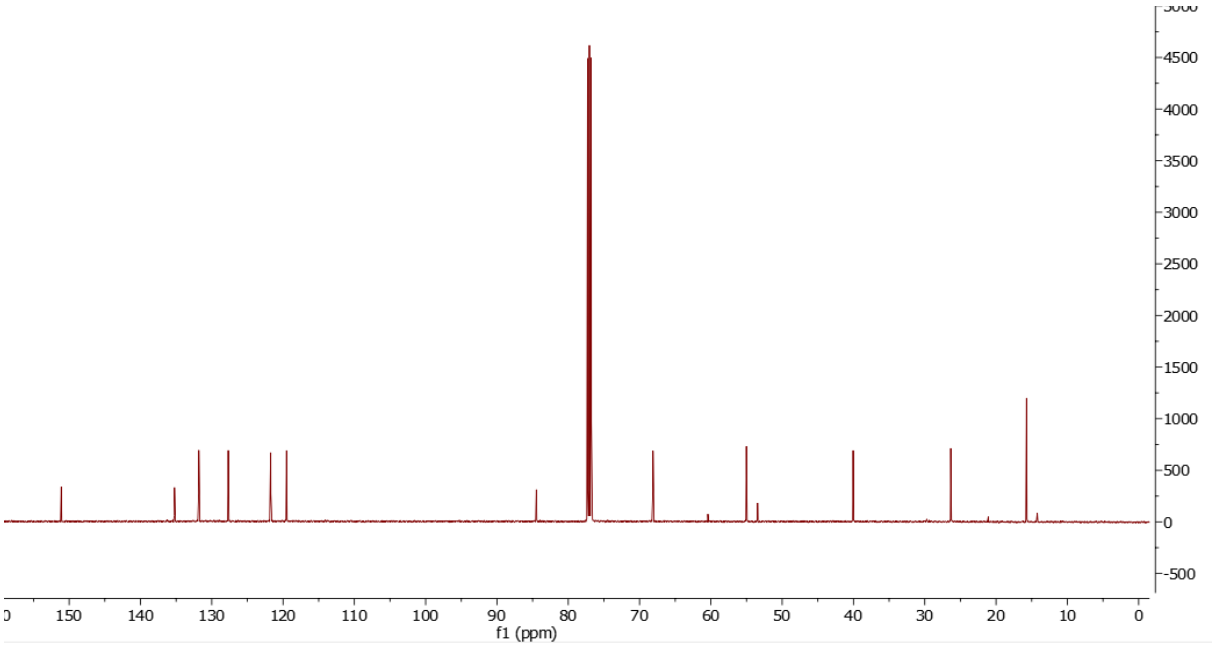

Figure 64 – ***^{13}C NMR spectra of c4-17 in $CDCl_3$.***

Gel preparation

A 50mg/mL Cu catalyst solution was prepared using a literature procedure[150] by first placing CuBr in water and adding a tenfold excess of L–ascorbic acid before stirring for 15 min. The

suspension was filtered using a medium fritted glass funnel and washed with copious amounts of deionized water. The resulting white powder (CuBr purified of contaminating Cu(II)) was washed sequentially with glacial acetic acid and diethyl ether, dried under vacuum, and then brought into a glovebox. The CuBr was stored in a vial in the dark. Me_6TREN was sparged with nitrogen for 3 h, freeze–pump–thawed and brought into the glovebox. CuBr was suspended in propylene carbonate, and 1.1 equivalents of Me_6TREN was dissolved in propylene carbonate in a separate vial then transferred to the vial with CuBr. The catalyst solution was vortexed until all of the CuBr was converted to the complex. 5 kda, tetra–armed–azide–terminated PEG (1 equiv.) and **c4-17** (2 equiv.) were combined in propylene carbonate (1.9 mL) in a glass vial in the glovebox. The mixture was vortexed until complete dissolution (20 min). The copper catalyst solution prepared above (2 equiv.) was added followed by a further 30 seconds of vortexing. The solution was poured into a 3.3*3.3*3 cm silicone mold , gently tapped to release any bubbles, and left to react in the glovebox for 24 hours to ensure complete conversion of the reactive groups.

Matlab code for model

Determination of optimum T_a value

```
%allows me to vary values of Ta and find out how it effects absorbance
%relative to km 0 for various km levels
syms A
k1s(:,1)=0.001:0.001:0.08;
k1=1.83;
k2=1/3;


Tb=0.04;
for km=0:0.25:5
for i=1:height(k1s)

    Ta=k1s(i,1);

  eqn=(A^2*(km + 1))/((Ta-A)*(Tb-A)*((k2*km)/k1 + 1)) - k1;

  sola=double(solve(eqn==0,A));

   sola(sola>0.04)=[];
   sola(sola<-0.00001)=[];
    k1s(i,(km/0.25)+2)=sola(1,1);

end
end
frac=[];
for i=2:width(k1s)

frac(1:80,i)= (k1s(1:end,i)-k1s(1:end,2))./k1s(1:end,2);
end
%row 5 is the fractional difference between A conc at kmech 0 and kmech 0.6
figure(100), plot(k1s(1:end,1), frac(1:end,2:end))
figure(101), plot(k1s(1:end,1), k1s(1:end,2:end))
```

Effects of K_m on $[A^-]$

%Varies K_m and solve for change in $[A^-]$

%define terms

```
syms A
kms(:,1)=0:0.05:10;
k1=1.83;
k2=1/3;


Tb=0.04;
Ta=0.04;

for i=1:height(kms)

    km=kms(i,1);

  eqn=(A^2*(km + 1))/((Ta-A)*(Tb-A)*((k2*km)/k1 + 1)) - k1; %solves eq for given
values

  sola=double(solve(eqn==0,A));

   sola(sola>0.04)=[];  %disregards aphysical values
   sola(sola<-0.00001)=[];
    kms(i,2)=sola(1,1);

end


kms(:,3)= (kms(:,2)-kms(1,2))./kms(1,2); %represent results as % change of km=0


figure(100), plot(kms(1:end,1), kms(:,2))
figure(101), plot(kms(1:end,1), kms(:,3))
```

Synthesis of SS_o22 macrocycle

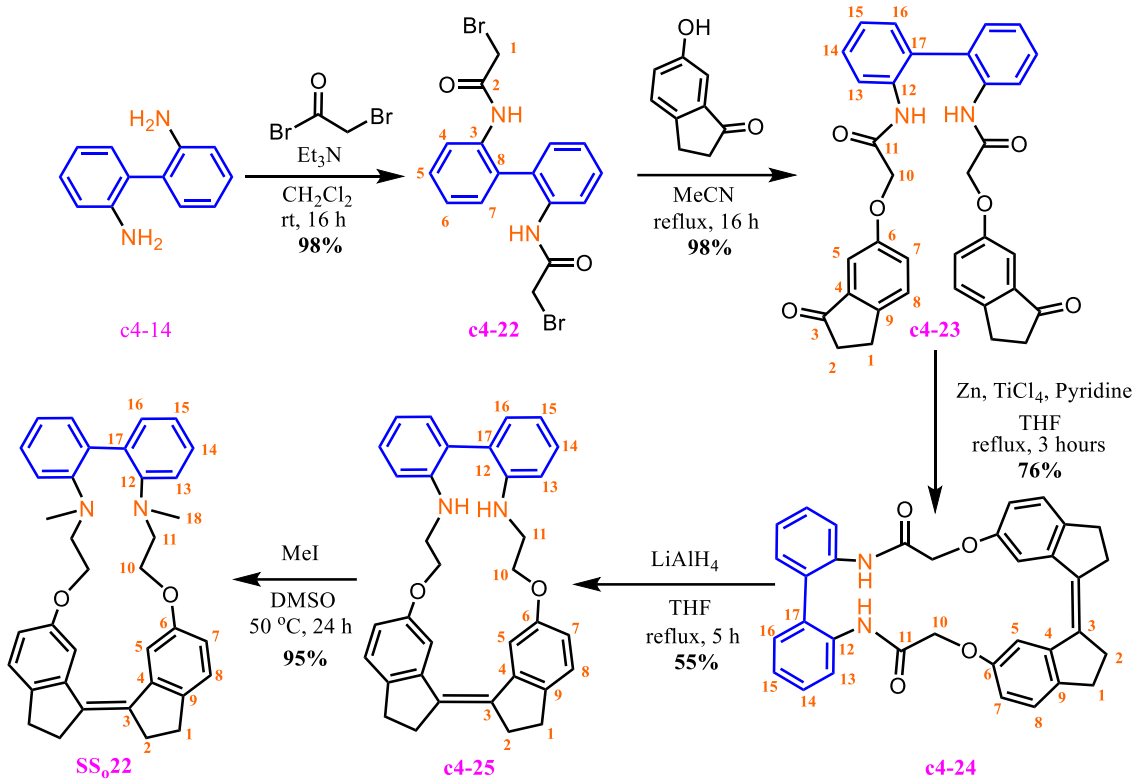

N,N'-([1,1'-biphenyl]-2,2'-diyl)bis(2-bromoacetamide) c4-22

c4-14 (prepared as described above) (0.13 g, 0.72 mmol, 1 equiv.) was dissolved in dry CH_2Cl_2 (5 mL) with Et_3N (0.35 mL, 0.25 g, 2.5 mmol, 3.5 equiv.) and bromoacetyl bromide (0.12 mL, 0.29 g, 1.4 mmol, 2 equiv.) in CH_2Cl_2 (4 mL) was slowly added at 0 °C. The solution was warmed to rt and stirred for 16 h and then diluted with CH_2Cl_2 and washed with H_2O (4 × 10 mL). Drying over Na_2SO_4 followed by removal of the solvent under reduced pressure gave the product in good purity (0.27 g, 88%). ^{1}H NMR (500 MHz, $CDCl_3$) 8.31 (d, 2H, $H_{4/7}$) 7.98 (s, 2H, N*H*), 7.48 (t, 2H, $H_{5/6}$), 7.32–7.26 (m, 4H, H_{Ar}), 3.82 (s, 4H, H_1). HRESI–MS *m/z* = 446.9314 calc. for $[M+Na]^+$ 446.9315 found. Spectroscopic data was in agreement with that reported previously.[162]

c4-23

To a solution of 6–hydroxy–1–indanone (0.49 g, 3.3 mmol, 2 equiv.) and **c4-22** (0.71 g, 1.7 mmol, 1 equiv.) in MeCN (50mL) was added K_2CO_3 (0.92 g, 6.7 mmol, 4 equiv.) and the solution was refluxed for 16 h. After cooling to rt, the solvent was removed under reduced pressure and the remaining brown solid was dissolved in CH_2Cl_2 (15 mL) and washed with H_2O (5 × 15 mL). The aqueous layer was extracted with CH_2Cl_2 (3 × 10 mL) and the combined organic layers were dried over Na_2SO_4 and evaporated under reduced pressure to give the pure

product (920 mg, 98%). ^{1}H NMR (500 MHz, $CDCl_3$) 8.44 (d, 2H, **H_{13}**), 8.07 (s, 2H, **N*H***), 7.47 (td, 2H, **H_{15}**), 7.33 (d, 2H, **H_5**), 7.22 (td, 2H, **H_{14}**), 7.19 (dd, 2H, **H_{16}**), 6.96 (d, 2H, **H_8**), 6.75 (dd, 2H, **H_7**), 4.41 (m, 4H, **H_{10}**), 3.09 (m, 4H, **H_1**), 2.72 (m, 4H, **H_2**).^{13}C NMR (100 MHz, $CDCl_3$) 206.5 (**C_3**), 165.6 (**C_{11}**), 156.2 (**C_6**), 149.3 (**C_9**), 138.4 (**C_4**), 135.2 (**C_{17}**), 130.1 (**C_{16}**), 130.0, (**C_{15}**), 127.8 (**C_5**), 126.2 (**C_{12}**), 124.8 (**C_{14}**), 123.4 (**C_7**), 120.3 (**C_{13}**), 106.3 (**C_8**), 67.4 (**C_{10}**), 37.0 (**C_2**), 25.2 (**C_1**). HRESI–MS *m/z* = 583.1845 calc. for $[M+Na]^+$ 583.1842 found.

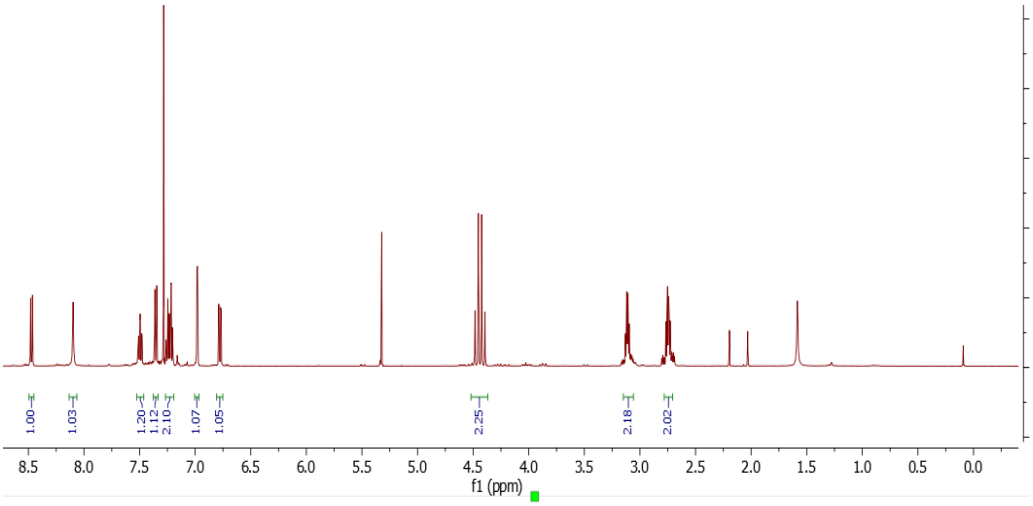

*Figure 65 – **^{1}H NMR spectra of c4-23 in $CDCl_3$.***

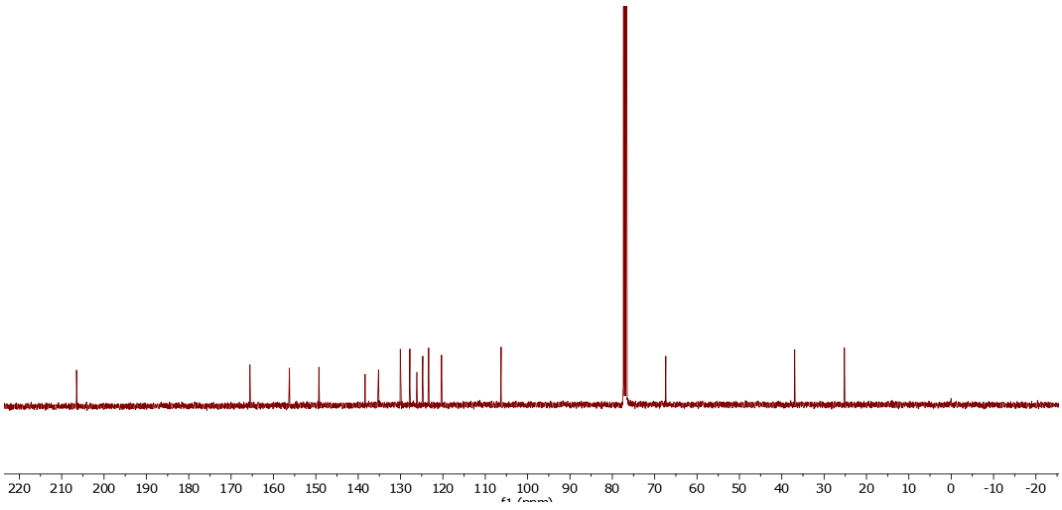

*Figure 66 – **^{13}C NMR spectra of c4-23 in $CDCl_3$.***

c4-24

To a stirred suspension of zinc powder (1.53 g, 24 mmol, 13.2 equiv.) in 30 mL dry THF, $TiCl_4$ (1.1 mL, 1.9 g, 9.8 mmol, 5.5 equiv.) was added over 2 min at 0 °C. The resulting slurry was heated at reflux for 1.5 h, before addition of pyridine (0.79 mL, 0.78 g, 9.8 mmol, 5.5 equiv.). A THF solution (30 mL) of **c4-23** (1.0 g, 1.8 mmol, 1 equiv.) was added over a 3 h period by

dropping funnel to the refluxing reaction mixture. The heating was continued for 0.5 h after the addition was complete. After this time the solution was cooled to 0 ℃ , the reaction mixture was quenched with NH_4OH (10 mL, 10 % aq.) and filtered. The THF was removed under reduced pressure and the aqueous layer was extracted with CH_2Cl_2 (5 × 15 mL). The combined organic phase was washed with NH_4OH (10 mL, 10% aq.) and HCl (5 × 10 mL, 2M) and then H_2O (10 mL). The organic phase was dried over Na_2SO_4 and evaporated under reduced pressure to give the **c4-24** macrocycle (0.72 g, 76%). ^{1}H NMR (500 MHz, $CDCl_3$) 8.19 (s, 2H, **N*H***), 7.59 (d, 2H, **H$_{5\8\9}$**), 7.54 (d, 2H, **H$_{13\16}$**), 7.34 (td, 2H, **H$_{15\14}$**), 7.27 (m, 2H, **H$_{15\14}$**), 7.25 (m, 2H, **H$_{16\13}$**), 7.20 (d, 2H, **H$_{5\8\9}$**), 6.70 (dd, 2H, **H$_{5\8\9}$**), 4.41 (m, 4H, **H$_{10}$**), 2.95 (m, 4H, **H$_{1\2}$**), 2.83 (m, 4H, **H$_{1\2}$**). ^{13}C NMR (100 MHz, $CDCl_3$) 167.6 (**C$_{11}$**), 156.0 (**C$_6$**), 143.1 (**C$_{4\9}$**), 142.1 (**C$_{9\4}$**), 135.8 (**C$_3$**), 134.1 (**C$_{15\14}$**), 132.8 (**C$_{12}$**), 131.2 (**C$_{13\16}$**), 129.3 (**C$_{14\15}$**), 126.3 (**C$_{17}$**), 126.0 (**C$_{5\7\8}$**), 123.7 (**C$_{13\16}$**), 114.6 (**C$_{5\7\8}$**), 112.0 (**C$_{5\7\8}$**), 69.2 (**C$_{10}$**), 35.6 (**C$_{1\2}$**), 30.1 (**C$_{2\1}$**).HRESI–MS *m/z* = 551.1941 calc. for $[M+Na]^+$ 551.1942 found.

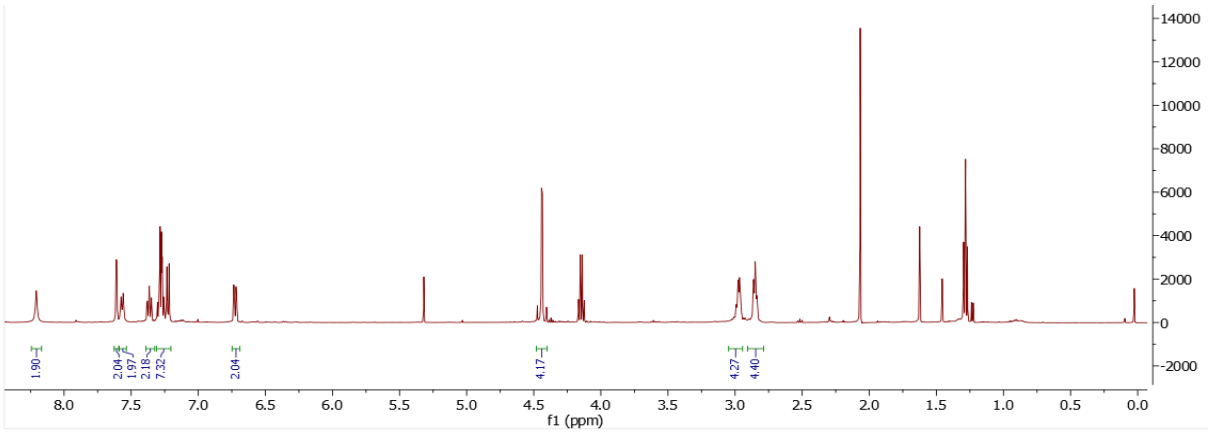

Figure 67 – ***^{1}H NMR spectra of c4-24 in $CDCl_3$.***

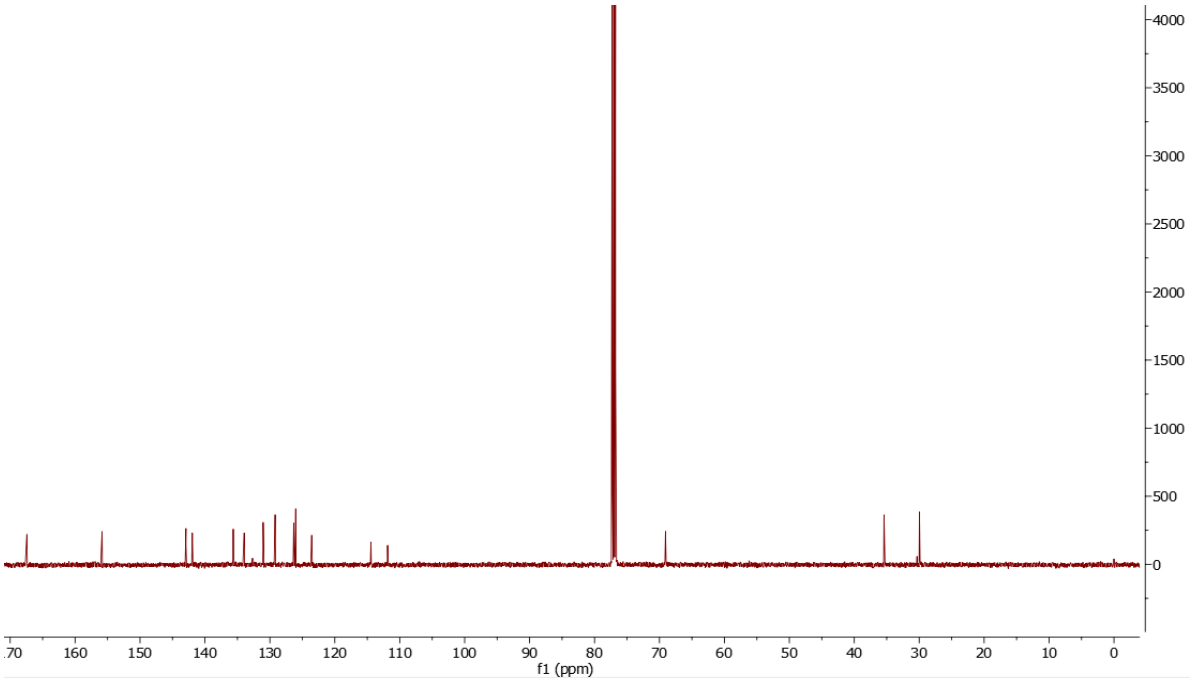

*Figure 68 – **^{13}C NMR spectra of c4-24 in $CDCl_3$.***

c4-25

$LiAlH_4$ (85 mg, 2.3 mmol, 8 equiv.) was added slowly to a solution of **c4-24** (150 mg, 0.28 mmol, 1equiv.) in THF (10 mL) at 0 °C. The mixture was then refluxed for 5 h before cooling to 0 °C and quenching with NH_4OH (2 mL, 10% aq.). After filtering through celite the THF was removed under reduced pressure and the product extracted from the remaining aqueous layer with CH_2Cl_2 (4 × 15 mL). The organic layer was washed with H_2O (10 mL) and dried over Na_2SO_4 before removal of solvents under reduced pressure gave the product (75 mg, 55%). ^{1}H NMR (500 MHz, $CDCl_3$) 7.69 (d, 2H, **$H_{5\backslash7\backslash8}$**), 7.28 (t, 2H, **$H_{14}$**), 7.18 (d, 2H, **$H_{5\backslash7\backslash8}$**), 7.10 (d, 2H, **$H_{13}$**), 6.81 (t, 2H, **$H_{15}$**), 6.76 (d, 2H, **$H_{16}$**), 6.73 (d, 2H, **$H_{5\backslash7\backslash8}$**), 4.23 (m, 2H, **$H_{10}$**), 4.11 (t, 2H, **N*H***), 4.03 (m, 2H, **H_{10}**), 3.64 (m, 2H, **H_{11}**), 3.45 (m, 2H, **H_{11}**), 2.77–2.99 (m, 8H, **$H_{1\ and\ 2}$**). ^{13}C NMR (100 MHz, $CDCl_3$) 157.2 (**C_6**), 144.9 (**C_{12}**), 141.4 (**$C_{3,4\ or\ 9}$**), 141.0 (**$C_{3,4\ or\ 9}$**), 135.5 (**$C_{3,4\ or\ 9}$**), 131.7 (**C_{13}**), 129.3 (**C_{14}**), 125.8 (**$C_{8,7\ or\ 5}$**) 124.6 (**C_{17}**), 117.7 (**C_{15}**), 114.3 (**$C_{8,7\ or\ 5}$**), 109.7 (**C_{16}**), 109.2 (**$C_{8,7\ or\ 5}$**), 66.7 (**C_{10}**), 43.0 (**C_{11}**), 35.4 (**C_1**), 29.7 (**C_2**). HRESI–MS *m/z* = 501.2537 calc. for $[M+H]^+$501.2536 found.

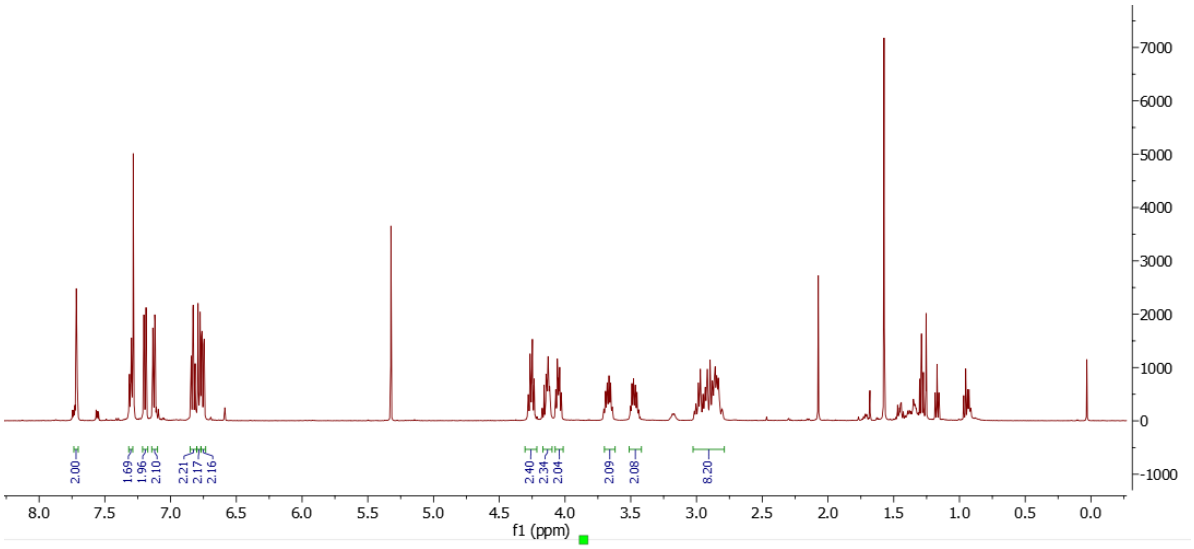

*Figure 69 – **^{1}H NMR spectra of c4-25 in $CDCl_3$.***

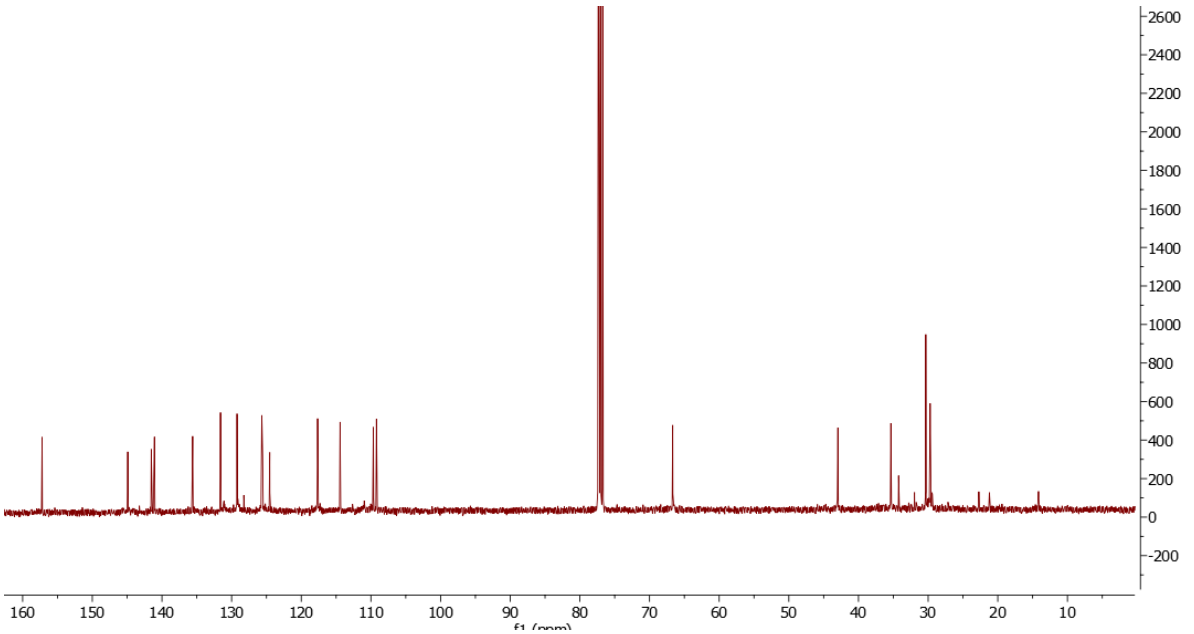

*Figure 70 – **^{13}C NMR spectra of c4-25 in $CDCl_3$.***

SS_o22

The amine (**c4-25**) (20 mg, 0.04 mmol, 1 equiv.) was dissolved in DMSO (3 mL) with KOH (29 mg, 0.52 mmol, 13 equiv.) and MeI (73 mg, 0.52 mmol, 13 quiv.) was added dropwise as a 20% weight solution in DMSO. The mixture was left to stir at 50 °C overnight before quenching with aqueous KOH (1M, 20 mL). The solution was extracted with CH_2Cl_2 (1 x 15 mL) and EtOAc (3 x 15 mL). The combined organic layers were washed with brine and evaporated under reduced pressure to give an off yellow solid that was subjected to automated column

chromatography (4 g silica, CH_2Cl_2). The first peak was collected and evaporated to yield **SS_o22** (20 mg, 0.038 mmol, 95 %). ^{1}H NMR (500 MHz, $CDCl_3$) 7.53 (d, 2H, **$H_{5\backslash7\backslash8}$**), 7.28 (dd, 2H, **$H_{14}$**), 7.19 (t, 2H, **$H_{5\backslash7\backslash8}$**), 7.15 (d, 2H, **$H_{13}$**), 7.04 (d, 2H, **$H_{15}$**), 6.96 (td, 2H, **$H_{16}$**), 6.72 (dd, 2H, **$H_{5\backslash7\backslash8}$**), 3.91 (m, 2H, **$H_{10}$**), 3.75 (m, 2H, **N*H***), 3.26 (m, 2H, **H_{10}**), 3.16 (m, 2H, **H_{11}**), 3.45 (m, 2H, **H_{11}**), 2.91 (m, 4H, **$H_{1\text{ and }2}$**). 2.81 (m, 4H, **$H_{1\text{ and }2}$**), 2.72 (s, 6H, **H_{18}**). ^{13}C NMR (100 MHz, $CDCl_3$) 157.2(**C_6**), 150.1(**C_{12}**), 141.6(**C_4**), 141.2(**C_9**), 135.6(**C_3**), 134.3(**C_{17}**), 132.2(**C_{13}** or **16**), 127.9(**C_{14}** or **15**), 125.8(**$SS_{8\ 5\text{ or }7}$**), 121.6(**C_{14}** or **15**), 119.3(**$C_{13\text{ or }16}$**), 116.1(**$SS_{8\ 5\text{ or }6}$**), 109.7(**$SS_{8\ 5\text{ or }7}$**), 67.3(**$C_{10\text{ or }11}$**), 54.4(**$C_{10\text{ or }11}$**), 41.4 (**C_{18}**), 35.4(**C_2**), 29.9(**C_1**).

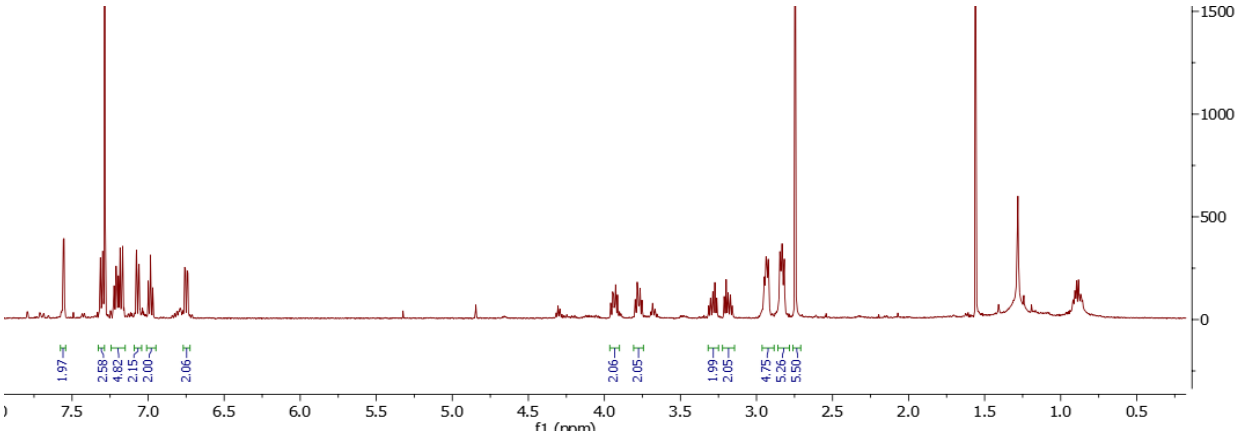

*Figure 71 – **^{1}H NMR spectra of SS_o22 in $CDCl_3$.***

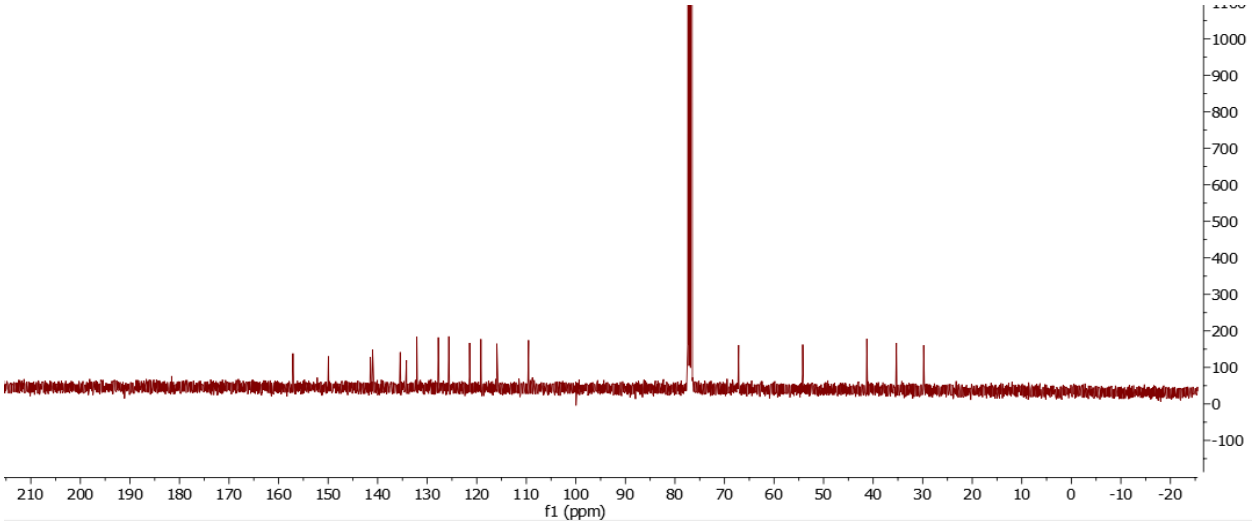

*Figure 72 – **^{1}H NMR spectra of SS_o22 in $CDCl_3$.***

The purity of the compound is inconclusive because the data does allow definitive assignment of the peaks at 4.5 and 3.5 ppm. Specifically, the 4.5 ppm peaks correlate via HMBS to the same carbon as that of the larger alkyl peaks assigned as alkyl protons expected in the product

(4.3 ppm) Figure 73. Additionally, the carbon atoms that correlate to the expected product aromatic protons also have correlation to some of the smaller peaks in the aromatic region which supports the potential for multiple conformers. However some other peaks such as that at 3.5 ppm and some small peaks between 6.5 and 8.5 ppm have no such correlation to any carbon in the spectra making it unclear whether they represent impurities or conformers. I was unable to remove these impurities by column chromatography with several eluents.

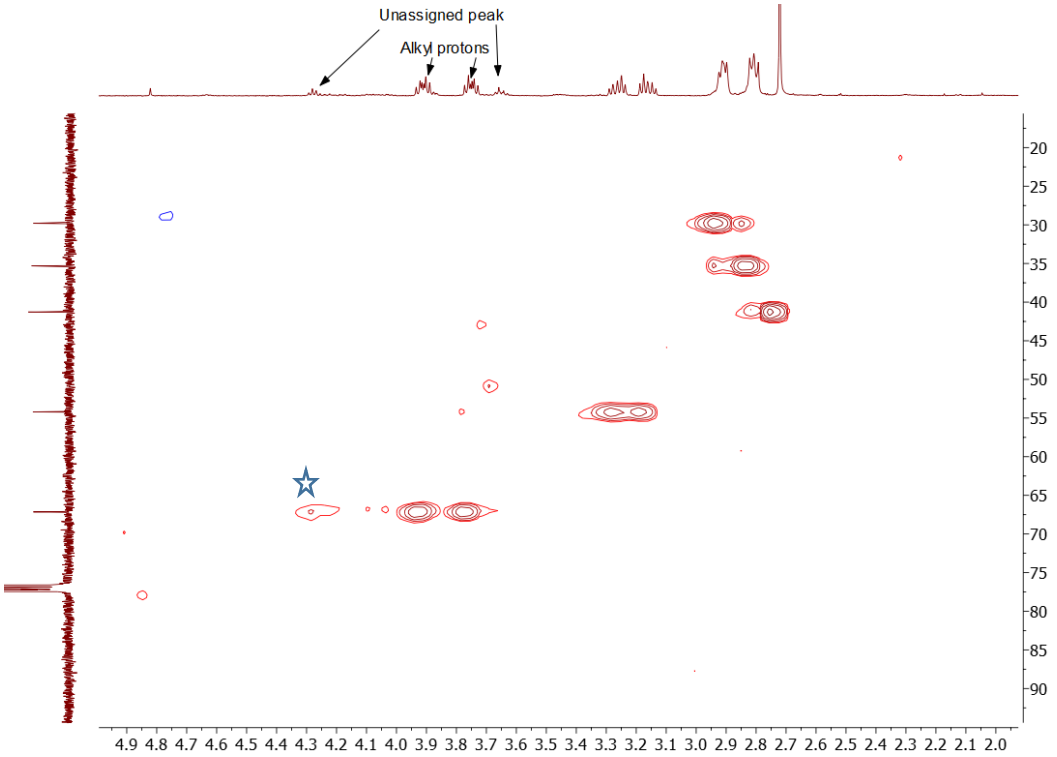

*Figure 73 – **^{1}H–^{13}C HSQC NMR spectra of SS_o22 in $CDCl_3$**. Star labels correlation between unassigned peak at 4.5 ppm and product carbon peak.*

1 Lauterborn, W. & Kurz, T. Physics of bubble oscillations. *Reports on Progress in Physics* **73**, doi:10.1088/0034-4885/73/10/106501 (2010).
2 Akbulatov, S. & Boulatov, R. Experimental Polymer Mechanochemistry and its Interpretational Frameworks. *Chemphyschem* **18**, 1422-1450, doi:10.1002/cphc.201601354 (2017).
3 Balaz, P. *et al.* Hallmarks of mechanochemistry: from nanoparticles to technology. *Chem. Soc. Rev.* **42**, 7571-7637, doi:10.1039/c3cs35468g (2013).
4 Horie, K. *et al.* Definitions of terms relating to reactions of polymers and to functional polymeric materials (IUPAC Recommendations 2003). *Pure Appl Chem* **76**, 889-906, doi:https://doi.org/10.1351/pac200476040889 (2004).
5 O'Neill, R. T. & Boulatov, R. The many flavours of mechanochemistry and its plausible conceptual underpinnings. *Nature Reviews Chemistry* **5**, 148-167, doi:10.1038/s41570-020-00249-y (2021).
6 Friscic, T. New opportunities for materials synthesis using mechanochemistry. *J Mater Chem* **20**, 7599-7605, doi:10.1039/c0jm00872a (2010).
7 Cross, R. A. Mechanochemistry of the Kinesin-1 ATPase. *Biopolymers* **105**, 476-482, doi:10.1002/bip.22862 (2016).
8 Cross, R. A. & McAinsh, A. Prime movers: the mechanochemistry of mitotic kinesins. *Nat. Rev. Mol. Cell Biol.* **15**, 257-271, doi:10.1038/nrm3768 (2014).
9 Vogel, V. Unraveling the Mechanobiology of Extracellular Matrix. *Annu. Rev. Physiol.* **80**, 353-387, doi:10.1146/annurev-physiol-021317-121312 (2018).
10 Butler, P. J., Dey, K. K. & Sen, A. Impulsive enzymes: A new force in mechanobiology. *Cell. Mol. Bioeng.* **8**, 106-118, doi:10.1007/s12195-014-0376-1 (2015).
11 Sepelak, V., Duevel, A., Wilkening, M., Becker, K.-D. & Heitjans, P. Mechanochemical reactions and syntheses of oxides. *Chem. Soc. Rev.* **42**, 7507-7520, doi:10.1039/c2cs35462d (2013).
12 Munoz-Batista, M. J., Rodriguez-Padron, D., Puente-Santiago, A. R. & Luque, R. Mechanochemistry: Toward Sustainable Design of Advanced Nanomaterials for Electrochemical Energy Storage and Catalytic Applications. *ACS Sustainable Chem. Eng.* **6**, 9530-9544, doi:10.1021/acssuschemeng.8b01716 (2018).
13 Zhu, S.-E., Li, F. & Wang, G.-W. Mechanochemistry of fullerenes and related materials. *Chem. Soc. Rev.* **42**, 7535-7570, doi:10.1039/c3cs35494f (2013).
14 Isayev, A. I. *Recycling of natural and synthetic isoprene rubbers*. (Woodhead Publishing Ltd., 2014).
15 Yin, S. *et al.* Mechanical reprocessing of polyolefin waste: A review. *Polym. Eng. Sci.* **55**, 2899-2909, doi:10.1002/pen.24182 (2015).
16 Stratigaki, M. & Göstl, R. Methods for Exerting and Sensing Force in Polymer Materials Using Mechanophores. *Chempluschem* **85**, 1095-1103, doi:10.1002/cplu.201900737 (2020).
17 Izak-Nau, E., Campagna, D., Baumann, C. & Göstl, R. Polymer mechanochemistry-enabled pericyclic reactions. *Polym Chem-Uk* **11**, 2274-2299, doi:10.1039/C9PY01937E (2020).
18 De Bo, G. Mechanochemistry of the mechanical bond. *Chem Sci* **9**, 15-21, doi:10.1039/c7sc04200k (2018).
19 Kucharski, T. J. *et al.* Kinetics of Thiol/Disulfide Exchange Correlate Weakly with the Restoring Force in the Disulfide Moiety. *Angew. Chem., Int. Ed.* **48**, 7040, doi:10.1002/anie.200901511 (2009).

20 Yang, Q.-Z. *et al.* A molecular force probe. *Nat. Nanotechnol.* **4**, 302-306, doi:10.1038/nnano.2009.55 (2009).
21 Akbulatov, S., Tian, Y. C. & Boulatov, R. Force-Reactivity Property of a Single Monomer Is Sufficient To Predict the Micromechanical Behavior of Its Polymer. *Journal of the American Chemical Society* **134**, 7620-7623, doi:10.1021/ja301928d (2012).
22 Akbulatov, S., Tian, Y., Kapustin, E. & Boulatov, R. Model Studies of the Kinetics of Ester Hydrolysis under Stretching Force. *Angew. Chem., Int. Ed.* **52**, 6992-6995, doi:10.1002/anie.201300746 (2013).
23 Akbulatov, S. *et al.* Experimentally realized mechanochemistry distinct from force-accelerated scission of loaded bonds. *Science* **357**, doi:10.1126/science.aan1026 (2017).
24 O'Neill, R. T. & Boulatov, R. The Contributions of Model Studies for Fundamental Understanding of Polymer Mechanochemistry. *Synlett* **33**, 851-862, doi:10.1055/a-1710-5656 (2022).
25 O'Neill, R. T. & Boulatov, R. in *Molecular Photoswitches: Chemistry, Properties, and Applications* (ed Zbigniew L. Pianowski) Ch. 12, (Wiley, 2022).
26 Chan, A. P. Y. *et al.* Selective ortho-C-H Activation in Arenes without Functional Groups. *Journal of the American Chemical Society* **144**, 11564-11568, doi:10.1021/jacs.2c0462111564 (2022).
27 Fuss, W., Kosmidis, C., Schmid, W. E. & Trushin, S. A. The photochemical cis-trans isomerization of free stilbene molecules follows a hula-twist pathway. *Angew Chem Int Edit* **43**, 4178-4182, doi:10.1002/anie.200454221 (2004).
28 Gerwien, A., Schildhauer, M., Thumser, S., Mayer, P. & Dube, H. Direct evidence for hula twist and single-bond rotation photoproducts. *Nat Commun* **9**, doi:ARTN 2510

10.1038/s41467-018-04928-9 (2018).
29 Villaron, D. & Wezenberg, S. Stiff-Stilbene Photoswitches: From Fundamental Studies to Emergent Applications. *Angew Chem Int Ed Engl* **59**, 13192-13202, doi:10.1002/anie.202001031 (2020).
30 Huang, Z. *et al.* Method to Derive Restoring Forces of Strained Molecules from Kinetic Measurements. *J. Am. Chem. Soc.* **131**, 1407-1409, doi:10.1021/ja807113m (2009).
31 Kucharski, T. J. & Boulatov, R. in *Optical Nano and Micro Actuator Technology* (ed G. K. Knopf) Ch. 3, 83-106 (CRC Press, 2012).
32 Mcmurry, J. E. Carbonyl-Coupling Reactions Using Low-Valent Titanium. *Chemical Reviews* **89**, 1513-1524, doi:DOI 10.1021/cr00097a007 (1989).
33 Akbulatov, S., Tian, Y. & Boulatov, R. Force-Reactivity Property of a Single Monomer Is Sufficient To Predict the Micromechanical Behavior of Its Polymer. *J. Am. Chem. Soc.* **134**, 7620-7623, doi:10.1021/ja301928d (2012).
34 Wu, D., Lenhardt, J. M., Black, A. L., Akhremitchev, B. B. & Craig, S. L. Molecular Stress Relief through a Force-Induced Irreversible Extension in Polymer Contour Length. *J Am Chem Soc* **132**, 15936-15938, doi:10.1021/ja108429h (2010).
35 Kucharski, T. J. & Boulatov, R. The physical chemistry of mechanoresponsive polymers. *J. Mater. Chem.* **21**, 8237-8255, doi:10.1039/c0jm04079g (2011).
36 Tian, Y. & Boulatov, R. Quantum-Chemical Validation of the Local Assumption of Chemomechanics for a Unimolecular Reaction. *ChemPhysChem* **13**, 2277-2281, doi:10.1002/cphc.201200207 (2012).

37 Huang, Z. & Boulatov, R. Chemomechanics: chemical kinetics for multiscale phenomena. *Chem. Soc. Rev.* **40**, 2359-2384, doi:10.1039/c0cs00148a (2011).
38 Barbee, M. H. *et al.* Substituent Effects and Mechanism in a Mechanochemical Reaction. *J Am Chem Soc* **140**, 12746-12750, doi:10.1021/jacs.8b09263 (2018).
39 Zhang, H. *et al.* Multi-modal mechanophores based on cinnamate dimers. *Nat Commun* **8**, doi:10.1038/s41467-017-01412-8 (2017).
40 Do, J.-L. & Friscic, T. Mechanochemistry: A Force of Synthesis. *ACS Cent. Sci.* **3**, 13-19, doi:10.1021/acscentsci.6b00277 (2017).
41 Stolle, A. in *Ball Milling Towards Green Synthesis: Applications, Projects, Challenges* Vol. 31 *RSC Green Chem. Ser.* 241-276 (Royal Society of Chemistry, 2015).
42 Margetic, D. & Strukil, V. Applications of Ball Milling in Supramolecular Chemistry. *Mechanochemical Organic Synthesis*, 343-350, doi:10.1016/B978-0-12-802184-2.00008-X (2016).
43 Friscic, T., Mottillo, C. & Titi, H. M. Mechanochemistry for Synthesis. *Angew. Chem., Int. Ed.* **59**, 1018-1029, doi:10.1002/anie.201906755 (2020).
44 Egorov, I. N. *et al.* Ball milling: an efficient and green approach for asymmetric organic syntheses. *Green Chem.* **22**, 302-315, doi:10.1039/c9gc03414e (2020).
45 Andersen, J. & Mack, J. Mechanochemistry and organic synthesis: from mystical to practical. *Green Chem* **20**, 1435-1443, doi:10.1039/c7gc03797j (2018).
46 Howard, J. L., Cao, Q. & Browne, D. L. Mechanochemistry as an emerging tool for molecular synthesis: what can it offer? *Chem. Sci.* **9**, 3080-3094, doi:10.1039/c7sc05371a (2018).
47 Sokolov, A. N., Bucar, D.-K., Baltrusaitis, J., Gu, S. X. & MacGillivray, L. R. Supramolecular Catalysis in the Organic Solid State through Dry Grinding. *Angew. Chem., Int. Ed.* **49**, 4273-4277, doi:10.1002/anie.201000874 (2010).
48 Chen, L. R., Regan, M. & Mack, J. The Choice Is Yours: Using Liquid-Assisted Grinding To Choose between Products in the Palladium-Catalyzed Dimerization of Terminal Alkynes. *Acs Catal* **6**, 868-872, doi:10.1021/acscatal.5b02001 (2016).
49 Friscic, T. *et al.* Ion- and Liquid-Assisted Grinding: Improved Mechanochemical Synthesis of Metal-Organic Frameworks Reveals Salt Inclusion and Anion Templating. *Angew. Chem., Int. Ed.* **49**, 712, doi:10.1002/anie.200906583 (2010).
50 Tricker, A. W., Samaras, G., Hebisch, K. L., Realff, M. J. & Sievers, C. Hot spot generation, reactivity, and decay in mechanochemical reactors. *Chemical Engineering Journal* **382**, 122954, doi:https://doi.org/10.1016/j.cej.2019.122954 (2020).
51 Rothenberg, G., Downie, A. P., Raston, C. L. & Scott, J. L. Understanding solid/solid organic reactions. *Journal of the American Chemical Society* **123**, 8701-8708, doi:10.1021/ja0034388 (2001).
52 Kulla, H. *et al.* Warming up for mechanosynthesis - temperature development in ball mills during synthesis. *Chem Commun* **53**, 1664-1667, doi:10.1039/c6cc08950j (2017).
53 Colacino, E. *et al.* Processing and Investigation Methods in Mechanochemical Kinetics. *ACS Omega* **3**, 9196-9209, doi:10.1021/acsomega.8b01431 (2018).
54 Wang, C. *et al.* The molecular mechanism of constructive remodeling of a mechanically-loaded polymer. *Nature Communications* **13**, 3154, doi:10.1038/s41467-022-30947-8 (2022).
55 Rubinstein, M. & Colby, R. H. *Polymer physics*. (Oxford University Press, 2007).

56 Boger, D. V. Viscoelastic Flows Through Contractions. *Annual Review of Fluid Mechanics* **19**, 157-182, doi:10.1146/annurev.fl.19.010187.001105 (1987).
57 Graham, M. D. Fluid Dynamics of Dissolved Polymer Molecules in Confined Geometries. *Annual Review of Fluid Mechanics* **43**, 273-298, doi:10.1146/annurev-fluid-121108-145523 (2011).
58 Price, G. J. The use of ultrasound for the controlled degradation of polymer solutions. *Advances in Sonochemistry* **1**, 231-287 (1990).
59 Cintas, P., Cravotto, G., Barge, A. & Marina, K. in *Polymer Mechanochemistry* (ed Roman Boulatov) 239-284 (Springer International Publishing, 2015).
60 Larson, R. G. The rheology of dilute solutions of flexible polymers: Progress and problems. *Journal of Rheology* **49**, 1-70, doi:10.1122/1.1835336 (2005).
61 Schroeder, C. M. Single polymer dynamics for molecular rheology. *Journal of Rheology* **62**, 371-403, doi:10.1122/1.5013246 (2018).
62 Kausch, H. H. *Polymer Fracture*. (Mir, 1981).
63 Rognin, E., Willis-Fox, N., Zhao, T. Z., Aljohani, T. A. & Daly, R. Laminar flow-induced scission kinetics of polymers in dilute solutions. *Journal of Fluid Mechanics* **924**, doi:10.1017/jfm.2021.646 (2021).
64 Poole, R. J. Editorial for the special issue on "Polymer degradation in turbulent drag reduction". *Journal of Non-Newtonian Fluid Mechanics* **281**, doi:ARTN 104283

10.1016/j.jnnfm.2020.104283 (2020).
65 Rognin, E., Willis-Fox, N., Aljohani, T. A. & Daly, R. A multiscale model for the rupture of linear polymers in strong flows. *Journal of Fluid Mechanics* **848**, 722-742, doi:10.1017/jfm.2018.411 (2018).
66 Garrepally, S., Jouenne, S., Olmsted, P. D. & Lequeux, F. Scission of flexible polymers in contraction flow: Predicting the effects of multiple passages. *Journal of Rheology* **64**, 601-614, doi:10.1122/1.5127801 (2020).
67 Nguyen, T. Q. & Kausch, H. H. Chain Scission in Transient Extensional Flow Kinetics and Molecular-Weight Dependence. *Journal of Non-Newtonian Fluid Mechanics* **30**, 125-140, doi:Doi 10.1016/0377-0257(88)85020-1 (1988).
68 Haward, S. J., Oliveira, M. S. N., Alves, M. A. & McKinley, G. H. Optimized Cross-Slot Flow Geometry for Microfluidic Extensional Rheometry. *Physical Review Letters* **109**, 128301, doi:10.1103/PhysRevLett.109.128301 (2012).
69 Boulatov, R. The Challenges and Opportunities of Contemporary Polymer Mechanochemistry. *Chemphyschem* **18**, 1419-1421, doi:10.1002/cphc.201700127 (2017).
70 Hsieh, C.-C., Park, S. J. & Larson, R. G. Brownian Dynamics Modeling of Flow-Induced Birefringence and Chain Scission in Dilute Polymer Solutions in a Planar Cross-Slot Flow. *Macromolecules* **38**, 1456-1468, doi:10.1021/ma0491255 (2005).
71 Stauch, T. & Dreuw, A. Advances in Quantum Mechanochemistry: Electronic Structure Methods and Force Analysis. *Chemical Reviews* **116**, 14137-14180, doi:10.1021/acs.chemrev.6b00458 (2016).
72 Kochhar, G. S., Heverly-Coulson, G. S. & Mosey, N. J. Theoretical approaches for understanding the interplay between stress and chemical reactivity. *Top. Curr. Chem.* **369**, 37-96, doi:10.1007/128_2015_648 (2015).
73 Kucharski, T. J. & Boulatov, R. The physical chemistry of mechanoresponsive polymers. *Journal of Materials Chemistry* **21**, 8237-8255, doi:10.1039/C0JM04079G (2011).

74 Lenhardt, J. M., Ramirez, A. L. B., Lee, B., Kouznetsova, T. B. & Craig, S. L. Mechanistic Insights into the Sonochemical Activation of Multimechanophore Cyclopropanated Polybutadiene Polymers. *Macromolecules* **48**, 6396-6403, doi:10.1021/acs.macromol.5b01677 (2015).
75 Lenhardt, J. M. *et al.* Trapping a Diradical Transition State by Mechanochemical Polymer Extension. *Science (Washington, DC, U. S.)* **329**, 1057-1060, doi:10.1126/science.1193412 (2010).
76 Tian, Y. *et al.* A Polymer with Mechanochemically Active Hidden Length. *Journal of the American Chemical Society* **142**, 18687-18697, doi:10.1021/jacs.0c09220 (2020).
77 Zhang, H. *et al.* Multi-modal mechanophores based on cinnamate dimers. *Nature Commun.* **8**, 1147 (2017).
78 Bowser, B. H. & Craig, S. L. Empowering mechanochemistry with multi-mechanophore polymer architectures. *Polym Chem-Uk* **9**, 3583-3593, doi:10.1039/c8py00720a (2018).
79 Kean, Z. S., Gossweiler, G. R., Kouznetsova, T. B., Hewage, G. B. & Craig, S. L. A coumarin dimer probe of mechanochemical scission efficiency in the sonochemical activation of chain-centered mechanophore polymers. *Chem Commun* **51**, 9157-9160, doi:10.1039/c5cc01836f (2015).
80 Overholts, A. C. & Robb, M. J. Examining the Impact of Relative Mechanophore Activity on the Selectivity of Ultrasound-Induced Mechanochemical Chain Scission. *ACS Macro Letters* **11**, 733-738, doi:10.1021/acsmacrolett.2c00217 (2022).
81 Vanapalli, S. A., Ceccio, S. L. & Solomon, M. J. Universal scaling for polymer chain scission in turbulence. *P Natl Acad Sci USA* **103**, 16660-16665, doi:10.1073/pnas.0607933103 (2006).
82 Okkuama, M. & Hirose, T. Mechanics of ultrasonic degradation of linear high polymer and ultrasonic cavitation. *Journal of Applied Polymer Science* **7**, 591-602, doi:https://doi.org/10.1002/app.1963.070070216 (1963).
83 Ryskin, G. Calculation of the effect of polymer additive in a converging flow. *Journal of Fluid Mechanics* **178**, 423-440, doi:10.1017/S0022112087001290 (1987).
84 Lorenzo, T. & Marco, L. Brownian Dynamics Simulations of Cavitation-Induced Polymer Chain Scission. *Ind Eng Chem Res* **60**, 10539-10550, doi:10.1021/acs.iecr.1c00233 (2021).
85 Jendrejack, R. M., Pablo, J. J. d. & Graham, M. D. Stochastic simulations of DNA in flow: Dynamics and the effects of hydrodynamic interactions. *The Journal of Chemical Physics* **116**, 7752-7759, doi:10.1063/1.1466831 (2002).
86 Huo, S. *et al.* Mechanochemical bond scission for the activation of drugs. *Nature Chemistry* **13**, 131-139, doi:10.1038/s41557-020-00624-8 (2021).
87 Liu, Y. *et al.* Flyby reaction trajectories: Chemical dynamics under extrinsic force. *Science* **373**, 208-212, doi:10.1126/science.abi7609 (2021).
88 Lee, B., Niu, Z. B., Wang, J. P., Slebodnick, C. & Craig, S. L. Relative Mechanical Strengths of Weak Bonds in Sonochemical Polymer Mechanochemistry. *Journal of the American Chemical Society* **137**, 10826-10832, doi:10.1021/jacs.5b06937 (2015).
89 Nixon, R. & De Bo, G. Isotope Effect in the Activation of a Mechanophore. *Journal of the American Chemical Society* **143**, 3033-3036, doi:10.1021/jacs.0c11259 (2021).
90 Piermattei, A., Karthikeyan, S. & Sijbesma, R. P. Activating catalysts with mechanical force. *Nature Chemistry* **1**, 133-137, doi:10.1038/nchem.167 (2009).

91 Nixon, R. & De Bo, G. Three concomitant C–C dissociation pathways during the mechanical activation of an N-heterocyclic carbene precursor. *Nature Chemistry* **12**, 826-831, doi:10.1038/s41557-020-0509-1 (2020).
92 Pan, Y. *et al.* A mechanochemical reaction cascade for controlling load-strengthening of a mechanochromic polymer. *Angewandte Chemie International Edition* **49**, 21980-21985, doi:10.1002/anie.202010043 (2020).
93 Yang, J. *et al.* Bicyclohexene-peri-naphthalenes: Scalable Synthesis, Diverse Functionalization, Efficient Polymerization, and Facile Mechanoactivation of Their Polymers. *Journal of the American Chemical Society* **142**, 14619-14626, doi:10.1021/jacs.0c06454 (2020).
94 Anderson, L. & Boulatov, R. Polymer Mechanochemistry: A New Frontier for Physical Organic Chemistry. *Adv. Phys. Org. Chem.* **52**, 87-143, doi:10.1016/bs.apoc.2018.08.001 (2018).
95 Nguyen, T. Q., Liang, O. Z. & Kausch, H. H. Kinetics of ultrasonic and transient elongational flow degradation: A comparative study. *Polymer* **38**, 3783-3793, doi:Doi 10.1016/S0032-3861(96)00950-0 (1997).
96 Larson, R. G. & Desai, P. S. Modeling the Rheology of Polymer Melts and Solutions. *Annual Review of Fluid Mechanics* **47**, 47-65, doi:10.1146/annurev-fluid-010814-014612 (2015).
97 Willis-Fox, N., Rognin, E., Aljohani, T. A. & Daly, R. Polymer Mechanochemistry: Manufacturing Is Now a Force to Be Reckoned With. *Chem* **4**, 2499-2537, doi:https://doi.org/10.1016/j.chempr.2018.08.001 (2018).
98 Peterson, G. I. & Choi, T.-L. The influence of polymer architecture in polymer mechanochemistry. *Chem Commun* **57**, 6465-6474, doi:10.1039/D1CC02501E (2021).
99 Zhang, H., Lin, Y., Xu, Y. & Weng, W. Mechanochemistry of topologically complex polymer systems. *Top. Curr. Chem.* **369**, 135-208, doi:10.1007/128_2014_617 (2015).
100 Lin, Y., Zhang, Y., Wang, Z. & Craig, S. L. Dynamic Memory Effects in the Mechanochemistry of Cyclic Polymers. *J. Am. Chem. Soc.* **141**, 10943-10947, doi:10.1021/jacs.9b03564 (2019).
101 De Bo, G. Mechanochemistry of the mechanical bond. *Chemical Science* **9**, 15-21, doi:10.1039/C7SC04200K (2018).
102 Lin, Y., Kouznetsova, T. B., Chang, C.-C. & Craig, S. L. Enhanced polymer mechanical degradation through mechanochemically unveiled lactonization. *Nat. Commun.* **11**, 4987, doi:10.1038/s41467-020-18809-7 (2020).
103 Brown, C. L. & Craig, S. L. Molecular engineering of mechanophore activity for stress-responsive polymeric materials. *Chem. Sci.* **6**, 2158-2165, doi:10.1039/c4sc01945h (2015).
104 Wang, S. *et al.* Mechanism Dictates Mechanics: A Molecular Substituent Effect in the Macroscopic Fracture of a Covalent Polymer Network. *J. Am. Chem. Soc.* **143**, 3714-3718, doi:10.1021/jacs.1c00265 (2021).
105 Patrick, J. F., Robb, M. J., Sottos, N. R., Moore, J. S. & White, S. R. Polymers with autonomous life-cycle control. *Nature (London, U. K.)* **540**, 363-370, doi:10.1038/nature21002 (2016).
106 Chen, Y., Mellot, G., van Luijk, D., Creton, C. & Sijbesma, R. P. Mechanochemical tools for polymer materials. *Chemical Society Reviews* **50**, 4100-4140, doi:10.1039/D0CS00940G (2021).

107 Xu, J.-F. *et al.* Photoresponsive Hydrogen-Bonded Supramolecular Polymers Based on a Stiff Stilbene Unit. *Angewandte Chemie International Edition* **52**, 9738-9742, doi:https://doi.org/10.1002/anie.201303496 (2013).
108 Tan, D. & García, F. Main group mechanochemistry: from curiosity to established protocols. *Chemical Society Reviews* **48**, 2274-2292, doi:10.1039/C7CS00813A (2019).
109 Anderson, L. & Boulatov, R. Polymer Mechanochemistry: A New Frontier for Physical Organic Chemistry. *Advances in Physical Organic Chemistry* **52**, 87-143, doi:10.1016/bs.apoc.2018.08.001 (2018).
110 Garcia-Manyes, S. & Beedle, A. E. M. Steering chemical reactions with force. *Nat. Rev. Chem.* **1**, 0083, doi:10.1038/s41570-017-0083 (2017).
111 Yang, B., Liu, Z., Liu, H. & Nash, M. A. Next generation methods for single-molecule force spectroscopy on polyproteins and receptor-ligand complexes. *Front. Mol. Biosci.* **7**, 85, doi:10.3389/fmolb.2020.00085 (2020).
112 Rief, M., Oesterhelt, F., Heymann, B. & Gaub, H. E. Single molecule force spectroscopy on polysaccharides by atomic force microscopy. *Science* **275**, 1295-1297, doi:DOI 10.1126/science.275.5304.1295 (1997).
113 Friscic, T. Supramolecular concepts and new techniques in mechanochemistry: cocrystals, cages, rotaxanes, open metal-organic frameworks. *Chemical Society Reviews* **41**, 3493-3510, doi:10.1039/c2cs15332g (2012).
114 Kean, Z. S. *et al.* Photomechanical Actuation of Ligand Geometry in Enantioselective Catalysis. *Angew Chem Int Edit* **53**, 14508-14511, doi:10.1002/anie.201407494 (2014).
115 Syeda, R. *et al.* Piezo1 Channels Are Inherently Mechanosensitive. *Cell Rep* **17**, 1739-1746, doi:10.1016/j.celrep.2016.10.033 (2016).
116 Buyan, A. *et al.* Understanding Piezo1's Relationship with Lipids. *Biophysical Journal* **116**, 459a-459a, doi:DOI 10.1016/j.bpj.2018.11.2481 (2019).
117 Cox, C. D. *et al.* Removal of the mechanoprotective influence of the cytoskeleton reveals PIEZO1 is gated by bilayer tension. *Nature Communications* **7**, doi:ARTN 10366

10.1038/ncomms10366 (2016).
118 Katta, S., Krieg, M. & Goodman, M. B. Feeling Force: Physical and Physiological Principles Enabling Sensory Mechanotransduction. *Annu Rev Cell Dev Bi* **31**, 347-371, doi:10.1146/annurev-cellbio-100913-013426 (2015).
119 Wang, L. Q. *et al.* Mechanochemical Regulation of Oxidative Addition to a Palladium(0) Bisphosphine Complex. *Journal of the American Chemical Society* **142**, 17714-17720, doi:10.1021/jacs.0c08506 (2020).
120 Yu, Y. C. *et al.* Force-modulated reductive elimination from platinum(ii) diaryl complexes. *Chemical Science* **12**, 11130-11137, doi:10.1039/d1sc03182a (2021).
121 Larsen, M. B. & Boydston, A. J. Successive Mechanochemical Activation and Small Molecule Release in an Elastomeric Material. *J. Am. Chem. Soc.* **136**, 1276-1279, doi:10.1021/ja411891x (2014).
122 Shi, Z. Y., Wu, J. N., Song, Q. C., Gostl, R. & Herrmann, A. Toward Drug Release Using Polymer Mechanochemical Disulfide Scission. *Journal of the American Chemical Society* **142**, 14725-14732, doi:10.1021/jacs.0c07077 (2020).

123 Monod, J., Changeux, J.-P. & Jacob, F. Allosteric proteins and cellular control systems. *Journal of Molecular Biology* **6**, 306-329, doi:10.1016/s0022-2836(63)80091-1 (1963).
124 Guo, J. & Zhou, H.-X. Protein Allostery and Conformational Dynamics. *Chemical Reviews* **116**, 6503-6515, doi:10.1021/acs.chemrev.5b00590 (2016).
125 Wodak, S. J. *et al.* Allostery in Its Many Disguises: From Theory to Applications. *Structure* **27**, 566-578, doi:10.1016/j.str.2019.01.003 (2019).
126 Thirumalai, D., Hyeon, C., Zhuravlev, P. I. & Lorimer, G. H. Symmetry, Rigidity, and Allosteric Signaling: From Monomeric Proteins to Molecular Machines. *Chem. Rev. (Washington, DC, U. S.)* **119**, 6788-6821, doi:10.1021/acs.chemrev.8b00760 (2019).
127 Berezovsky, I. N. Thermodynamics of allostery paves a way to allosteric drugs. *Bba-Proteins Proteom* **1834**, 830-835, doi:10.1016/j.bbapap.2013.01.024 (2013).
128 Raynal, M., Ballester, P., Vidal-Ferran, A. & van Leeuwen, P. W. N. M. Supramolecular catalysis. Part 2: artificial enzyme mimics. *Chem. Soc. Rev.* **43**, 1734-1787, doi:10.1039/c3cs60037h (2014).
129 Kovbasyuk, L. & Krämer, R. Allosteric Supramolecular Receptors and Catalysts. *Chemical Reviews* **104**, 3161-3188, doi:10.1021/cr030673a (2004).
130 Henkelis, J. J. *et al.* Allosteric Modulation of Substrate Binding within a Tetracationic Molecular Receptor. *Journal of the American Chemical Society* **137**, 13252-13255, doi:10.1021/jacs.5b08656 (2015).
131 Fukuhara, G. Allosteric signal-amplification sensing with polymer-based supramolecular hosts. *Journal of Inclusion Phenomena and Macrocyclic Chemistry* **93**, 127-143, doi:10.1007/s10847-019-00881-2 (2019).
132 Casey, C. P. & Whiteker, G. T. The Natural Bite Angle of Chelating Diphosphines. *Israel Journal of Chemistry* **30**, 299-304, doi:10.1002/ijch.199000031 (1990).
133 Dierkes, P. & van Leeuwen, P. W. N. M. The bite angle makes the difference: a practical ligand parameter for diphosphine ligands. *Journal of the Chemical Society, Dalton Transactions*, 1519-1530, doi:10.1039/a807799a (1999).
134 Akbulatov, S. *et al.* Experimentally realized mechanochemistry distinct from force-accelerated scission of loaded bonds. *Science (Washington, DC, U. S.)* **357**, 299-303, doi:10.1126/science.aan1026 (2017).
135 Santos, O. M. M. *et al.* Protonation Pattern, Tautomerism, Conformerism, and Physicochemical Analysis in New Crystal Forms of the Antibiotic Doxycycline. *Cryst Growth Des* **14**, 3711-3726, doi:10.1021/cg500877z (2014).
136 Ozturk, S., Shahabi, S. & Kutuk, H. Kinetics and Mechanisms of Acid-Catalyzed Hydrolysis of Some N-(4-Substitutedaryl) Succinimide Compounds. *J Chem Soc Pakistan* **44**, 186-193, doi:10.52568/000998/Jcsp/44.02.2022 (2022).
137 Staab, H. A. & Saupe, T. Proton Sponges and the Geometry of Hydrogen-Bonds - Aromatic Nitrogen Bases with Exceptional Basicities. *Angewandte Chemie-International Edition in English* **27**, 865-879, doi:DOI 10.1002/anie.198808653 (1988).
138 Emmett, M. Metabolic Alkalosis A Brief Pathophysiologic Review. *Clin J Am Soc Nephro* **15**, 1848-1856, doi:10.2215/Cjn.16041219 (2020).
139 Peters, M. V., Stoll, R. S., Kuehn, A. & Hecht, S. Photoswitching of basicity. *Angew Chem Int Edit* **47**, 5968-5972, doi:10.1002/anie.200802050 (2008).
140 Samanta, S., Babalhavaeji, A., Dong, M. X. & Woolley, G. A. Photoswitching of ortho-Substituted Azonium Ions by Red Light in Whole Blood. *Angew Chem Int Edit* **52**, 14127-14130, doi:10.1002/anie.201306352 (2013).

141 Koeppe, B., Ruhl, S. & Rompp, F. Towards More Effective, Reversible pH Control by Visible Light Alone: A Thioindigo Photoswitch Undergoing a Strong pK(a) Modulation by Isomer-Specific Hydrogen Bonding. *Chemphotochem* **3**, 71-74, doi:10.1002/cptc.201800209 (2019).
142 Szymanski, W., Beierle, J. M., Kistemaker, H. A. V., Velema, W. A. & Feringa, B. L. Reversible Photocontrol of Biological Systems by the Incorporation of Molecular Photoswitches. *Chemical Reviews* **113**, 6114-6178, doi:10.1021/cr300179f (2013).
143 Weston, C. E., Richardson, R. D. & Fuchter, M. J. Photoswitchable basicity through the use of azoheteroarenes. *Chem Commun* **52**, 4521-4524, doi:10.1039/c5cc10380k (2016).
144 Gurke, J., Budzak, S., Schmidt, B. M., Jacquemin, D. & Hecht, S. Efficient Light-Induced pK(a) Modulation Coupled to Base-Catalyzed Photochromism. *Angew Chem Int Edit* **57**, 4797-4801, doi:10.1002/anie.201801270 (2018).
145 Lin, Y., Kouznetsova, T. B. & Craig, S. L. A Latent Mechanoacid for Time-Stamped Mechanochromism and Chemical Signaling in Polymeric Materials. *J. Am. Chem. Soc.* **142**, 99-103, doi:10.1021/jacs.9b12861 (2020).
146 Nagamani, C., Liu, H. & Moore, J. S. Mechanogeneration of Acid from Oxime Sulfonates. *J. Am. Chem. Soc.* **138**, 2540-2543, doi:10.1021/jacs.6b00097 (2016).
147 Diesendruck, C. E. *et al.* Proton-Coupled Mechanochemical Transduction: A Mechanogenerated Add. *Journal of the American Chemical Society* **134**, 12446-12449, doi:10.1021/ja305645x (2012).
148 Zhang, Y. D. *et al.* Molecular Damage Detection in an Elastomer Nanocomposite with a Coumarin Dimer Mechanophore. *Macromolecular Rapid Communications* **42**, doi:ARTN 2000359

10.1002/marc.202000359 (2021).
149 Gostl. R, C. J. M., Sijbesma. in *Mechanochemistry in Materials* (ed Y Simon. C, Craig. L. S.) Ch. 3, (The Royal Society of Chemistry, 2018).
150 Zhong, M. J., Wang, R., Kawamoto, K., Olsen, B. D. & Johnson, J. A. Quantifying the impact of molecular defects on polymer network elasticity. *Science* **353**, 1264-1268, doi:10.1126/science.aag0184 (2016).
151 Cao, N. P. *et al.* Poly(ethylene glycol) Becomes a Supra-Polyelectrolyte by Capturing Hydronium Ions in Water. *Macromolecules* **55**, 4656-4664, doi:10.1021/acs.macromol.2c00014 (2022).
152 Wang, S. *et al.* Mechanism Dictates Mechanics: A Molecular Substituent Effect in the Macroscopic Fracture of a Covalent Polymer Network. *Journal of the American Chemical Society* **143**, 3714-3718, doi:10.1021/jacs.1c00265 (2021).
153 Haynes, W. M. *CRC Handbook of Chemistry and Physics*. 97th edn, (CRC PRESS, 2016).
154 Huang, Z. & Boulatov, R. Chemomechanics with molecular force probes. *Pure Appl. Chem.* **82**, 931-951, doi:10.1351/pac-con-09-11-36 (2010).
155 Passera, A., Iuliano, A., Perez-Torrente, J. J. & Passarelli, V. Mechanistic insights into the tropo-inversion of the biphenyl moiety in chiral bis-amido phosphites and in their palladium(II) complexes. *Dalton T* **47**, 2292-2305, doi:10.1039/c7dt04829g (2018).
156 Mazzanti, A., Chiarucci, M., Prati, L., Bentley, K. W. & Wolf, C. Computational and DNMR Analysis of the Conformational Isomers and Stereodynamics of Secondary 2,2'-Bisanilides. *J Org Chem* **81**, 89-99, doi:10.1021/acs.joc.5b02330 (2016).

157 Maslak, P. *et al.* Optical properties of spiroconjugated charge-transfer dyes. *Journal of the American Chemical Society* **118**, 1471-1481, doi:DOI 10.1021/ja9533003 (1996).
158 Scarborough, C. C. *et al.* Pd-II complexes possessing a seven-membered N-heterocyclic carbene ligand. *Angew Chem Int Edit* **44**, 5269-5272, doi:10.1002/anie.200501522 (2005).
159 Aharonovich, S., Gjineci, N., Dekel, D. R. & Diesendruck, C. E. An Effective Synthesis of N,N-Diphenyl Carbazolium Salts. *Synlett* **29**, doi:10.1055/s-0036-1591848 (2018).
160 Wada, S., Urano, M. & Suzuki, H. The newborn surface of dull metals in organic synthesis. Bismuth-mediated solvent-free one-step conversion of nitroarenes to azoxy- and azoarenes. *J Org Chem* **67**, 8254-8257, doi:10.1021/jo0203645 (2002).
161 Kaur, J. & Pal, B. Selective formation of benzo[c]cinnoline by photocatalytic reduction of 2,2 '-dinitrobiphenyl using TiO2 and under UV light irradiation. *Chem Commun* **51**, 8500-8503, doi:10.1039/c5cc02713f (2015).
162 Jung, K. H. *et al.* Gd Complexes of DO3A-(Biphenyl-2,2 '-bisamides) Conjugates as MRI Blood-Pool Contrast Agents. *Acs Med Chem Lett* **3**, 1003-1007, doi:10.1021/ml300223b (2012).